BALLOON-TYPE CLT SHEARWALLS:

LATERAL DEFORMATION AND KINEMATIC BEHAVIOURS

by

Dalu Xing

Thesis submitted to the University of Ottawa

in partial fulfillment of the requirements for the degree of

Doctor of Philosophy

in Civil Engineering

Under the auspices of the Ottawa-Carleton Institute for Civil Engineering

Department of Civil Engineering

Faculty of Engineering

University of Ottawa

Abstract

Balloon-type Cross-Laminated Timber (CLT) shearwall systems have been increasingly adopted as lateral load-resisting systems in mid-rise timber buildings. Compared with platform-type configurations, balloon-type shearwalls mitigate bearing failure associated with perpendicular-to-grain compression at floor levels, while also reducing cumulative vertical shrinkage and the number of structural connectors and panels. Despite these advantages, research on balloon-type CLT shearwalls remains limited, and their behaviour is not explicitly addressed in many current timber design codes.

This thesis presents a comprehensive investigation of the lateral deformation behaviour and kinematic mechanisms of balloon-type CLT shearwall systems through a combined analytical, numerical, and experimental approach. A parametric sensitivity analysis was first conducted using finite-element (FE) modelling to examine the influence of hold-down stiffness, vertical joint stiffness, panel aspect ratio, number of panels and vertical loading on lateral stiffness, kinematic modes, and deformation components of multi-panel shearwalls. The results demonstrate that bending deformation is a fundamental component of the lateral response of balloon-type shearwalls, and that kinematic mode transitions significantly affect the contribution of rocking deformation.

Based on these observations, an analytical model was developed to estimate the total lateral displacement of balloon-type CLT shearwalls. The model accounts for bending deformation using the γ-method, as well as shear and rocking deformation components, initially formulated for a two-panel configuration. Validation against FE simulations showed good agreement, with the analytical predictions of top lateral displacement exhibiting an average error of less than 5%.

A full-scale experimental programme was subsequently carried out on eleven two-storey multi-panel balloon-type CLT shearwall specimens. The test matrix covered a wide range of parameters, including the number of hold-downs (one to four), number of vertical joints (eight to sixty-five), panel aspect ratio (4.17 to 8.33), and the number of panels (one to four). The experimental results provided detailed insight into deformation sequences, failure mechanisms, kinematic modes and deformation compatibility among panels.

A systematic comparison between experimental results and corresponding analytical and numerical predictions was performed, highlighting both consistencies and sources of discrepancy. The findings confirm the validity of the proposed analytical framework while also identifying its limitations.

Overall, this research advances the understanding of deformation and kinematic mechanisms in balloon-type CLT shearwalls and provides a foundation for further development of analytical models and future design provisions. The results demonstrate that bending deformation represents a significant component of the lateral response of balloon-type CLT shearwalls and should not be neglected in the deformation prediction. The study also shows that the kinematic behaviour of multi-panel shearwalls is strongly influenced by panel aspect ratio and connector stiffness, which govern the contribution of rocking deformation and the transition of kinematic modes. Experimental observations further indicate that hold-down failure is generally the governing failure mechanism. Moreover, for a given total wall width, the use of slender panels can significantly enhance deformation capacity without reducing lateral resistance, providing favourable implications for the seismic design of balloon-type CLT shearwall systems.

Acknowledgements

I would like to express my deepest gratitude to my supervisor, Prof. Ghasan Doudak, for his continuous and patient guidance, encouragement, and support throughout my doctoral studies. His broad vision, academic rigour, and trust have been invaluable to my development as a researcher. Through his thoughtful guidance and critical insight, he consistently helped me focus on the core scientific questions and maintain clarity and direction in my research. His long-term support and trust in my abilities provided both reassurance and motivation, forming a solid foundation for my academic and professional growth. I am also sincerely grateful to Dr. Daniele Casagrande for his meticulous supervision, insightful discussions, and constant guidance over the years. His dedication to research and rigorous way of thinking have profoundly shaped both my work and my approach to scientific inquiry.

I would like to acknowledge Dr. Muslim Majeed and Dr. Gamal Elnabelsy for their valuable assistance and constructive suggestions during the experimental programme. I am grateful to Dr. Mohammad Masroor for his support during the early stages of the project, Antoine Bérubé and Esmaeil Morshedi for their help in my testing and all other my colleagues in the research group for their collaboration and generosity. I also thank the experimental assistants, including Tom Martin**,** Jiachen Hu, and others, for their contributions, as well as the campus machine shop for the assistance with the welding work, which greatly facilitated the experimental programme.

Finally, I would like to express my heartfelt gratitude to my family for their constant love and support throughout this journey. I especially wish to remember my grandfather, who rests in peace, and whose affection and spirit continue to inspire me along this path. Their love and belief in me have made this achievement possible.

Table of Contents

Abstract ii

Acknowledgements iv

Table of Contents v

List of Tables ix

Table of symbols and notations xvi

List of definitions xxi

1. Introduction 2

 1.1. Background 2

 1.2. Objectives, methodology and contributions 6

 1.3. Scope and limitations 8

 1.4. Organisation of thesis 10

2. Literature review 12

 2.1. Materials and connections of CLT shearwall systems 12

 2.2. CLT Shearwall systems 14

  2.2.1. Experimental investigations 14

  2.2.2. Numerical analysis 17

  2.2.3. Analytical models 18

 2.3. Current codes and standards 19

2.4. Summary 20

3. Sensitivity analysis.. 23

3.1. Validation of the numerical model 23

3.2. Description of the FE model 26

3.3. Description of the model configuration and parameters 29

3.4. Results and discussions of two-panel models 31

3.4.1. The impact of the stiffness of connectors and aspect ratios 33

3.4.2. The impact of vertical loads 41

3.5. Shearwalls consisting of more than two panels 42

4. Analytical model 47

4.1. Model assumptions 47

4.2. Bending deformation 50

4.3. Shear deformation 57

4.4. Rocking deformation 58

4.4.1. CP mode 59

4.4.2. SW mode 61

4.5. Verification of the proposed model 63

4.5.1. Bending and shear deformation 63

4.5.2. Rocking deformation 65

4.5.3. Verification of the total wall deformation 66

5. Full-scale shearwall tests 72
5.1. Materials and properties 72
5.2. Test set-up and load protocol 78
5.3. Test results 85
5.3.1. Deformation sequence and failure mechanism 85
5.3.2. Kinematic modes and deformation characteristics 98
6. Discussion on the experimental, numerical and analytical model 108
6.1. Lateral resistance and stiffness of tested shearwalls 108
6.2. Rocking deformation of tested shearwalls 119
6.3. Numerical model 122
6.4. Analytical model 127
6.5. Comparisons between modelling techniques and experimental results 129
7. Conclusions and future research studies 144
7.1. Conclusions 144
7.2. Future research studies 146
References 148
Appendix A. 162
Construction details of the steel foundation beam and lateral sliding restraint 162
A.1. Steel foundation beam 162
A.2. Steel sliding restraint 162

Appendix B. 175
Correction for deformation of the steel foundation beam 175
B.1. Definition of corrected displacement 175
B.2. Instrumentation and monitored points 175
B.3. Rocking component induced by foundation-beam rotation 176
B.4. Estimation of foundation-beam movement for early-stage tests 177
B.5. Correction procedure 179
Appendix C. 190
Estimation of mechanical properties of the foundation beam 190
Appendix D. 192
Re-evaluation of tensile stiffness of hold-down for specimen W0.6-P2-H2V8a 192

List of Tables

Table 3.1: Comparison of maximum lateral deformations from the model M9/1-P2-VL0-H10V15 26

Table 3.2: Basic parameters of FE models 30

Table 3.3: Aspect ratio matrix for modelling analysis 30

Table 3.4: Percentage of CP mode with varying k_{hd} 39

Table 3.5: Percentage of SW mode with varying k_{vj}/h 39

Table 4.1: The values of p_0 and q_0 58

Table 4.2: Values of γ in varying aspect ratios and vertical stiffness 63

Table 4.3: Values of $(EI)_{eff}$ in varying aspect ratio and vertical stiffness 63

Table 4.4: Values of $\Delta_{bending+shear}$ in varying aspect ratios and vertical stiffness 64

Table 4.5: The total deformation calculated from the analytical model and FE model 67

Table 5.1: Details of the metal connections 74

Table 5.2: Materials and properties 75

Table 5.3: Test matrix 76

Table 5.4: Displacement details (along the direction of the height of walls) at the bottom of each panel at peak loads 106

Table 6.1: Mechanical properties of shearwalls 110

Table 6.2: Basic parameters used in the analytical model and estimated total lateral deformation 128

Table 6.3: Comparisons of peak lateral load, corresponding displacement and lateral stiffness of specimens between FE modelling and testing results 142

List of Figures

Figure 1.1: Example of the configuration of a 5-layer CLT panel 2

Figure 1.2: Example of balloon-type construction: Photographs from the 13-storey Origine building in Quebec City, Canada (2018) (photographed by Stéphane Groleau; source: https://www.nordic.ca/en/projects/structures/origine). 3

Figure 1.3: (a) Platform-type and (b) balloon-type CLT structural system................................. 4

Figure 1.4: Another example of balloon-type construction: Photographs from the Arbora Condos project in Griffintown, Montreal.. 5

Figure 3.1: (a) Duplicated shearwall configuration and (b) FE model....................................... 24

Figure 3.2: The mechanical properties of (a) lateral restraints (b) vertical joints along the horizontal and vertical axes (c) hold-downs along the horizontal and vertical axes 25

Figure 3.3: Comparison between the load-displacement curves of monotonic loading test (Chen and Popovski, 2020) and pushover modelling. 25

Figure 3.4: (a) Three-storey two-panel balloon-type CLT shearwall model and (b) the details of connections of FE modelling as an example.. 28

Figure 3.5: Examples of deformed numerical FE models following the defined naming convention.. 31

Figure 3.6: $\Delta_{rocking}$ and Δ_{total} defined in (a) CP mode and (b) SW mode 32

Figure 3.7: Relationship between normalised total lateral stiffness K_{hd}^{*} and k_{hd} when k_{vj}/h equals 7.5 kN/mm/m and vertical loads equal zero, with b=1 m (a); b=2 m (b); b=3 m (c) 33

Figure 3.8: Relationship between normalised total lateral stiffness K_{hd}^{*} and k_{hd} when k_{vj}/h equals 7.5 kN/mm/m (V7.5) for the same aspect ratios equal to 3 without vertical loads (VL0) 34

Figure 3.9: Stiffness of the hold-downs for which the transition from SW to CP is achieved versus aspect ratio (a) and height (b) of panels when k_{vj}/h equals 7.5 kN/mm/m (V7.5) without vertical loads (VL0) 35

Figure 3.10: Relationship between the normalised total lateral stiffness K^*_{vj} and unit vertical joints stiffness k_{vj}/h when k_{hd} equals 50 kN/mm (H50), and vertical loads equal 20 kN/m (VL20), with b=1 m (a); b=2 m (b); b=3 m (c)... 37

Figure 3.11: Relationship between the normalised total lateral stiffness K^*_{vj} and unit vertical joints stiffness k_{vj}/h when k_{hd} equals 25 kN/mm (H25), and vertical loads equal 20 kN/m (VL20), with b=1 m (a); b=2 m (b); b=3 m (c)... 38

Figure 3.12: Stiffness of vertical joints for which the transition from CP to SW is achieved versus the height of panels when k_{hd} equals 25 kN/mm (H25) and vertical loads equal 20 kN/m (VL20)... 39

Figure 3.13: Relationship (a) between rocking percentage and k_{hd}, (b) between rocking percentage and k_{vj}/h, (c) between bending percentage and k_{hd}, (d) between bending percentage and k_{vj}/h, (e) between shear percentage and k_{hd}, and (f) between shear percentage and k_{vj}/h when vertical loads equal to 20kN/m for all cases. 41

Figure 3.14: Impact of the vertical loads on the total lateral stiffness with (A) b=1m (B) b=2m (C) b=3m.. 42

Figure 3.15: FE models of multi-panel CLT shearwalls 43

Figure 3.16: Relationship between the number of panels and K when h/B is fixed to be 12:4 and vertical loads equal to 20 kN/m 43

Figure 3.17: Relationship between the number of panels and rocking percentage for the models when h/B is fixed to be 12:4 and vertical loads equal to 20 kN/m 44

Figure 3.18: Kinematic modes of the models with varying panel numbers 45

Figure 3.19: Relationship between the number of panels and K when h/b is fixed to be 12:1 and vertical loads equal to 20 kN/m 45

Figure 4.1: (a) Analytical model and (b) Simplified model for estimating bending deformation48

Figure 4.2: Components of the lateral deformation of the balloon-type CLT panel 49

Figure 4.3: Definition of variable a_i for a 5-layer CLT shearwall 51

Figure 4.4: Impact of the vertical joints on the flexural deformation of the two-panel shearwall system 52

Figure 4.5: Reactions and the stress distribution of the cross-section of the panels.................... 55

Figure 4.6: Sketch of the relationship between Δ_{hd} and Δ_{vj} for (a) CP mode (b) SW mode...... 59

Figure 4.7: Force analysis based on free-body diagrams for CP mode 61

Figure 4.8: Force analysis based on free-body diagrams for SW mode 62

Figure 4.9: Comparisons between the values of $\varDelta_{bending+shear}$ obtained from the FE numerical modelling result and the analytical expression 65

Figure 4.10: Comparisons between the values of $\varDelta_{rocking}$ obtained from the FE numerical modelling result and the analytical expression 66

Figure 5.1: Test specimens and comparative groups 77

Figure 5.2: An overview of test setup with the details of hold-downs and vertical joints system 83

Figure 5.3: Displacement monitored points by LVDTs 84

Figure 5.4: Structural deformation development of specimen W0.6-P2-H1V32 under the lateral loads 87

Figure 5.5: Structural deformation of specimens W1.2-P1-H2 and W0.6-P2-H2V8a under the lateral loads 89

Figure 5.6: Rupture and deformation characteristics of connectors in specimen W0.6-P2-H2V8a 92

Figure 5.7: Failure mode and details of specimen W0.6-P2-H2V8b........ 93

Figure 5.8: Failure comparison between specimens W0.6-P4-H2V32a, W0.8-P3-H2V32, and W1.2-P2-H2V32 96

Figure 5.9: Failure details of specimen W0.6-P4-H2V32b 98

Figure 5.10: Monitored points for measuring the tensile displacement of hold-downs (P_1) and tracing the kinematic modes of shearwalls (P_6) for specimens W0.6-P2-H1V32, W0.6-P2-H2V32 and W0.6-P2-H4V32 99

Figure 5.11: Monitored points for measuring the tensile displacement of hold-downs (P_1) and tracing the kinematic modes of shearwalls (P_6) for specimens W1.2-P1-H2, W0.6-P2-H2V32, W0.6-P2-H2V8a and W0.6-P2-H2V8b 101

Figure 5.12: Comparison of slip displacements measured at the top and the bottom of the interface between two panels from specimen W0.6-P2-H2V8a........ 101

Figure 5.13: Details of the kinematic modes varying with time in specimens (a) W1.2-P2-H2V32, (b) W0.8-P3-H2V32 and (c) W0.6-P4-H2V32a. 104

Figure 5.14: Comparison of the kinematic modes before and after the panel cracking near the hold-down for specimen W0.6-P4-H2V32b........ 105

Figure 6.1: Comparison of load-displacement curves between specimens W0.6-P2-H1V32, W0.6-P2-H2V32 and W0.6-P2-H4V32........ 109

Figure 6.2: Comparison of load-displacement curves between specimens (a) W1.2-P1-H2, W0.6-P2-H2V32, and W0.6-P2-H2V8a, (b) W0.6-P2-H2V8a and W0.6-P2-H2V8b 113

Figure 6.3: Comparison of load-displacement curves between specimens W0.6-P2-H1V32 and W0.6-P2-H1V65 114

Figure 6.4: Comparison of load-displacement curves between specimens (a) W1.2-P2-H2V32, W0.8-P3-H2V32, W0.6-P4-H2V32a; (b) W0.6-P4-H2V32a and W0.6-P4-H2V32b............... 116

Figure 6.5: Comparisons of the load-displacement curves of specimens (a) W0.6-P2-H2V32 versus W0.6-P4-H2V32a, and (b) W1.2-P1-H2 versus W1.2-P2-H2V32 118

Figure 6.6: Percentage of rocking deformation with the varying number of (a) hold-downs and (b) vertical joints at $0.4F_{peak}$ 120

Figure 6.7: Rocking percentage at $0.4F_{peak}$ and F_{peak} 121

Figure 6.8: Mechanical properties of hold-down and vertical joint (a) hold-down tension, (b) hold-down shear and (c) vertical joint shear (Masroor et al., 2024).. 124

Figure 6.9: Numerical model for specimen S5/0.6-P2-H2V32 in both conditions (a) with and (b) without foundation 125

Figure 6.10: Mechanical properties of the foundation beam movement along (a) y-axis direction and (b) x-axis direction in FE modelling 126

Figure 6.11: Comparisons between experimental results, FE numerical modelling and analytical estimation for the tested specimens 139

Figure 6.12: (a) Corrected hold-down uplift property, and (b) corrected FE modelling curves with foundation and (c) without foundation for specimen W0.6-P2-H2V8a 141

Figure A.1: Drawings of steel foundation beam... 170

Figure A.2: Drawings of steel sliding restraint... 174

Figure B.1: Displacement monitor points on the foundation beam 176

Figure B.2: Rotation development of the foundation beam in the loading process of specimen W0.8-P3-H2V32 as an example 177

Figure B.3: Load-displacement relationships measured at Point B (uplift displacement in the vertical direction) and Point C (lateral sliding displacement) for specimens W0.6-P4-H2V32, W0.8-P3-H2V32, and W1.2-P2-H2V32, together with the corresponding averaged polynomial fitting curves used for estimating movement of the foundation beam....................................... 179

Figure B.4: Calculated results of $\Delta_{rocking,B}$ and $\Delta_{sliding,B}$ for tested specimens...................... 189

Figure C.1: Simplified static force model of the shearwall-foundation beam system used for estimating the equivalent spring properties of the steel foundation beam................................. 191

Table of symbols and notations

$\boldsymbol{A}$	Total cross-section area of the shearwall resisting system
$\boldsymbol{A_0}$	Cross-section area of each panel
$\boldsymbol{B}$	Total width of shearwall system
$\boldsymbol{D}$	Distance between the centroid of two panels
$\boldsymbol{E}$	Modulus of elasticity or Young's modulus
$\boldsymbol{E_L}$	Modulus of elasticity of longitudinal layers (parallel to grain)
$\boldsymbol{E_T}$	Modulus of elasticity of transverse layers (parallel to grain)
$\boldsymbol{E_0}$	Modulus of elasticity parallel to grain
$\boldsymbol{E_{90}}$	Modulus of elasticity perpendicular to grain
$\boldsymbol{E_{0,eff}}$	Effective modulus of elasticity along the vertical direction (parallel to the outer-layer grain)
$\boldsymbol{E_{90,eff}}$	Effective modulus of elasticity along the lateral direction (perpendicular to the outer-layer grain)
$\boldsymbol{EA}$	Axial stiffness of entire shearwall system
$\boldsymbol{EA_i}$	Axial stiffness of the panel *i*
$\boldsymbol{EA_0}$	Axial stiffness of each panel when dimensions of two panels are the same
$\boldsymbol{EI}$	Bending stiffness of the shearwall system without composite behaviour
$\boldsymbol{EI_i}$	Bending stiffness of the panel *i*
$\boldsymbol{EI_0}$	Bending stiffness of each panel when dimensions of two panels are the same
$\boldsymbol{EI_{eff}}$	Effective bending stiffness of shearwall system
$\boldsymbol{F_{hd}}$	Tensile force of hold-down
$\boldsymbol{F_{vj}}$	Total shear force vertical joints
$\boldsymbol{F_T}$	Total lateral load applied on shearwalls
$\boldsymbol{F}$	Lateral load applied on each storey
$\boldsymbol{F_i}$	Lateral load applied on the i^{th} storey

$\boldsymbol{F_{sl}}$	Total horizontal shear force transferred at the wall-foundation interface
$\boldsymbol{F_1}$, $\boldsymbol{F_2}$	Distributed horizontal forces at each storey on the first and second panel
$\boldsymbol{F_{max}}$, $\boldsymbol{F_{peak}}$	Peak lateral load applied on tested specimens
$\boldsymbol{F_u}$	Ultimate load applied on tested specimens
$\boldsymbol{G}$	Shear modulus
$\boldsymbol{G_0}$	In-plane shear modulus of laminas
$\boldsymbol{G_{90}}$	Rolling shear modulus
$\boldsymbol{G^*}$	Effective in-plane shear modulus
$\boldsymbol{I}$	Effective second moment of inertia
$\boldsymbol{I_0}$	Effective second moment of inertia of each panel
$\boldsymbol{I_{eff}}$	Total effective second moment of inertia
$\boldsymbol{K}$	Total lateral stiffness of shearwall system
$\boldsymbol{K^*}$	Normalised total lateral stiffness of shearwall system
$\boldsymbol{K^*_{hd}}$	Ratio between *K* and specific total lateral stiffness value when k_{hd} is 10kN/mm
$\boldsymbol{K^*_{vj}}$	Ratio between *K* and specific total lateral stiffness value when *k* is 3kN/mm/m
$\boldsymbol{K_{l,40}}$	Estimated lateral stiffness of tested shearwall specimens
$\boldsymbol{N(x)}$	Function of the axial force on each panel
$\boldsymbol{P}$	Number of panels in a shearwall system
$\boldsymbol{R_{1,y}}$, $\boldsymbol{R_{2,y}}$	Vertical reactions of the first and second panel
$\boldsymbol{R_{Point\ A}}$	Reaction force (y-direction) of the equivalent spring placed at Point A
$\boldsymbol{R_{Point\ B}}$	Reaction force (y-direction) of the equivalent spring placed at Point B
$\boldsymbol{R_{Point\ C}}$	Reaction force (x-direction) of the equivalent spring placed at Point C
$\boldsymbol{S_{vj,\ max}}$	Maximum shear resistance of vertical joints from connection tests
$\boldsymbol{S_{vj,\ u}}$	Ultimate shear resistance of vertical joints from connection tests
$\boldsymbol{T}$	Total thickness of wall panel
$\boldsymbol{T_0}$	Total thickness of laminae with grain direction parallel to the wall height

T_{90}	Total thickness of laminae with grain direction perpendicular to the wall height
$T_{hd,\ max}$	Maximum tensile resistance of hold-down from connection tests
$T_{hd,\ u}$	Ultimate tensile resistance of hold-down from connection tests
a_i	Sum of the specific layers
a_1	Distance between the centroid and the neutral axis of the first panel
a_2	Distance between the neutral axis of the first panel and the centroid of the second panel
b	Width of each wall panel
d	Distance between point B and rotation centre defined on steel foundation beam
h	Total height of wall panels
h_{eff}	Effective height of wall panels
h_i	Height of the i^{th} storey
h_{int}	Height of each storey
k	Shear stiffness of vertical joints per unit length
k_3	Compositions factor for CLT panels when in-plane loads are applied perpendicular to the outermost-layer fibres
k_{ea}	Stiffness of each vertical joint
k_f	Compressive stiffness of the foundation in FE modelling
k_{hd}	Tensile stiffness of hold-down
k_{hd}*	Normalised tensile stiffness of hold-down
k_{vj}	Total shear stiffness of vertical joints
k_{vj}*	Normalised total shear stiffness of vertical joints
k_{sl}	Horizontal stiffness of angle brackets
$\widetilde{k}$	Relative stiffness defined as ratio between k_{hd} and k_{vj}
m	Number of total layers of CLT panel
n	Number of storeys spanned by the shearwall system
n_r	Number of rows of vertical joints

p_0, q_0	Parameters in determining value of α_T
q	Uniformly distributed vertical load applied at each floor
$q(x)$	Function of the lateral loads
s_{eff}	Spacing between vertical joints along the vertical direction
t	Thickness of each lamina
t_{mean}	Mean thickness of each laminar layer of CLT panels
w_l	Width of each lamina strip
$w(x)$	Function of lateral deflection
Δ_{hd}	Tensile displacement (uplift) of hold-down
Δ_{vj}	Shear displacement (slip) of vertical joints between two panels
Δ_{total}	Total lateral displacement of shearwalls
$\Delta_{bending}$	Lateral deformation of shearwalls caused by bending
Δ_{shear}	Lateral deformation of shearwalls caused by shear
$\Delta_{sliding}$	Lateral deformation of shearwalls caused by sliding
$\Delta_{rocking}$	Lateral deformation of shearwalls caused by rocking
$\Delta_{rocking,CP}$	Rocking deformation under CP mode
$\Delta_{rocking,SW}$	Rocking deformation under SW mode
Δ_{max}	Lateral displacement of tested shearwall specimens at peak load
Δ_u	Ultimate displacement of tested shearwall specimens
$\Delta_{total,C}$	Total lateral displacement at the top of tested shearwall specimens
$\Delta_{total,G}$	Gross total lateral displacement measured at the top of shearwalls Corrected
$\Delta_{rocking,B}$	Displacement component induced by rotation of the foundation beam
$\Delta_{sliding,B}$	Displacement component induced by rigid-body translation (sliding) of the foundation beam
$\Delta_{Point\ A}$	Vertical displacement measured at Point A on the foundation beam
$\Delta_{Point\ B}$	Vertical displacement measured at Point B on the foundation beam

$\Delta_{Point\ C}$	Lateral displacement measured at Point C on the foundation beam
$\Delta_{T\text{-}hd,\ max}$	Tensile displacement at the maximum resistance of hold-down
$\Delta_{T\text{-}hd,\ u}$	Ultimate tensile displacement of hold-down
$\Delta_{S\text{-}vj,\ max}$	Shear (slip) displacement at the maximum resistance of vertical joint
$\Delta_{S\text{-}vj,\ u}$	Ultimate shear displacement of vertical joint
$\boldsymbol{\alpha_T}$	Correction factor in determining the value of G^*
$\boldsymbol{\gamma}, \boldsymbol{\gamma_1}, \boldsymbol{\gamma_2}$	Correction parameters in determining the value of EI_{eff}
$\boldsymbol{\kappa}$	Form factor for cross-section area in determining the value of Δ_{shear}
$\boldsymbol{\theta}$	Rotation angle of panels in rocking deformation
$\boldsymbol{\varphi}$	Rotation angle of the foundation beam under lateral loads
$\boldsymbol{\Phi}$	Diameter of circular cross-section or openings
$\boldsymbol{\varepsilon}$	Error between FE modelling and testing results

List of definitions

Aspect ratio (*h/b*): the ratio of the height to the width of an individual wall panel.

Coupled-panel (CP) behaviour: the kinematic mode in which individual panels rotate about their respective local rotation points.

Single-wall (SW) behaviour: the kinematic mode in which the entire shearwall system rotates about a single rotation centre located at one end of the wall.

Intermediate (IN) behaviour: a transitional kinematic mode exhibiting characteristics between CP behaviour and SW behaviour.

Longitudinal layer: a CLT layer in which the grain direction is parallel to the longitudinal (major) axis of the panel.

Transverse layer: a CLT layer in which the grain direction is parallel to the transverse (minor) axis of the panel.

Hold-down: a steel connector installed between the wall panel and the foundation to resist uplift forces induced by overturning moments under lateral loading.

Vertical joint: a steel connector installed between adjacent wall panels to provide shear resistance against relative slip induced by lateral loads.

CHAPTER ONE

INTRODUCTION

1. Introduction

1.1. Background

Cross-Laminated Timber (CLT) has been increasingly adopted in mass timber construction since the 1990s (Karacabeyli and Gagnon, 2019). These structural elements are plates that typically comprise of an odd number of lumber layers arranged orthogonally (i.e., at 90 degrees) to each other and bonded along their wide faces using structural adhesives. Some manufacturers would also glue the narrow faces of the boards, however due to the natural development of shrinkage cracks, this technique is less common. The number of layers typically ranges from three to nine, with individual lamina thicknesses varying between 16 mm (5/8 inch) and 51 mm (2 inches), and widths ranging from 60 mm (2.4 inches) to 240 mm (9.5 inches). CLT panels can be manufactured in lengths of up to 18 m (60 feet) and widths of up to 3 m (10 feet). ANSI/APA PRG 320 (ANSI/APA, 2021) governs the manufacturing of CLT panels in North America, while design is performed in accordance with CSA O86 (CSA Group, 2024) and the National Design Specifications (NDS, 2024), in Canada and US, respectively. An example of a typical 5-ply CLT panel is shown in Figure 1.1.

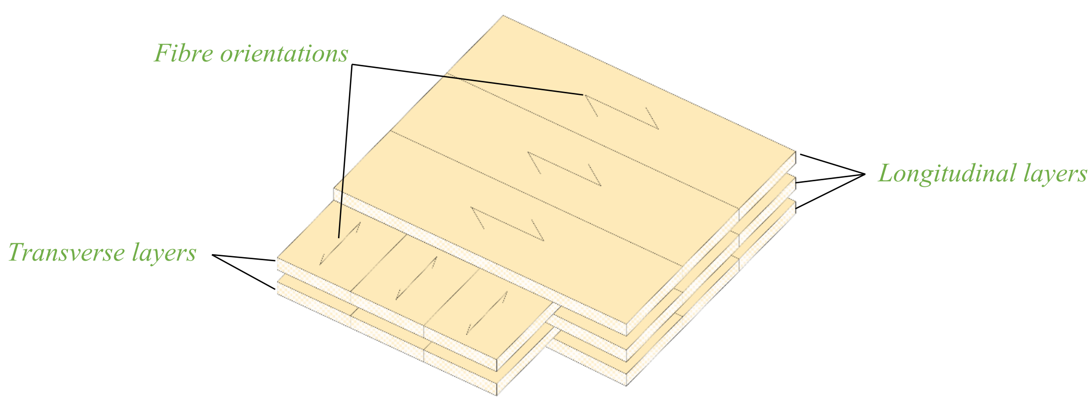

Figure 1.1: *Example of the configuration of a 5-layer CLT panel*

Due to its high in-plane strength and stiffness, ease of handling, favourable strength-to-weight ratio, and excellent thermal and acoustic insulation properties, CLT has been widely utilised in both wall and floor systems. It is particularly prominent in the construction of shearwalls and diaphragm systems that comprise a building's lateral load-resisting system (Blass and Fellmoser, 2004; Brandner and Flatscher, 2016; Izzi et al., 2018). In addition, CLT demonstrates considerable potential in the construction of taller buildings. Notable examples include the 18-storey Brock Commons Tallwood House in British Columbia, Canada (2017), where CLT was used for the floor system while concrete cores were used to resist the lateral loads, and the 13-storey Origine building in Quebec City, Canada (2018) with CLT floors and shearwalls constructed on a concrete podium. The Origine building consists of balloon-type CLT shearwalls akin to those investigated in the present study (Figure 1.2).

Figure 1.2: *Example of balloon-type construction: Photographs from the 13-storey Origine building in Quebec City, Canada (2018) (photographed by Stéphane Groleau[1]; source: https://www.nordic.ca/en/projects/structures/origine).*

Two primary typologies are commonly employed for CLT buildings: platform- and balloon-type construction. In platform-type construction, each floor level is completed with supporting walls, which then serve as a platform for the subsequent upper storey (Figure 1.3a). In contrast, balloon-

[1] *The images are reproduced here with authorisation from the photographer.*

type construction involves continuous shearwalls that extend across multiple storeys, with floor panels connected to the interior face of the walls using various types of angle brackets (Figure 1.3b). Compared to platform-type construction, balloon-type systems offer significant advantages, particularly in avoiding bearing failure (i.e., compression perpendicular to the grain) that typically occurs at floor levels due to the cumulative vertical load from upper storeys. Moreover, balloon-type construction effectively reduces issues related to overall building shrinkage (Karacabeyli and Gagnon, 2019; Dickof et al., 2020; Shahnewaz, Dickof, and Tannert, 2021; Chen and Popovski, 2020), which makes it suitable for application in mid- to high-rise timber construction.

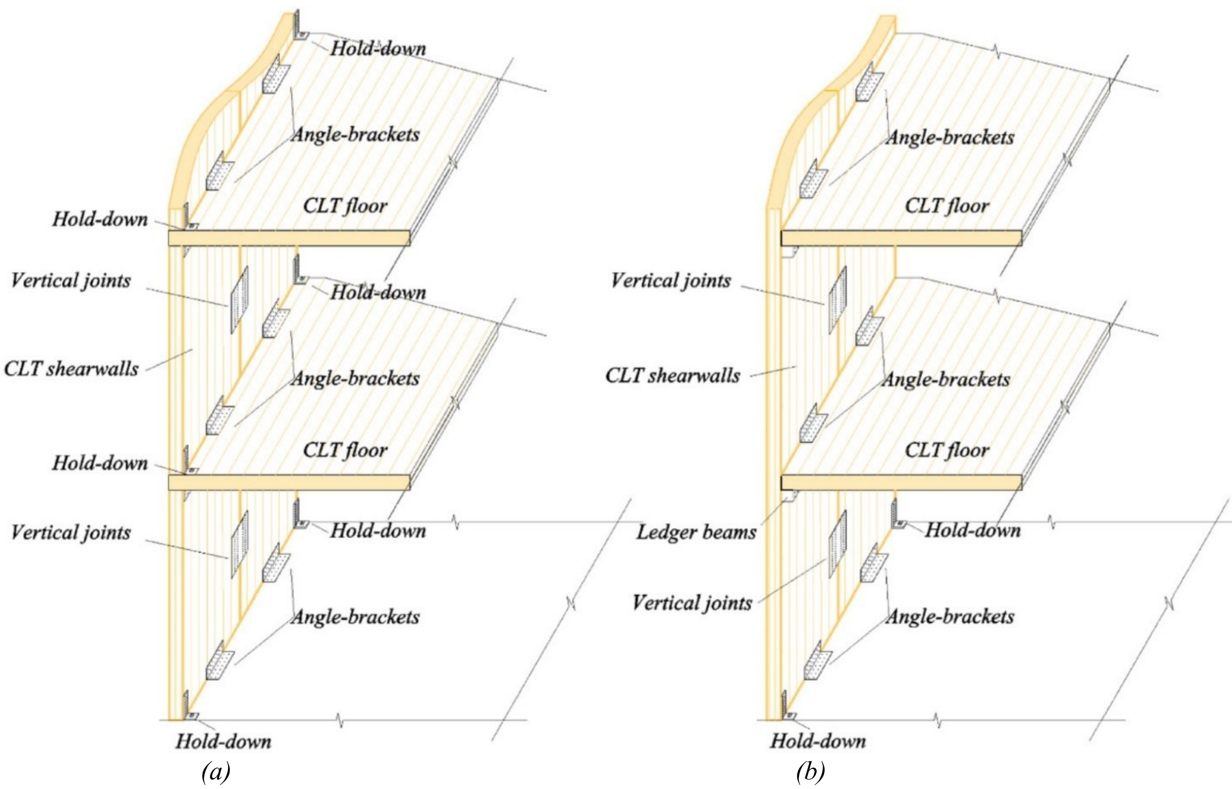

Figure 1.3: *(a) Platform-type and (b) balloon-type CLT structural system*

Recent projects incorporating balloon-type shearwall systems in commercial and public buildings offer valuable precedents for both design practice and academic research. For instance, the Arboretum Project in New Hampshire, United States (AMC, 2019), features a three-storey structure with a central core wall system composed of balloon-type CLT shearwalls, reaching a total height of 14 metres. The aspect ratios (height-to-width, *h/b*) of the panels in this project ranged from 5:1 to 20:1. Similarly, the Edifice 620 Saint-Paul project in Quebec, completed in 2018 (MB, 2017), utilised a balloon-type shearwall core to resist lateral loads, where shearwall height was 13.2 metres, with aspect ratios ranging from 3:1 to 10:1.

Another notable example is the Arbora Condos Griffin town project in Montreal (MB, 2018), which adopted a decentralised layout for the shearwall system. The panels spanned seven storeys, reaching a total height of 23.6 metres. Aspect ratios in this project ranged from 3:1 to 11:1, and each shearwall zone typically consisted of two or three panels (Figure 1.4). These examples offer practical benchmarks, particularly in terms of wall height, panel configuration, and aspect ratio, which serve to guide the parameters and model adopted in the present study.

Figure 1.4: *Another example of balloon-type construction: Photographs from the Arbora Condos project in Griffintown, Montreal.*
(photographed by Adrien Williams[2]; source: https://www.nordic.ca/en/projects/structures/arbora)

[2] *The images are reproduced here with authorisation from the photographer.*

Despite the increasing adoption of balloon-type CLT shearwalls in modern timber construction, the current body of design standards and research remains insufficient. Existing codes and standards, including Eurocode 5 (CEN, 2004) and CSA O86 (CSA Group, 2024), do not provide explicit provisions and details tailored to balloon-type CLT shearwalls. Instead, the design approaches are primarily developed for platform-type assemblies and thus cannot adequately capture the distinctive deformation characters of balloon-type systems.

At the same time, academic investigations on balloon-type CLT shearwalls remain scarce compared with the extensive studies on platform-type configurations. Limited experimental and numerical data are available to quantify the influence of key parameters such as stiffness of hold-down and vertical joints and panel aspect ratio on the lateral response. Consequently, the understanding of their lateral resistance and deformation performance, as well as their failure mechanisms, remains incomplete.

Given the increasing practical implementation of balloon-type CLT construction and the absence of corresponding design provisions, there is a critical need for systematic research to characterise their deformation behaviour and establish reliable design models. The present study therefore seeks to address this knowledge gap and to provide foundational data and analytical insights that can inform future development of design provisions.

1.2. Objectives, methodology and contributions

The overarching goal of this research project is to investigate the lateral deformation contribution and kinematic behaviour of balloon-type CLT shearwall systems. More specifically, the objectives of the study are as follow:

- investigate the critical factors contributing to the lateral deformation of balloon-type CLT shearwalls,
- investigate the individual components' contributions to the total lateral displacement of the shearwalls，
- develop a simplified theoretical model that that can describe the deformation behaviour of two-panel CLT walls,
- validate the accuracy of the developed theoretical models against experimental results.

To address these objectives in a systematic and rigorous manner, the research adopts a methodology comprising the following steps:

1. Literature review:

   A comprehensive review of existing research, design standards, and practical projects is conducted to establish the knowledge base, identify research gaps, and define the scope of the study. This step ensures the proposed work is grounded in existing theory while addressing unmet needs in the field.
2. Numerical modelling and sensitivity analysis:

   A Finite Element (FE) model simulating the behaviour of balloon-type CLT shearwalls is developed to initially explore the influence of key parameters, such as hold-down stiffness, vertical joints (wall-to-wall connectors) stiffness, number of panels and geometrical dimensions (e.g. aspect ratio of a single panel), on lateral deformation. Sensitivity analyses are performed to isolate and evaluate the contribution of each parameter to overall wall performance. The model would later be assessed and validated using the results from the experimental study.

3. Development of a simplified analytical model:

   Based on insights from the numerical study, a simplified analytical model is formulated for predicting the lateral displacement in two-panel balloon-type shearwall configurations. The model integrates the deformation components such as panel rocking, shear, and bending. Its results are compared with those obtained from the numerical simulations.

4. Full-scale experimental testing:

   An experimental program involving full-scale balloon-type CLT shearwall assemblies is undertaken. The testing captures failure mechanisms, load-deformation behaviours and kinematic modes under controlled monotonic lateral loading. The data collected serve both as a validation for the proposed model and as a reference for future design guidelines.

This integrated approach ensures that both theoretical and practical aspects of balloon-type CLT shearwall behaviours are comprehensively addressed, as well as contributes new knowledge to support the development of relevant design provisions.

The main contributions and novelty of this research lie in the identification of the critical parameters influencing lateral deformation through sensitivity analysis, and in the quantification of their respective contributions to the overall deformation response of balloon-type CLT shearwalls. Based on these findings, an analytical framework was developed in which the gamma method was employed to estimate the bending deformation component, while rocking models were formulated to represent different kinematic modes of the wall system. Furthermore, a series of full-scale two-storey multi-panel tests were conducted to investigate the structural performance, deformation characteristics, and failure mechanisms of balloon-type CLT shearwall systems.

1.3. Scope and limitations

This section defines the boundaries of the current investigation into the lateral response of balloon-type CLT shearwalls. While the research integrates analytical modelling, numerical simulation, and full-scale testing to fulfill its objectives, some limitations due to practical constraints and simplifications need to be acknowledged:

- In the sensitivity analysis, the stiffness of hold-downs and vertical joints was assumed to be linear. This assumption was adopted because the primary objective was to understand the role of key parameters governing the behaviour of balloon-type CLT shearwall systems rather than to investigate detailed failure mechanisms.
- The assumption of elasticity was also incorporated into the analytical model with the aim to predict the lateral deformation within the elastic phase.
- The analytical formulation focuses only on two-panel configurations.
- Although the sensitivity analysis includes models up to four storeys, the experimental campaign is limited to two-storey specimens due to laboratory constraints and the practical challenges associated with constructing taller test assemblies. The floor diaphragms were also omitted from the experimental setup.
- A uniform lateral load distribution is adopted, and only monotonic loading is applied in the experiments. They were implemented since the current emphasis is more on establishing the deformed and kinematic behaviour especially for multi-panel walls, which remain insufficiently explored in the literature. It is however recognised that future research and tests that include the dynamic or cyclic loading effects are required.
- In order to isolate and evaluate the effects of hold-down and vertical joint stiffness on the lateral deformation and kinematic behaviour, no lateral sliding of the panels was allowed in the experimental campaign. This simplification helps to clarify the contributions of the

studied parameters.

- Due to equipment limitations and construction complexity, vertical loads are not applied during experimental testing. However, their effects are examined and discussed in the analytical and numerical models to provide a more complete understanding of their influence on the lateral deformation behaviour.

1.4. Organisation of thesis

This thesis is organised into seven chapters as follows:

- Chapter 1 introduces the research background and foundational concepts, outlines the research objectives and methodology, and defines the scope and limitations of the study.
- Chapter 2 presents a comprehensive literature review relevant to balloon-type CLT shearwalls and related research.
- Chapter 3 details a sensitivity analysis conducted through FE modelling to evaluate key parameters influencing the behaviour of balloon-type CLT shearwalls.
- Chapter 4 proposes a simplified analytical model and provides verification of the derived expressions through comparison with numerical results.
- Chapter 5 describes the experimental investigation, including specimen preparation, test setup, loading procedures and test results.
- Chapter 6 compares the experimental findings with the outcomes from both analytical and numerical models, discussing consistencies and discrepancies.
- Chapter 7 summarises the key findings of the study and provides recommendations for future research.

CHAPTER TWO

LITERATURE REVIEW

2. Literature review

This chapter begins with a review of fundamental studies on CLT material properties and connection systems (Section 2.1). Subsequently, research efforts focusing on CLT shearwall systems are examined (Section 2.2). Relevant codes and current design standards are discussed (Section 2.3), followed by a summary of the reviewed literature (Section 2.4).

2.1. Materials and connections of CLT shearwall systems

CLT, as an engineered wood product, has been defined by CSA O86 (CSA Group, 2024) to consist of five layup and grade classes: E1, E2, E3 (machine stress-rated (MSR) layups), and V1, V2 (visually stress-graded (V-grades) layups). The manufacturing of CLT panels is governed by the ANSI/APA PRG 320 (ANSI/APA, 2021) standard, which specifies seven standardised layups based on species combinations and performance criteria. Several analytical and experimental studies have suggested a relationship between the wood properties in the parallel- and perpendicular-to grain directions, including the modulus of elasticity (MOE), where E_{90} is commonly determined as $E_0/30$, longitudinal shear modulus G_0 as $E_0/16$, and the rolling-shear modulus G_{90} as $G_0/10$ (e.g., Blass and Fellmoser, 2004; Bejtka and Lam, 2008; Mestek et al., 2008; CSA Group, 2019; Karacabeyli and Gagnon, 2019). Using composite-beam theory, Blass and Fellmoser (2004) provided mechanics-based procedures to evaluate effective stiffness/strength of CLT products for in- and out-of-plane bending and axial actions. Subsequent work refined the global shear evaluation and proposed methods for estimating effective in-plane shear modulus G of CLT panels considering laminar properties and dimensions (Bogensperger et al., 2010; Brandner et al., 2017).

The stiffness, strength and ductility in CLT assemblies is typically governed by the mechanical connectors (Karacabeyli and Gagnon, 2019). Experimental programs have characterised hold-downs, angle brackets, and panel-to-panel joints under monotonic and cyclic actions, including wall-to-wall, wall-to-floor, and floor-to-floor interfaces (Gavric et al., 2015a, b; Tomasi and Smith, 2015; Hossain et al., 2015). Recent tests further quantified the contributions of hold-downs, angle brackets, and vertical joints in order to introduce capacity-based design provisions for platform type CLT shearwalls (Masroor et al., 2024). Studies on damping, ductility, and energy dissipation of connections have contributed to understanding the seismic behaviour of shearwall systems (e.g., Pulgar et al., 2018; Amini, 2018; Hayes et al., 2023). Numerical frameworks have also been developed to capture connection nonlinearity and failure mechanisms, including axial-shear interaction, stiffness degradation, and low-cycle fatigue under seismic loading in order to support reliable hysteretic representations used in analysis (Izzi et al., 2018; Pozza et al., 2018; Casagrande et al., 2020). Innovation in connector technology has included slip-friction and resilient slip-friction devices for energy dissipation and re-centering, as well as high-capacity hold-downs and ductile X-brackets for improved hysteretic performance (Loo et al., 2014a, b; Hashemi et al., 2017, 2018; Zhang et al., 2018; Trutalli et al., 2019).

Schneider et al. (2012) documented damage mechanisms at wall-foundation interfaces under seismic actions. Stiff shear-key vertical joints were investigated as alternatives to dense screw patterns in order to tailor joint stiffness and energy dissipation (Polastri and Casagrande, 2022) and perforated steel plates with self-drilling dowels that promote coupled-panel action were also explored (Dires and Tannert, 2022).

Overall, the combined understanding of CLT material orthotropy, effective property evaluation, and connection mechanics provides the foundation for subsequent discussion of CLT shearwall resisting systems and code/standard provisions in the following sections.

2.2. CLT Shearwall systems

2.2.1. Experimental investigations

2.2.1.1. Platform-type CLT shearwalls and related research

Extensive testing on platform-type CLT shearwalls from component to full-building scales have established a baseline understanding that has largely shaped current modelling and design practice for CLT lateral load resisting systems. It includes the research on panels (Ceccotti et al., 2006; Hummel et al., 2013; Popovski et al., 2010; Yasumura and Ito, 2014), single-storey structures (Dujic et al., 2006; Hristovski et al., 2013), two-storey buildings (Matos et al., 2019; Pei et al., 2018; Popovski and Gavric, 2015; Van de Lindt et al., 2018, 2019; Yasumura et al., 2016; Masroor et al., 2024), and three- to seven-storey full-scale tests (Ceccotti et al., 2006, 2008, 2010, 2013; Costa et al., 2013).

Other research includes an assessment of hysteretic behaviour in both single-panel and coupled CLT shearwalls (Shahnewaz et al., 2023), investigations on seismic force modification factors (Pei et al., 2012, 2013a, 2013b; Van de Lindt et al., 2018), CLT structure with openings (Khajehpour et al., 2022, 2023) and post-tensioned or self-centering systems (Chen et al., 2018; Dunbar et al., 2014; Moroder et al., 2018; Pei et al., 2019; Hajimirza et al., 2019), offering design solutions for enhancing the seismic resilience of CLT structures.

Although the findings from the aforementioned studies do not directly relate to balloon-type shearwalls, they offer base knowledge and strategies to develop feasible methodologies for balloon-type research. It also highlights the differences in theoretical development for taller and high aspect-ratio wall systems and motivates full-scale studies.

2.2.1.2. Balloon-type CLT shearwalls

Research on the in-plane behaviour of CLT shearwalls commonly treats panels as rigid elements, where wall rocking controls the global lateral response (Brandner et al., 2016; Izzi et al., 2018; Breneman, 2015; Casagrande et al., 2020; Ceccotti et al., 2006a; Ceccotti et al., 2013; Popovski and Gavric, 2016; Pei et al., 2018). It is very important to note that these studies were all based on platform-type CLT shearwall systems and that due to the relatively higher aspect ratio in the balloon-type shearwalls, the behaviour is expected to be significantly different. Because of the in-elevation continuity of the panels (hold-downs and angle brackets are used on the ground floor only) and higher values of panel aspect ratios, balloon-frame walls are expected to involve a higher deformation contribution related to bending and shear deformations of the panels compared to platform-type shearwall systems (Karacabeyli and Gagnon, 2019; Chen and Popovski, 2020; Li, Wang, and He, 2020; Krauss et al., 2024).

Chen and Popovski (2020) examined four balloon-type shearwalls with aspect ratios of 4.9:1 (single-panel) and 9.8:1 (double-panel), revealing that although the peak lateral capacities were comparable, double-panel walls exhibited greater plastic and ultimate deformations due to improved energy dissipation, with hold-downs identified as the critical failure component.

Li et al. (2020) performed quasi-static cyclic tests on four one-third scale shear wall specimens, representing both platform-type and balloon-type configurations in single-panel and double-panel arrangements. Their results demonstrated that balloon-type walls exhibited higher initial stiffness and greater energy dissipation, though lateral capacity was largely unaffected by the construction method. Subsequent testing by Wang et al. (2023) incorporated supplemental energy dissipators, demonstrating that balloon-type walls can achieve superior energy dissipation under rocking motion relative to platform-type, however, the panels used in this study had relatively low aspect ratios compared to typical balloon-type designs.

Zhang et al. (2021) tested four full-scale, three-story buildings constructed with both platform and balloon-type shearwalls using narrow and wide panels. While providing valuable insights, the discussion was not focused on balloon-type performance, and all walls were primarily designed to behave as single-panel system.

Dickof et al. (2020) and Shahnewaz et al. (2021) investigated the impact of ledger beams used to support floor systems from various materials and connection types. They concluded that ledger elements did not hinder wall rocking nor compromise their vertical load-carrying capacity. Krauss et al. (2024) conducted a study on coupled balloon-type CLT shearwalls with high-capacity screwed connections. Their findings indicated significantly higher strength and stiffness relative to traditional platform systems. However, their tests were limited to relatively low aspect ratios (< 4) and did not consider multiple loading points along each diaphragm level, which are more representative of real multi-story balloon-type buildings.

In summary, while platform-type behaviour is connection-dominated and rocking-controlled, balloon-type systems shift a significant share of deformation into panel bending and shear due to the high aspect ratios and vertical continuity. Existing tests, often at lower aspect ratio, with smaller scale or less focuses on investigating impacts of connectors' stiffness, aspect ratios or the panel numbers, highlight the need for further full-scale investigations on tall, multi-panel balloon-type shearwalls.

2.2.2. Numerical analysis

Izzi et al. (2018) summarised prevalent numerical modelling approaches employed for platform-type CLT shearwall systems, in which CLT wall panels are represented using truss elements, two-dimensional shell elements, or three-dimensional solid elements (e.g., Casagrande et al., 2016; Rinaldin and Fragiacomo, 2016; Izzi, Polastri and Fragiacomo, 2018). Connections in these models were commonly idealized as nonlinear link or spring elements with either uniaxial (Yasumura et al., 2016; Pozza et al., 2016) or biaxial (Fragiacomo, Dujic and Sustersic, 2011; Shen et al., 2013) stiffness properties. Broader building-scale modelling efforts are also represented in studies by Polastri et al. (2019), Pozza and Trutalli (2017), Rinaldin and Fragiacomo (2016), Sustersic et al. (2016), and Yasumura et al. (2016), providing insights into overall seismic behaviour and system-level interactions. In addition, Shahnewaz et al. (2017) investigated the effect of panel openings on in-plane stiffness through numerical parametric studies.

Zhang et al. (2021) applied such modelling techniques to investigate the global seismic performance of 12-storey and 18-storey balloon-framed CLT structures, incorporating nonlinear connection modelling. Jafari et al. (2022) developed a nonlinear dynamic model to investigate the influence of ground motion duration on a two-storey balloon-type CLT building. Yang et al. (2022) conducted nonlinear time-history analyses of four 12-storey balloon-type rocking shearwall systems, validating their compliance with seismic performance objectives and supporting the design of high-rise resilient mass timber structures. Pan et al. (2023a) numerically evaluated the collapse fragility of a balloon-framed CLT school building under a suite of 21 ground motions. Their findings confirmed the structure met drift and collapse safety requirements at design-level intensity. In a follow-up study, Pan et al. (2023b) analysed the seismic performance of a four-storey balloon-framed CLT building incorporating self-centring, friction-based hold-downs.

2.2.3. Analytical models

Analytical modelling of CLT shearwall systems has predominantly focused on platform-type configurations. Casagrande et al. (2018) developed a multiple-panel analytical model incorporating three kinematic modes: coupled-panel (CP), single-wall (SW), and intermediate (IN). Based on the principle of minimum total potential energy, their model highlighted the importance of panel geometry and the stiffness of both hold-downs and vertical joints in governing kinematic modes and lateral deformation characteristics. Gavric, Fragiacomo and Ceccotti (2013) presented a two-dimensional analytical model for a platform-type two-panel wall system, emphasising the critical role of rocking behaviour in enhancing energy dissipation and ductility compared to sliding mechanisms. Tamagnone and Fragiacomo (2018) further contributed by formulating closed-form expressions for predicting rocking-induced deformation in CLT assemblies, assuming monolithic action and rigid vertical joints. Nolet et al. (2019) developed an analytical model to predict the nonlinear behaviour of multi-panel CLT shearwalls under lateral loads, distinguishing CP and SW responses. The validated model enables accurate force-displacement predictions and supports simplified design development. Masroor et al. (2020, 2021) introduced analytical expressions for the capacity-based design of multi-panel CLT shearwalls, considering bidirectional mechanical anchor behaviour. Their models offered improved predictive accuracy for lateral force-deformation response and panel contact behaviour.

In the context of balloon-type systems, Chen and Popovski (2020) proposed a mechanics-based analytical model to predict the lateral deformation of a two-panel CLT shearwall. The model incorporated deformation contributions from panel bending and shear, as well as from sliding and rocking, both under rigid-base and elastic-base assumptions. Particular attention was given to the role of hold-down and vertical joint flexibility in controlling rocking behaviour. Li et al. (2020) identified bending, shear, rocking, and sliding as the primary deformation contributors in the proposed model. They recommended incorporating the effect of local crushing at the panel-to-foundation interface to improve model accuracy.

Based on the review of the analytical literature, it is evident that current analytical models for estimating the lateral deformation of balloon-type CLT shearwalls lack considerations of coupled behaviours between panels and kinematic modes, which requires further investigation.

2.3. Current codes and standards

In the current Canadian national standard (CSA Group, 2024), provisions related to CLT shearwall design apply exclusively to platform-type systems. The 2024 version introduces calculation methods for the resistance of shearwalls exhibiting different kinematic behaviours, including CP and SW responses. It also provides procedures for evaluating lateral stiffness resulting from shear, bending, rocking, and sliding mechanisms. In accordance with capacity-based design principles, the standard classifies energy-dissipative and non-dissipative connections and further specifies that the aspect ratio (height-to-length) of wall segments in platform-type systems should fall between 2:1 and 4:1.

The current Eurocode (CEN, 2004) includes no specific provisions for CLT structures. However, the draft second generation edition, prEN 1995-1-1:2025 and prEN 1998-1-2:2025 (CEN, 2025), is expected to introduce explicit references to CLT products and associated structural design approaches. In particular, the new timber chapter of Eurocode 8 (prEN 1998-1-2:2025) includes guidance for multi-storey monolithic shearwalls and single-storey segmented shearwalls constructed with CLT.

In comparison, CLT shearwall design has received limited attention in other national or regional standards. In the United States, SDPWS-2021 (AWC, 2021) lists requirements for CLT shearwalls, but the method of construction is limited to platform-type systems. In Japan, the AIJ Standard for Structural Design of Timber Structures provides general principles for timber structural design, however, it does not address the design of balloon-type CLT shearwalls or their associated detailing (AIJ, 2018). In Australia, AS 1720.1 (Standards Australia, 2010) primarily focuses on member-level design of timber structures and does not provide explicit system-level design procedures for CLT shearwalls or alternative construction configurations, including balloon-type systems. Finally, in China, the national timber design standard GB 50005-2017 (MHURD, 2017) and the technical code GB/T 50708-2012 (MHURD, 2012) do not currently include CLT shearwall systems. Although research initiatives and working drafts are underway, comprehensive design guidance for CLT shearwalls, particularly balloon-type configurations, has yet to be incorporated into formal standards.

2.4. Summary

The extensive body of literature on CLT material properties, connection behaviour, shearwall systems, and related code provisions shows that while platform-type shearwalls have been widely studied, comprehensive investigations involving full-scale experiments on balloon-type CLT shearwall systems remain scarce, albeit necessary and essential.

Some key observations based on the literature review include:

- Balloon-type CLT shearwall systems exhibit fundamental differences from platform-type systems due to continuous panel layouts in elevation and higher aspect ratios. These features may result in non-negligible panel bending deformation and different structural stiffness and strength performance.
- Compared to the well-studied platform-type systems, experimental investigations of balloon-type configurations are still relatively limited. Key studies have explored single- and double-panel walls, ledger beam effects, and connection behaviour, but full understanding under multi-storey and multi-panel remains lacking.
- Despite some analytical models have been developed to describe deformation characteristics, accounting for shear, bending, rocking, and sliding of balloon-type shearwalls, the impact of composite behaviour between panels due to the vertical joints and kinematic modes still needs to be considered in evaluating lateral displacement of balloon-type CLT shearwall systems.
- Current design codes do not explicitly address balloon-type systems. The absence of code guidance highlights the importance of continued research to support eventual codification and safe design practice.
- This thesis builds upon prior work by investigating the lateral deformation and kinematic modes of multi-panel balloon-type shearwalls experimentally, numerically and analytically, providing critical data to fill the gap in current literature and standards.

CHAPTER THREE

SENSITIVITY ANALYSIS

3. Sensitivity analysis

A preliminary sensitivity analysis is conducted with the aim of understanding the role of key parameters governing the behaviour of balloon-type CLT shearwall systems. A secondary goal of conducting the sensitivity analysis is to inform the test matrix and specimen dimensions in following experimental programme. In general, the impact of the aspect ratios, stiffness of the hold-downs and vertical joints, and vertical loads are considered. In conducting the analysis, the commercial FE software package SAP2000 was employed (CSI, 2021). In total, 548 models were analysed.

3.1. Validation of the numerical model

To verify the methodology used in sensitivity analysis, the results obtained from the numerical model were compared with the backbone curve of the cyclically tested shearwall performed by Chen and Popovski (2020). The investigated shearwall consisted of two panels, each with dimensions 4,125 mm in height and 420 mm in length, as illustrated in Figure 3.1. The panels consisted of 5-ply CLT of Grade E1, and they were connected to the base using two pairs of hold-downs (on the both sides of the panels), and panel-to-panel joints were arranged with an equal distance of 825 mm. A uniformly distributed gravity (vertical) load with a magnitude of 2.1 kN/m was applied at the top of two panels. A horizontal concentrated load was applied at the diaphragm level on top of the wall through a steel beam, which allowed rotation.

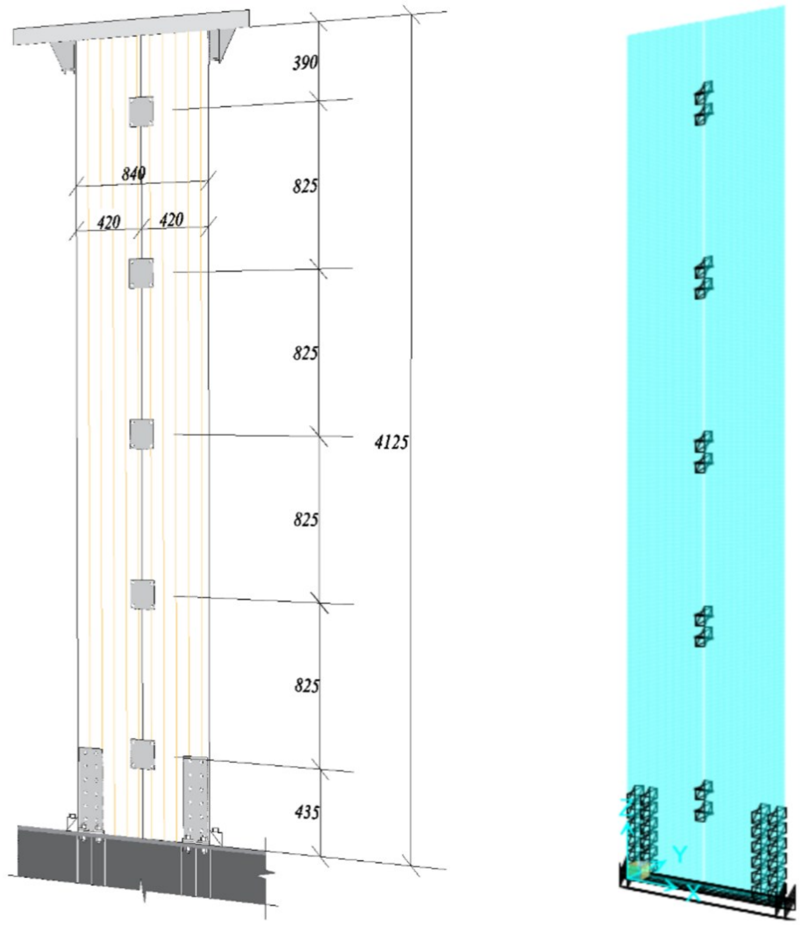

(a) *(b)*

Figure 3.1: *(a) Duplicated shearwall configuration and (b) FE model*

The moduli of elasticity of the longitudinal layers are assumed to be *11,700 MPa* and *390 MPa*, for E_0 and E_{90}, respectively, while values of E_0 equal to *9,000 MPa* and E_{90} equal to *300 MPa* are used in the transverse layers (Blass and Fellmoser, 2004; CSA Group, 2024). As a result, the effective moduli in the vertical $E_{0,\ eff}$ and horizontal $E_{90,\ eff}$ directions are calculated to be equal to 7,140 MPa and 3,834 MPa, respectively (Brandner et al., 2017). The shear modulus G_0 is taken equal to 731 MPa (CSA Group, 2024), hence, the effective shear modulus G^* is equal to 380 MPa (Bogensperger et al., 2010). It was assumed that the vertical gap links, which simulate the foundation reaction, provided an axial compression stiffness equal to 1.0×10^6 kN/m (Casagrande et al., 2018). The connection behaviour of the hold-downs, vertical joints and lateral restraints reported by Chen and Popovski (2020) are illustrated in Figure 3.2.

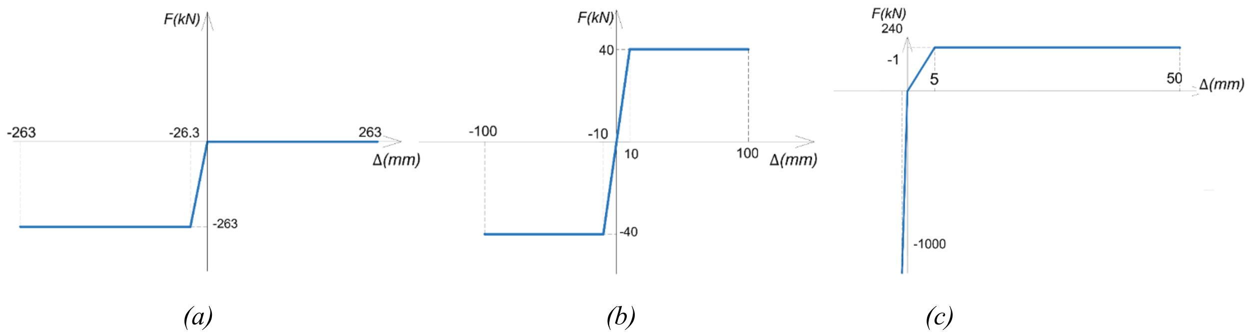

Figure 3.2: *The mechanical properties of (a) lateral restraints (b) vertical joints along the horizontal and vertical axes (c) hold-downs along the horizontal and vertical axes*

A comparison between the monotonically loaded shearwall obtained from the experimental results and the pushover modelling result is shown in Figure 3.3. In general, it can be observed that the fit between the model and the test results is reasonable, and deviations observed between the two curves could be attributed to the assumption related to the mechanical properties of connectors being idealized in the FE modelling analysis. As shown in Figure 3.3, the vertical joints yielded first, while the failure of the shearwalls is related to hold-down failure, which is consistent with that described by Chen and Popovski (2020).

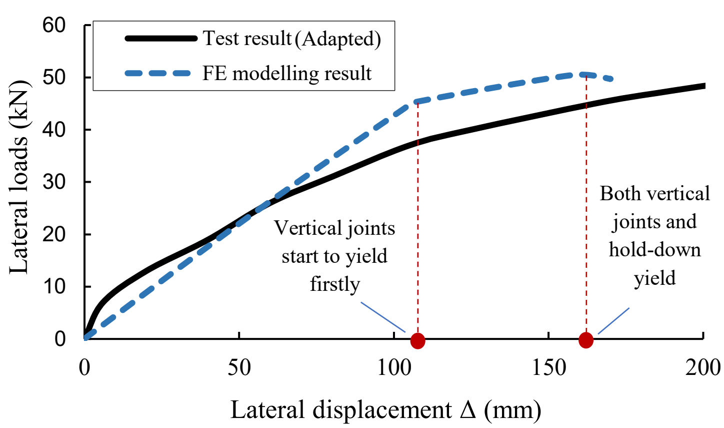

Figure 3.3: *Comparison between the load-displacement curves of monotonic loading test (Chen and Popovski, 2020) and pushover modelling.*

3.2. Description of the FE model

The proposed FE model consists of a multi-panel multi-storey shearwall system, subjected to lateral point forces simulating wind or seismic loads, assumed to be applied at the heights of each diaphragm level. The total height and the width of each panel are taken as h and b, respectively. The panels are assumed to be connected to the foundation by hold-downs with axial stiffness k_{hd} along the vertical direction, while the panel sliding along the horizontal direction is limited. As such, the angle brackets were replaced by lateral restraints since the current standard for CLT shearwalls in the CSA O86 (CSA Group, 2024) restricts sliding behaviour. Adjacent panels are connected to each other by means of uniformly placed vertical joints with the total shear stiffness k_{vj}. Vertical uniformly distributed gravity loads are assumed to be applied at each diaphragm level (Figure 3.4a).

The FE model adopted thick-shell elements to simulate the behaviour of shearwall panels. Each meshing unit was defined as a four-node quadrilateral element because the model is simplified into a 2D plane, and the wall panels are all rectangular. The influence of mesh size for FE analysis was investigated. Table 3.1 presents the maximum lateral deformations obtained from a representative FE model under different mesh sizes. The model identifier (M9/1-P2-VL0-H10V15) follows the notation system defined later in this chapter. When the mesh size decreases from 100 mm × 100 mm to 10 mm × 10 mm, the maximum lateral deformation varies less than 3%. Considering both accuracy and the time of analysis, the mesh size was suggested to be 100 mm × 100 mm.

Table 3.1: *Comparison of maximum lateral deformations from the model M9/1-P2-VL0-H10V15*

Mesh size (mm × mm)	***100 × 100***	***50 × 50***	***25 × 25***	***10 × 10***
Maximum lateral deformation (mm)	*212.7*	*215.03*	*216.75*	*218.72*

The material properties of the CLT panels were considered using the equivalent method proposed by Brandner et al. (2017). In this approach, CLT is idealised as an orthotropic material, and its effective elastic properties are obtained based on layer orientation and thickness:

$$E_{0,eff} = \frac{E_0 T_0 + E_{90} T_{90}}{T} \tag{3.1}$$

$$E_{90,eff} = \frac{E_0 T_{90} + E_{90} T_0}{T} \tag{3.2}$$

where

$E_{0,eff}$ is the effective modulus of elasticity along the vertical direction (parallel to the grain of the outer layer),

$E_{90,eff}$ is the effective modulus of elasticity along the lateral direction (perpendicular to the grain of the outer layer),

E_0 is the modulus of elasticity parallel to the grain,

E_{90} is the modulus of elasticity perpendicular to the grain,

T_0 is the total thickness of the layers with the vertical grain direction,

T_{90} is the total thickness of the layers with the lateral grain direction,

T is the total thickness of the panel.

According to Blass and Fellmoser (2004) and CSA O86 (CSA Group, 2024), it is suggested that E_{90} is assumed as $E_0/30$. Considering that E_{90} is often ignored due to a minor contribution to the strength of CLT panels in practice, Eq. 3.1 and Eq. 3.2 can be simplified if assuming the values of E_0 at both the longitudinal layers and transverse layers are the same:

$$E_{0,eff} = E_0 \cdot \frac{T_0}{T} \tag{3.3}$$

$$E_{90,eff} = E_0 \cdot \frac{T_{90}}{T} \tag{3.4}$$

The behaviours of hold-downs, vertical joints and the foundation reaction are simulated by link/spring elements. Hold-downs are defined as "one-joint link" which connect to the ground, and only linear tensile behaviour is considered. Vertical joints are defined as "two-joint links" that connect adjacent panels together and provide only shear resistance. The foundation support is modelled by means of a series of "gap links" that behave only in compression.

Additionally, restraints are applied at the bottom of each panel to restrain the lateral sliding of structures. Diaphragm constraints are applied to ensure that the same lateral displacement is attained in the two panels at each storey level. Figure 3.4b illustrates relevant details of modelling assumptions.

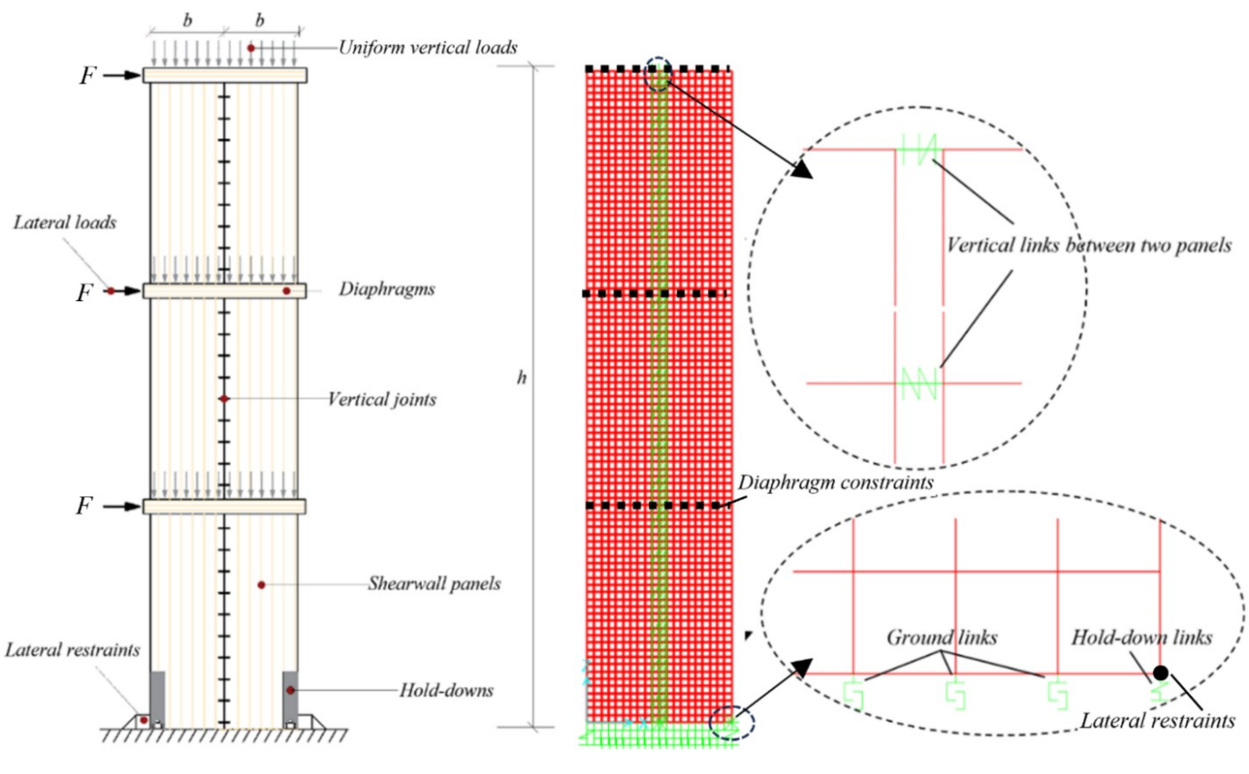

(a) (b)

Figure 3.4: *(a) Three-storey two-panel balloon-type CLT shearwall model and (b) the details of connections of FE modelling as an example*

3.3. Description of the model configuration and parameters

The parameters used in the sensitivity analysis are summarised in Table 3.2, and they include elastic input parameters for the CLT panels and the mechanical connections. The aim of this investigation is to establish an understanding of the kinematic modes for balloon-frame CLT shearwalls, and as such, the model does not include capabilities for detecting failure mechanisms in the CLT panels or the mechanical connections. The shearwalls were simulated with varying heights along 1～4 storeys, while the storey height was kept at 3 m. Uniformly distributed vertical loads were applied at each floor with values of 0 or 20 kN/m. The lateral loads were applied at the edges of the diaphragm levels.

With regards to the material parameters, it is assumed that all CLT panels consist of 5 layers, where the orientations of the first, third and fifth layers are parallel to the vertical direction, and those of the second and fourth layers are parallel to the horizontal direction (i.e., 0°/90°/0°/90°/0°). The total thickness of CLT panels is taken as 175 mm with 35 mm thickness in the individual laminae. Young's modulus in the direction parallel to the grain (E_0), is assumed to equal 12,000 MPa (CSA Group, 2024) and the in-plane shear modulus (G_0) is taken as 690 MPa (ETA, 2020).

In addition to considering different aspect ratios of panels in the analysis, the impact of the stiffness of the hold-downs and vertical joints is investigated. It is assumed that hold-downs and vertical joints are characterised by a linear elastic behaviour along the tensile and shear direction, respectively. As such, the stiffness of vertical joints is calculated per unit height (per meter) on the panel, while ignoring the friction between panels. It should be noted that the assumption of limiting the behaviour of hold-down to the vertical-uplift direction is generally acceptable for commercially available hold-down devices. While special hold-down devices, manufactured specifically to resist loads in the vertical and horizontal directions, may be available, they are outside the scope of the parametric analyses undertaken in this chapter.

Table 3.2: *Basic parameters of FE models*

Parameters	*Symbols*	*Values*
No. of storey	n (-)	*1; 2; 3; 4*
Unit lateral load applied at each storey	F *(kN/m)*	*20*
Uniform vertical load applied at each storey	q *(kN/m)*	*0; 20*
Number of panels	*P (-)*	*1; 2; 3; 4*
Compressive stiffness of the foundation	k_f *(kN/m)*	*1,000,000**
Total thickness of panel	*T (mm)*	*175*
Modulus of Elastic and Modulus of Shear	E_0; G_0 *(MPa)*	*12,000; 690*
Tensile stiffness of per hold-down	k_{hd} *(kN/mm)*	*10; 25; 50; 100*
Unit shear stiffness of vertical joints	k_{vj}/h *(kN/mm/m)*	*3; 7.5; 15*

**Note: the value of k_f refers to that used by Casagrande et al. (2018).*

Table 3.3 presents the matrix for the numerical models according to aspect ratio.

Table 3.3: *Aspect ratio matrix for modelling analysis*

Aspect ratios (h/b)	***h=3m***	***h=6m***	***h=9m***	***h=12m***
b=0.25m	*12*	-	-	-
b=0.5m	*6*	*12*	-	-
b=0.75m	*4*	*8*	*12*	-
b=1m	*3*	*6*	*9*	*12*
b=2m	*1.5*	*3*	*4.5*	*6*
b=3m	*1*	*2*	*3*	*4*
b=6m	-	*1*	*1.5*	*2*
b=9m	-	-	*1*	*1.3*
b=12m	-	-	-	*1*

A consistent format is followed in naming convention of the models, where, for example, for model "M9/1-P2-VL20-H10V3", the "M9/1" refers to panel aspect ratio of 9 to 1; "P2" refers to the number of panels; "VL20" indicates that the value of the vertical load is 20 kN/m/storey; and "H50V15" shows that the values of the stiffness of hold-downs and the unit stiffness of vertical joint are 50 and 15 kN/mm/m, respectively. Figure 3.5 provides some examples following this naming convention.

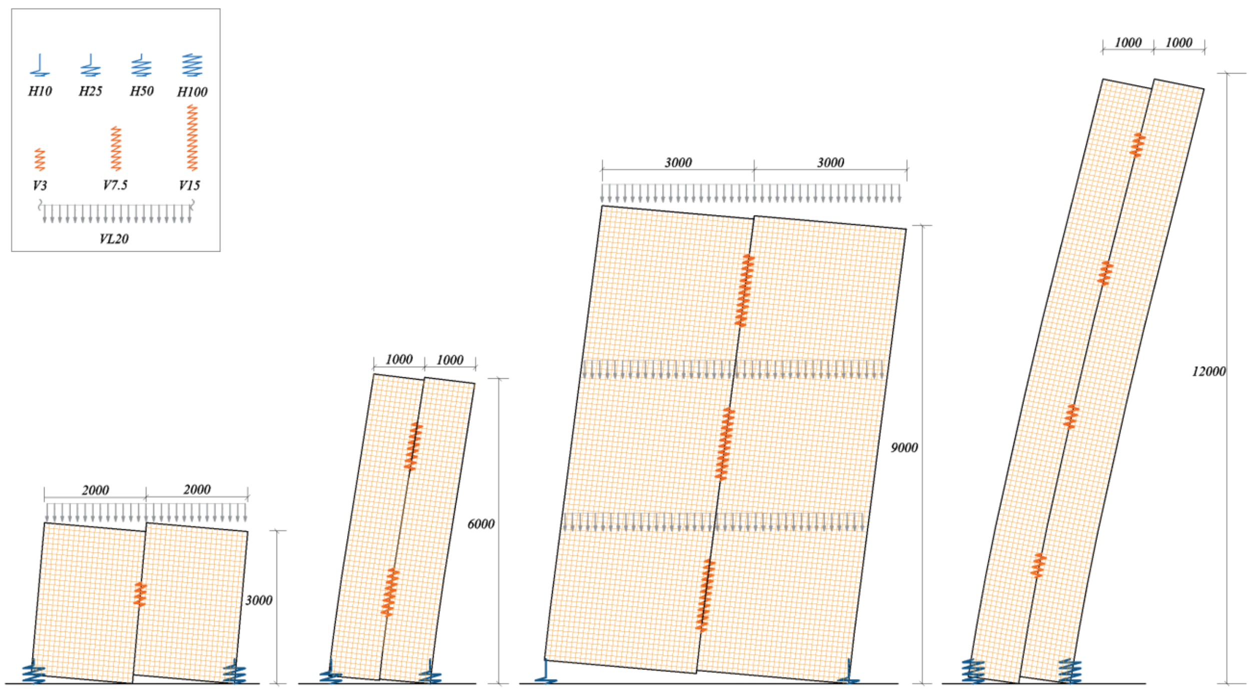

(a) M3/2-P2-VL20-H50V3 (b) M6/1-P2-VL0-H25V7.5 (c) M9/3-P2-VL20-H10V15 (d) M12/1-P2-VL0-H100V3

Figure 3.5: *Examples of deformed numerical FE models following the defined naming convention*

3.4. Results and discussions of two-panel models

The focus of the sensitivity analysis was on the effects related to the total lateral stiffness, percentage of rocking deformation and kinematic behaviours. Total lateral stiffness K of the structure is defined by:

$$K = \frac{\sum F_i}{\Delta_{total}} \tag{3.5}$$

where

F_i is the lateral load (kN) on the i^{th} storey,

Δ_{total} is the total lateral displacement (mm) at the top of the shearwall.

The percentage of rocking deformation is defined as a percent ratio of rocking deformation, $\Delta_{rocking}$, to the total deformation Δ_{total} (Figure 3.6), and $\Delta_{rocking}$ can be calculated according to Eq. 3.6:

$$\Delta_{rocking} = \Delta_2 \cdot \frac{h}{b} \tag{3.6}$$

where

Δ_2 is the vertical uplift of the second (right) panel.

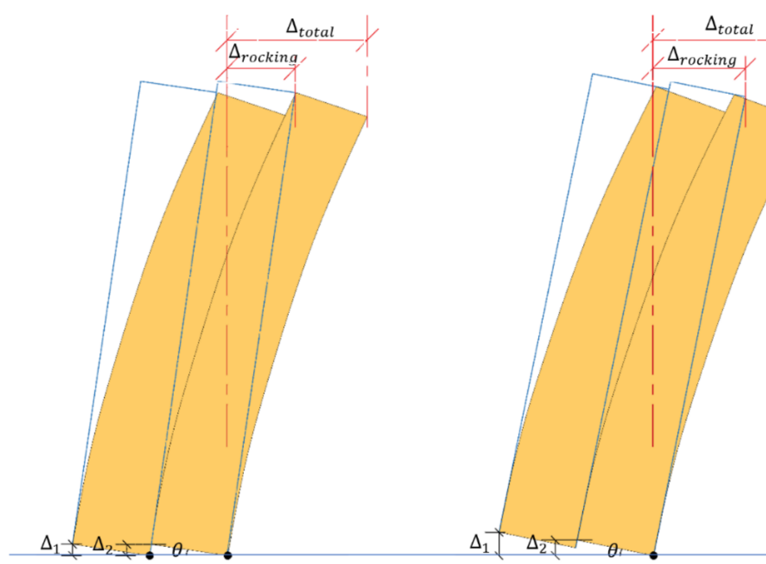

(a) *(b)*

Figure 3.6: *$\Delta_{rocking}$ and Δ_{total} defined in (a) CP mode and (b) SW mode*

3.4.1. The impact of the stiffness of connectors and aspect ratios

In order to present the impact of the connection stiffness, a normalised total lateral stiffness K^* was adopted. This parameter is defined as the ratio between the total lateral stiffness K and the specific total lateral stiffness value when hold-down stiffness is 10kN/mm or the vertical joints stiffness per unit length is 3kN/mm/m (i.e., $K_{hd}^* = K/K_{(k_{hd}=10kN/mm)}$ or $K_{vj}^* = K/K_{(k_{vj}/\mathrm{h}=3\mathrm{kN/mm/m})}$). Figure 3.7 shows the relationship between K_{hd}^* and k_{hd} when b equals $1\ m$, $2\ m$, and $3\ m$ and when no vertical loads are applied.

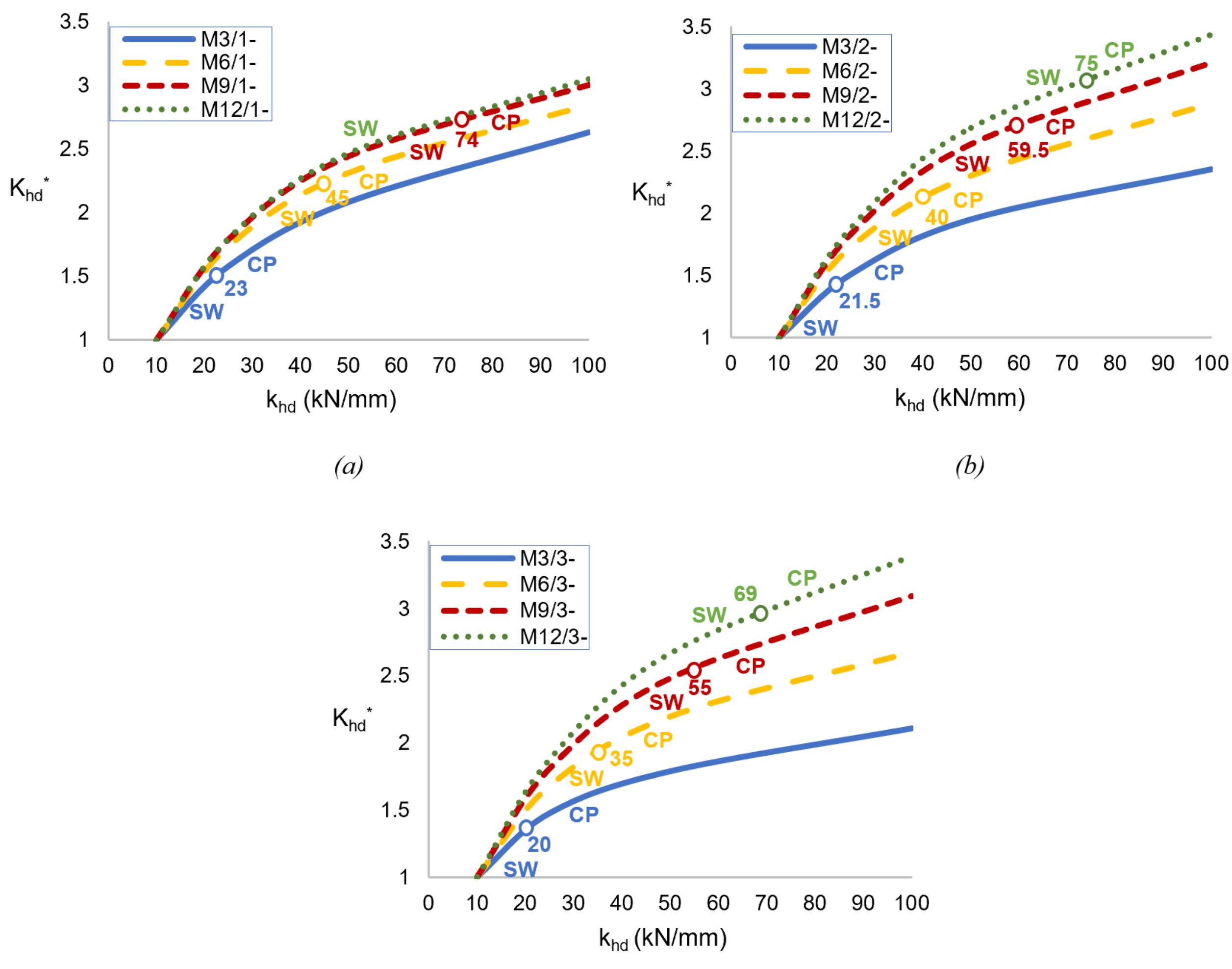

(a) *(b)*

(c)

Figure 3.7: *Relationship between normalised total lateral stiffness K_{hd}^* and k_{hd} when k_{vj}/h equals 7.5 kN/mm/m and vertical loads equal zero, with b=1 m (a); b=2 m (b); b=3 m (c)*

It can be observed from Figure 3.7 that a non-linear relationship exists between K^*_{hd} and k_{hd}, where the variation in K^*_{hd} seems much greater for low values of k_{hd}, while reaching an almost linear relationship for high values of k_{hd}. This is reasonable since the deformation contributions in a CLT balloon-type shearwall can be simulated as in-series springs. As a result, the rocking deformation contribution dominates the behaviour for low values of hold-down stiffness (i.e., flexible hold-downs). It can also be observed that the normalised total lateral stiffness, K^*_{hd}, is greater for high values of panel aspect ratios, where significant rocking deformation contribution is observed for walls with slender panels. The influence of the height of the panel seems less significant for narrow panels in Figure 3.7a, where the curves are much closer to each other than those shown in Figure 3.7c.

Figure 3.8 illustrates the behaviour for the same aspect ratio (i.e. M3/1, M6/2 and M9/3), obtained from Figure 3.7, where it can be observed that the wall stiffness increases with the height and width of the panels, however, the difference is relatively small as the three curves are in close proximity to each other.

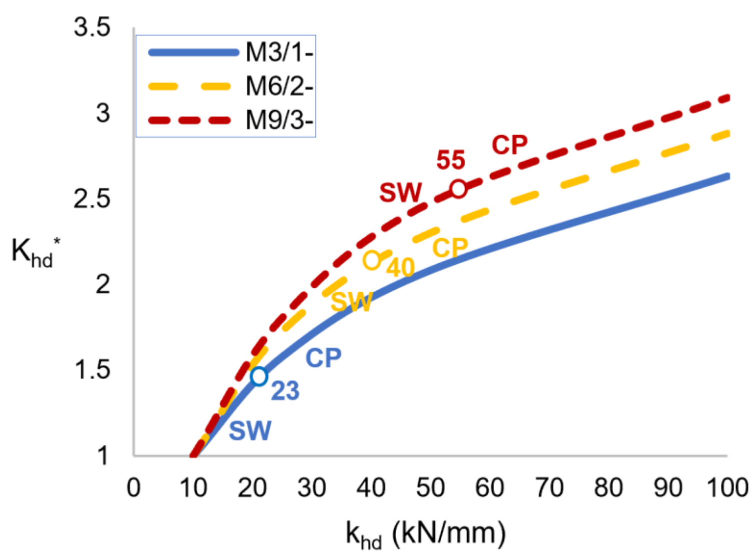

Figure 3.8: *Relationship between normalised total lateral stiffness K^*_{hd} and k_{hd} when k_{vj}/h equals 7.5 kN/mm/m (V7.5) for the same aspect ratios equal to 3 without vertical loads (VL0)*

The figures (Figure 3.7 and Figure 3.8) also show that when a transition occurs between two kinematic modes, SW to CP, the slope of the curves associated with the CP mode is generally smaller than those related to the SW mode. This is deemed reasonable since the influence of hold-down is greater for SW kinematic mode, and for CP mode, the vertical joints significantly impact on deformation contribution.

The transition between SW and CP is strongly influenced by the aspect ratio of the panels, as shown in Figure 3.9a, where a nearly linear relationship is observed between the value of hold-down stiffness at the transition points as a function of panel aspect ratios. However, even when the panel aspect ratio is varied, walls with varied widths but the same height seem to exhibit similar behaviour, as shown in Figure 3.9b.

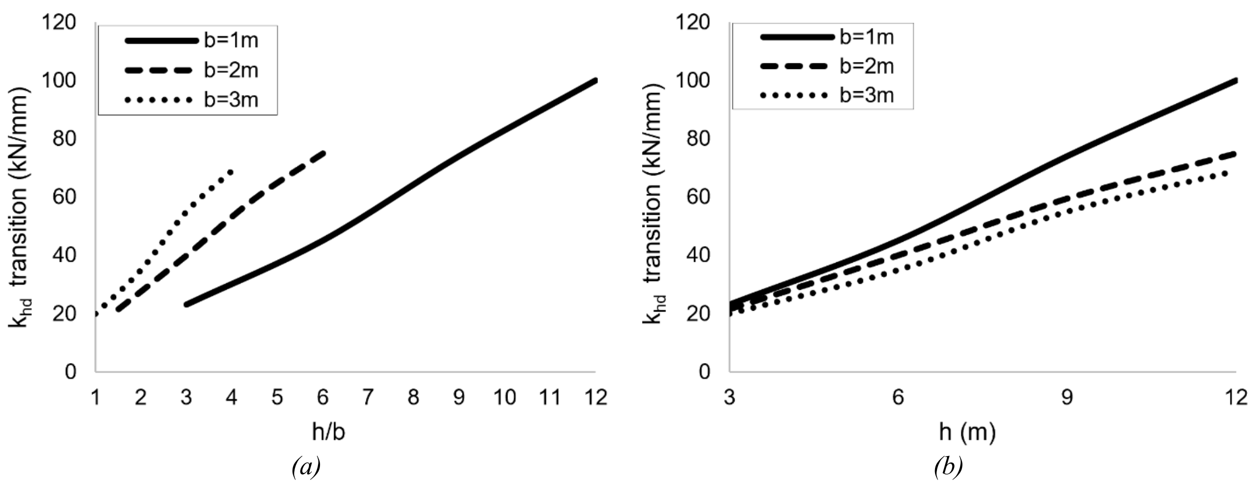

Figure 3.9: *Stiffness of the hold-downs for which the transition from SW to CP is achieved versus aspect ratio (a) and height (b) of panels when* k_{vj}/h *equals 7.5 kN/mm/m (V7.5) without vertical loads (VL0)*

The relationship between K_{vj}^{*} and the unit vertical joint stiffness k_{vj}/h for $h = 3\ m,\ \ h = 6\ m$ $h = 9\ m$, and $h = 12\ m$ is presented in Figure 3.10 and 3.11 for values of k_{hd} equals 50 kN/mm and 25 kN/mm, respectively, in order to investigate whether the behaviour differs for high and low hold-down stiffness values. The general trends appear similar to those observed for variation in the hold-down stiffness (see Figure 3.7), where a non-linear relationship exists between normalised total lateral stiffness and unit vertical joint stiffness, and where the variation in K^*_{vj} seems greater for low values of k_{vj}/h, with the slight difference that the relationship seems almost bi-linear.

A significant change in slope is observed when the kinematic mode changes from CP to SW, which can be attributed to the fact that in SW the contribution of vertical joints is less significant than it is in CP mode. It can be observed that the trend where K^*_{vj} is greater for high values of panel aspect ratios only holds true for CP behaviour (e.g., Figure 3.10c for k_{vj}/h < 8 kN/mm/m). Contrarily, K^*_{vj} seems greater for low values of panel aspect ratios when SW is attained (e.g., Figure 3.11a for k_{vj}/h > 10 kN/mm/m). The influence of the hold-down stiffness seems significant when the graphs in Figure 3.10 and Figure 3.11 are compared. It can be observed that CP behaviour is attained in the case of high hold-down stiffness equal to 50 kN/mm (Figure 3.10), while for hold-down stiffness equal to 25 kN/mm (Figure 3.11), transitions between CP and SW are much more evident.

When the behaviour for the same aspect ratio (i.e. M3/1, M6/2 and M9/3) was compared, it was observed, consistent with the observation made in Figure 3.8 for varying hold-down stiffness, that the wall stiffness increases with the width and the height of the panels, but the difference is relatively small.

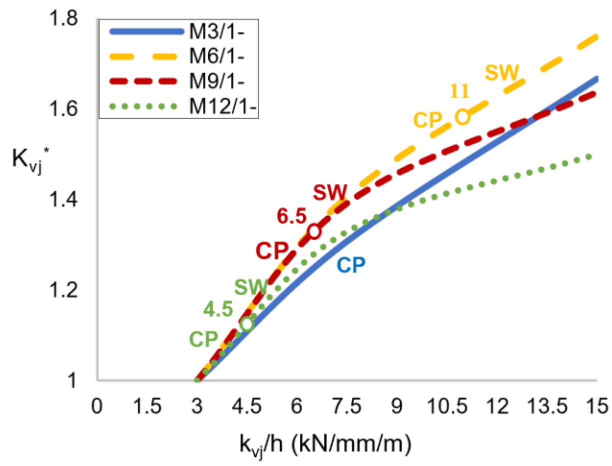

(a)

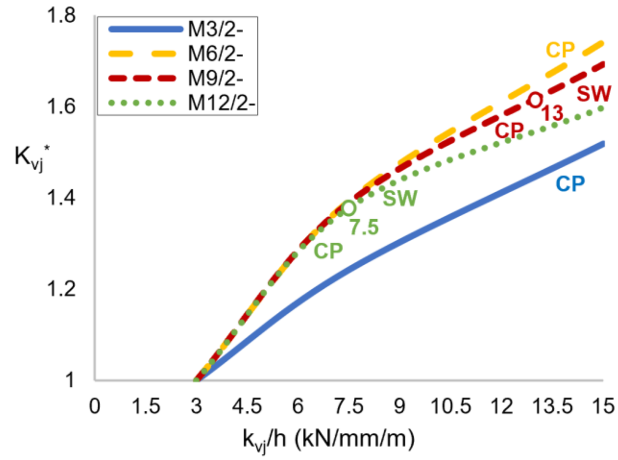

(b)

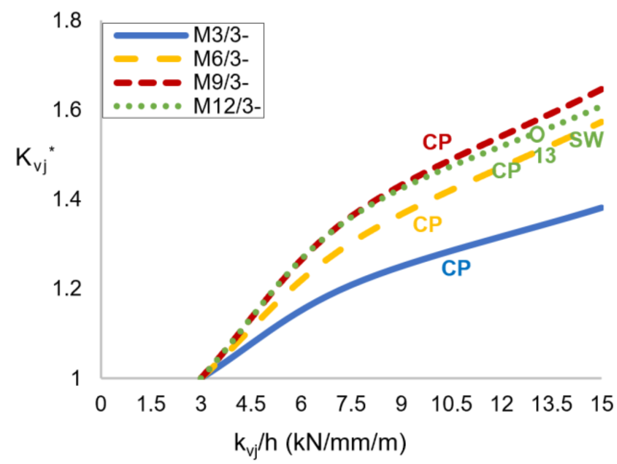

(c)

Figure 3.10: *Relationship between the normalised total lateral stiffness K_{vj}^* and unit vertical joints stiffness k_{vj}/h when k_{hd} equals 50 kN/mm (H50), and vertical loads equal 20 kN/m (VL20), with b=1 m (a); b=2 m (b); b=3 m (c).*

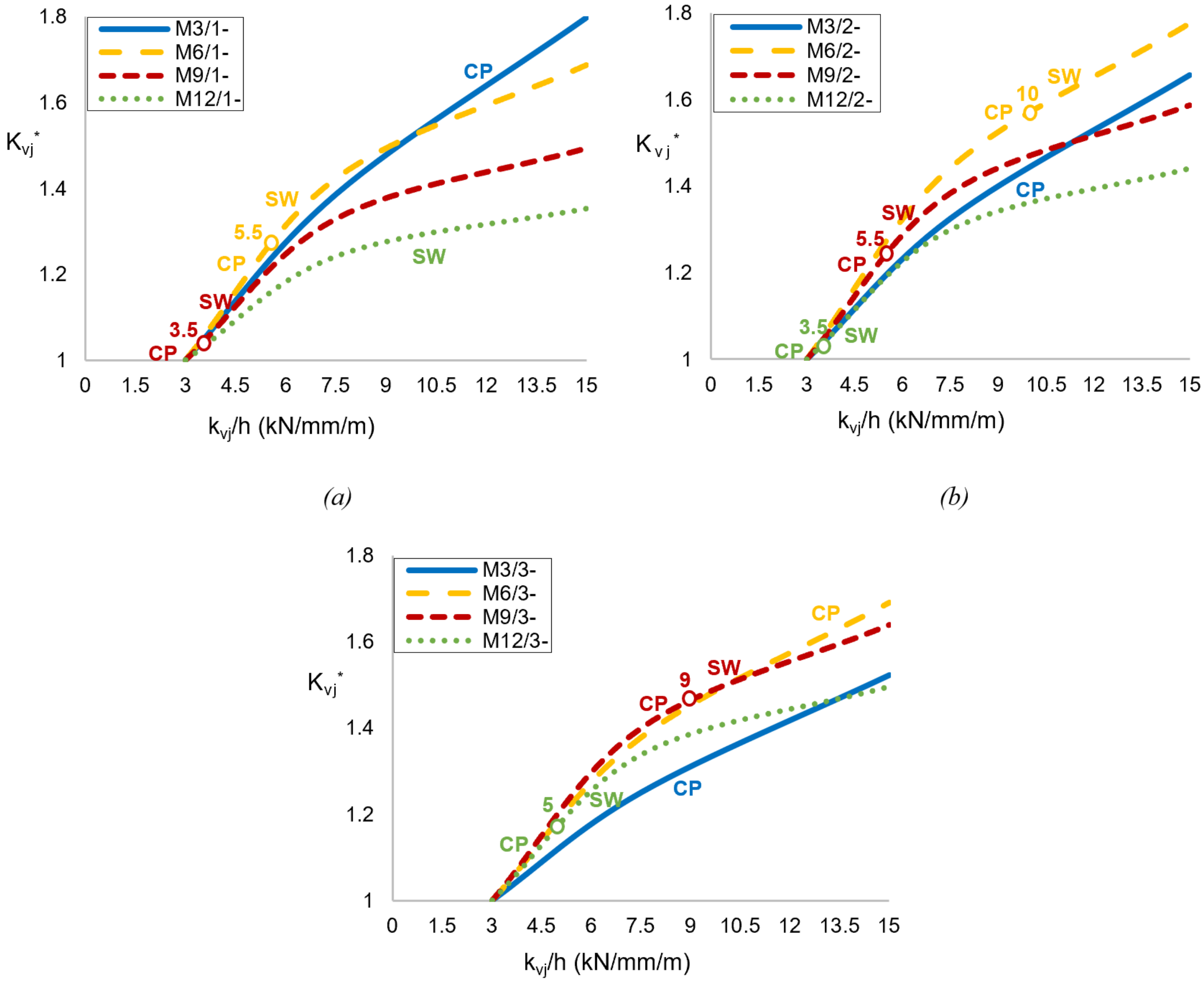

(a) *(b)* *(c)*

Figure 3.11: *Relationship between the normalised total lateral stiffness K^*_{vj} and unit vertical joints stiffness k_{vj}/h when k_{hd} equals 25 kN/mm (H25), and vertical loads equal 20 kN/m (VL20), with b=1 m (a); b=2 m (b); b=3 m (c).*

For hold-down stiffness equal to 25 kN/mm (Figure 3.11), values k_{vj}/h representing the transitions between CP and SW decreases with increasing height of the panels as shown in Figure 3.12.

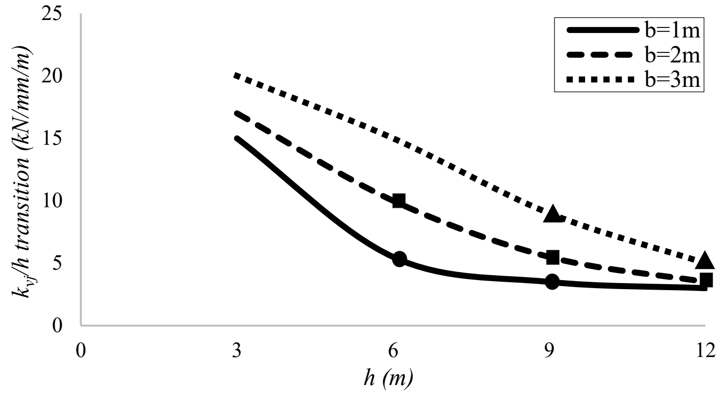

Figure 3.12: *Stiffness of vertical joints for which the transition from CP to SW is achieved versus the height of panels when k_{hd} equals 25 kN/mm (H25) and vertical loads equal 20 kN/m (VL20)*

Table 3.4 shows the percentages of models with CP mode when the stiffness of hold-downs increases from 10 to 100 kN/mm with vertical loads (each stiffness value contains 72 models), while Table 3.5 presents the percentages of models with SW mode when the unit stiffness of vertical joints increases from 3 to 15 kN/mm/m with vertical loads (each stiffness value contains 96 models). It can be observed that the behaviour seems dominated by CP mode when k_{hd} increases, while the SW mode is prevalent when the unit vertical joint stiffness increases.

Table 3.4: *Percentage of CP mode with varying k_{hd}*

k_{hd} (kN/mm)	***10***	***25***	***50***	***100***
Percentages of CP mode*	*17%*	*42%*	*68%*	*89%*

$$* \, Note: Percentage\ of\ CP\ mode = \frac{No.of\ the\ models\ shown\ as\ CP\ mode}{No.of\ the\ total\ models\ (= 72)} \times 100\%.$$

Table 3.5: *Percentage of SW mode with varying k_{vj}/h*

k_{vj}/h (kN/mm/m)	***3***	***7.5***	***15***
Percentages of SW mode*	*22%*	*47%*	*70%*

$$* \, Note: Percentage\ of\ SW\ mode = \frac{No.of\ the\ models\ with\ SW\ mode}{No.of\ the\ total\ models\ (= 96)} \times 100\%.$$

The aspect ratio of the panels played a significant role in the deformation behaviour of the wall.

As expected, when the aspect ratio increased, the total lateral stiffness decreased. It is interesting to note, however, that the rocking dominates the behaviour for panel aspect ratios less than 6, whereas bending deformation becomes significant for higher aspect ratios. It should also be noted that shear deformation also contributes to aspect ratios less than 2. Figure 3.13a, c and 3.13b, d present the percentage of the rocking and bending deformation of the total deformation as a function of the hold-down stiffness k_{hd} and vertical joint stiffness k_{vj}, respectively. The figures clearly show the significant contribution of the rocking deformation at low values of hold-down and vertical joints stiffness. The percentage of rocking deformation seems to drop significantly when the stiffness of hold-downs or vertical joints increases, particularly in the case of hold-down stiffness increase and slender panels (i.e. panels with aspect ratios of 12:1 in Figure 3.13a). Conversely, the contribution of bending deformation increases with increasing stiffness of hold-downs and vertical joints. Although the contribution of shear deformation is independent of the hold-down and vertical joint stiffness, shear percentage shows a slight increase due to the use of different configurations leading to differences in the total lateral deformation for each analysed case (Figure 3.13e, f). As a result, the contribution of bending deformation (Figure 3.13c, d) appears to be complementary to that of rocking deformation (Figure 3.13a, b).

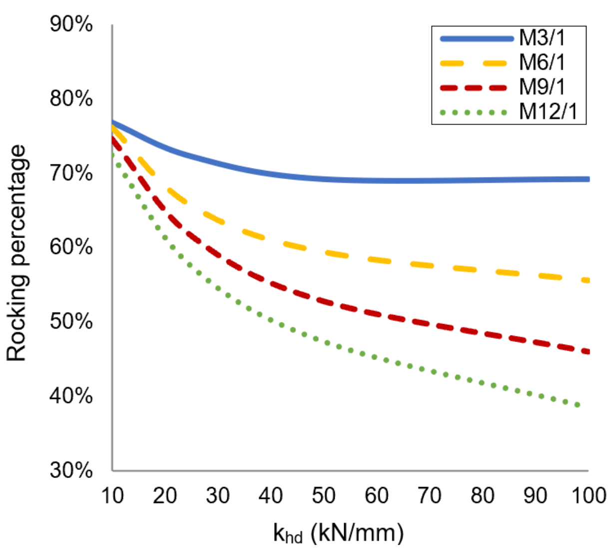

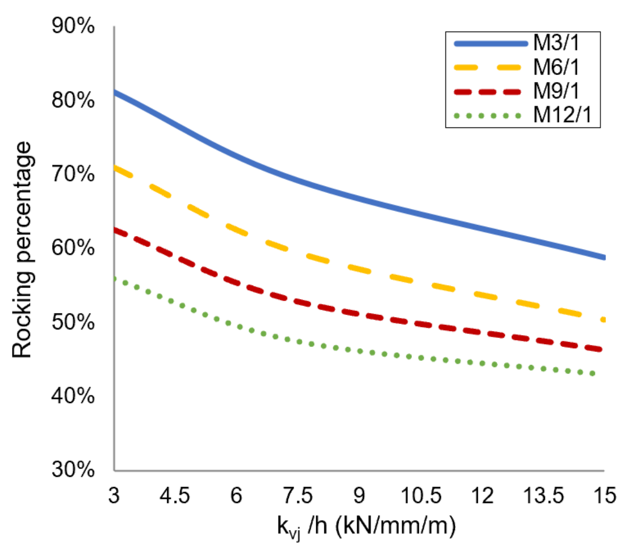

(a) k_{vj}/h = 7.5kN/mm/m (b) k_{hd} = 50 kN/mm

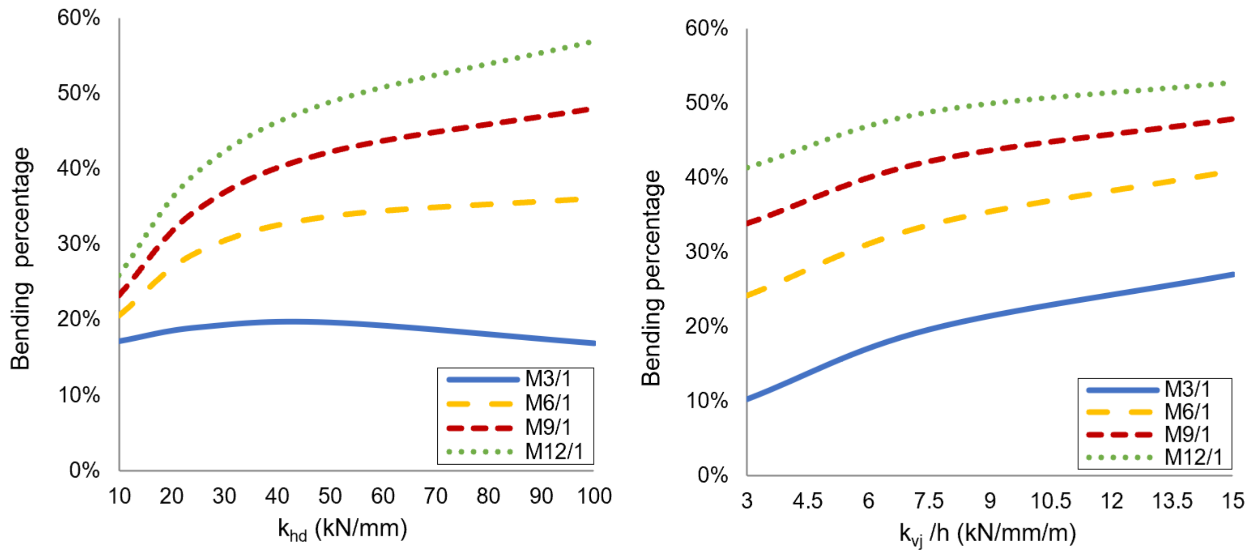

(c) k_{vj}/h = 7.5kN/mm/m (d) k_{hd} = 50 kN/mm

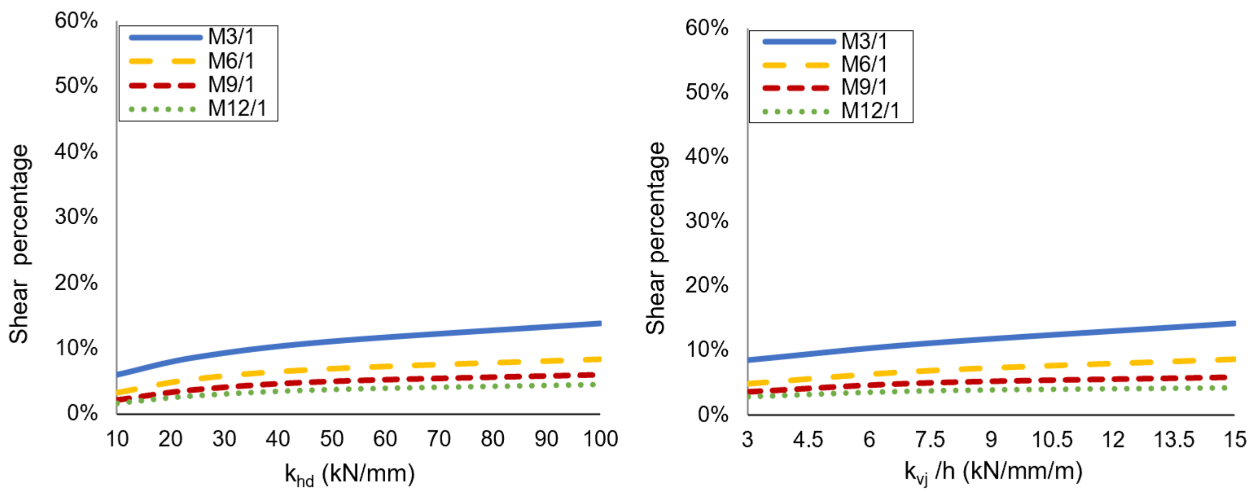

(e) k_{vj}/h = 7.5kN/mm/m (f) k_{hd} = 50 kN/mm

Figure 3.13: *Relationship (a) between rocking percentage and k_{hd}, (b) between rocking percentage and k_{vj}/h, (c) between bending percentage and k_{hd}, (d) between bending percentage and k_{vj}/h, (e) between shear percentage and k_{hd}, and (f) between shear percentage and k_{vj}/h when vertical loads equal to 20kN/m for all cases.*

3.4.2. The impact of vertical loads

Figure 3.14 compares the values of the average lateral stiffness between the cases with and without vertical loads when the width of panels b is 1 m, 2 m and 3 m. As expected, the total lateral stiffness

K is positively affected by the increase in vertical loads, however, it can be noted that the effect is much less pronounced when aspect ratio increases. It was also found that the presence of the vertical loads yields more cases with CP mode. The data indicates that when a vertical load of 20 kN/m/storey is applied, the number of the cases with the CP mode increases from 130 out of 288 (45.1%) to 180 out of 288 (62.5%).

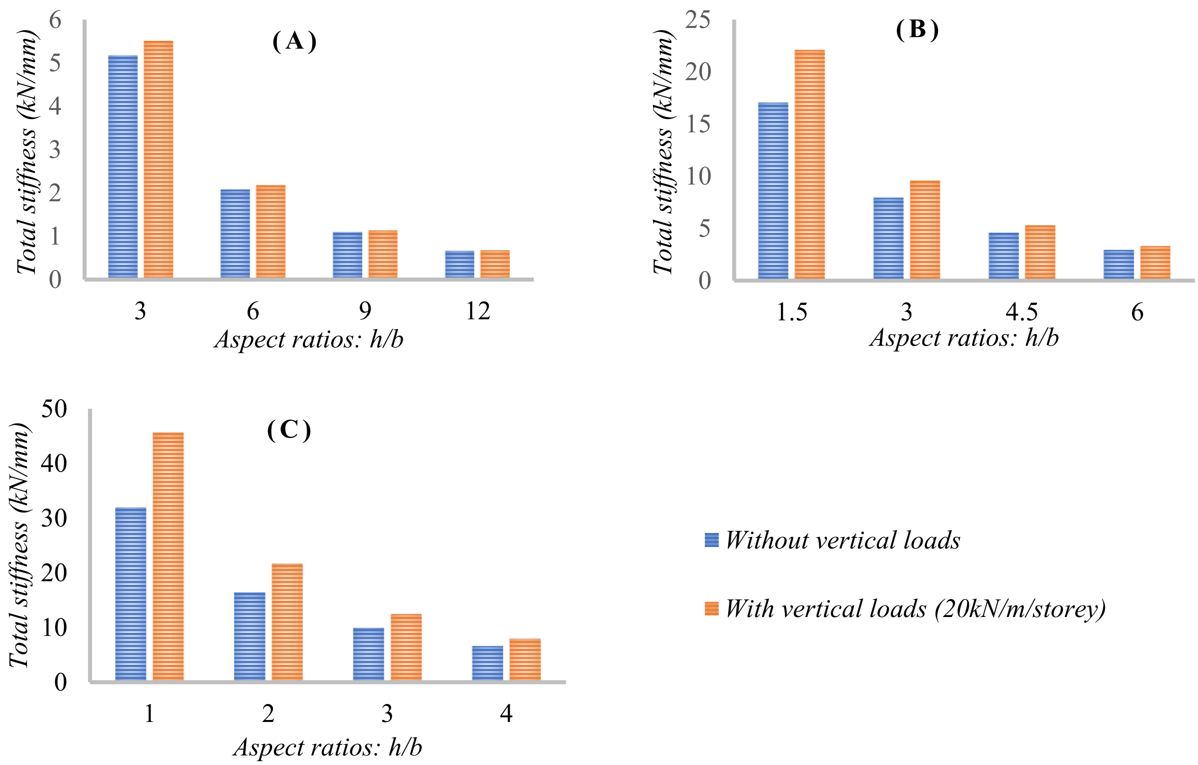

Figure 3.14: *Impact of the vertical loads on the total lateral stiffness with (A) b=1m (B) b=2m (C) b=3m*

3.5. Shearwalls consisting of more than two panels

An investigation is expanded further to multi-panel (>2) balloon-type CLT shearwall systems considering the impact of the number of panels. The expanded model consists of shearwalls up to 4 panels and considers two conditions as shown in Figure 3.15:

- C1: a fixed ratio of height of panels *h (h=12m)* to total width of shearwalls *B (B=4m)*,

- C2: a fixed ratio of height of panels *h (h=12m)* to width of single panel *b (b=1m)*.

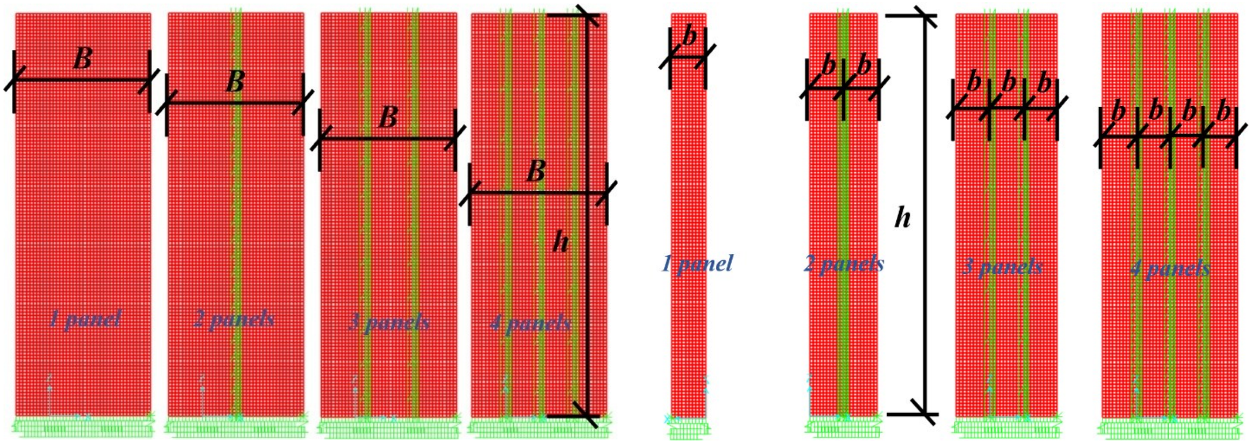

(a) C1: Varying panel number with fixed h/B (12:4) *(b) C2: Varying panel number with fixed h/b (12:1)*

Figure 3.15: *FE models of multi-panel CLT shearwalls*

The analysis for the fixed h/B ratio found that increasing the number of panels within a fixed total width resulted in a decrease in the total lateral stiffness of shearwall system (Figure 3.16). In comparison, it is found that the models with higher relative stiffness $\tilde{k}$ (defined as a ratio between k_{hd} and k_{vj}) showed a more significant reduction in stiffness than those with lower relative stiffness values.

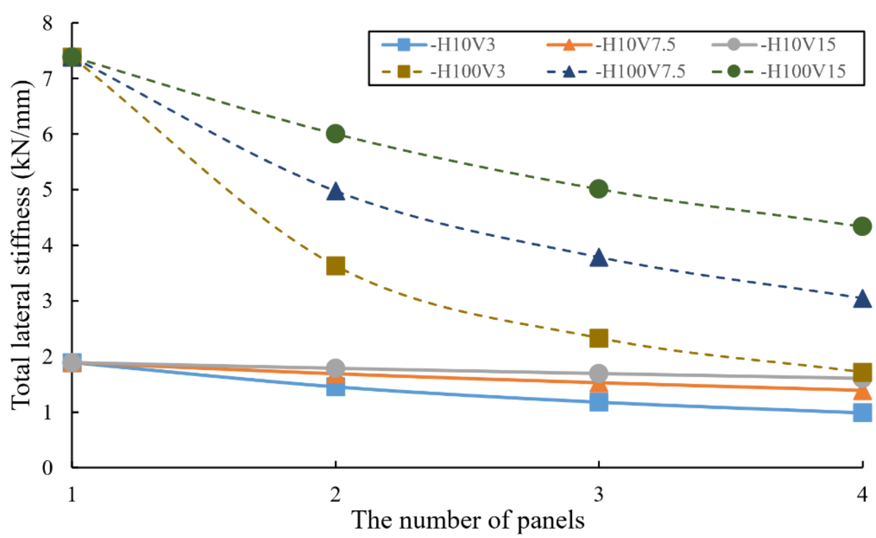

Figure 3.16: *Relationship between the number of panels and K when h/B is fixed to be 12:4 and vertical loads equal to 20 kN/m*

With an increasing number of panels, the partitioning of deformation between bending and rocking becomes increasingly complex. When the unit stiffness of vertical joints is fixed at 7.5 kN/mm/m, a higher percentage of rocking behaviour is shown when more panels are used with fixed h/B, as illustrated in Figure 3.17a. However, when $\tilde{k}$ is very low, (H10V15 in Figure 3.17b), the percentage of rocking deformation shows a slight reduction with increasing panel number. This behaviour may be attributed to the influence of kinematic mode transitions, which tend to be more complex in multi-panel shearwall systems.

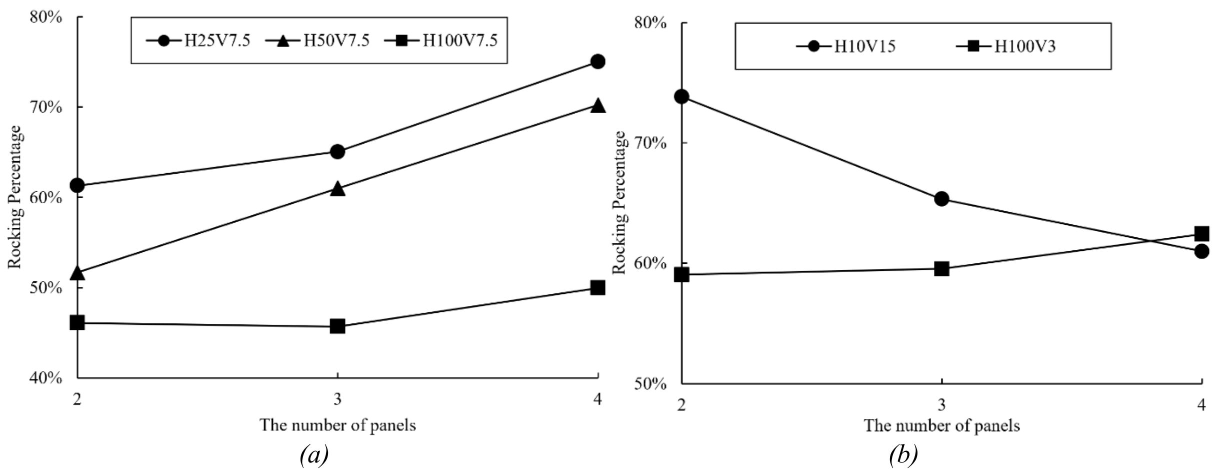

Figure* 3.17*: Relationship between the number of panels and rocking percentage for the models when h/B is fixed to be 12:4 and vertical loads equal to 20 kN/m

With respect to the kinematic modes, the models with CP mode tend to maintain that behaviour following an increase in the number of panels. However, models with SW mode could shift to IN behaviour when more panels are added. Figure 3.18 shows an example from model M h/b-P#-VL20-H25V15, where when the number of panels increases from 2 to 4, the kinematic mode changes from SW to IN.

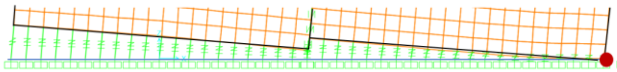

Panel Number=2 (SW mode)

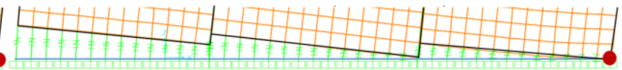

Panel Number=3 (SW mode)

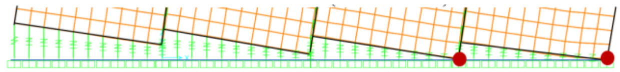

Panel Number=4 (IN mode)

Figure 3.18: *Kinematic modes of the models with varying panel numbers*

When a constant ratio of h/b (C2) is maintained, the total lateral stiffness tends to increase when the number of panels is increased as shown in Figure 3.19. With respect to the percentage of rocking deformation, it is found that the result is similar to that obtained in the case fixed h/B ratio.

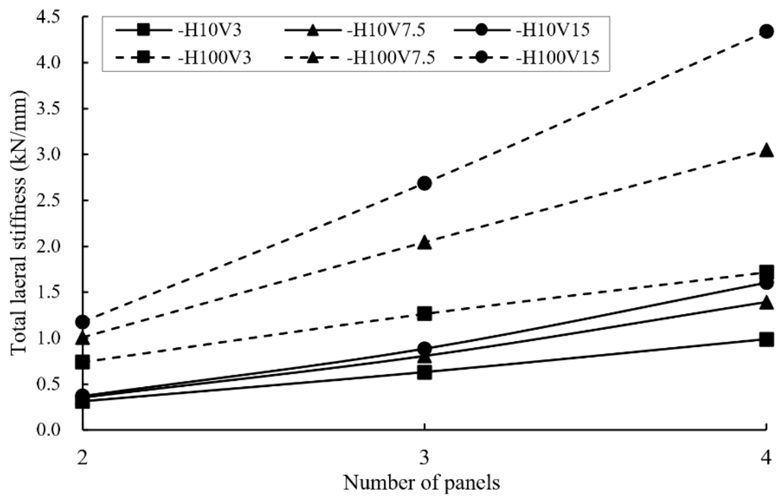

Figure 3.19: *Relationship between the number of panels and K when h/b is fixed to be 12:1 and vertical loads equal to 20 kN/m*

CHAPTER FOUR

ANALYICAL MODEL

4. Analytical model

The development of the analytical model takes into account the key parameters affecting the lateral deformation of balloon-type CLT shearwall system, which were identified in the sensitivity analysis, including the stiffness of connectors, panel aspect ratios and vertical loads. The bending deformation becomes particularly critical in shearwalls with high aspect ratios (e.g., ≥ 6), and as such the panels can no longer be assumed rigid. This chapter describes the model assumptions and development for rocking, in-plane panel bending and shear, as well as sliding deformations.

4.1. Model assumptions

The geometrical dimensions of the panels comprising the wall are assumed to be equal, as shown in Figure 4.1 (a). Panels are connected to each other through vertical joints with a total stiffness k_{vj} and to the foundation using hold-downs with stiffness k_{hd} and angle brackets with horizontal stiffness equal to k_{sl}. The shearwalls span a total of n storeys, each with height of h_{int}. A constant lateral load F is applied at each diaphragm level. Vertical joints are distributed uniformly along the height of the panels, and hold-downs are placed at both base corners of the wall. A vertical uniformly distributed gravity load q is assumed to be applied at each storey.

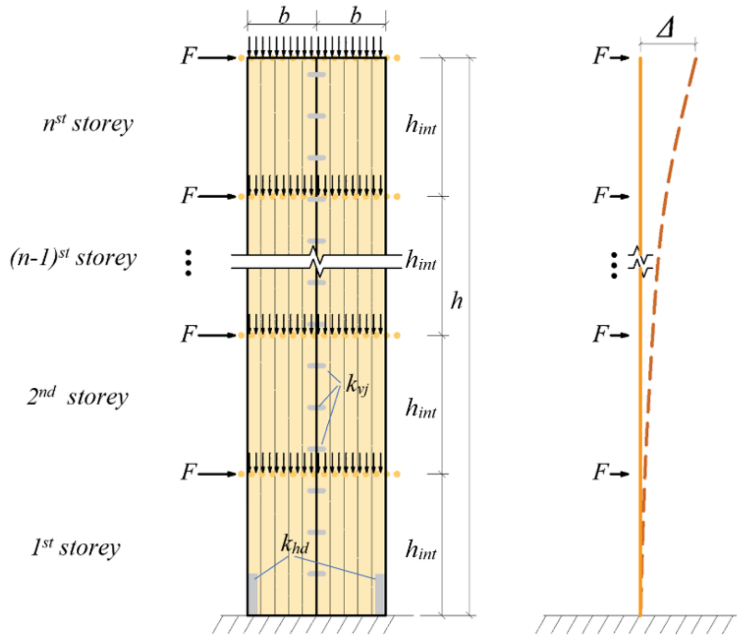

(a) (b)

Figure 4.1: *(a) Analytical model and (b) Simplified model for estimating bending deformation*

The contributions to the total horizontal deformation are assumed to include bending, shear, rocking, and sliding (Figure 4.2), as expressed in Eq. 4.1:

$$\Delta_{total} = \Delta_{bending} + \Delta_{shear} + \Delta_{sliding} + \Delta_{rocking} \tag{4.1}$$

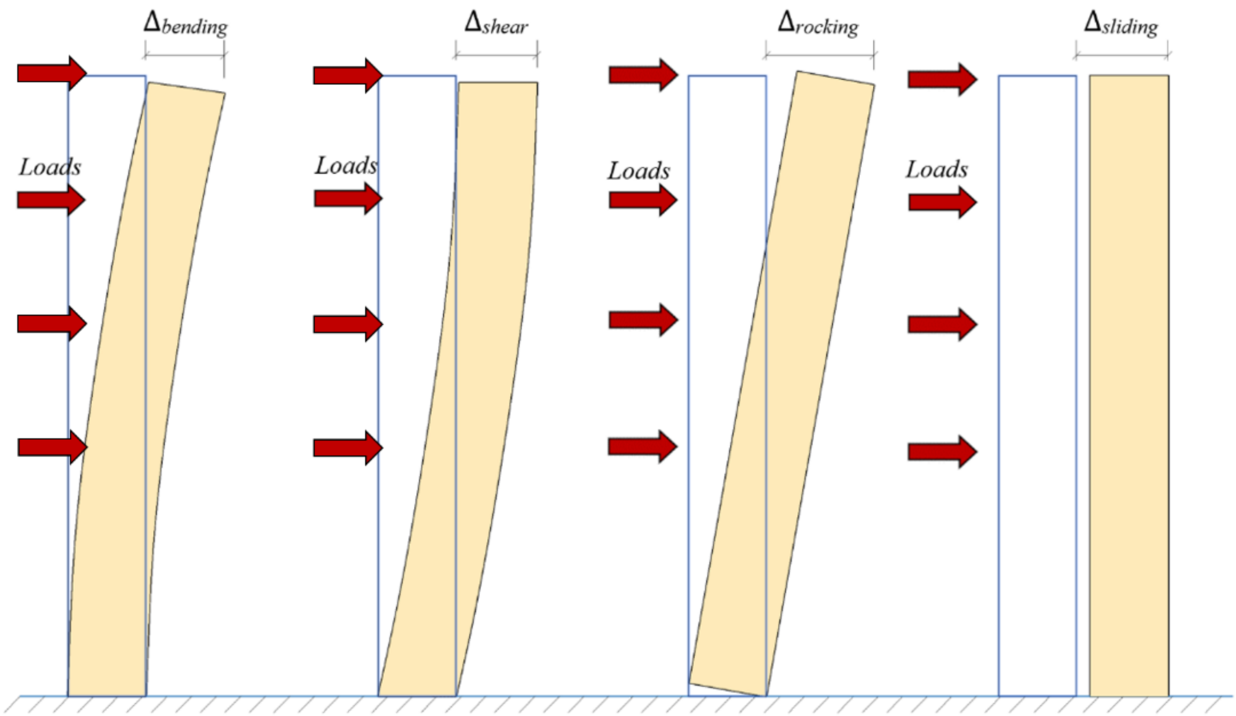

Figure 4.2: *Components of the lateral deformation of the balloon-type CLT panel*

Although it is desired to limit sliding deformation, due to the consequence of such failure mode, the deformation contribution from sliding can be limited but should not be ignored. Considering the sliding deformation can be included in the overall deformation estimate by adding the contribution obtained using Eq. 4.2, which was developed for platform-type CLT shearwalls (Casagrande et al., 2018).

$$\Delta_{sliding} = \frac{F_{sl}}{k_{sl}} \tag{4.2}$$

where

F_{sl} is the total horizontal shear force transferred at the wall-foundation interface,

k_{sl} is the total lateral shear stiffness of the base shear connections resisting relative sliding between the wall and the foundation.

In accordance with the provisions of CSA O86 (CSA Group, 2024), explicit consideration of sliding deformation is generally limited, and hence the model developed and analysed in this thesis addresses bending, shear and rocking deformation, as presented in the following sections.

4.2. Bending deformation

In order to estimate the flexural deformation in isolation, the rocking deformation is restricted by adding a fixed connection between the panels and foundation, allowing the shearwall system to be considered as a cantilever (Figure 4.1b). This permits the classical beam theory to be employed, where the effective stiffness EI_{eff} can be evaluated.

According to Blass and Fellmoser (2004), the effective modulus of elasticity along the vertical direction (parallel to the outer layer) $E_{0,eff}$ can be estimated by:

$$E_{0,eff} = E_0 \cdot k_3 \tag{4.3}$$

where

E_0 is the modulus of elasticity parallel to the grain,

k_3 is the composition factor for cross-layer defined by Blass and Fellmoser (2004) when external in-plane loads are applied perpendicular to the outermost-layer fibres and can be determined by:

$$k_3 = 1 - \left(1 - \frac{E_{90}}{E_0}\right) \cdot \frac{a_{m-2} - a_{m-4} + \cdots \pm a_1}{a_m} \tag{4.4}$$

where

E_{90} is the modulus of elasticity perpendicular to the grain,

m is the number of total layers,

a_i is the sum of the specific layers shown in Figure 4.3, and $i = 1, 3, 5, \ldots, m-4, m-2$.

For five-layer CLT panels with laminates consisting of the same thickness and grain directions shown in Figure 4.3, $E_{0,eff}$ is simplified as:

$$E_{0,eff} = E_0 \cdot \left[1 - \left(1 - \frac{E_{90}}{E_0}\right) \cdot \frac{3t - t}{5t}\right] = E_0 \cdot \left[\frac{3}{5} + \frac{2E_{90}}{5E_0}\right] \tag{4.5}$$

where

t is the thickness of each lamina.

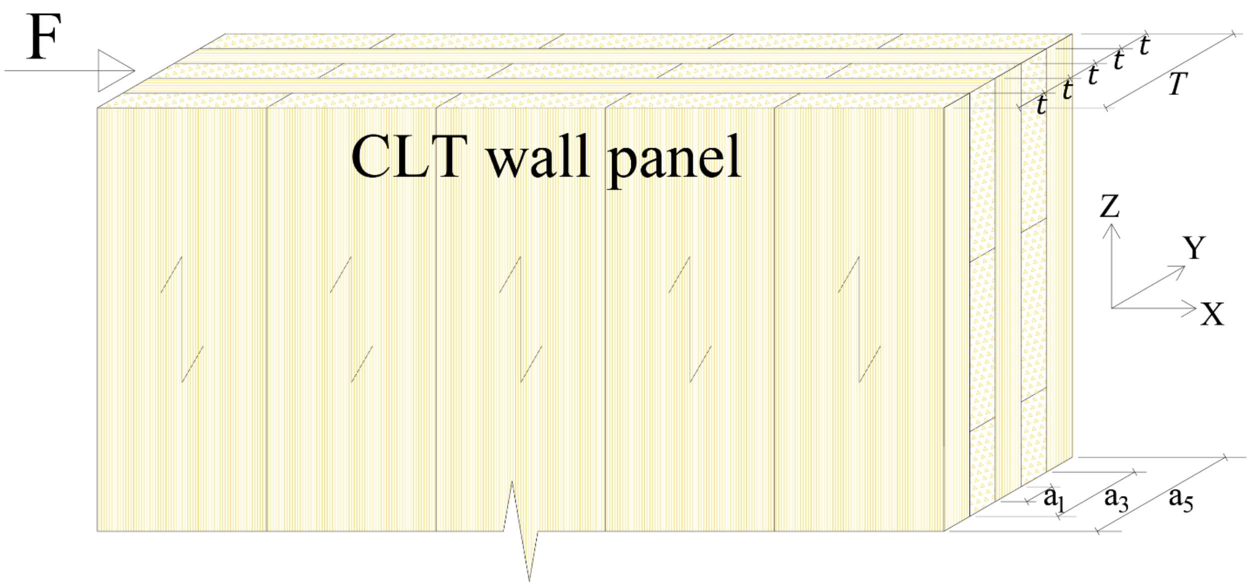

Figure 4.3: *Definition of variable a_i for a 5-layer CLT shearwall*

Although the second moment of inertia I can simply be calculated using Eq. 4.6 for the single panel with the rectangular cross-section, the total effective second moment of inertia I_{eff} for a two-panel system is more complicated to be estimated since the shear stiffness of vertical joints between panels should be taken into account.

$$I = \frac{Tb^3}{12} \tag{4.6}$$

where

T is the total thickness of a panel,

b is the width of a panel.

When fully composite behaviour is assumed ($k_{vj} = \infty$) between panels, I_{eff} can be expressed by:

$$I_{eff} = \frac{TB^3}{12} = \frac{2Tb^3}{3} \tag{4.7}$$

where

B is the total width and is equal to 2b for a two-panel system.

When no composite behaviour ($k_{vj} = 0$) between panels is assumed, the panels move separately, and thus, I_{eff} can be expressed by:

$$I_{eff} = \frac{Tb^3}{12} + \frac{Tb^3}{12} = \frac{Tb^3}{6} \tag{4.8}$$

However, the real state of deformation falls between Eq. 4.7 and Eq. 4.8, and is illustrated in Figure 4.4:

$$\frac{Tb^3}{6} < I_{eff} < \frac{2Tb^3}{3} \tag{4.9}$$

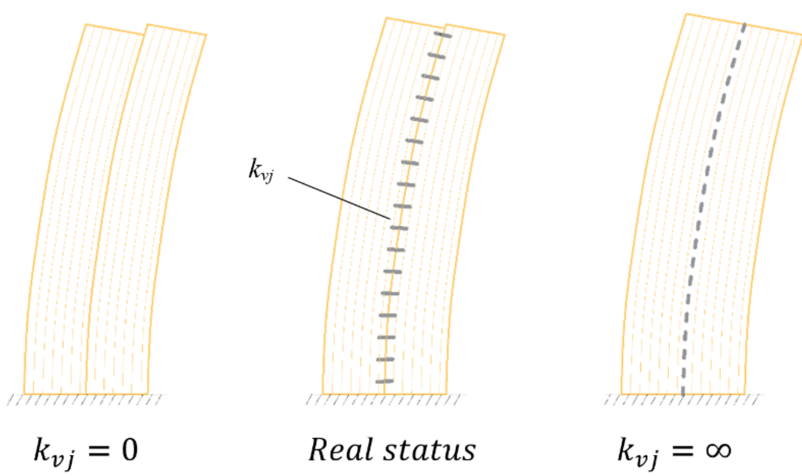

Figure 4.4: *Impact of the vertical joints on the flexural deformation of the two-panel shearwall system*

In order to better estimate EI_{eff} for balloon-type CLT shearwalls, the methodology proposed in this research is based on the γ method (Möhler et al., 1962), which is an approach typically used to analyse mechanically jointed beams in Eurocode 5 (CEN, 2004). The assumptions associated with this approach include:

- The shearwall is equivalent to a simply supported beam with an effective length equal to twice the height of the shearwall,
- The spacing s between each vertical joint is constant, and as such the stiffness of vertical joints is assumed to be uniformly distributed along the vertical direction.
- All panels have the same deflection, rotation, and curvature and can be analysed based on the Bernoulli beam theory.
- Vertical joints only provide the shear resistance.
- No friction is assumed between panels.

According to the Euler-Bernoulli equation:

$$EI\frac{d^4w(x)}{dx^4} = q(x) \tag{4.10}$$

where

$w(x)$ is the function of deflection,

$q(x)$ is the function of load.

It is noted that a sinusoidal load distribution is assumed to acquire the closed-form solution of the differential equation, however, previous studies have demonstrated that the choice of load pattern has a negligible influence on EI_{eff} (Girhammar, 2009; Cuerrier-Auclair, 2020). Therefore, the analytical model presented in Figure 4.1, which assumes a uniform load distribution at each storey, is also applicable for the implementation of the γ method.

When the vertical joints provide shear resistance, the differential equations can be established as follows (Cuerrier-Auclair, 2020):

$$EI\frac{d^4w(x)}{dx^4} + D\cdot\frac{d^2N(x)}{dx^2} = q(x) \tag{4.11}$$

$$\frac{d}{dx}\left(\frac{1}{k}\frac{dN(x)}{dx}\right) - \frac{1}{EA}N(x) + D\cdot\frac{d^2w(x)}{dx^2} = 0 \tag{4.12}$$

where

$N(x)$ is the function of axial force on each panel,

D is the distance between the centroid of two panels,

EI is the bending stiffness of the shearwall system without composite behaviour,

EA is the axial stiffness of the shearwall system,

k is the vertical joints stiffness per unit length, equal to k_{vj}/h.

Solving the differential equation presented in Eq. 4.11 and Eq.4.12, EI_{eff} can be expressed by:

$$EI_{eff} = EI + \frac{(EA)\cdot D^2}{1+\frac{\pi^2(EA)}{k(h_{eff})^2}} \tag{4.13}$$

where

h_{eff} is the effective length of the shearwalls assumed equal to twice the total height of the panels.

By introducing the γ factor to describe the composite behaviour between panels, EI_{eff} can be expressed as follows:

$$EI_{eff} = (EI)_1 + (EI)_2 + \gamma_1(EA)_1a_1^2 + \gamma_2(EA)_2a_2^2 \tag{4.14}$$

where

γ_i and a_i can be determined according to Kreuzinger (1995) and Cuerrier-Auclair (2020):

$$\gamma_1 = 1 \tag{4.15}$$

$$\gamma_2 = \frac{1}{1 + \frac{\pi^2 (EA)_2}{k(h_{eff})^2}} \tag{4.16}$$

$$a_1 = \frac{\gamma_2 (EA)_2 D}{\gamma_1 (EA)_1 + \gamma_2 (EA)_2} \tag{4.17}$$

$$a_2 = \frac{\gamma_1 (EA)_1 D}{\gamma_1 (EA)_1 + \gamma_2 (EA)_2} \tag{4.18}$$

a_1 is the distance between the centroid and the neutral axis of the first panel, and a_2 is the distance between the neutral axis of the first panel and the centroid of the second panel,

EA_i is the axial stiffness of panel *i,*

EI_i is the bending stiffness of panel *i*.

From the Eq. 4.16, it is known that the non-dimensional factor $\gamma_2 = 0$ if $k_{vj} = 0$ ($k = 0$), while $\gamma_2 = 1$ if $k_{vj} = \infty$ ($k = \infty$). Thus, the value of γ_2 between 0 and 1 represents the real condition of partial composite action (Figure 4.5).

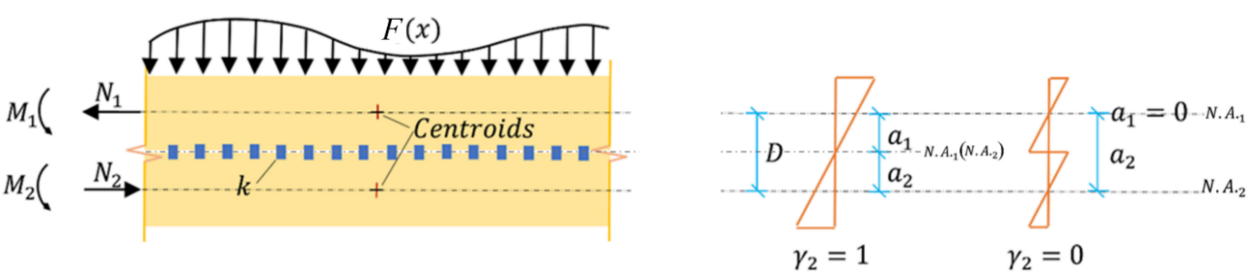

Figure 4.5: *Reactions and the stress distribution of the cross-section of the panels*

When two panels with identical dimensions are used in the shearwall system, the equation can be further simplified to:

$$EI_{eff} = 2EI_0 + \frac{\gamma}{\gamma + 1} EA_0 \cdot b^2 \tag{4.19}$$

where

EI_0 equals EI_1or EI_2 once the dimensions of the two panels are the same,

EA_0 equals EA_1or EA_2 once the dimensions of the two panels are the same,

γ equals γ_2, which could be rewritten by:

$$\gamma = \frac{1}{1 + \frac{\pi^2 EA_0}{4kh^2}} \tag{4.20}$$

Since $I_0 = Tb^3/12$ and $A_0 = Tb$, substituting in Eq. 4.19, one obtains:

$$EI_{eff} = E_{0,eff} \cdot \left(\frac{1}{6} + \frac{1}{\frac{\pi^2 E_{0,eff} Tb}{4kh^2} + 2} \right) \cdot Tb^3 \tag{4.21}$$

This expression can also be written as shown in Eq. 4.22 by replacing k by $n_r k_{ea}/s$, when the vertical joints are uniformly distributed along the vertical direction:

$$EI_{eff} = E_{0,eff} \cdot \left(\frac{1}{6} + \frac{1}{\frac{\pi^2 E_{0,eff} Tbs}{4n_r k_{ea} h^2} + 2} \right) \cdot Tb^3 \tag{4.22}$$

where

n_r is the number of rows in the vertical joints,

k_{ea} is the stiffness of each vertical joint,

s is the spacing between the vertical joints along the vertical direction,

h is the height of panels.

The lateral bending displacement $\Delta_{bending}$ of a balloon-type CLT shearwall system can be estimated by Eq. 4.23 for a cantilever subjected to equal concentrated loads at each storey (Hibbeler, 2015):

$$\Delta_{bending} = \frac{Fh^3}{3(EI)_{eff}} \cdot \left[\frac{(n+1)(3n+1)}{8n} \right] \tag{4.23}$$

where

F is the horizontal load applied at each storey,

n is the number of storeys.

4.3. Shear deformation

The effective in-plane shear modulus G^* can be estimated (Bogensperger, Moosbrugger and Silly, 2010; Brandner et al., 2017) by:

$$G^* = \frac{G_0}{1 + 6\alpha_T \left(\frac{t_{mean}}{w_l}\right)^2} \tag{4.24}$$

where

G_0 is the in-plane shear modulus of laminas,

t_{mean} is the mean thickness of each laminar layer of CLT panels, which can be calculated by:

$$t_{mean} = \frac{T}{m} \tag{4.25}$$

Where

m is the number of layers of CLT panels,

w_l the width of each lamina strip,

α_T can be determined by:

$$\alpha_T = p_0 \left(\frac{t_{mean}}{w_l}\right)^{q_0} \tag{4.26}$$

where the values of the parameters p_0 and q_0 could refer to Table 4.1 below according to Droscher (2014):

***Table 4.1:** The values of p_0 and q_0*

No. of layers	*3*	*5*	*7*
p_0	*0.53*	*0.43*	*0.39*
q_0	*-0.79*	*-0.79*	*-0.79*

As a result, the shear deformation can be written as:

$$\Delta_{shear} = \frac{\kappa F h(n+1)}{2G^* A} \tag{4.27}$$

where

A is the total cross-section area of the shearwall resisting system,

κ is the form factor for the cross-section area. It is noted that the modelling analysis defaults to an assumed value of 1.0 for shell elements and 1.2 for frame elements.

In total, the bending and shear deformation of a balloon-type shearwall system can be calculated by:

$$\Delta_{bending+shear} = \frac{Fh^3}{3EI_{eff}} \cdot \left[\frac{(n+1)(3n+1))}{8n}\right] + \frac{\kappa F h(n+1)}{2G^* A} \tag{4.28}$$

4.4. Rocking deformation

The assumptions used in the derivation of the rocking deformation equations include:

- The centres of rotation in rocking deformation are located at the corners of the panels,
- The in-plane rotation angle of each panel in the rocking deformation is the same in both CP mode and SW mode,
- The vertical joints possess only shear stiffness along the vertical direction between two panels,
- There is no friction between panels.

It is found that different kinematic modes influence the rocking deformation, and as a result the CP and SW modes are discussed separately.

4.4.1. CP mode

In the CP mode, it is assumed that the deformation in the hold-down and vertical joints is equal, as shown in Figure 4.6:

$$\Delta_{hd} = \Delta_{vj} \tag{4.29}$$

where

Δ_{hd} is the vertical tensile displacement (uplift) of the hold-down,

Δ_{vj} is the slip displacement between panels.

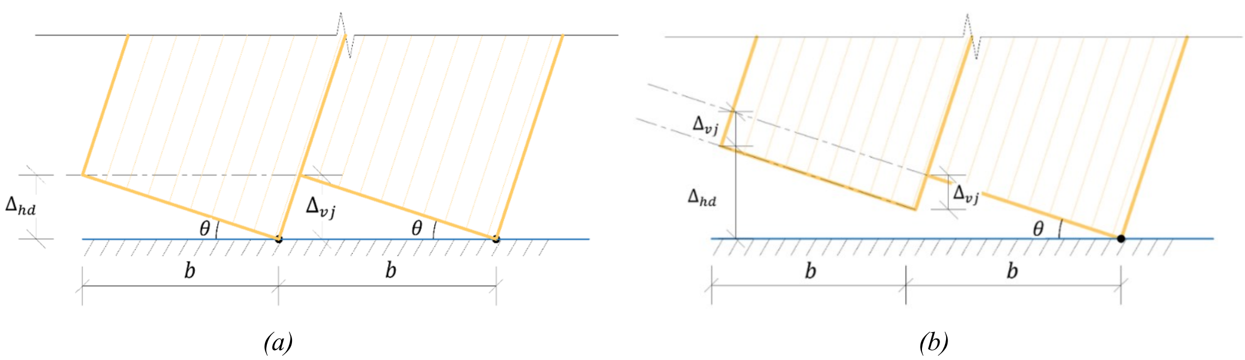

Figure 4.6: *Sketch of the relationship between Δ_{hd} and Δ_{vj} for (a) CP mode (b) SW mode*

The rocking displacement can be estimated by Eq. 4.30, and in-plane rotation angle θ could be determined by Eq. 4.31:

$$\Delta_{rocking} = \theta h \tag{4.30}$$

$$\theta = \frac{\Delta_{hd}}{b} = \frac{\Delta_{rocking,CP}}{h} \tag{4.31}$$

Due to the assumption of linear behaviour, the tensile force in the hold-down and the total shear force in the vertical joints can be calculated by:

$$F_{hd} = k_{hd}\Delta_{hd} \tag{4.32}$$

$$F_{vj} = k_{vj}\Delta_{vj} \tag{4.33}$$

where

F_{hd} are the vertical tensile force of the hold-down,

F_{vj} are total shear force between panels.

According to the force diagram (Figure 4.7), the equilibrium could be written by:

$$F_{hd} = R_{1,y} + R_{2,y} - 2qbn \tag{4.34}$$

$$\sum_{i=1}^{n} Fh_i + R_{1,y}b = Fh \cdot \frac{n+1}{2} + R_{1,y}b = F_{hd} \cdot 2b + 2b^2qn \tag{4.35}$$

$$F = F_1 + F_2 \tag{4.36}$$

$$F_{hd} \cdot b + \frac{1}{2}qb^2n = \sum_{i=1}^{n} F_1 \cdot h_i = F_1h \cdot \frac{n+1}{2} \tag{4.37}$$

$$F_{vj} \cdot b + \frac{1}{2}qb^2n = \sum_{i=1}^{n} F_2 \cdot h_i = F_2h \cdot \frac{n+1}{2} \tag{4.38}$$

where

$R_{1,y}$ and $R_{2,y}$ are the vertical reactions of the first and second panel, respectively,

F_1 and F_2 are the distributed horizontal forces at each storey on the first and second panel, respectively,

h_i is the height from the foundation level to the i^{th} storey,

q is the vertical uniformly distributed loads on each storey.

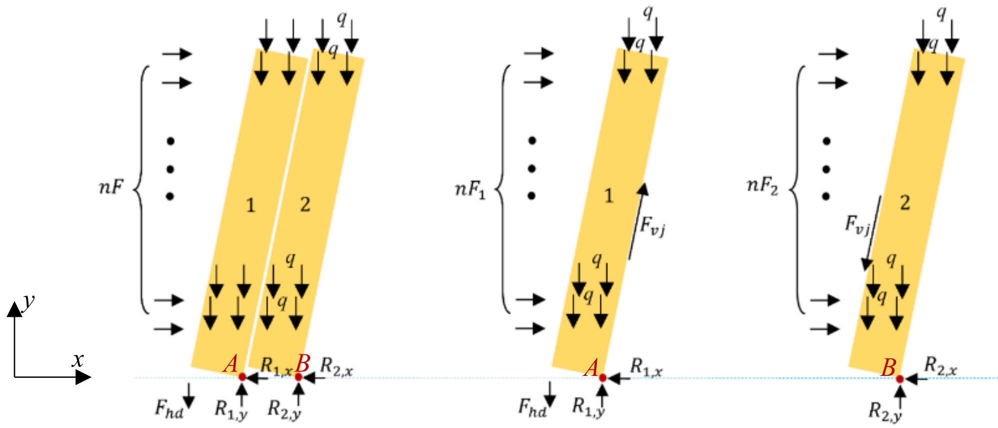

Figure 4.7: *Force analysis based on free-body diagrams for CP mode*

From the above equations, it is deduced that the distribution of the horizontal forces on each panel in the CP mode satisfies:

$$\frac{F_{hd}}{F_{vj}} = \frac{k_{hd}}{k_{vj}} \tag{4.39}$$

$$(F_{hd} + F_{vj})b + qb^2n = Fh\frac{n+1}{2} \tag{4.40}$$

Substituting the conditions into Eq. 4.30, one obtains:

$$\Delta_{rocking,CP} = (F \cdot \frac{n+1}{2} \cdot \frac{h^2}{b^2} - qhn) \cdot \frac{1}{k_{hd} + k_{vj}} \tag{4.41}$$

4.4.2. SW mode

In the SW mode, the wall deformation is assumed to conform to the following condition:

$$\theta \cdot 2b = \Delta_{hd} + \Delta_{vj} \tag{4.42}$$

Substitute θ from Eq. 4.42 into Eq. 4.30, one obtains:

$$\Delta_{rocking} = h\theta = h \cdot \frac{\Delta_{hd} + \Delta_{vj}}{2b} \tag{4.43}$$

According to the force diagram (Figure 4.8), the equilibrium could be written by:

$$F_{hd} = R_{2,y} - 2qbn \tag{4.44}$$

$$\sum_{i=1}^{n} Fh_i = Fh \cdot \frac{n+1}{2} = F_{hd} \cdot 2b + 2qb^2 n \tag{4.45}$$

$$F = F_1 + F_2 \tag{4.46}$$

$$F_{hd} \cdot b + \frac{1}{2} qb^2 n = \sum_{i=1}^{n} F_1 \cdot h_i = F_1 h \cdot \frac{n+1}{2} \tag{4.47}$$

$$F_{vj} \cdot b + \frac{1}{2} qb^2 n = \sum_{i=1}^{n} F_2 \cdot h_i = F_2 h \cdot \frac{n+1}{2} \tag{4.48}$$

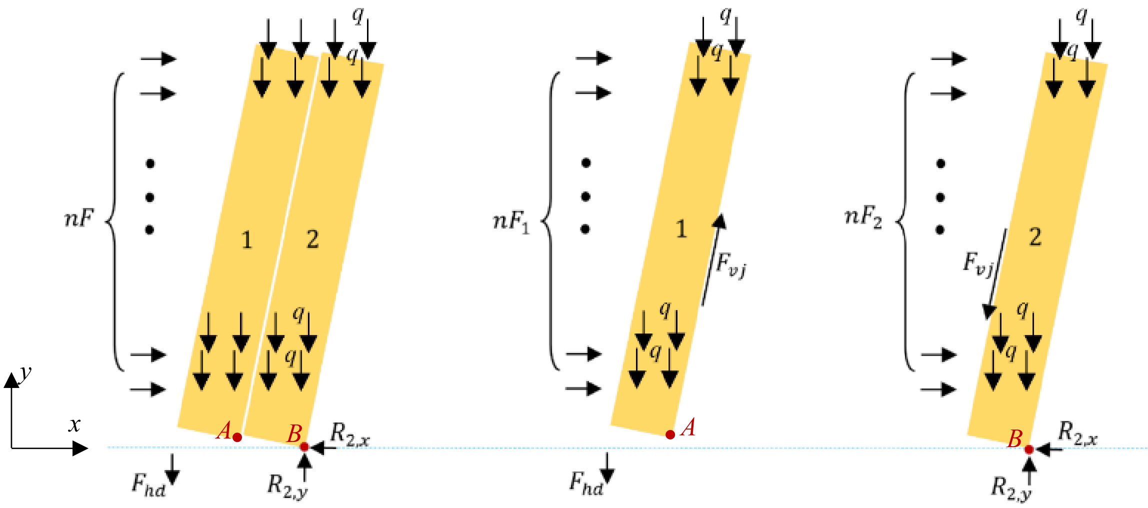

Figure 4.8: *Force analysis based on free-body diagrams for SW mode*

From the above equations, it is deduced that the distribution of the horizontal force on each panel in the SW mode satisfies:

$$F_{hd} = \frac{Fh\frac{n+1}{2} - 2qb^2 n}{2b} \tag{4.49}$$

$$F_{vj} = F_{hd} + qbn = \frac{Fh\frac{n+1}{2} - 2qb^2 n}{2b} + qbn = \frac{Fh(n+1)}{4b} \tag{4.50}$$

Substituting the conditions into Eq. 4.43, one obtains:

$$\Delta_{rocking,SW} = \frac{F}{4}\left(\frac{1}{k_{hd}} + \frac{1}{k_{vj}}\right) \cdot \frac{n+1}{2} \cdot \frac{h^2}{b^2} - \frac{qhn}{2k_{hd}} \quad (4.51)$$

4.5. Verification of the proposed model

4.5.1. Bending and shear deformation

The parameters chosen in the verification include varying aspect ratio *h/b* (from 3:1 to 12:1) and k_{vj}/h (3kN/mm/m, 7.5kN/mm/m and 15kN/mm/m), as summarised in Table 4.2. The values of γ are calculated according to Eq. 4.20:

Table 4.2: *Values of γ in varying aspect ratios and vertical stiffness*

		h=3m	***h=6m***	***h=9m***	***h=12m***
b=1m	k_{vj}/h**=3kN/mm/m**	*0.014*	*0.055*	*0.115*	*0.188*
	k_{vj}/h**=7.5kN/mm/m**	*0.035*	*0.126*	*0.246*	*0.367*
	k_{vj}/h**=15kN/mm/m**	*0.067*	*0.224*	*0.394*	*0.537*

Table 4.3 provides the calculated values of $(EI)_{eff}$ using Eq. 4.21:

Table 4.3: *Values of $(EI)_{eff}$ in varying aspect ratio and vertical stiffness*

		h=3m	***h=6m***	***h=9m***	***h=12m***
b=1m	k_{vj}/h**=3kN/mm/m**	*1.366*	*1.652*	*2.041*	*2.457*
	k_{vj}/h**=7.5kN/mm/m**	*1.515*	*2.109*	*2.751*	*3.288*
	k_{vj}/h**=15kN/mm/m**	*1.738*	*2.646*	*3.398*	*3.900*

Finally, the values of bending and shear deformation could be calculated by Eq. 4.28, as shown in Table 4.4.

Table 4.4: *Values of* $\Delta_{bending+shear}$ *in varying aspect ratios and vertical stiffness*

		h=3m	***h=6m***	***h=9m***	***h=12m***
b=1m	k_{vj}/h***=3kN/mm/m***	*2.35*	*17.22*	*59.19*	*142.04*
	k_{vj}/h***=7.5kN/mm/m***	*2.24*	*14.62*	*46.16*	*107.12*
	k_{vj}/h***=15kN/mm/m***	*2.10*	*12.30*	*37.61*	*88.37*

A numerical FE modelling analysis is conducted with identical parameters to those used in the analytical model. The results show that the deviations in the values of $\Delta_{bending+shear}$ between numerical modelling and analytical expression are less than 4%, as illustrated in Figure 4.9. This comparison shows that the proposed analytical solution for the bending and shear deformation can provide reasonable estimates.

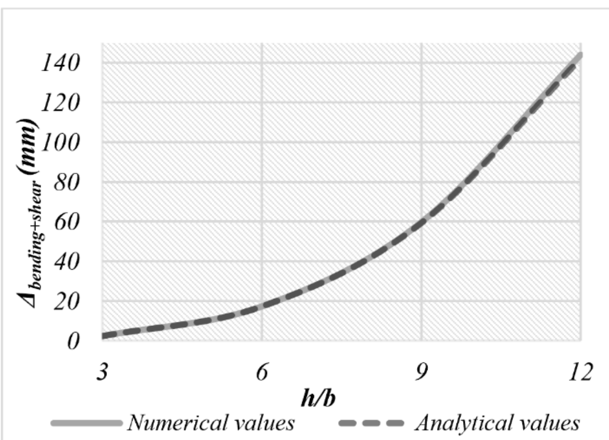

(a) $k_{vj}/h = 3kN/mm/m$

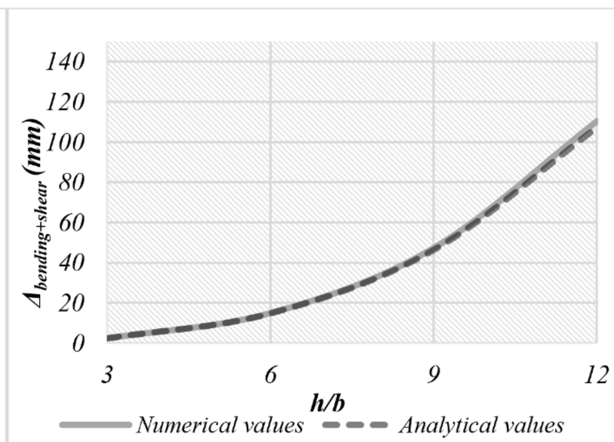

(b) $k_{vj}/h = 7.5kN/mm/m$

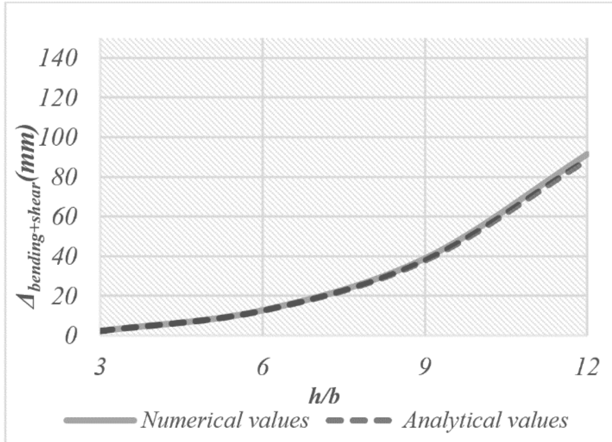

(c) $k_{vj}/h = 15kN/mm/m$

Figure 4.9: *Comparisons between the values of* $\Delta_{bending+shear}$ *obtained from the FE numerical modelling result and the analytical expression*

4.5.2. Rocking deformation

The parameters selected for this verification include varying wall aspect ratio *h/b* from 3:1 to 12:1, while maintaining a constant panel width b equal to 1 m, hold-down stiffness $k_{hd}$with 10 kN/mm, 25 kN/mm, 50 kN/mm and 100 kN/mm, and unit vertical joint stiffness k_{vj}/h with 3 kN/mm/m, 7.5 kN/mm/m and 15 kN/mm/m. A vertical load equal to 20 kN/m is applied on each floor. The values are calculated according to Eq. 4.41 and 4.51.

In order to isolate the rocking behaviour in the numerical FE model, the panels are assumed to be rigid. The results are illustrated in Figure 4.10 and it can be seen that the proposed model matches the rocking deformation behaviour obtained numerical of the modelled walls with maximum errors below 10%.

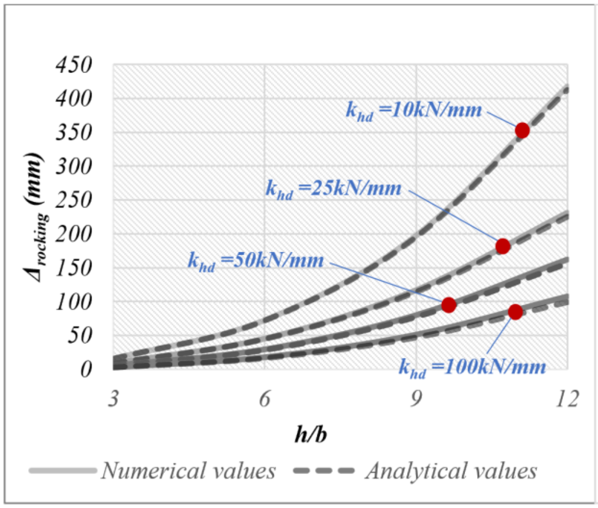

(a) $k_{vj}/h = 3kN/mm/m$

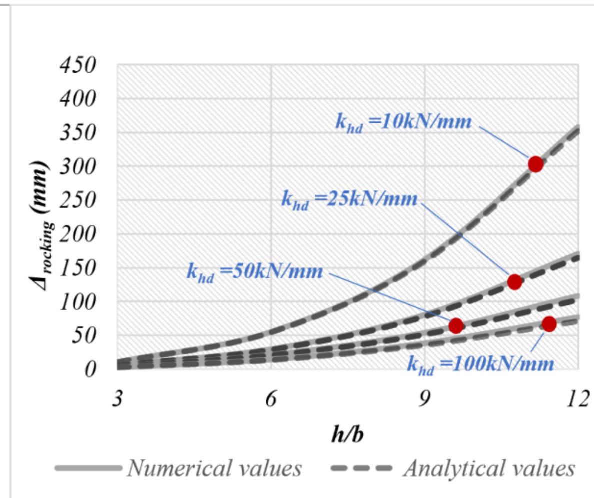

(b) $k_{vj}/h = 7.5kN/mm/m$

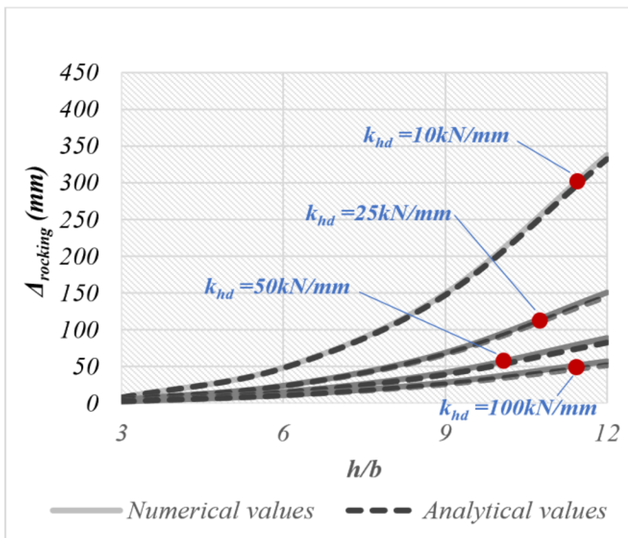

(c) $k_{vj}/h = 15kN/mm/m$

Figure 4.10: *Comparisons between the values of $\Delta_{rocking}$ obtained from the FE numerical modelling result and the analytical expression*

4.5.3. Verification of the total wall deformation

In this verification, the contribution to deformation considers bending, shear and rocking. The total deformation of the proposed analytical model can be calculated using Eq. 4.52 and 4.53 for the CP and SW modes, respectively. The relative stiffness $\tilde{k}$ delineates between CP and SW when it is equal to unity without gravity load. However, it should be noted that the transition point will be impacted when gravity load is included.

- For the CP mode:

$$\Delta_{total} = \frac{Fh^3}{3EI_{eff}} \cdot \left[\frac{(n+1)(3n+1)}{8n}\right] + \frac{Fh(n+1)}{2G^*A} + (F \cdot \frac{n+1}{2} \cdot \frac{h^2}{b^2} - qhn) \cdot \frac{1}{k_{hd} + k_{vj}} \quad (4.52)$$

- For the SW mode:

$$\Delta_{total} = \frac{Fh^3}{3EI_{eff}} \cdot \left[\frac{(n+1)(3n+1)}{8n}\right] + \frac{Fh(n+1)}{2G^*A} + \frac{F}{4}(\frac{1}{k_{hd}} + \frac{1}{k_{vj}}) \cdot \frac{n+1}{2} \cdot \frac{h^2}{b^2} - \frac{qhn}{2k_{hd}} \quad (4.53)$$

The analytical model used in this verification considers varying parameters of *h/b*, k_{hd} and k_{vj}. The result of the verification is shown in Table 4.5 for a range of $\tilde{k}$ between 0.1 and 10.

Table 4.5: *The total deformation calculated from the analytical model and FE model*

Aspect ratio	k_{hd} *(kN/mm)*	k_{vj} *(kN/mm)*	$\tilde{k} = k_{hd}/k_{vj}$	$\Delta_{total,ana}$ *(mm) from analytical model*	$\Delta_{total,FE}$ *(mm) from FE model*	*Error (%) =* $\Delta_{total,ana}/\Delta_{total,FE} - 1$	*Kinematic mode*
3/1	*10*	*9.0*	*1.1*	*18.1*	*17.8*	*1.9*	*CP*
	10	*22.5*	*0.4*	*12.2*	*12.1*	*1.2*	*SW*
	25	*45.0*	*0.2*	*10.1*	*10.1*	*0.0*	*SW*
	25	*9.0*	*2.8*	*11.2*	*11.5*	*-2.8*	*CP*
	25	*22.5*	*1.1*	*8.6*	*8.3*	*3.1*	*CP*
	50	*45.0*	*0.6*	*6.5*	*6.4*	*1.6*	*SW*
	50	*9.0*	*5.6*	*7.4*	*8.5*	*-12.5*	*CP*
	50	*22.5*	*2.2*	*6.4*	*6.5*	*-1.9*	*CP*
	100	*9.0*	*11*	*5.3*	*5.1*	*3.1*	*CP*

	100	*22.5*	*4.4*	*4.7*	*5.2*	*-9.8*	*CP*
	100	*45.0*	*2.2*	*4.2*	*4.2*	*-0.7*	*CP*
6/1	*10*	*18.0*	*0.6*	*89.2*	*84.2*	*6.0*	*SW*
	10	*45.0*	*0.2*	*68.6*	*66.1*	*3.8*	*SW*
	10	*90.0*	*0.1*	*60.3*	*60*	*0.5*	*SW*
	25	*18.0*	*1.4*	*61.9*	*57.2*	*8.2*	*CP*
	25	*45.0*	*0.6*	*43.4*	*40.2*	*8.0*	*SW*
	25	*90.0*	*0.3*	*35.1*	*33.9*	*3.5*	*SW*
	50	*18.0*	*2.8*	*45.5*	*44.0*	*3.3*	*CP*
	50	*45.0*	*1.1*	*34.8*	*31.3*	*11.3*	*CP*
	50	*90.0*	*0.6*	*26.7*	*25*	*6.8*	*SW*
	100	*18.0*	*5.6*	*33.5*	*35.5*	*-5.7*	*CP*
	100	*45.0*	*2.2*	*27.9*	*25.9*	*7.6*	*CP*
	100	*90.0*	*1.1*	*22.4*	*20.4*	*9.8*	*CP*
9/1	*10*	*27.0*	*0.4*	*254.2*	*235.4*	*8.0*	*SW*
	10	*67.5*	*0.1*	*205.2*	*199*	*3.1*	*SW*
	25	*27.0*	*0.9*	*173.4*	*153.3*	*13.1*	*SW*
	25	*67.5*	*0.4*	*124.2*	*115.4*	*7.6*	*SW*
	25	*135.0*	*0.2*	*103.6*	*102.7*	*0.9*	*SW*
	50	*27.0*	*1.9*	*136.3*	*120.9*	*12.8*	*CP*

	50	*67.5*	*0.7*	*97.2*	*86.9*	*11.8*	*SW*
	50	*135.0*	*0.4*	*76.6*	*73.9*	*3.7*	*SW*
	100	*27.0*	*3.7*	*106.0*	*100.4*	*5.5*	*CP*
	100	*67.5*	*1.5*	*81.6*	*72.3*	*12.9*	*CP*
	100	*135.0*	*0.7*	*63.1*	*59*	*7.0*	*SW*
12/1	*10*	*36.0*	*0.3*	*554.0*	*512.8*	*8.0*	*SW*
	10	*90.0*	*0.1*	*459.1*	*451.9*	*1.6*	*SW*
	25	*36.0*	*0.7*	*366.8*	*321.2*	*14.2*	*SW*
	25	*90.0*	*0.3*	*271.9*	*258.6*	*5.2*	*SW*
	25	*180.0*	*0.1*	*233.2*	*237.3*	*-1.7*	*SW*
	50	*36.0*	*1.4*	*298.3*	*255.7*	*16.7*	*CP*
	50	*90.0*	*0.6*	*209.5*	*192.4*	*8.9*	*SW*
	50	*180.0*	*0.3*	*170.8*	*170.5*	*0.2*	*SW*
	100	*36.0*	*2.8*	*240.9*	*216.1*	*11.5*	*CP*
	100	*90.0*	*1.1*	*177.9*	*158.8*	*12.0*	*SW*
	100	*180.0*	*0.6*	*139.6*	*136*	*2.6*	*SW*

Note: all the models are applied a vertical load of 20kN/m/storey.

The results show that an average error of +4.70% is obtained based on 45 cases. In all cases, the maximum error is less than 16.7%, which seems reasonable for practical engineering design cases. The increase in error when considering the total deformation may be an indication of some dependency and coupled behaviour between the bending and rocking deformation mechanisms.

Furthermore, the prediction error tends to increase with increasing panel aspect ratio, which may indicate stronger coupling effects between slender panels.

CHAPTER FIVE

FULL-SCALE SHEARWALL TESTS

5. Full-scale shearwall tests

This chapter documents the full-scale experimental programme undertaken to examine the lateral deformation behaviour of multi-panel balloon-type CLT shearwall systems. It introduces the testing materials and their properties, details the experimental setup and loading protocol, and presents the test results. Emphasis is placed on the deformation sequence, failure mechanisms, kinematic modes, and deformation characteristics observed during testing.

5.1. Materials and properties

The experimental campaign employed five-layer CLT wall panels with a total thickness of 175 mm (35/35/35/35/35), featuring a 0°/90°/0°/90°/0° layup, consistent with the material configuration adopted in Chapter 3. All panels were manufactured to grade E1 requirements in accordance with the Canadian standard CSA O86 (CSA Group, 2024) and were supplied by Nordic Structures. Each individual panel measured 5,000 mm in height with widths varying between 600 mm and 1,200 mm, allowing systematic evaluation of different panel aspect ratios.

The mechanical connections were provided by Rothoblaas and included both hold-down and vertical (spline) joint systems (Table 5.1). The hold-down, designated as WHT620, has nominal dimensions of 620 mm × 80 mm, and was fastened to the CLT panel using fifty-five annular-shank nails (type LBA460, diameter Φ4 mm, length 60 mm). A Φ20 mm 475mm steel threaded rod was adopted to anchor the hold-down to the steel foundation beam, and a steel washer was used to limit bending deformation of the bottom steel plate of the hold-down. The vertical connection between adjacent panels consisted of screwed spline joints, fabricated using 25.4 mm (1 inch) thick structural plywood and secured with Φ8 mm × 80 mm countersunk partially threaded screws.

The moduli of elasticity of the CLT panels, can be taken from the reference values in CSA O86 (CSA Group, 2024), since the panels have standard layup and were manufactured according to the PRG320 (ANSI/APA, 2021) standard. The hold-downs and vertical joints used in this study are the same as those investigated by Masroor et al. (2024), and as such the mechanical properties of these mechanical anchors, including their maximum and ultimate tensile and shear capacities and corresponding displacements, can be obtained from the study by Masroor et al. (2024). More details on the material properties of the test specimens are provided in Table 5.1 and Table 5.2.

The test matrix is summarised in Table 5.3 and illustrated in Figure 5.1. The experimental campaign investigated a range of specimen configurations with the number of shearwall panels varying from one to four, and panel aspect ratios (height-to-width) ranging from 4.2 to 8.3. The number of hold-downs connected to each bottom edge of the panel varied from one to four, while the number of vertical joints ranged from eight to sixty-five. Similar with the naming convention adopted in the FE sensitivity analysis, a specimen-naming scheme was employed to clearly identify each test configuration. For instance, in specimen “W0.6-P4-H2V32b”, the letter “W” refers to the width of each CLT panel with the value “0.6” indicating that each panel has a width of 0.6 m, “P4” indicates that the specimen comprises four panels, while “H2V32” denotes a connector arrangement with two hold-downs, positioned at the bottom right edge of shearwalls, and thirty-two vertical joints, provided at each interface between adjacent panels, and the suffix “b” denotes the second specimen of an identical configuration.

Table 5.1: *Details of the metal connections*

Code	***Description***	***Detail****	***Figure***
WHT620	*Hold-down panel*	*B (mm): 80* *P (mm): 83* *H (mm): 620* *Number of holes: 55*	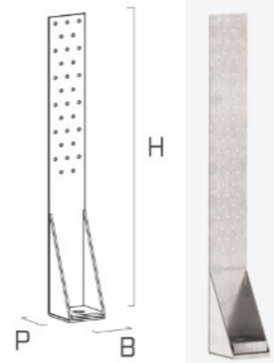
LBA460	*Anker nail*	*d_1 (mm): 4* *b (mm): -* *L (mm): 60*	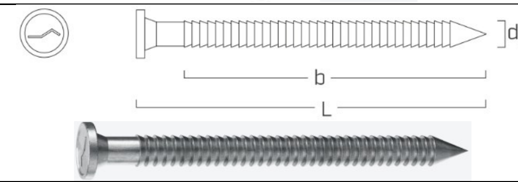
MGS12088	*Steel rod*	*d (mm): M20* *L (mm): 1000*	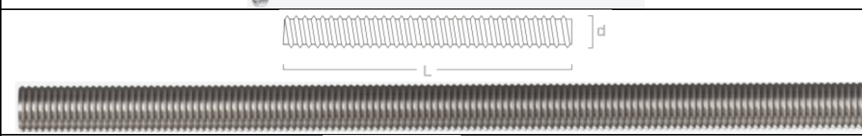
MUT93420	*Nut*	*d (mm): M20* *H (mm): 16* *SW: SW30*	
WHTW70L	*Washer*	*d_1 (mm): 26* *B (mm): 70* *P (mm): 77* *s (mm): 20*	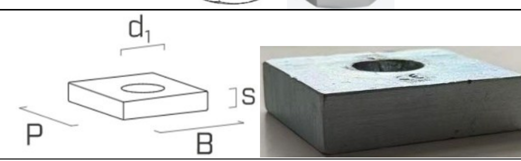
HBS880	*Countersunk Screw*	*d_1 (mm): 8* *b (mm): 52* *L (mm): 80*	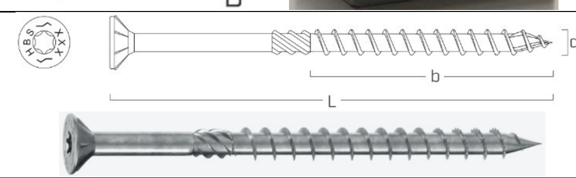

**Note: The symbols listed in this column are defined solely for use within this table.*

Table 5.2: *Materials and properties*

Name	***Properties***	
CLT panel [(1)]	*Young's modulus of longitudinal layers E_L (MPa)*	*11,700*
	Young's modulus of transverse layers E_T (MPa)	*9,000*
Hold-down [(2)]	*Maximum tensile resistance $T_{hd, max}$ (kN)*	*93.4*
	Displacement at the maximum tensile resistance point $\Delta_{T\text{-}hd, max}$ (mm)	*14.1*
	Ultimate tensile resistance $T_{hd, u}$ (kN)	*73.9*
	Ultimate tensile displacement $\Delta_{T\text{-}hd, u}$ (mm)	*17.2*
Vertical joint [(2)]	*Maximum shear resistance $S_{vj, max}$ (kN)*	*7.5*
	Displacement at the maximum shear resistance point $\Delta_{S\text{-}vj, max}$ (mm)	*43.2*
	Ultimate shear resistance $S_{vj, u}$ (kN)	*6.5*
	Ultimate shear displacement $\Delta_{S\text{-}vj, u}$ (mm)	*55.7*

Note: (1) The values of CLT properties are from CSA O86 (CSA group, 2024).

(2) The values of connectors' properties are obtained from the test reports by Masroor et al. (2024).

Table 5.3: *Test matrix*

Specimen No.	***Panel aspect ratio (h/b)***	***Number of panels***	***Number of hold-downs***	***Number of vertical joints***
W0.6-P2-H1V32	*8.3*	*2*	*1*	*32*
W0.6-P2-H2V32	*8.3*	*2*	*2*	*32*
W0.6-P2-H4V32	*8.3*	*2*	*4*	*32*
W1.2-P1-H2	*4.2*	*1*	*2*	*-*
W1.2-P2-H2V32	*4.2*	*2*	*2*	*32*
W0.8-P3-H2V32	*6.3*	*3*	*2*	*32*
W0.6-P4-H2V32a	*8.3*	*4*	*2*	*32*
W0.6-P4-H2V32b	*8.3*	*4*	*2*	*32*
W0.6-P2-H2V8a	*8.3*	*2*	*2*	*8*
W0.6-P2-H2V8b	*8.3*	*2*	*2*	*8*
W0.6-P2-H1V65	*8.3*	*2*	*1*	*65*

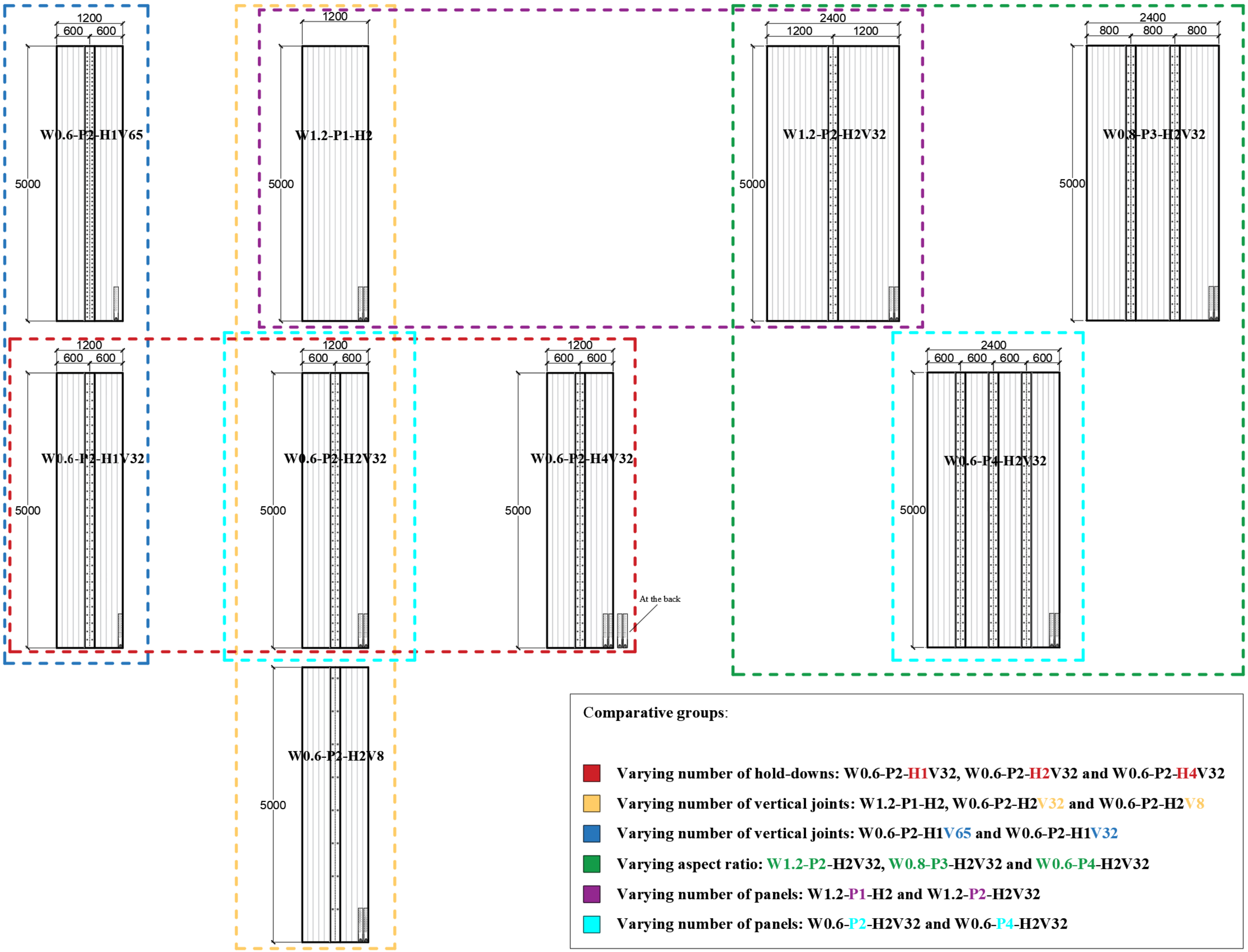

Figure 5.1: *Test specimens and comparative groups*

5.2. Test set-up and load protocol

Figure 5.2 illustrates the overall test setup, including key details on the systems of hold-down and vertical joints. Instead of erecting the shearwalls in an upright position on the laboratory floor, the CLT panels were laid horizontally and braced out of plane using timber supports placed on the ground. This configuration facilitated safe installation and avoided out-of-plane movement of a wall under in-plane lateral loads. It should be noted that no uplift of the walls from the support was observed in any of the tests.

The setup simulated a full-scale, two-storey balloon-type CLT shearwall subjected to two equal horizontal loads, each applied at the diaphragm level of its respective storey. To ensure equal force transfer to the two loading points, a single hydraulic actuator was positioned at the midspan of a rigid I-shaped steel spreader beam, thereby maintaining symmetrical load distribution across the wall.

A steel foundation beam with a length of 3,505 mm was anchored to the laboratory floor to simulate the foundation of the wall system. To prevent unintended lateral sliding during testing, a steel shear key was installed at the end of the shearwall (the left bottom corner). Additional details of the construction of the steel foundation beam and lateral-sliding restraint are provided in Appendix A.

A monotonic displacement-controlled loading protocol was employed, utilising a hydraulic actuator operating at a constant loading rate of 25 mm/min, in accordance with ASTM E2126 (ASTM International, 2019) and ISO 21581:2010 (International Organisation for Standardisation, 2010). In the process of testing, the laboratory environment was maintained at a temperature of

18 ~ 22°C and a relative humidity of 60 ~ 70%, while the equilibrium moisture content of the CLT specimens was measured with an average value of 12.1% and a coefficient of variation (COV) of 11.8% to ensure consistent conditioning of the material.

The lateral displacement of the shearwall was monitored at the diaphragm levels of 2.4 m and 4.8 m using linear variable differential transducers (LVDTs) positioned (Figure 5.3). In addition to the global lateral drift, other significant deformation parameters, including hold-down uplift, relative slip between adjacent panels, and local compressive deformation at the rotation centres of the CLT panels, were also recorded by means of LVDTs.

The monitoring points were systematically numbered according to their locations, as depicted in Figure 5.3, where both the position as well as the direction of the displacement measurement is provided. Point 1 (P_1) was placed along the central axis of the outermost hold-down to measure hold-down uplift. Points 2/2′ ($P_2/P_{2'}$) and 3/3′ ($P_3/P_{3'}$), positioned at the wall edges at 2.4 m and 4.8 m heights, respectively, recorded the lateral drifts at the first and second diaphragm levels. At Point 4 (P_4), located at the bottom left corner of each specimen, two LVDTs were installed along orthogonal directions to record end-panel compression and lateral sliding. For specimens comprising two, three, or four panels, additional instrumentation, Points 5 through 10 (P_5 ~ P_{10}), was installed at panel intersections to monitor panel-to-panel slip and individual panel uplift.

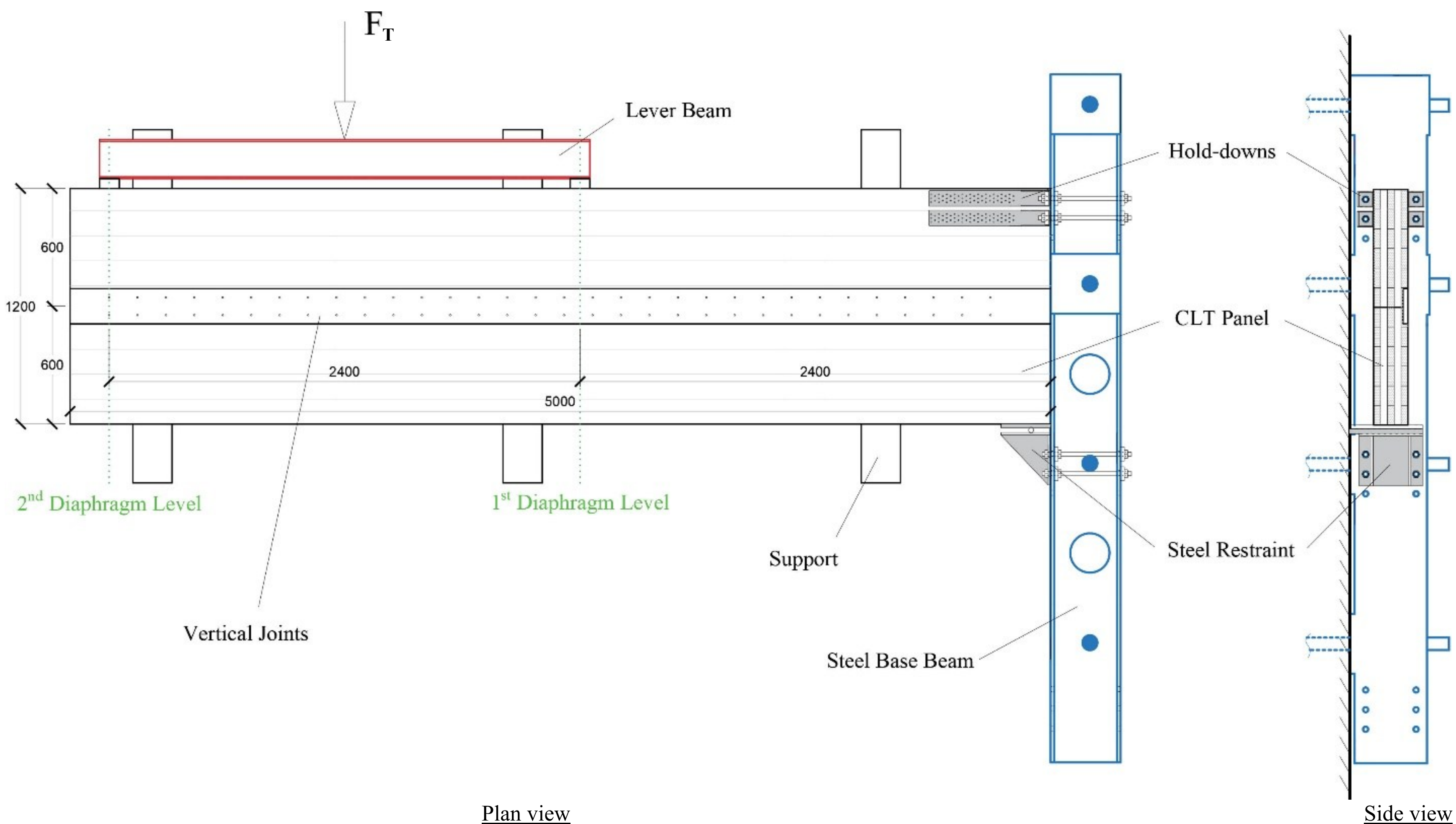

(a) Testing setup of specimen W0.6-P2-H4V32 as an example

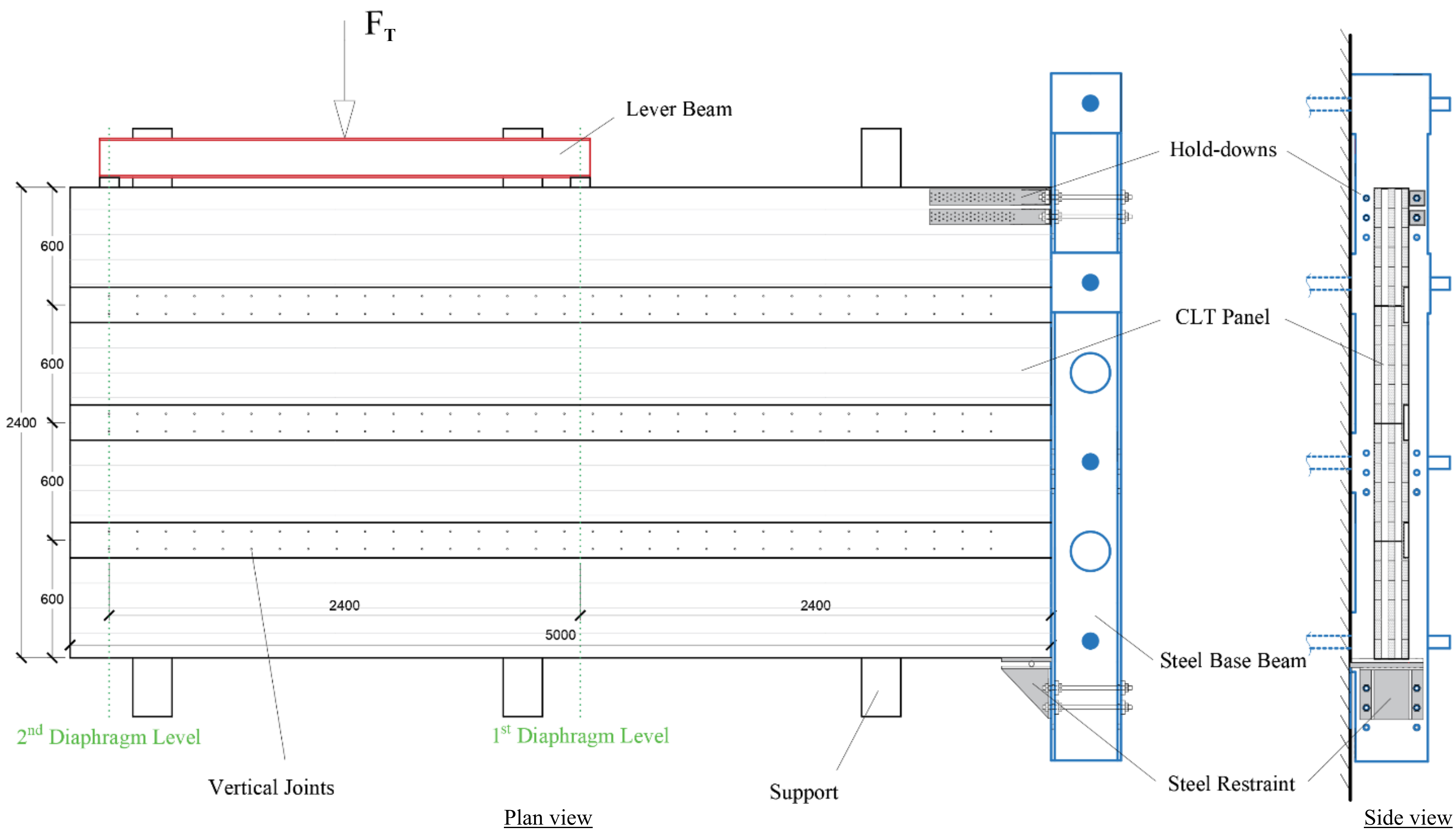

(b) Testing setup of specimen W0.6-P4-H2V32 as an example

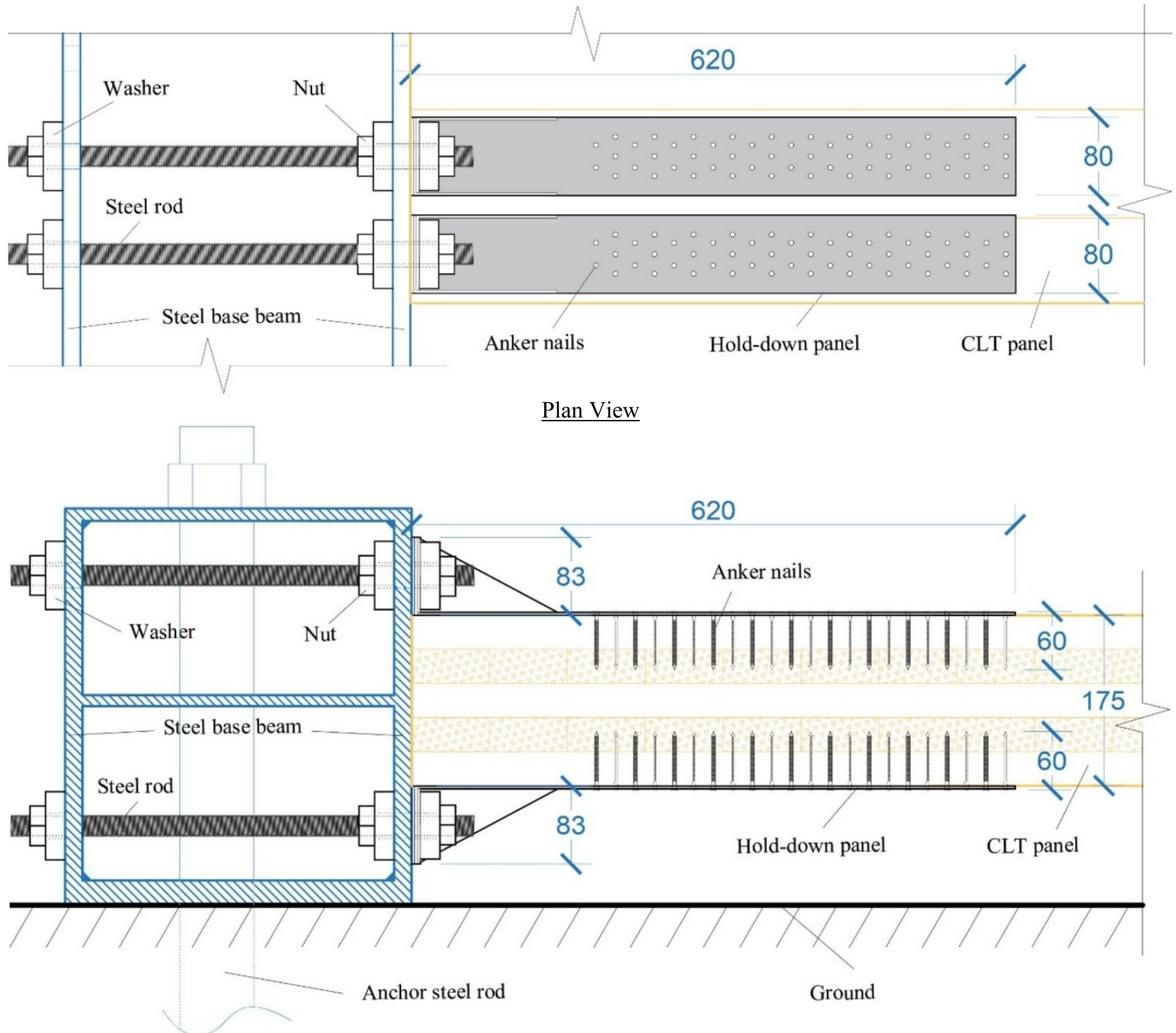

(c) Details of hold-down system for specimen W0.6-P2-H4V32 as an example

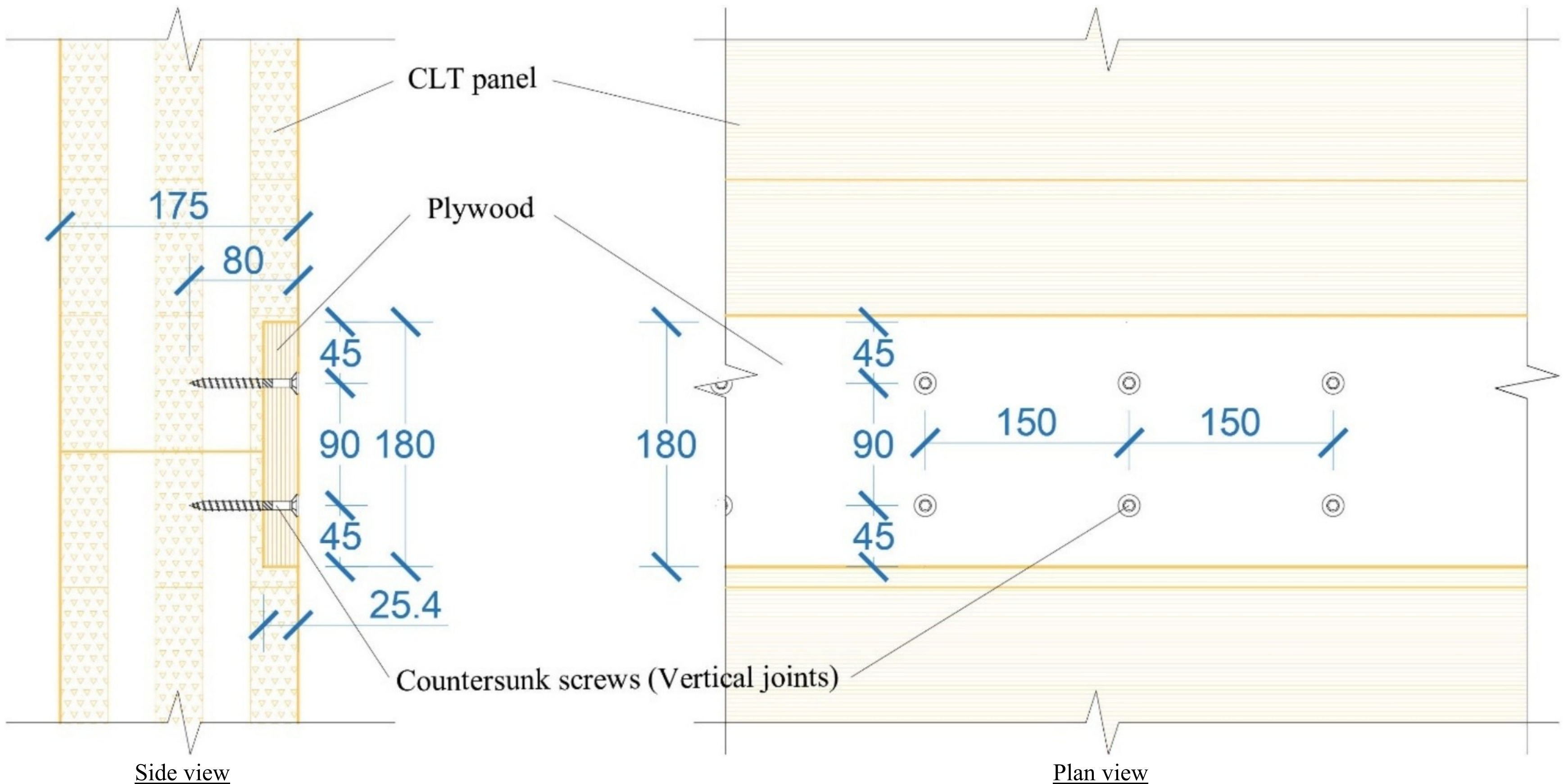

(d) Details of vertical joints system for specimen W0.6-P4-H2V32 as an example

Figure 5.2: *An overview of test setup with the details of hold-downs and vertical joints system*

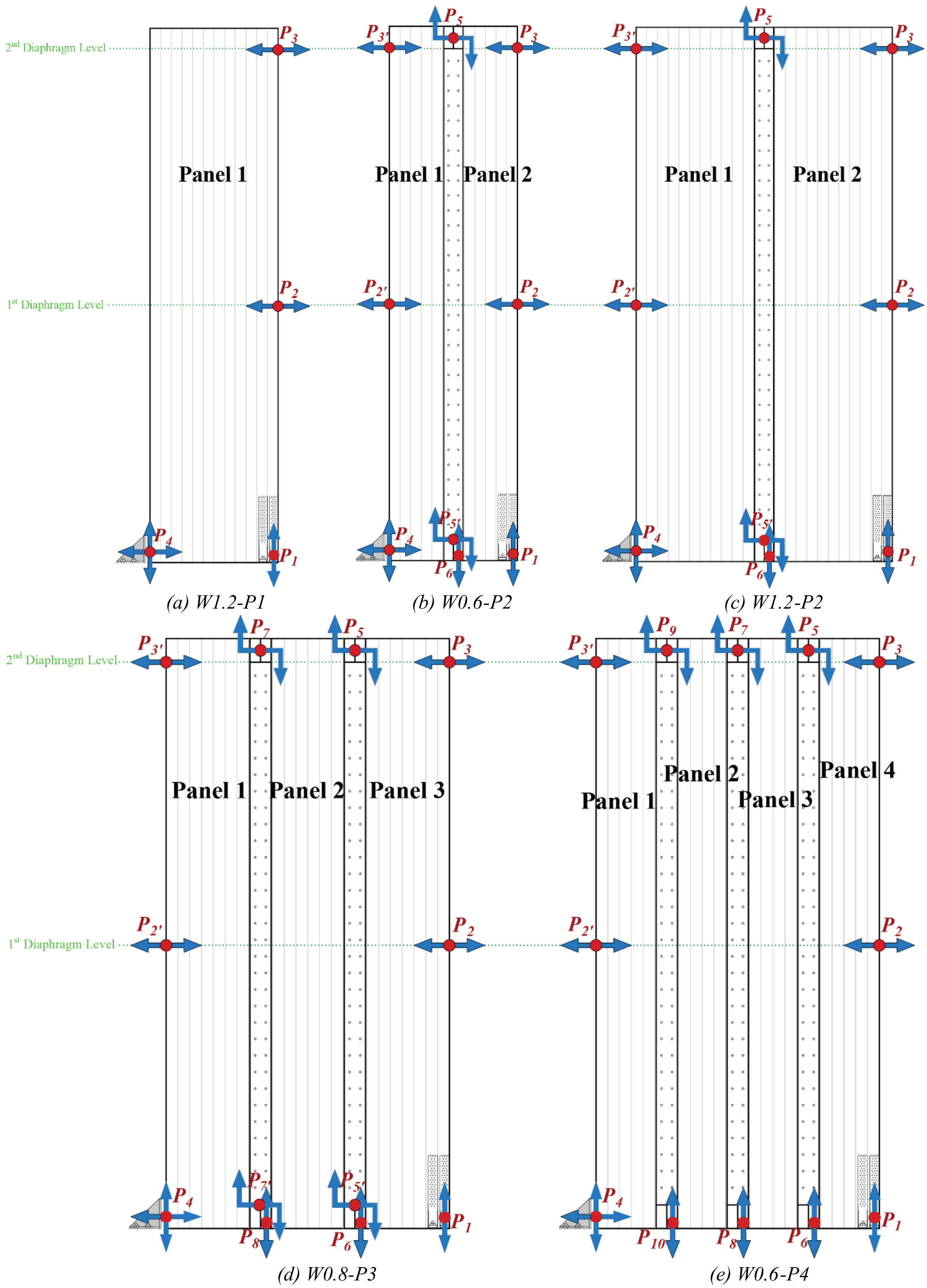

Figure 5.3: *Displacement monitored points by LVDTs*

5.3. Test results

5.3.1. Deformation sequence and failure mechanism

Figure 5.4 compares typical deformation sequences observed in specimens W0.6-P2-H1V32 and W0.6-P2-H4V32, which have similar overall layout and configurations but with the only exception of having different hold-down number, and hence different relative stiffness and strength ratios between the hold-down and the vertical joints. For specimen W0.6-P2-H1V32, the shearwall primarily exhibited a rocking motion about its rotation centre at P_4, accompanied by a slight uplift at point P_6. Increase in deformation in the vertical joints was also evident as the applied load increased. The ultimate failure mode was governed by rupture of the hold-down, which resulted in a complete loss of lateral resistance, with evident residual deformations at the panel-to-panel interface.

When the number of hold-downs was increased to four (W0.6-P2-H4V32), the specimens exhibited rocking about the rotation centres of each panel (P_6 and P_4), with larger slips developing between adjacent panels. Ultimately, the final failure was still caused by rupture of all hold-downs. This behaviour can be attributed to the mechanical properties of the connectors: the hold-downs exhibited a significantly lower ultimate tensile displacement ($\Delta_{T\text{-}hd,\ u}$) compared to the ultimate shear displacement of the vertical joints ($\Delta_{S\text{-}vj,\ u}$), as summarised in Table 5.2. Consequently, the hold-downs consistently reached their failure point earlier than the vertical joints.

(a) Entire structural deformation of specimen W0.6-P2-H1V32

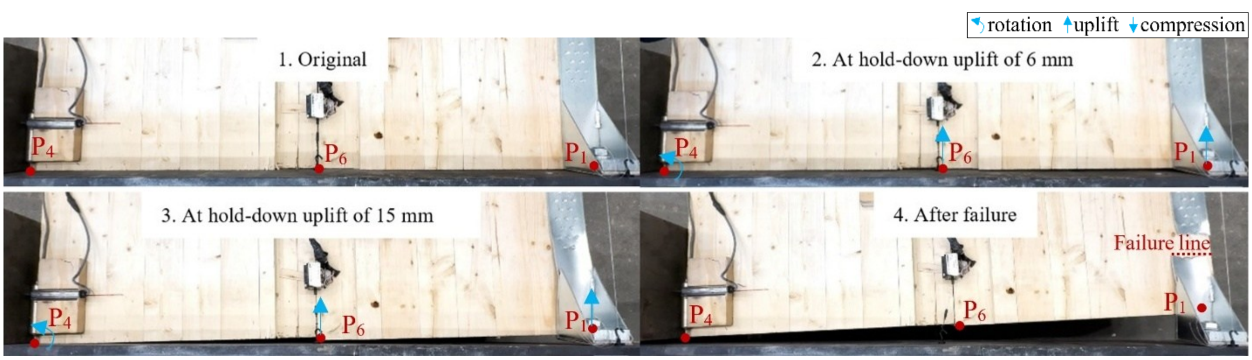

(b) Deformation development at the bottom of panels of specimen W0.6-P2-H1V32

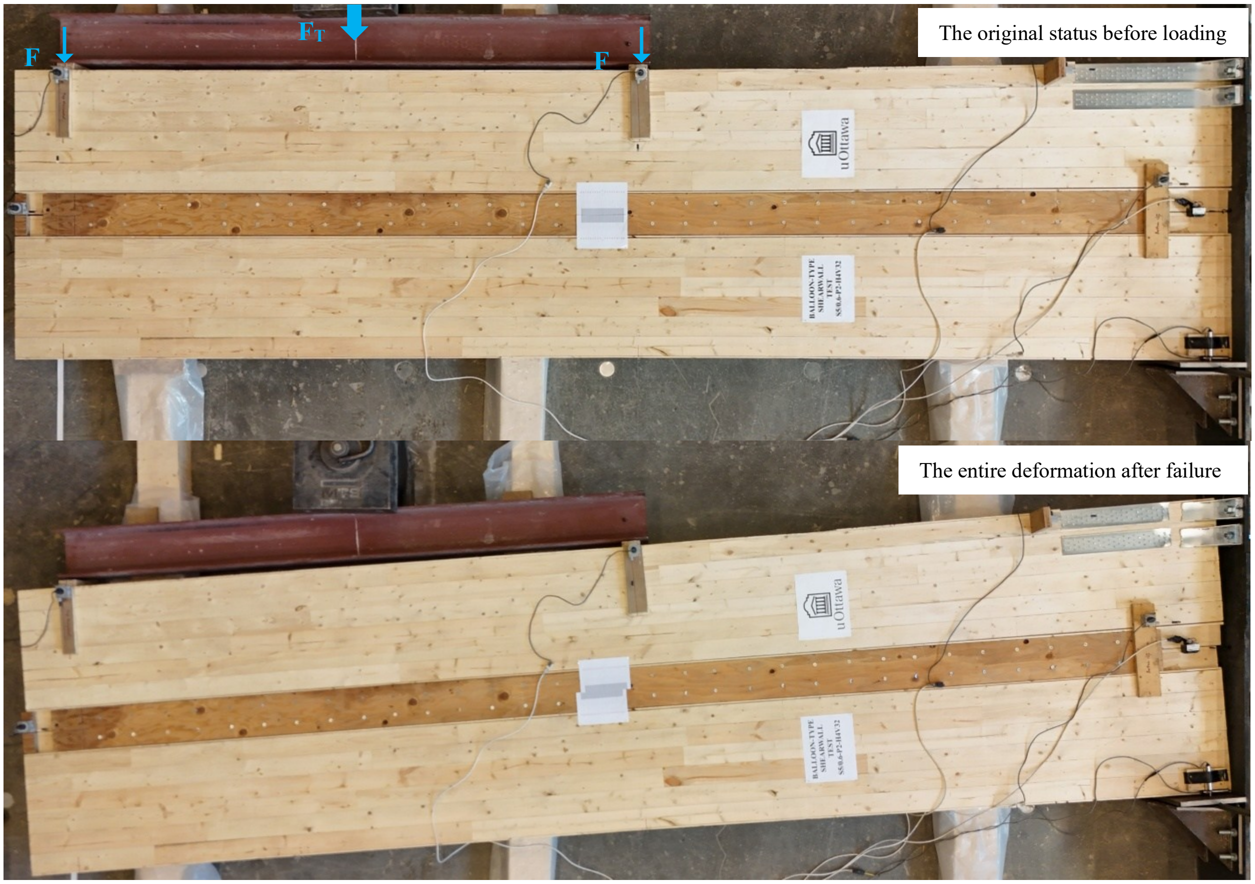

(c) Entire structural deformation of specimen W0.6-P2-H4V32

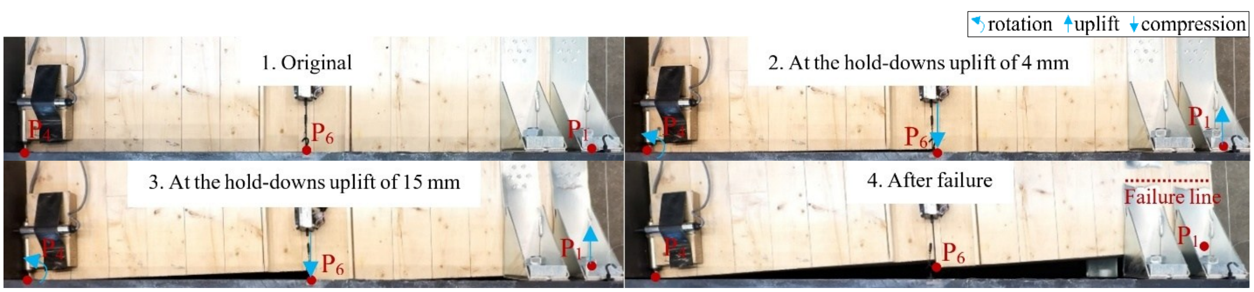

(d) Deformation development at the bottom of panels of specimen W0.6-P2-H4V32

Figure 5.4: *Structural deformation development of specimen W0.6-P2-H1V32 under the lateral loads*

Specimen W1.2-P1-H2, which consisted of only one panel, exhibited a relatively logical deformation sequence in comparison with specimen W0.6-P2-H2V32. These are two walls with the same width (1.2 m), same overall wall aspect ratio, and same number of hold-downs, and with the only difference being that in W1.2-P1-H2 the entire wall comprises of a monolithic panel, while for W0.6-P2-H2V32 the 1.2 m panel is divided into two 0.6 m panels connected together using vertical joints. It was observed that both specimens eventually failed governed by rupture of the hold-downs. In comparison, specimen W0.6-P2-H2V8a exhibited more complex deformation behaviour during the loading process (Figure 5.5). Unlike the typical failure mode governed by hold-down tensile rupture, a combined tensile-bending failure was observed at the hold-downs. This behaviour may be attributed to a high relative stiffness within the system, which resulted in an uneven distribution of resistance and deformation between the two panels. Owing to the relatively low stiffness of the vertical joints, the left panel (Panel 1) experienced more pronounced rocking deformation accompanied by larger uplift, whereas the uplift of the right panel (Panel 2) was restrained by comparatively stiffer hold-downs. This deformation incompatibility induced additional rotation at the hold-downs, leading to increased bending effects in combination with axial tensile forces. Consequently, the hold-downs failed under a combined bending-tension loading condition.

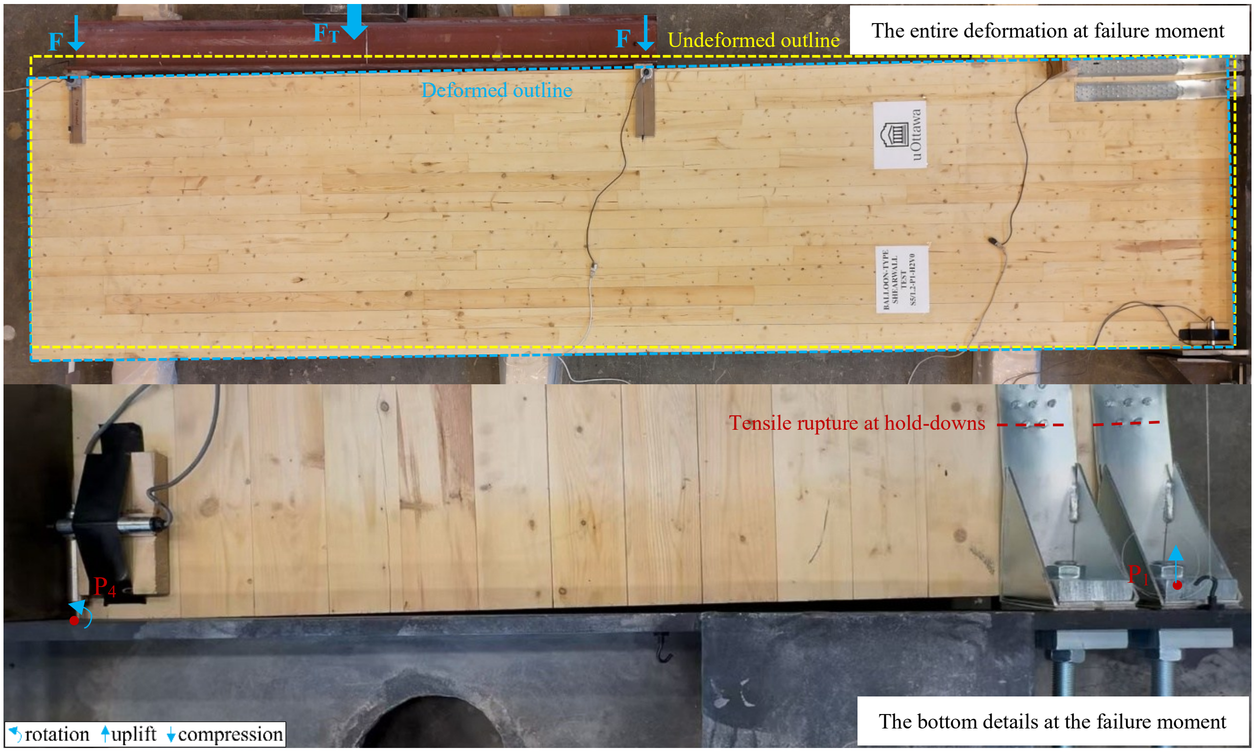

(a) Entire structural deformation and bottom details of specimen W1.2-P1-H2 at the failure moment

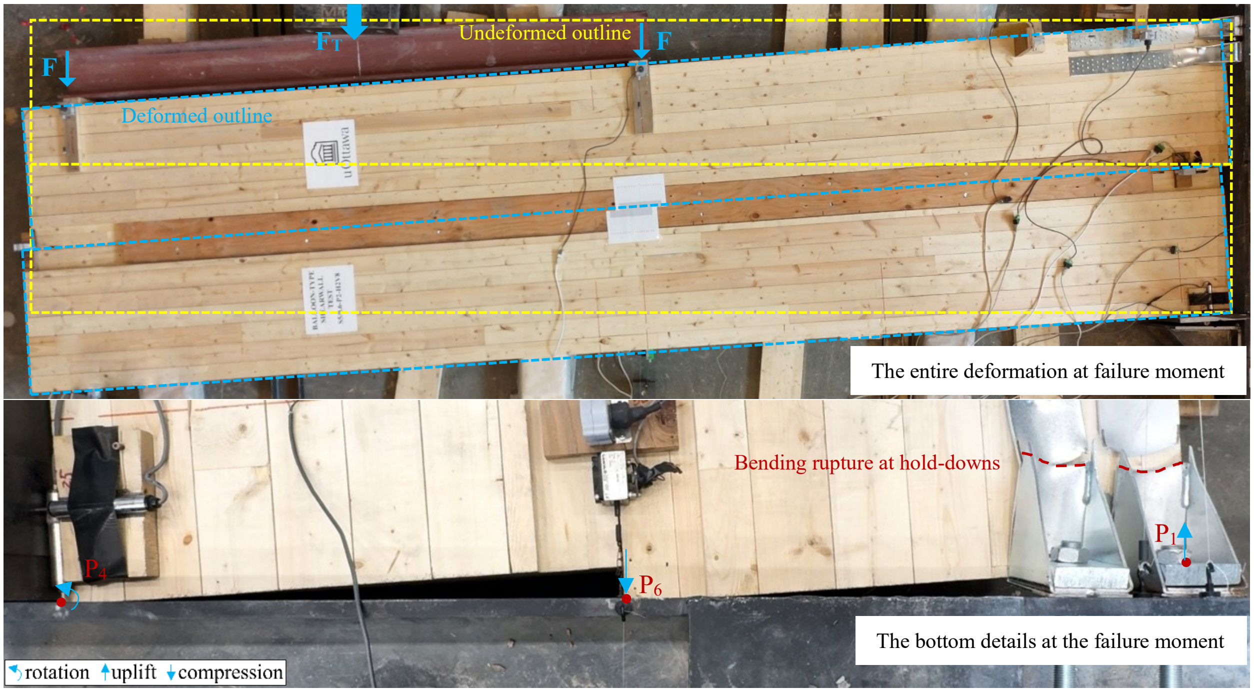

(b) Entire structural deformation and bottom details of specimen W0.6-P2-H2V8a at the failure moment

Figure 5.5: *Structural deformation of specimens W1.2-P1-H2 and W0.6-P2-H2V8a under the lateral loads*

Figure 5.6a provides a comparison between the hold-downs that failed in tension (i.e. W0.6-P2-H2V32) and that in combined tension and bending (i.e. W0.6-P2-H2V8a). It was found that the rupture lines in the hold-down that failed in tension were consistently located at the lowest nail holes due to stress concentration, whereas the bending rupture lines occurred lower, close to the flanges of the hold-down plates, and were accompanied by a pronounced out-of-plane deformation, caused by the combination of bending and tension . At the same time, partial failure of the vertical joints was observed, which included a bending deformation of some screws traced by clear deformed drilling holes, as shown in Figure 5.6b.

(a) Comparison of the rupture characteristics of hold-downs caused by tension and by combined tension and bending

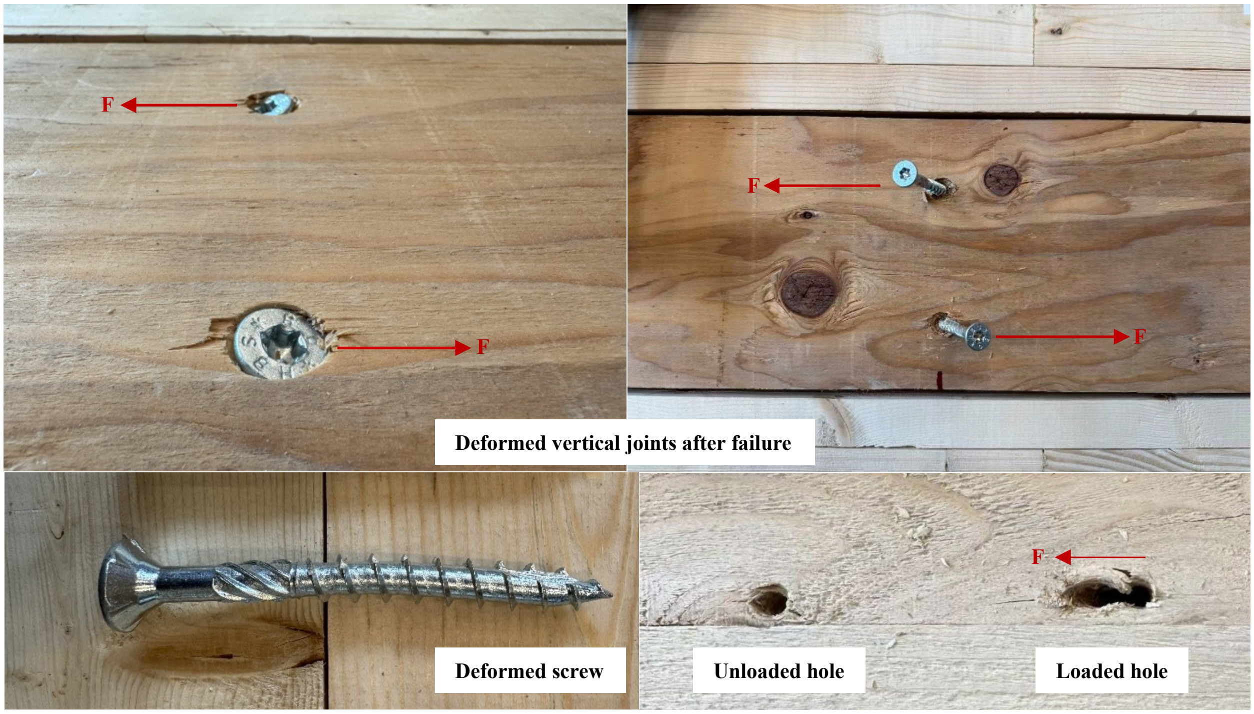

(b) Deformation details of the vertical joints (from specimen W0.6-P2-H2V8a)

Figure 5.6: *Rupture and deformation characteristics of connectors in specimen W0.6-P2-H2V8a*

Another repeated test of specimen W0.6-P2-H2V8b exhibited a different failure mechanism. In this case, the CLT panel developed a crack along the top edge of the outermost hold-down plate at an early stage of loading. Subsequently, the tensile stresses were redistributed to the underlying lamination. Due to the orthogonal orientation of its fibres relative to the applied tensile force, the deformation and crack development were governed by rolling shear mechanisms, resulting in rapid crack propagation along the interlaminar shear plane until the wood fibres were completely ruptured. Since the depth of the fasteners extended into the second lamination layer of the CLT panel, wood splitting was also observed as a result of nail deformation along a direction perpendicular to the grain. The ultimate wall failure did not occur until the inner hold-down plate eventually ruptured. Details on this failure mode are provided in Figure 5.7. This specimen illustrated the possibility of an alternative failure mode in which the wood panel experienced local rupture prior to the hold-downs reaching their maximum tensile resistance. This suggests that inherent material imperfections within the CLT panel contributed to the premature failure. To mitigate such behaviour, the use of longer fasteners with greater embedment depth may be required in order to allow additional lamination layers to be involved in and contribute to the tensile resistance of joint.

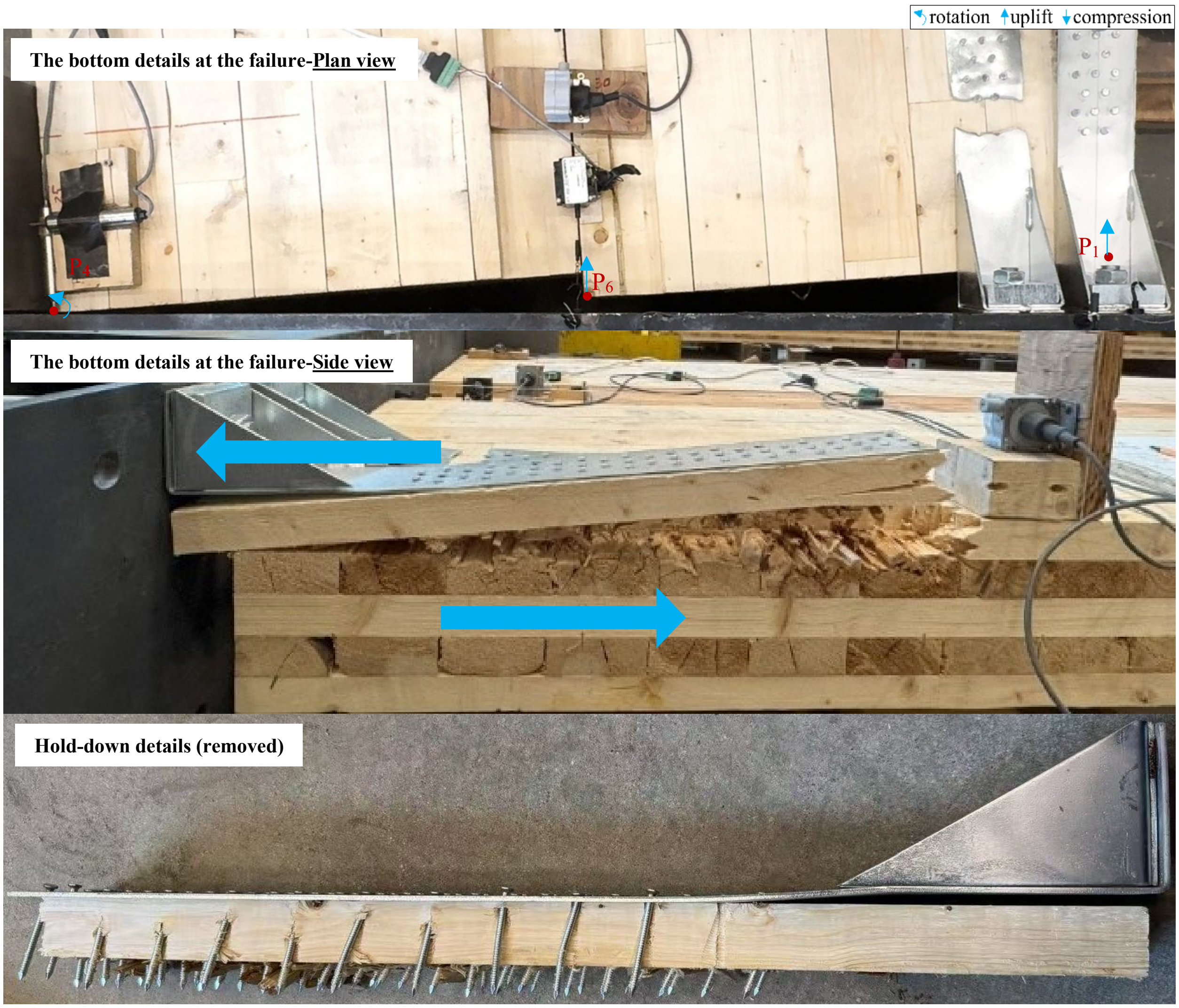

Figure 5.7: *Failure mode and details of specimen W0.6-P2-H2V8b*

Figure 5.8 presents typical deformation progressions observed in specimens W0.6-P4-H2V32a, W0.8-P3-H2V32, and W1.2-P2-H2V32. These specimens are in principle similar in terms of overall wall length and mechanical anchors but differ only in the number of panels to achieve the wall length of 2.4 m. As expected, and consistently with most other specimens, all three ultimately failed at the hold-downs due to tensile rupture. However, they exhibited different value of lateral stiffness and maximum lateral displacements. In addition, more complex kinematic behaviour was observed in the multi-panel shearwall system, as discussed in detail in Section 5.3.2.

(a) Entire structural deformation and the bottom details of specimen W0.6-P4-H2V32 at the failure moment

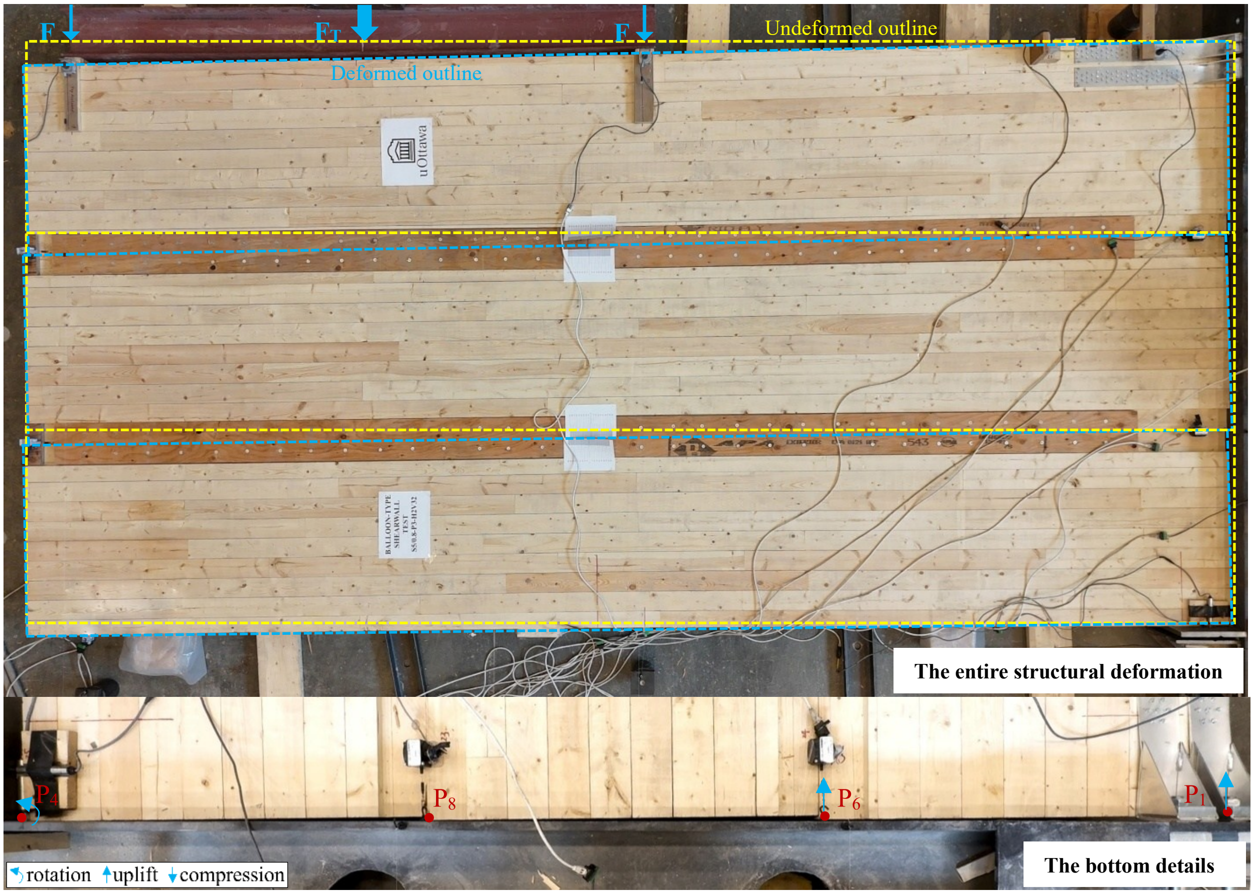

(b) Entire structural deformation and the bottom details of specimen W0.8-P3-H2V32 at the failure moment

(c) Entire structural deformation and the bottom details of specimen W1.2-P2-H2V32 at the failure moment

Figure 5.8: *Failure comparison between specimens W0.6-P4-H2V32a, W0.8-P3-H2V32, and W1.2-P2-H2V32*

In the repeated test of specimen W0.6-P4-H2V32b, similar to specimen W0.6-P2-H2V8b, the initial failure occurred in the CLT panel itself rather than in the hold-downs, although with notable differences between the two cases. It was found that the failure of W0.6-P4-H2V32b was initiated along a finger joint located at the top edge of the outermost hold-down panel. The CLT strip experienced a brittle tensile failure and rolling shear failure was observed at the transverse layer (underneath the first layer of CLT). Compared with specimen W0.6-P2-H2V8b, where crack development occurred slowly until the ultimate failure happened, the failure in this case occurred more abruptly. Figure 5.9 showed more failure details.

While the location of the finger-joint may be coincidental, the observed failure highlights how such common fabrication detail has the potential to trigger unexpected structural failures, that is not likely to be considered in the design. Furthermore, the lumber strips used in the CLT panel had a width of 82 mm, nearly identical to the width of the hold-down panel (80 mm). This alignment meant that once all fasteners were concentrated within a single strip, only one strip can resist the applied force. As a result, the likelihood of panel failure increased significantly. These observations suggest that adjustments to the strip width in commercial CLT panel fabrication may help reduce the risk of such premature and sudden panel failures.

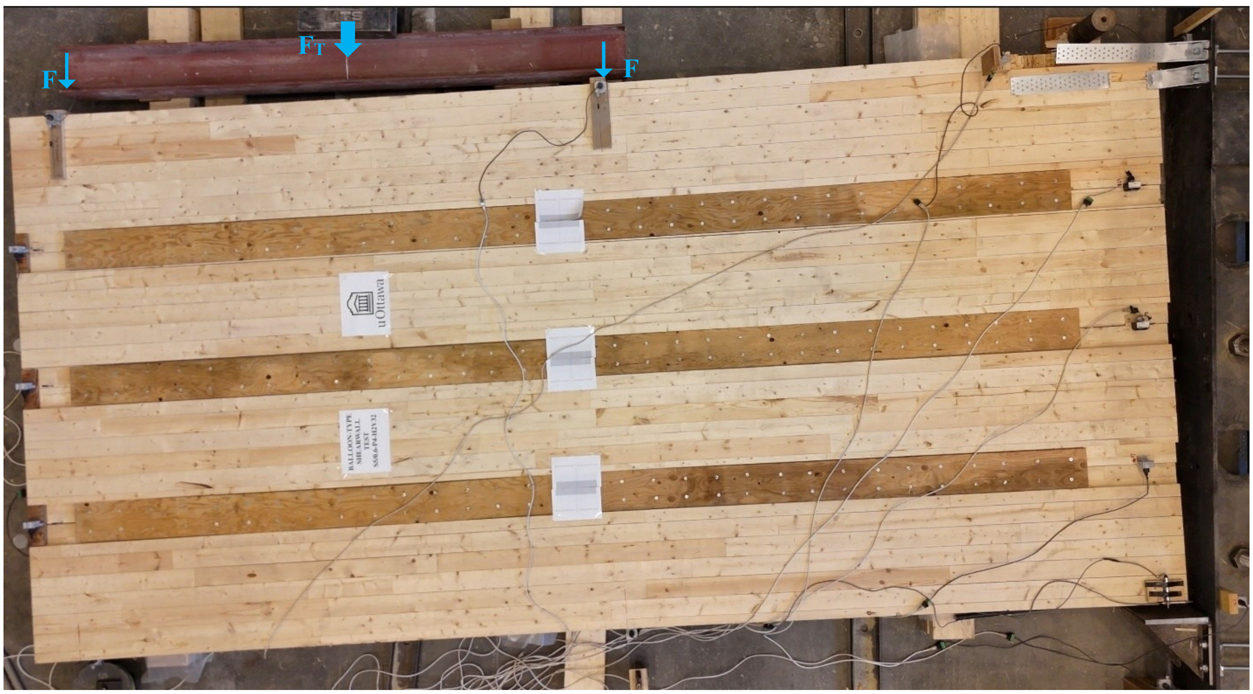

(a) Entire structural deformation of specimen W0.6-P4-H2V32b after failure

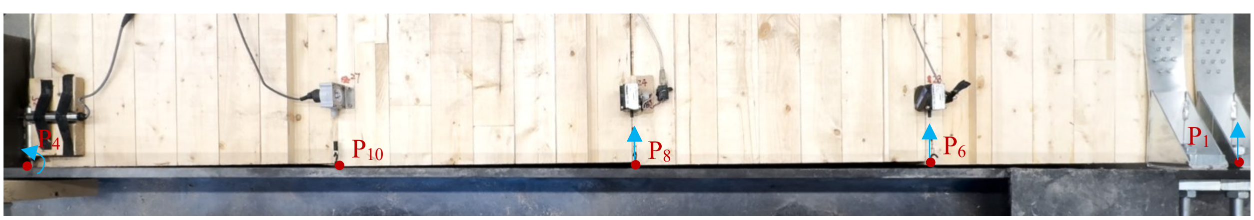

(b) Bottom details of specimen W0.6-P4-H2V32b at the failure moment

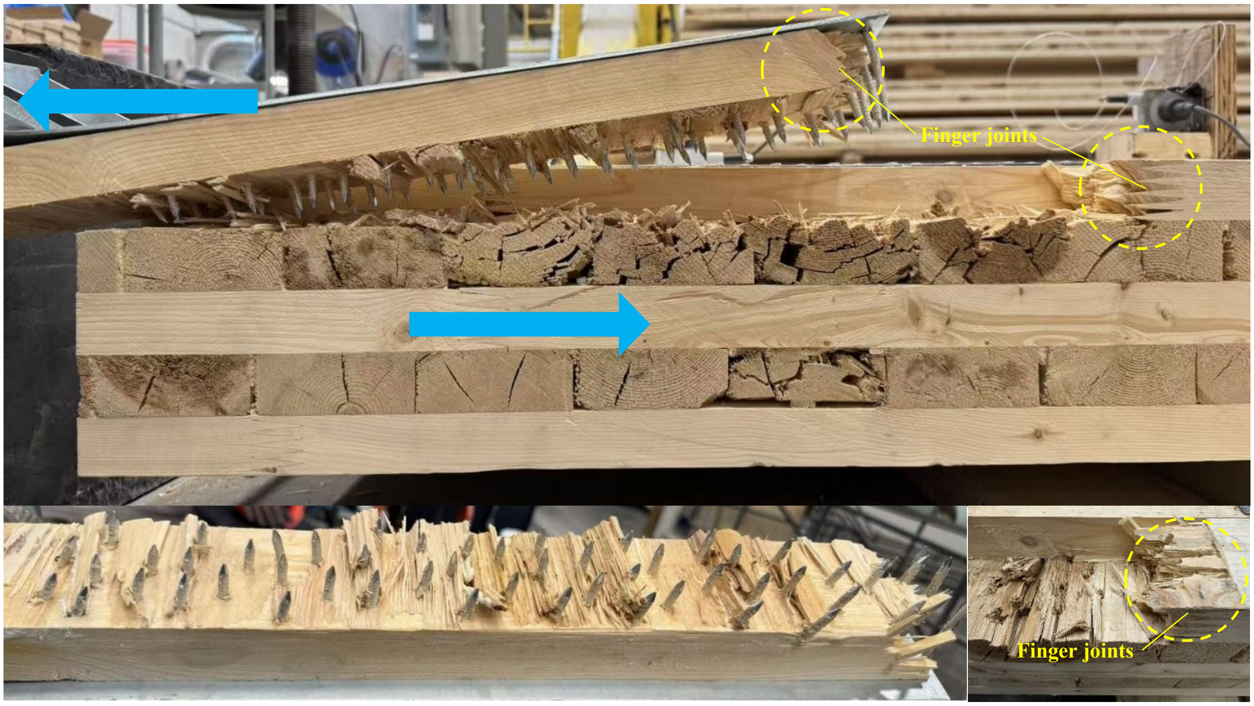

(c) Local details of specimen W0.6-P4-H2V32b after failure

Figure 5.9: *Failure details of specimen W0.6-P4-H2V32b*

5.3.2. Kinematic modes and deformation characteristics

In terms of kinematic response, different kinematic modes were observed based on rotational behaviour of the panels. Figure 5.10 provides a closer look at the panel uplift and deformation details for specimens W0.6-P2-H1V32, W0.6-P2-H2V32 and W0.6-P2-H4V32. These specimens differ only in the number of hold-downs. It was observed that SW mode was dominant when only one hold-down was used. However, as the number, and hence stiffness, of hold-downs increased, the system transitioned from SW mode to CP mode. For example, when four hold-downs were utilised, the CLT panel at P_6 was consistently in contact with the base support, as shown in Figure 5.10c.

More details about the displacement at the bottom of each panel are listed in Table 5.4. Although the uplift displacement of hold-downs at the peak load remained consistent across different specimens (W0.6-P2-H1V32, W0.6-P2-H2V32 and W0.6-P2-H4V32), generally ranging from 13 mm to 16 mm, the slip between two panels became significantly larger up to 26 mm, when using a greater number of hold-downs (from 1 to 4).

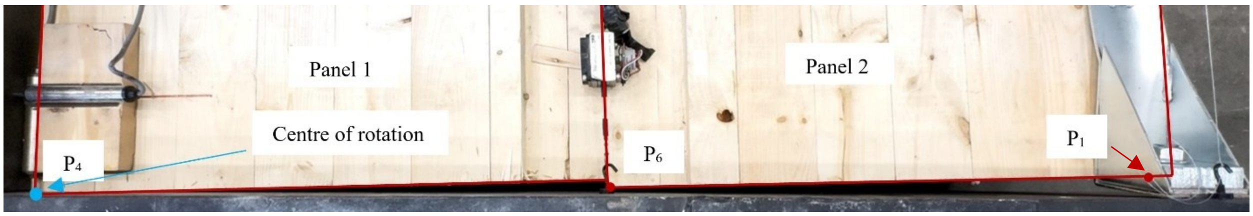

(a) Specimen W0.6-P2-H1V32 with SW mode

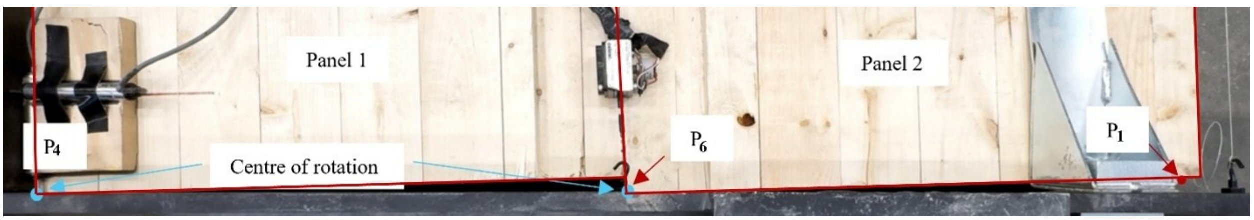

(b) Specimen W0.6-P2-H2V32 with CP mode

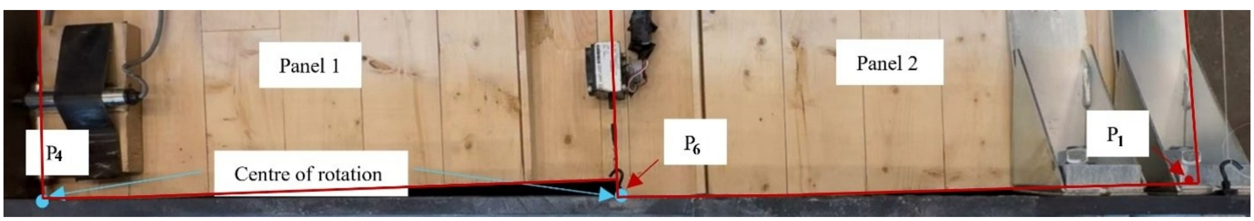

(c) Specimen W0.6-P2-H4V32 with CP mode

Figure 5.10: *Monitored points for measuring the tensile displacement of hold-downs (P_1) and tracing the kinematic modes of shearwalls (P_6) for specimens W0.6-P2-H1V32, W0.6-P2-H2V32 and W0.6-P2-H4V32*

Figure 5.11 presents details on the deformation mechanisms based on specimens W1.2-P1-H2, W0.6-P2-H2V32, W0.6-P2-H2V8a, and W0.6-P2-H2V8b. These walls differ in the number of vertical joints and as such the relative stiffness between the vertical joints and the hold-downs, with W1.2-P1-H2 included as the extreme case where the relative stiffness is infinite since this wall has no vertical joints but same total width as the other wall specimens considered. Except for the monolithic shearwall (W1.2-P1-H2), the other three specimens exhibited clear CP modes. Moreover, it was observed that the pronounced compressive regions were developed at P_6 in both specimens W0.6-P2-H2V8a and W0.6-P2-H2V8b, as illustrated in Figure 5.11c and 5.11d, respectively. In addition, a significant difference in panel uplift was found in specimen W0.6-P2-H2V8a. As shown in Table 5.4, the left panel (Panel 1) experienced a 33% greater uplift (32 mm) than the right panel (Panel 2, 24 mm) at peak load, whereas both panels in specimen W0.6-P2-H2V32 exhibited nearly identical uplifts. Similar phenomenon was observed for other shearwalls with high relative stiffness, such as specimen W0.6-P2-H4V32. As a results, the theoretical assumption in which panels with CP mode are considered to possess the same rotation seems not to be applicable when the shearwalls possess high relative stiffness. In such case, non-uniform force distribution between individual panels due to differential stiffnesses of hold-down and vertical joints, would lead to unequal uplifts and asymmetric panel rotations rather than a uniform coupled response.

In addition to the significant difference in panel uplift, it was observed that two CLT panels in specimen W0.6-P2-H2V8a exhibited differential deformation mechanisms. In the loading sequence, Panel 2 exhibited more bending than Panel 1, as illustrated by twice the slip value measured at the top (77 mm at P_5) compared to the bottom (37 mm at $P_{5'}$) of the interface between adjacent panels (Figure 5.12). This behaviour is attributed to a combination of high relative stiffness and high aspect ratio of shearwalls.

(a) Specimen W1.2-P1-H2

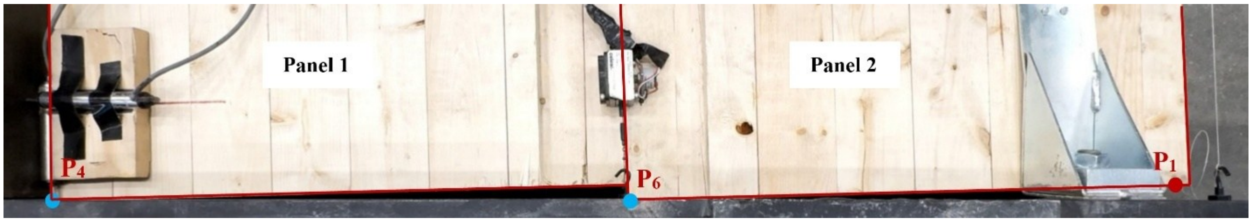

(b) Specimen W0.6-P2-H2V32

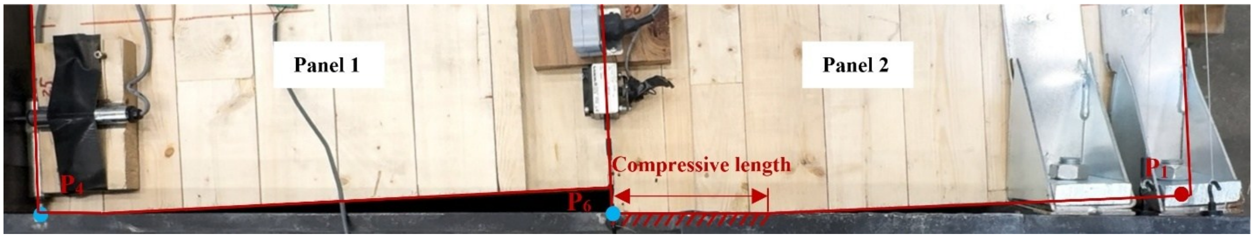

(c) Specimen W0.6-P2-H2V8a

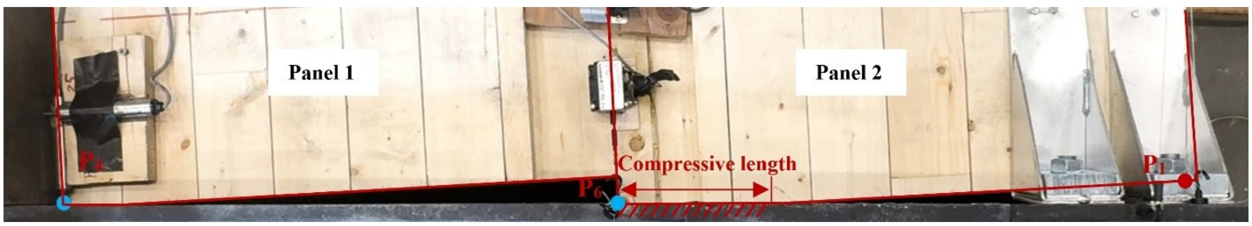

(d) Specimen W0.6-P2-H2V8b

Figure 5.11: *Monitored points for measuring the tensile displacement of hold-downs (P_1) and tracing the kinematic modes of shearwalls (P_6) for specimens W1.2-P1-H2, W0.6-P2-H2V32, W0.6-P2-H2V8a and W0.6-P2-H2V8b*

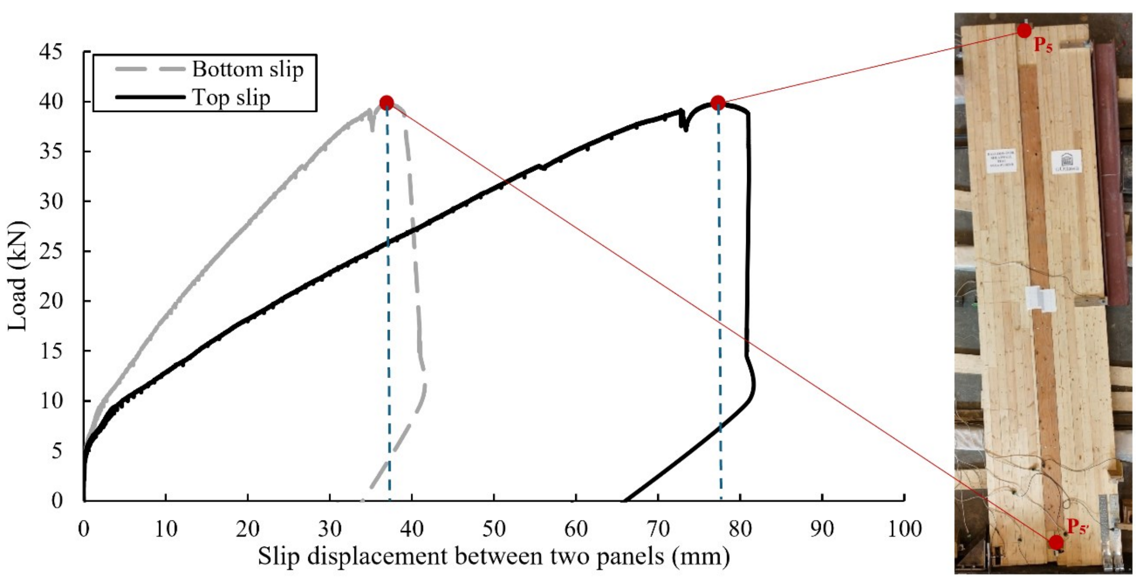

Figure 5.12: *Comparison of slip displacements measured at the top and the bottom of the interface between two panels from specimen W0.6-P2-H2V8a*

When investigating shearwalls consisting of more than two panels, more complex kinematic modes were observed than those with only two panels. Specimen W0.6-P4-H2V32a exhibited CP mode with multiple rotation centres observed at P_6, P_8, P_{10} and P_4 during the early stages of loading, However, when the load was further increased, the uplift recorded at P_6 and P_8 increased progressively. In contrast, P_{10} was characterised by very low values of uplift (i. e. ≤1 mm) until the shearwall failed. This observation indicates that the kinematic mode experienced a transition from CP to SW in the loading process. Similar phenomenon was observed for specimen W0.8-P3-H2V32. Figure 5.13 showed the details of the shift of kinematic modes varying with time in specimens W1.2-P2-H2V32, W0.8-P3-H2V32 and W0.6-P4-H2V32a.

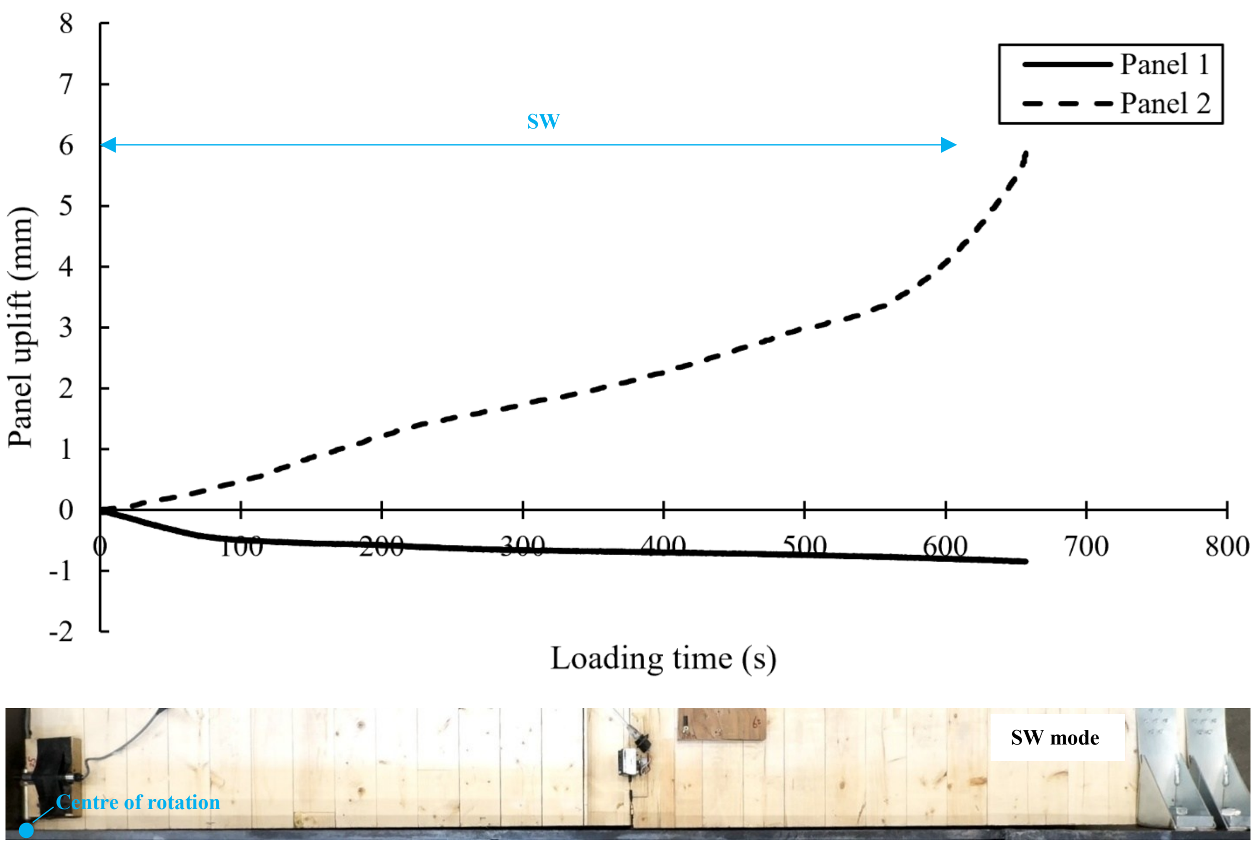

(a) Kinematic mode in specimen W1.2-P2-H2V32 (without transition)

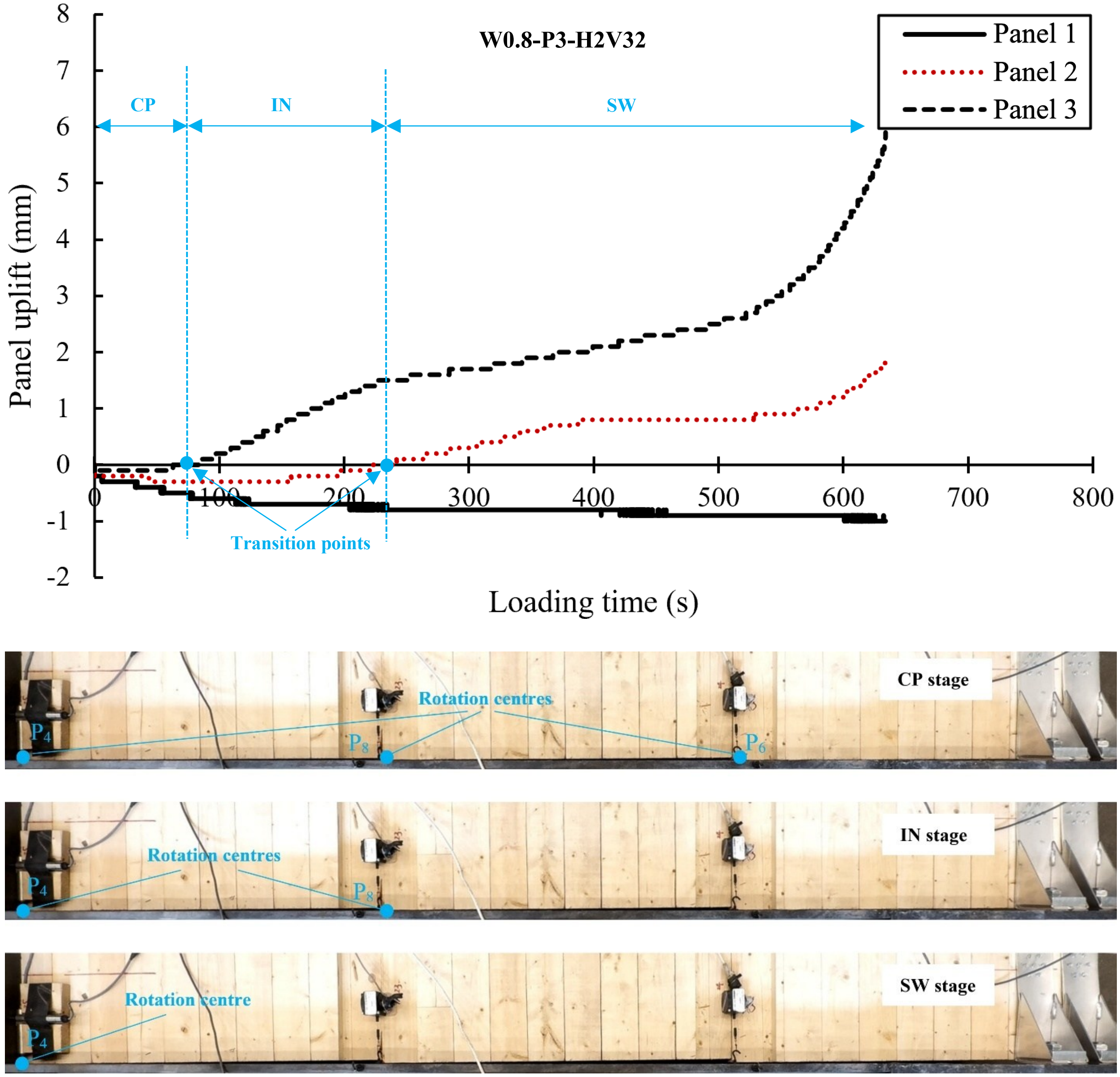

(b) Transitions of kinematic modes in specimen W0.8-P3-H2V32

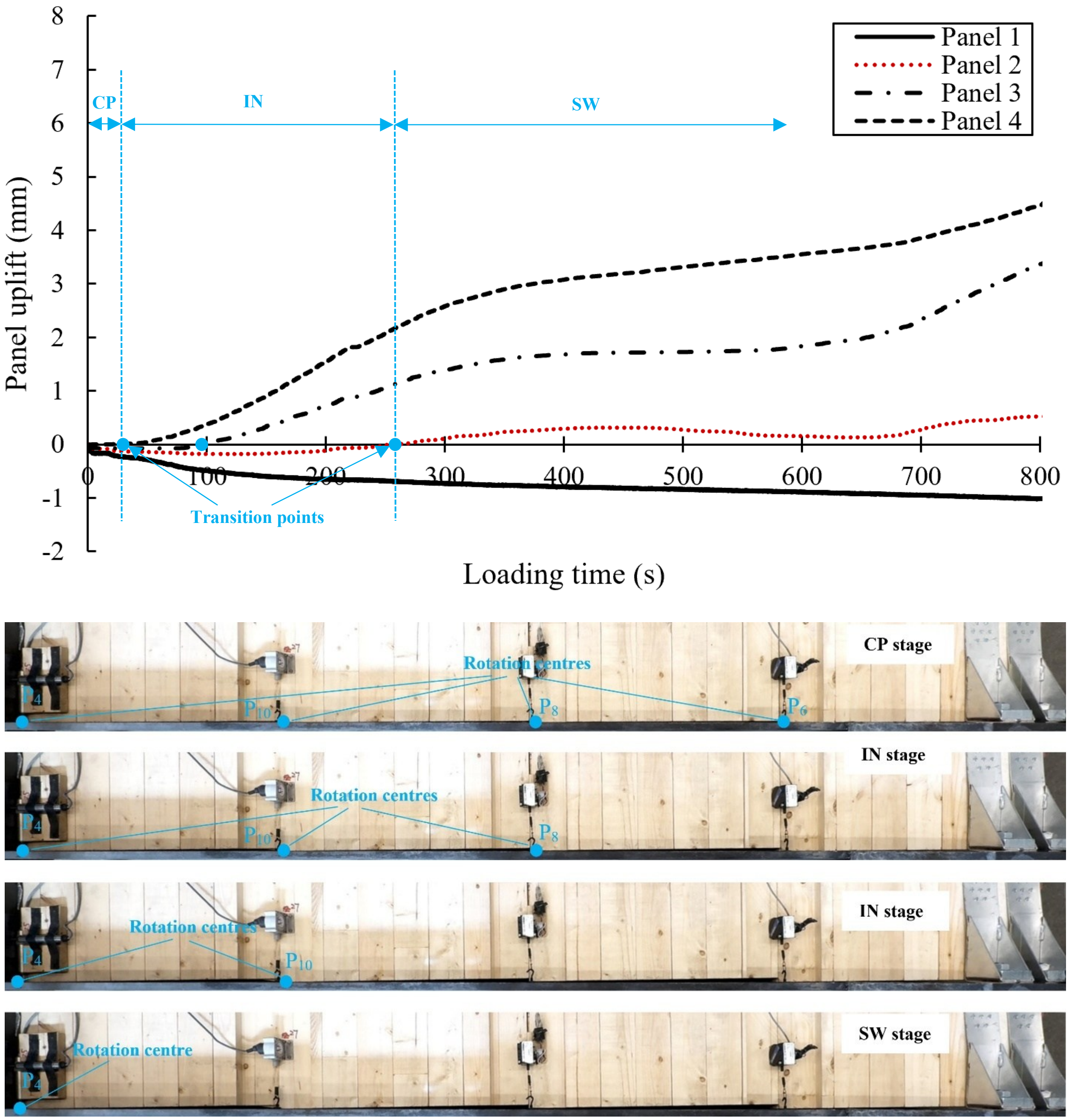

(c) Transitions of kinematic modes in specimen W0.6-P4-H2V32a

Figure 5.13: *Details of the kinematic modes varying with time in specimens (a) W1.2-P2-H2V32, (b) W0.8-P3-H2V32 and (c) W0.6-P4-H2V32a.*

Another transition in kinematic mode was observed in specimen W0.6-P4-H2V8b. Prior to the initiation of wood failure near the outermost hold-down, the response was dominated by CP mode. After the wood failure, the kinematic mode shifted to SW mode (Figure 5.14). It can be noted that the structure did not fail immediately after wood failure. Instead, it continued to hold the SW mode until the crack gradually expanded to result in entire rupture. This behaviour is attributed to the change in relative stiffness, where wood failure near the hold-down reduced the tensile stiffness of hold-downs, while the stiffness of vertical joints remained unaffected.

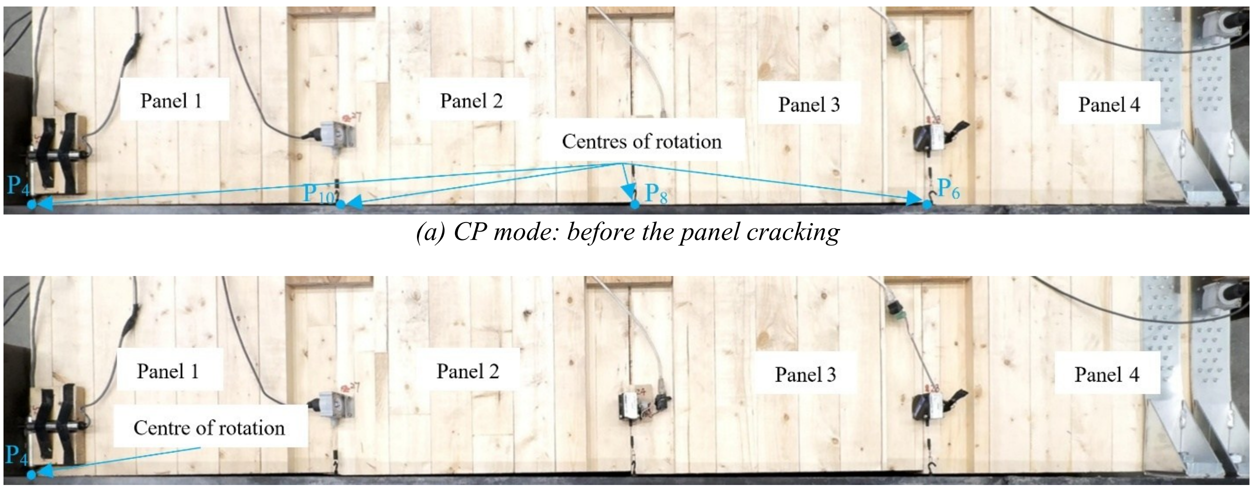

(a) CP mode: before the panel cracking

(b) SW mode: after the panel cracking

Figure 5.14: *Comparison of the kinematic modes before and after the panel cracking near the hold-down for specimen W0.6-P4-H2V32b*

Table 5.4: *Displacement details (along the direction of the height of walls) at the bottom of each panel at peak loads*

Specimens	***At the bottom of Panel 1***		***Slip between panels (mm)***	***At the bottom of Panel 2***		***Slip between panels (mm)***	***At the bottom of Panel 3***		***Slip between panels (mm)***	***At the bottom of Panel 4***		***Kinematic modes***
	Left corner (mm)	***Right corner (mm)***		***Left corner (mm)***	***Right corner (mm)***		***Left corner (mm)***	***Right corner (mm)***		***Left corner (mm)***	***Right corner (mm)***	
W1.2-P1-H2	*-2*	*14*	*-*	*-*	*-*	*-*	*-*	*-*	*-*	*-*	*-*	*SW*
W0.6-P2-H1V32	*-1*	*13*	*7*	*6*	*17*	*-*	*-*	*-*	*-*	*-*	*-*	*SW*
W0.6-P2-H2V32	*-2*	*15*	*18*	*-3*	*14*	*-*	*-*	*-*	*-*	*-*	*-*	*CP*
W0.6-P2-H4V32	*-2*	*22*	*26*	*-4*	*15*	*-*	*-*	*-*	*-*	*-*	*-*	*CP*
W0.6-P2-H2V8a	*-2*	*32*	*37*	*-5*	*24*	*-*	*-*	*-*	*-*	*-*	*-*	*CP*
W0.6-P2-H2V8b	*-2*	*21*	*27*	*-6*	*20*	*-*	*-*	*-*	*-*	*-*	*-*	*CP*
W0.6-P2-H1V65	*-1*	*8*	*0*	*8*	*20*	*-*	*-*	*-*	*-*	*-*	*-*	*SW*
W1.2-P2-H2V32	*-1*	*11*	*6*	*5*	*13*	*-*	*-*	*-*	*-*	*-*	*-*	*SW*
W0.8-P3-H2V32	*-1*	*9*	*7*	*2*	*14*	*8*	*6*	*11*	*-*	*-*	*-*	*SW*
W0.6-P4-H2V32a	*-1*	*9*	*8*	*1*	*13*	*8*	*5*	*16*	*9*	*7*	*12*	*SW*
W0.6-P4-H2V32b	*-1*	*6*	*6*	*0*	*8*	*6*	*2*	*9*	*6*	*3*	*6*	*SW*

Note: The negative values mean compressive displacement.

CHAPTER SIX

DISCUSSION ON THE EXPERIMENTAL, NUMERICAL AND ANALYTICAL RESULTS

6. Discussion on the experimental, numerical and analytical model

This chapter discusses the lateral resistance, stiffness and rocking deformation of tested shearwalls, and presents a comparison between the experimental findings and corresponding predictions obtained from the analytical and numerical models, highlighting consistencies as well as identifying potential sources of discrepancy. The discussion provides insight into the accuracy and limitations of each modelling approach.

6.1. Lateral resistance and stiffness of tested shearwalls

When the foundation beam was installed, it was recognised that one limitation could be that the stiffness would not be sufficiently high that there would be no anticipated deformation in the beam. Several analyses were made prior to designing and selecting the foundation beam and eliminating any deformation was very challenging. Therefore, it was decided that the movement of the foundation beam would be monitored and then subtracted from total displacement of the wall tests. This is not ideal as it may introduce some uncertainty in the results, but it was deemed acceptable given that the alternative is testing the walls vertically, which presented another set of challenges. As such, the curves presented in this section have been corrected for the movement of the steel foundation beam in the manner explained in Appendix B.

Figure 6.1 illustrates the relationship between the total lateral loads applied and the corresponding lateral displacements measured at the edge of the second diaphragm level (4.8 m) for specimens W0.6-P2-H1V32, W0.6-P2-H2V32 and W0.6-P2-H4V32, with progressively increasing (doubling) of the hold-downs. As summarised in Table 6.1, the specimen with a single hold-down (W0.6-P2-H1V32) attained a maximum lateral resistance of 35.4 kN, corresponding to a displacement of 126.6 mm. When the number of hold-downs was doubled (W0.6-P2-H2V32), the maximum lateral resistance increased by roughly 73%, accompanied by a 33% increase in displacement. Another doubling of the number of hold-downs (W0.6-P2-H4V32) resulted in an additional increase of only 47% the maximum lateral resistance and a 28% greater displacement. The observation of the horizontal resistance not increasing linearly with the number or stiffness of hold-downs is likely caused by the shift in kinematic mode from SW to CP. Additionally, it was observed that when multiple hold-downs were employed in the system, they failed at different points, where in general, the outermost hold-downs was observed to fail prior to the inner ones due to greater uplift experienced at the outer panel edges.

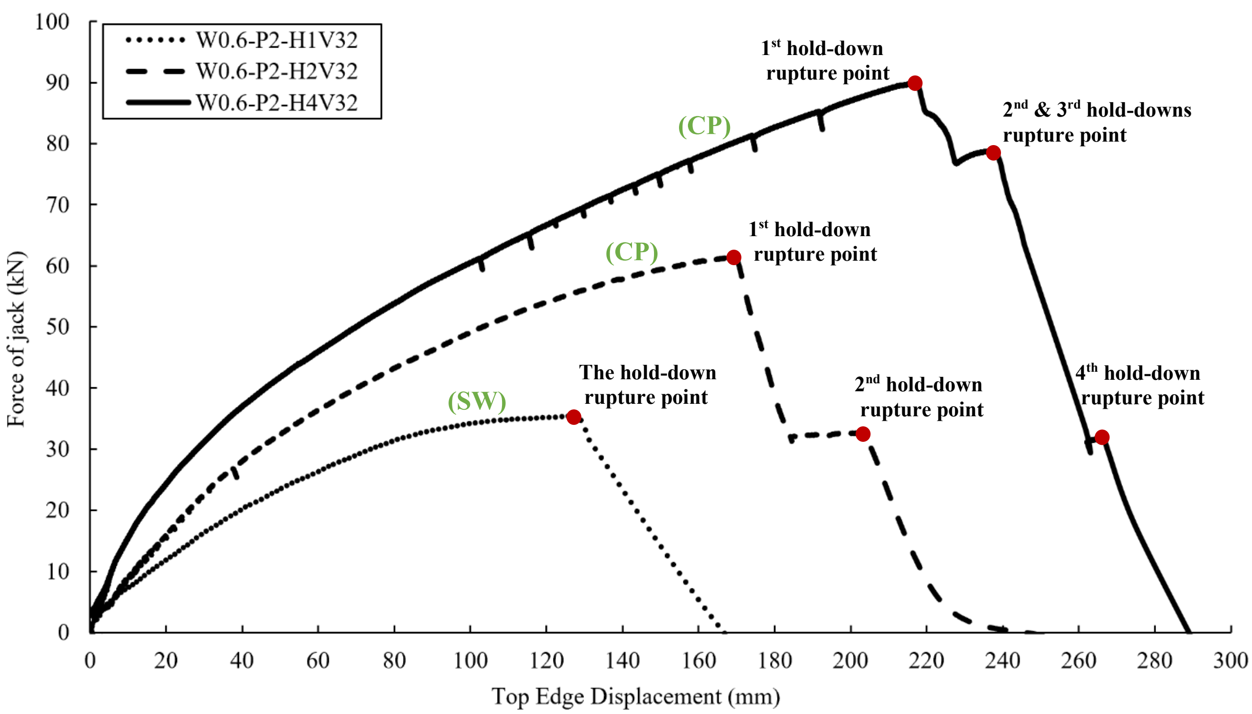

Figure 6.1: *Comparison of load-displacement curves between specimens W0.6-P2-H1V32, W0.6-P2-H2V32 and W0.6-P2-H4V32*

Table 6.1: *Mechanical properties of shearwalls*

Specimen No.	Number of hold-downs	Stiffness [1] $K_{l,40}$ ($\times 10^{-1}$kN/mm)	Peak load F_{max} (kN)	Displacement at peak load Δ_{max} (mm)	Ultimate load [2] F_u (kN)	Ultimate displacement Δ_u (mm)
W0.6-P2-H1V32	1	5.6	35.4	126.6	28.3	136.6
W0.6-P2-H2V32	2	7.4	61.3	168.7	49.1	191.9
W0.6-P2-H4V32	4	9.5	89.9	216.3	71.9	244.5
Specimen No.	**Number of vertical joints**	**Stiffness [1] $K_{l,40}$ ($\times 10^{-1}$kN/mm)**	**Peak load F_{max} (kN)**	**Displacement at peak load Δ_{max} (mm)**	**Ultimate load[2] F_u (kN)**	**Ultimate displacement Δ_u (mm)**
W1.2-P1-H2	-	11.2	64.4	99.6	51.5	116.4
W0.6-P2-H2V32	32	7.4	61.3	168.7	49.1	191.9
W0.6-P2-H2V8a	8	1.9	37.8	289.1	30.3	318.6
W0.6-P2-H2V8b	8	2.0	31.2	278.5	24.9	299.2
W0.6-P2-H1V32	32	5.6	35.4	126.6	28.3	136.6
W0.6-P2-H1V65	65	5.2	30.8	95.6	24.7	113.3
Specimen No.	**Aspect ratio**	**Stiffness [1] $K_{l,40}$ ($\times 10^{-1}$kN/mm)**	**Peak load F_{max} (kN)**	**Displacement at peak load Δ_{max} (mm)**	**Ultimate load [2] F_u (kN)**	**Ultimate displacement Δ_u (mm)**
W1.2-P2-H2V32	4.17	33.2	132.1	51.1	105.7	75.2
W0.8-P3-H2V32	6.25	23.3	124.1	77.8	99.3	84.0
W0.6-P4-H2V32a	8.33	20.5	128.3	103.2	102.6	119.8
W0.6-P4-H2V32b	8.33	22.6	112.0	72.7	89.6	91.6

Note: (1) Total lateral stiffness $K_{l,40}$ is calculated according to ASTM-E 2124 (ASTM International, 2019).

(2) Ultimate lateral load F_u is defined as 80% of the peak lateral load F_{max} after peak.

Figure 6.2 compares the load-displacement curves of specimens W1.2-P1-H2, W0.6-P2-H2V32, and W0.6-P2-H2V8a and W0.6-P2-H2V8b, in which the number of vertical joints ranges from eight to a continuous connection, behaving as a monolithic panel. It can be observed in Figure 6.2a that the specimen with a single panel (W1.2-P1-H2) reached a maximum lateral resistance of 64.4 kN at a corresponding displacement of 99.6 mm. When the monolithic wall was replaced with two panels connected by thirty-two vertical joints (W0.6-P2-H2V32), the maximum lateral resistance decreased slightly, but the corresponding displacement increased by 69%. When the number of vertical joints was further reduced to eight (W0.6-P2-H2V8a), the peak lateral resistance dropped to nearly half of the single-panel value, while the corresponding displacement nearly tripled.

As expected, improvement in lateral stiffness was observed when the number of vertical joints increases from eight (0.19 kN/mm) to thirty-two (0.74 kN/mm), since the stiffness was heavily influenced by the vertical joints. The additional stiffness gained when transitioning from thirty-two (0.74 kN/mm) to a continuous connection (monolithic wall) (1.12 kN/mm) did not follow the same trend since the flexibility is primarily dominated by that of the hold-down, with the vertical joints initially contributing to this flexibility while in the monolithic case the flexibility only stems from the hold-down. This observation is consistent with the sensitivity analysis in Chapter 3, which demonstrated dependency of kinematic modes and failure mechanisms associated with changes in vertical joint stiffness.

In observing the behaviour of specimen W0.6-P2-H2V8b, it could be seen that a sudden drop in the resistance curve occur where the panel failure near the hold-down happened at a displacement of 186 mm (Figure 6.2b). Following a 16.1% drop in resistance the curve gradually recovered but with a lower stiffness. Compared with the peak resistance prior to cracking (33.7 kN), the recovered peak increased by only 4.5% (35.2 kN), which may be attributed to the stress redistribution near the hold-downs after cracking. By contrast, specimen W0.6-P2-H2V8a, which did not experience panel cracking, achieved a 21.2% higher peak lateral resistance and a 3.8% greater corresponding displacement. Despite these differences in peak response and failure behaviour, two specimens exhibited comparable lateral stiffness, indicating that panel cracking primarily affected the post-peak response rather than the global stiffness of the shearwall.

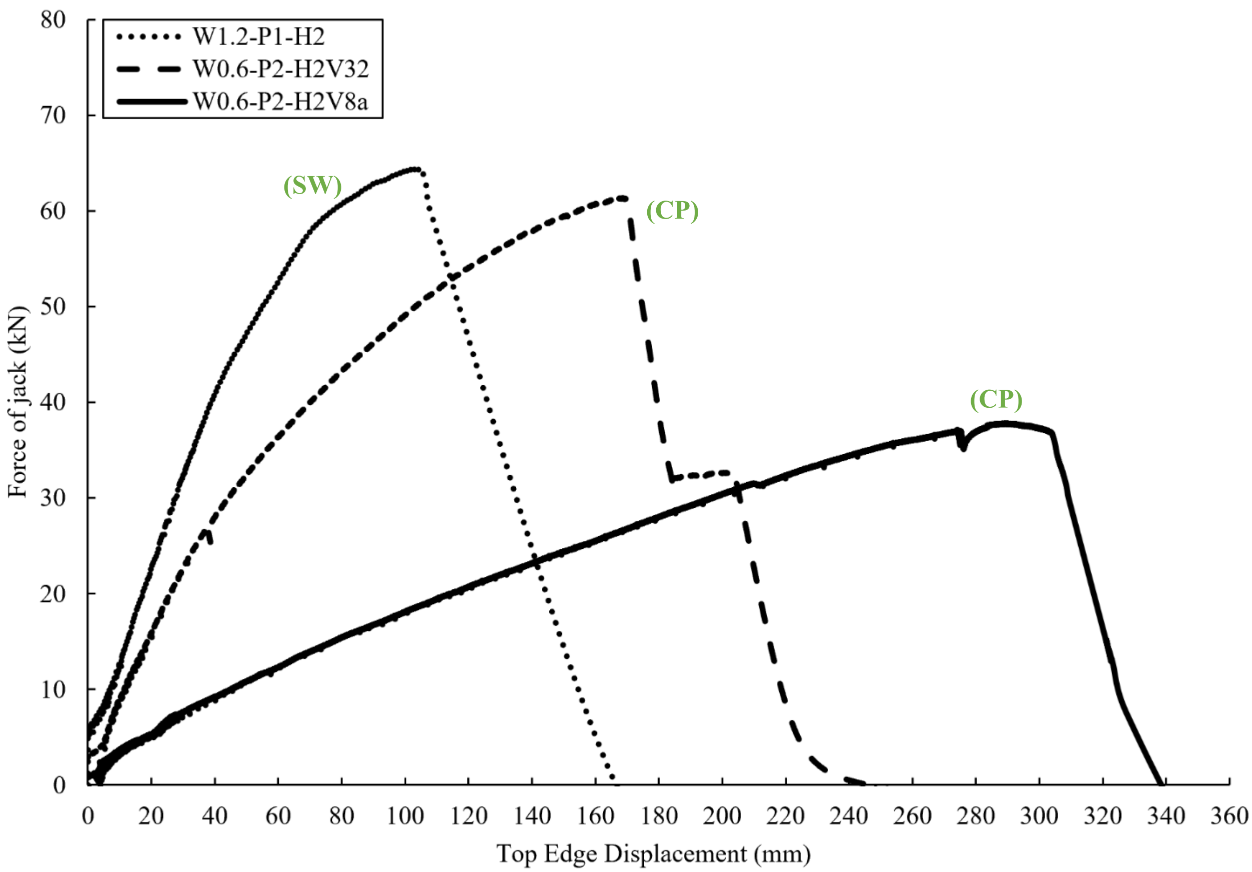

(a)

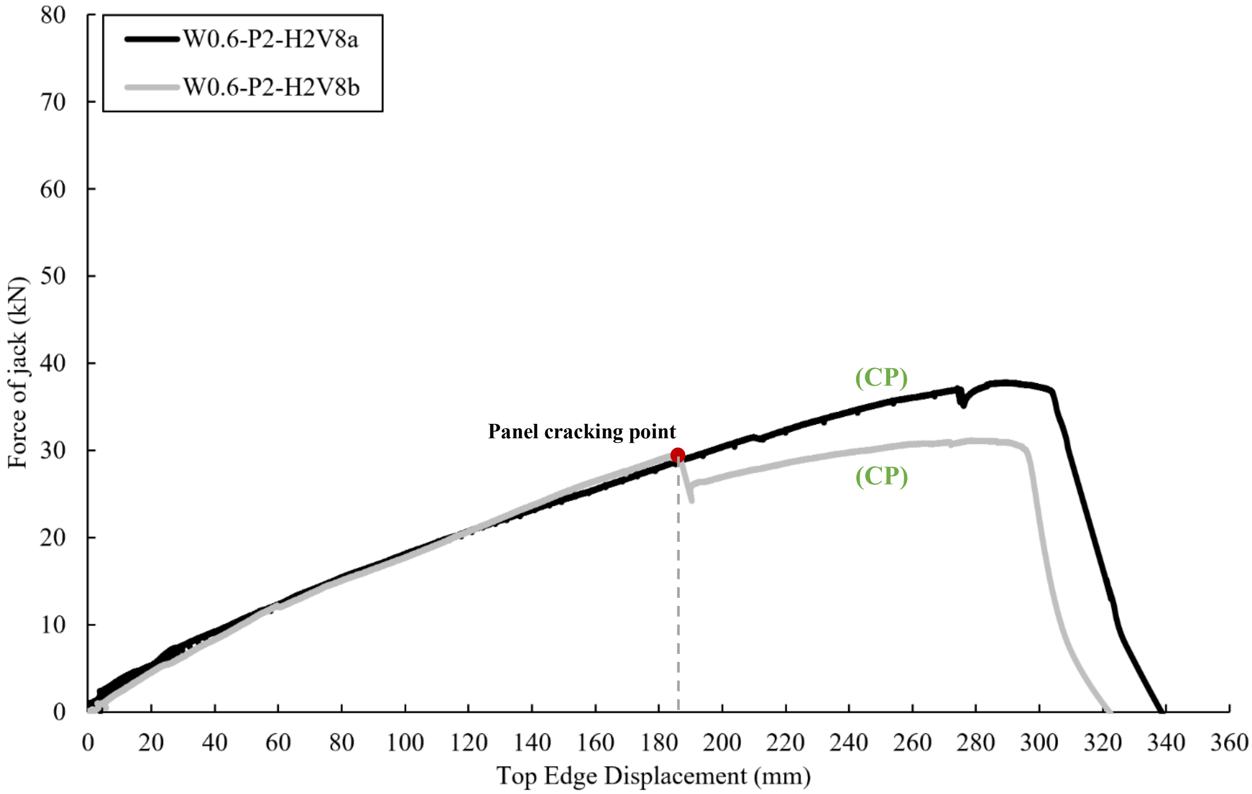

(b)

Figure 6.2: *Comparison of load-displacement curves between specimens (a) W1.2-P1-H2, W0.6-P2-H2V32, and W0.6-P2-H2V8a, (b) W0.6-P2-H2V8a and W0.6-P2-H2V8b*

Figure 6.3 compares the load-displacement responses of specimens W0.6-P2-H1V32 and W0.6-P2-H1V65, in which a single hold-down was employed while the number of vertical joints was increased from thirty-two to sixty-five. The results show that the specimen with a larger number of vertical joints (W0.6-P2-H1V65) exhibited a reduced lateral displacement at peak load, demonstrating that increasing vertical joint stiffness can effectively limit lateral drift even when the ultimate resistance remains unchanged.

In addition, specimen W0.6-P2-H1V65 exhibited 13% lower maximum resistance compared with W0.6-P2-H1V32, which is attributed to the modified hold-down position. In this specimen, the hold-down was installed 100 mm farther from the wall edge (Figure 6.3), resulting in a reduced lever arm for resisting overturning moments and, consequently, a lower contribution to overturning resistance. These observations further highlight the sensitivity of shearwall performance to hold-down placement, significantly influencing resistance capacity, particularly in balloon-type shearwall systems with relatively slender panels.

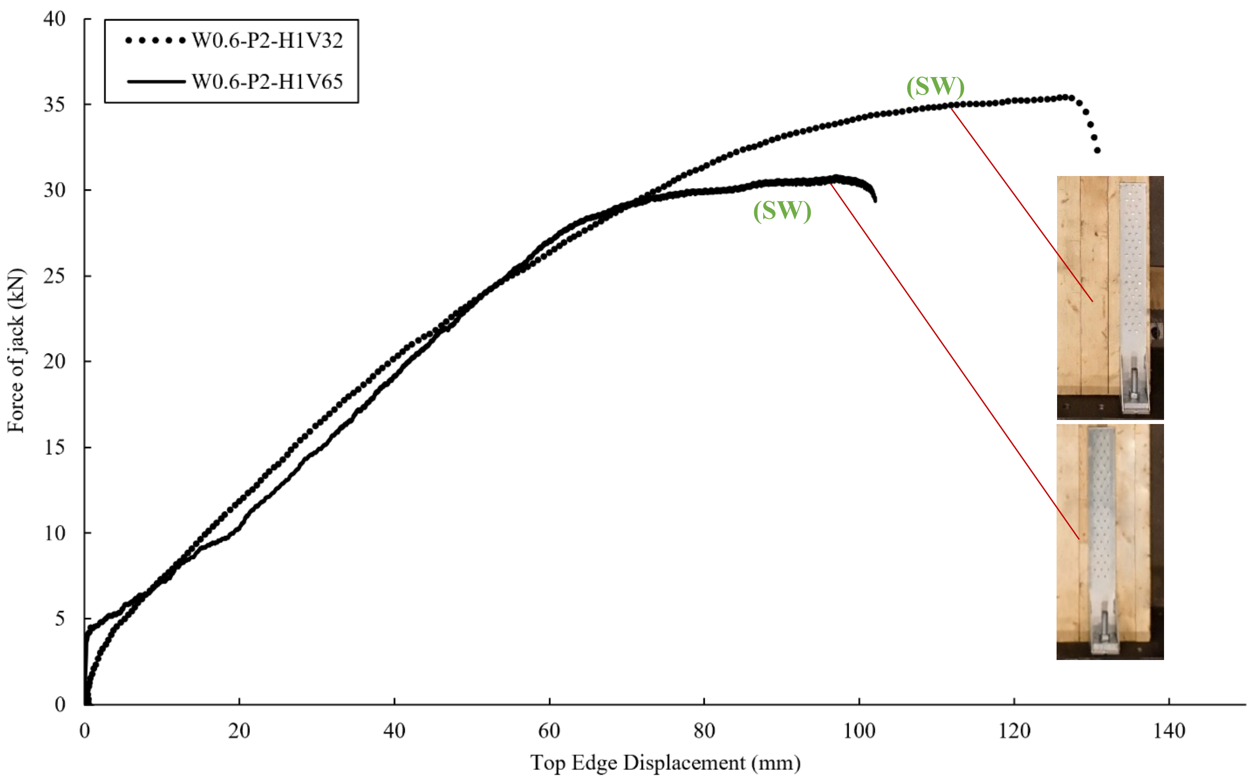

Figure 6.3: *Comparison of load-displacement curves between specimens W0.6-P2-H1V32 and W0.6-P2-H1V65*

Specimens W1.2-P2-H2V32, W0.8-P3-H2V32, W0.6-P4-H2V32a, and W0.6-P4-H2V32b had the same total width of 2.4 m but differed in panel aspect ratios and the number of panels. As observed in Figure 6.4a, specimens W1.2-P2-H2V32, W0.8-P3-H2V32, and W0.6-P4-H2V32a, exhibited similar maximum lateral resistances, with an average value of 128.18 ± 3.28 kN, while the corresponding lateral displacements varied considerably. For the shearwall consisting of two equal panels (panel aspect ratio = 4.17), the displacement at peak load was 51.1 mm. When replaced with three equal panels (panel aspect ratio = 6.25) and four equal panels (panel aspect ratio = 8.33), the displacements at the peak load increased by 52% and 102%, respectively. Although all three shearwalls exhibited SW modes at failure, more complex kinematic behaviour was observed during the loading process, as discussed in Section 5.3.2.

Although the estimated total lateral stiffness showed only a slight reduction from the two-panel to the four-panel configuration, the results indicate an important design implication. When the total wall width is fixed, shear walls composed of more slender panels are able to maintain comparable lateral resistance while developing larger lateral drift capacity. This behaviour suggests an increase in structural ductility under lateral loading, which is favourable for seismic design, as it allows the system to dissipate more energy without a significant loss in strength. Therefore, the use of more slender panels can be considered a viable design strategy for enhancing ductile performance, provided that drift demands remain within acceptable limits.

As mentioned in Section 5.3.1, specimen W0.6-P4-H2V32b experienced a sudden premature failure at finger joints, reaching 87% of the maximum resistance observed in specimen W0.6-P4-H2V32a (Figure 6.4b). A slight recovery of strength was observed after crack development in the CLT panel, whereby the tensile load was entirely carried by the inner hold-down. However, the recovery was very limited and transient with the second peak after cracking being 12% (from 112.0 kN to 98.8 kN) less compared with the recovery observed in specimen W0.6-P2-H2V8b.

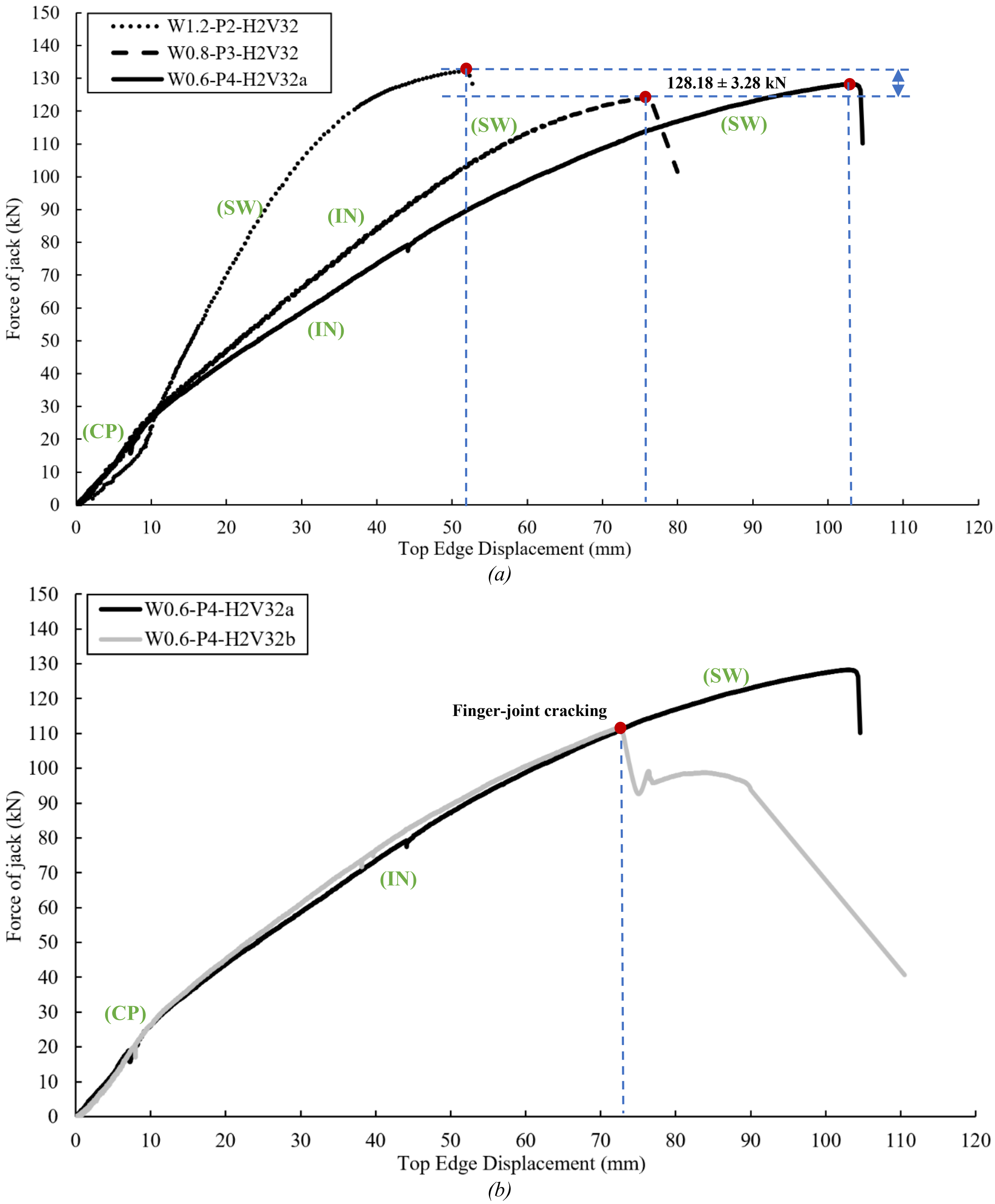

Figure 6.4: *Comparison of load-displacement curves between specimens (a) W1.2-P2-H2V32, W0.8-P3-H2V32, W0.6-P4-H2V32a; (b) W0.6-P4-H2V32a and W0.6-P4-H2V32b*

Specimens W0.6-P2-H2V32 versus W0.6-P4-H2V32a, and W1.2-P1-H2 versus W1.2-P2-H2V32, were compared for the purpose of evaluating the scaling effect of total wall width on the lateral resistance and stiffness of CLT shearwalls. It can be observed that doubling the total width of the shearwalls from 2.4 m to 4.8 m, while maintaining the same panel aspect ratios, resulted in approximately twice the maximum lateral resistance (from 61.3 kN to 128.3 kN and from 64.4 kN to 132.1 kN, respectively). Similarly, the total lateral stiffness roughly tripled (from 0.74 kN/mm to 2.05 kN/mm and from 1.12 kN/mm to 3.32 kN/mm, respectively). Although these results indicate that simply increasing the total width of the shearwall can indeed enhance structural resistance and stiffness, enhancing the stiffness of the connectors has been demonstrated to be an effective alternative strategy. For example, when the combination of hold-downs and vertical joints was increased from two hold-downs and eight pairs of vertical joints (-H2V8) to four hold-downs and thirty-two pairs of vertical joints (-H4V32) in shearwalls consisting of two panels with an aspect ratio of 8.33 (W0.6-P2-), the total lateral stiffness increased by four times (from 0.19 kN/mm to 0.95 kN/mm).

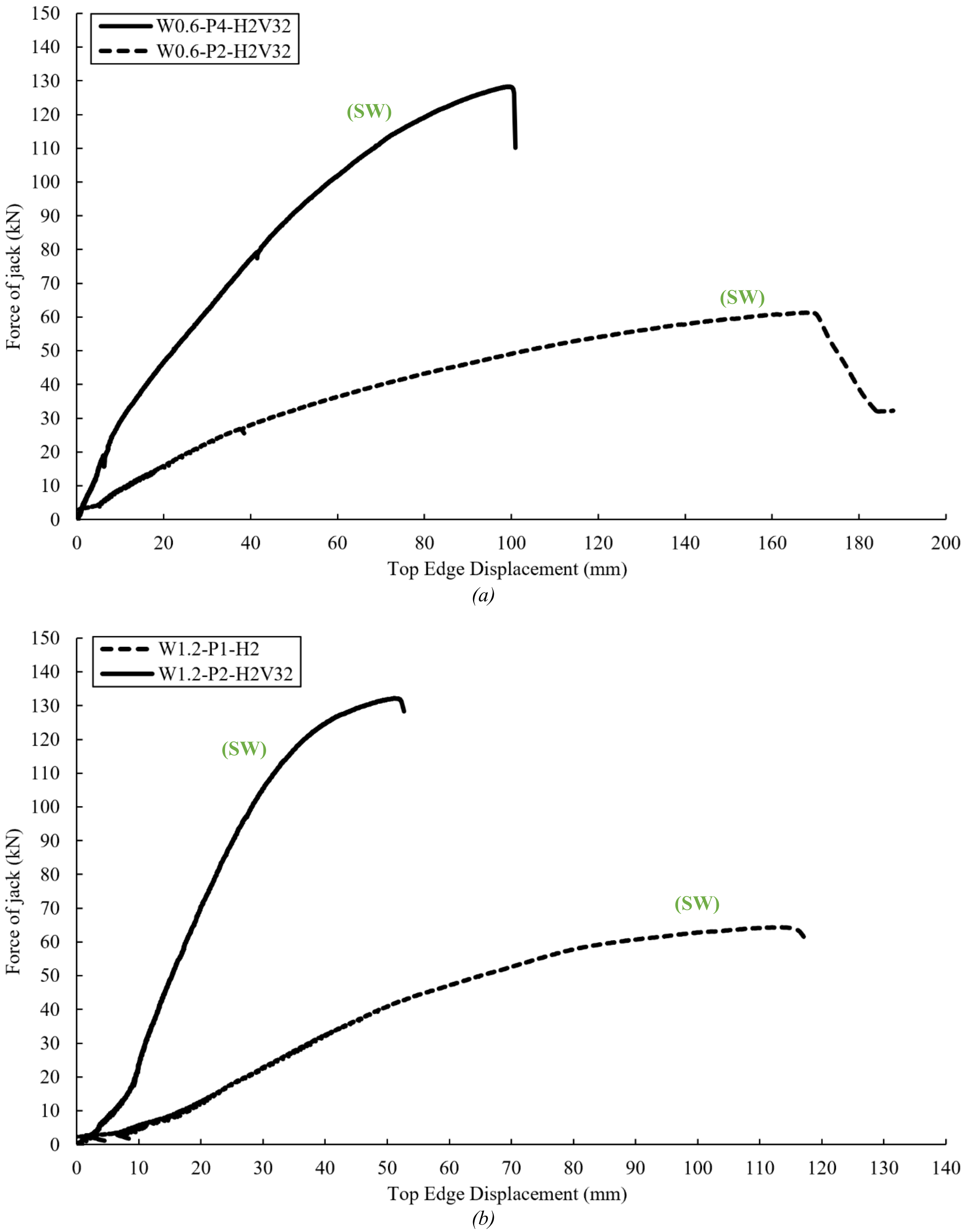

Figure 6.5: *Comparisons of the load-displacement curves of specimens (a) W0.6-P2-H2V32 versus W0.6-P4-H2V32a, and (b) W1.2-P1-H2 versus W1.2-P2-H2V32*

6.2. Rocking deformation of tested shearwalls

According to the definition of rocking deformation given in Equation 3.6 (Chapter 3), the rocking deformation of the tested shear walls was calculated. However, it was mentioned in Chapter 5 that several specimens exhibited significant differences in uplift among individual panels within the same shearwall, such as specimen W0.6-P2-H4V32 and W0.6-P2-H2V8a. These uneven uplift responses resulted in substantial variation in estimating overall rocking deformation. To address this issue, the definition of rocking deformation for specimens exhibiting CP behaviour was calculated by considering the average uplift of all panels.

In the investigation of rocking deformation, two representative loading states were considered:

- 0.4 F_{peak}, corresponding to a typical elastic response dominated by the initial stiffness of the connectors,
- the peak load, F_{peak}.

At $0.4F_{peak}$, a clear influence of connector stiffness on rocking deformation was observed. For specimens W0.6-P2-H1V32, W0.6-P2-H2V32, and W0.6-P2-H4V32, in which the number of hold-downs was progressively doubled, the percentage of rocking deformation decreased from 75% to 57% (Figure 6.6a). Similarly, when comparing specimens W0.6-P2-H2V8a and W0.6-P2-H2V32, an increase in vertical joint stiffness led to a reduction in rocking deformation from 75% to 69%. A comparable trend was also observed between specimen W0.6-P2-H1V32 and W0.6-P2-H1V65, where the rocking deformation percentage decreased from 75% to 60% with increased vertical joint stiffness (Figure 6.6b).

These results are consistent with the findings of the sensitivity analysis presented in Chapter 3 and verify the analytical theory in Chapter 4, which clearly highlight the critical role of connector stiffness in controlling rocking deformation. More importantly, the results further confirm that bending and shear deformation of panels cannot be neglected in balloon-type CLT shearwalls.

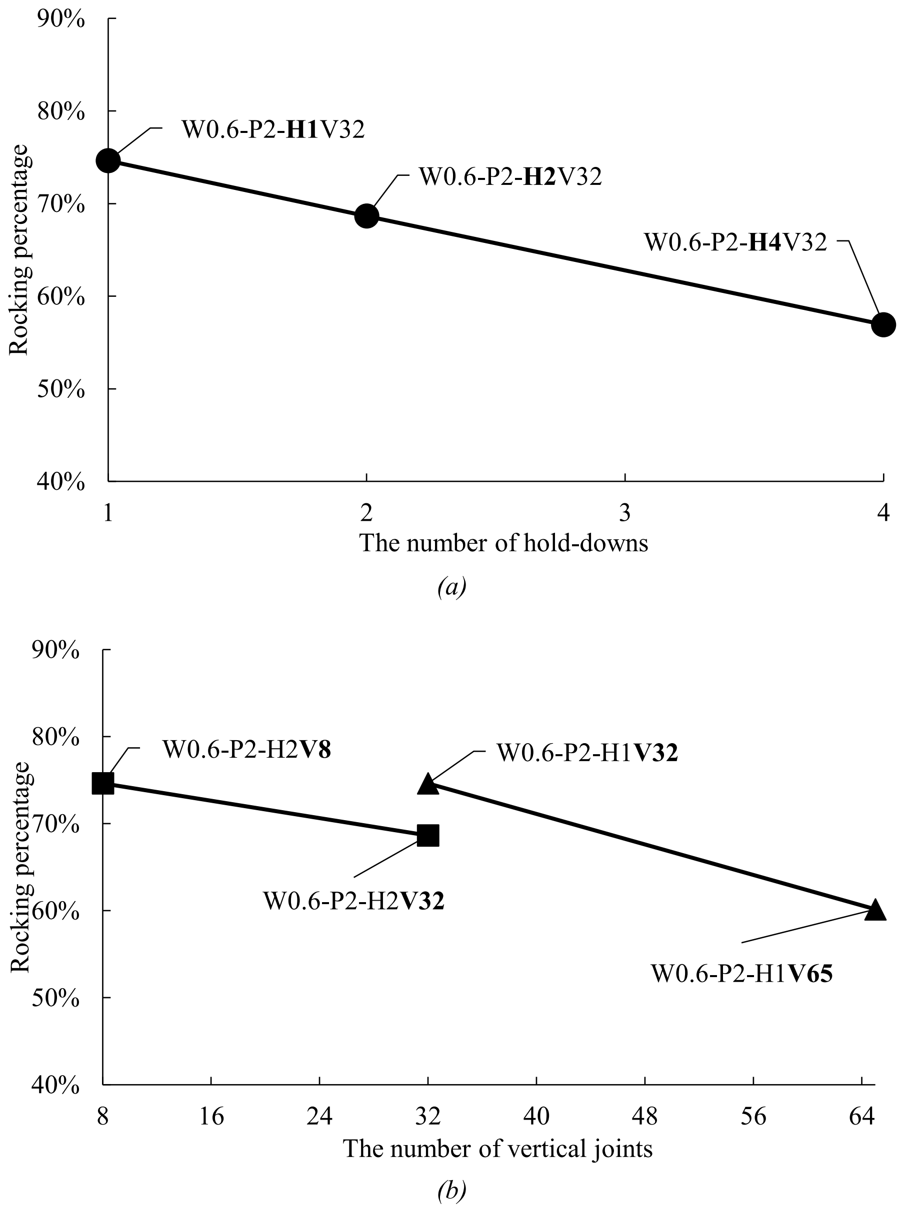

Figure 6.6: *Percentage of rocking deformation with the varying number of (a) hold-downs and (b) vertical joints at* $0.4F_{peak}$

For specimens consisting of more than two panels, a more complex rocking behaviour was observed. A comparison among specimens W1.2-P2-H2V32, W0.8-P3-H2V32, and W0.6-P4-H2V32a, which share the same total wall width but differ in the number of panels, indicates that the rocking deformation percentage decreased from 72% for the two-panel configuration (-P2-) to 48% for the three-panel configuration (-P3-), before increasing again to 62% for the four-panel configuration (-P4-). This trend is possible and consistent with the sensitivity analysis in Chapter 3, which demonstrates a varying number of panels under fixed total width can significantly influence the rocking percentage, but it is more complex in a muti-panel system, since the tendency is also relevant with the choice of stiffness of the connectors that may bring a transition of kinematic modes.

When examining the rocking deformation at F_{peak}, trends similar to those observed at $0.4\,F_{peak}$ were identified. However, the rocking deformation percentages at peak load were consistently higher for all specimens (Figure 6.7). This behaviour indicates that, as loading increases, the hold-downs and vertical joints progressively enter the plastic phase, leading to stiffness degradation and, consequently, a systematic increase in rocking contribution to the overall deformation response of the shearwalls.

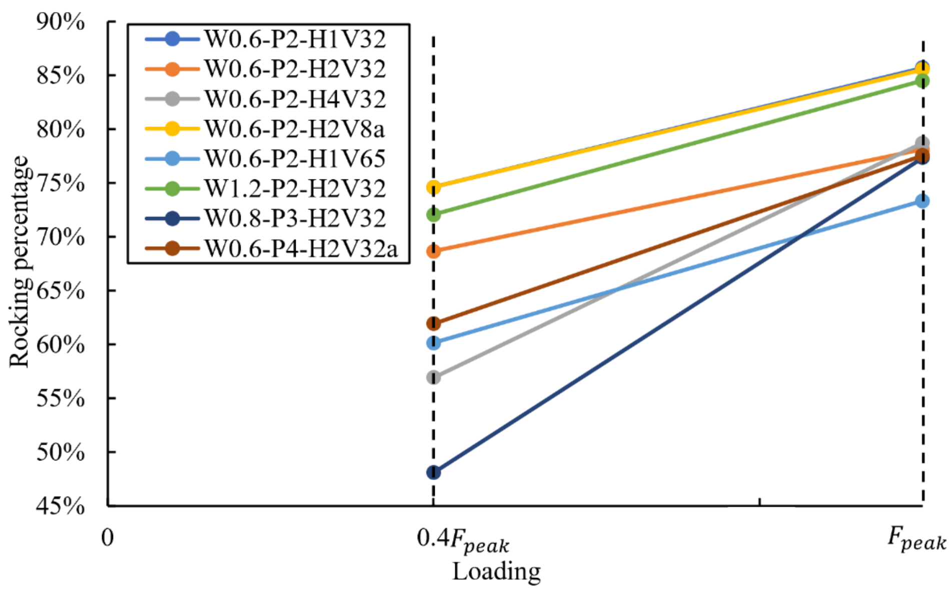

Figure 6.7: *Rocking percentage at 0.4F_{peak} and F_{peak}*

6.3. Numerical model

Consistent with the simulation approach adopted in the sensitivity analysis, the FE model employed two-dimensional shell elements with the same CLT material property assumptions described in Chapter 3. However, to achieve higher accuracy in comparison with the experimental results, a smaller mesh size of 10 mm × 10 mm was adopted in the present analyses.

The behaviours of hold-downs and vertical joints were modelled using link (spring) elements. Hold-downs were represented by two-node link elements connected to the steel foundation beam, accounting for both tensile and shear responses. Similarly, vertical joints were modelled as two-node links that connected adjacent panels, providing shear resistance along two orthogonal in-plane directions. The mechanical properties of the hold-downs and vertical joints were based on the test results reported by Masroor et al. (2024), as illustrated in Figure 6.8.

One of the contentious issues in the numerical model when attempting to simulate the experimental test setup was accounting for the potential movement of the foundation beam. Two models, one including and one excluding the foundation beam were developed and compared with the experimental results, as illustrated in Figure 6.9.

In the numerical simulation of the foundation beam, two-dimensional shell elements were adopted with steel material properties, assuming an effective Young's modulus of 200GPa. Based on the measured foundation beam movement presented in Appendix B, the foundation beam was observed to undergo predominantly rigid-body rotation on the ground floor.

As a result, the reactions provided by the steel rods (anchored to the ground) were idealised as equivalent non-linear springs. Specifically, two identical springs acting in the vertical direction (y-axis) were assigned along the height of shearwalls, and one spring acting in the horizontal direction (x-axis) was assigned along the width of shearwalls. These springs were located as follows:

- Point A: at the left end of the foundation beam model, where an LVDT was installed to measure the foundation beam displacement in the y-axis direction,
- Point B: at the right end of the foundation beam model, where a second LVDT was installed to measure the foundation beam displacement in the y-axis direction,
- Point C: at the lateral restraint fixed on the foundation beam, where another LVDT was installed to measure the foundation beam displacement in the x-axis direction.

This modelling approach avoids the need to explicitly account for the presence of opening holes and local discontinuities in the foundation beam, while effectively capturing its global movement behaviour through a simplified three-spring model. Figure 6.10 presents the estimated stiffness values of these equivalent springs, which were derived following the procedure described in Appendix C.

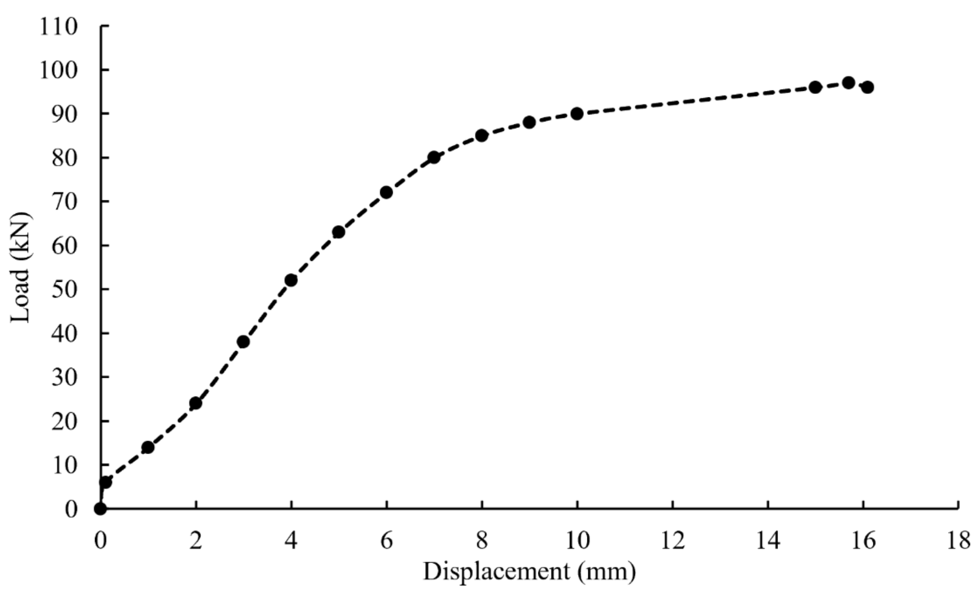

(a) Hold-down tension

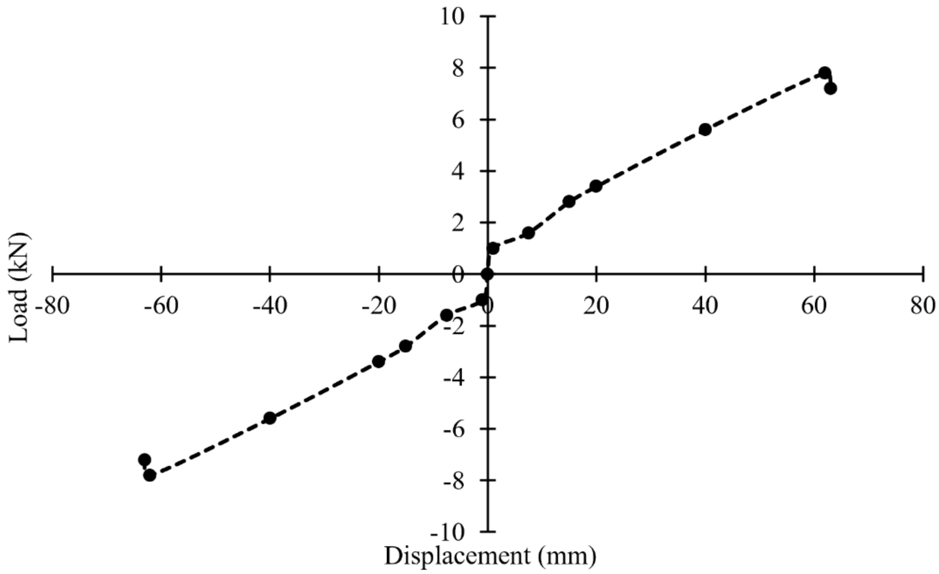

(b) Hold-down shear

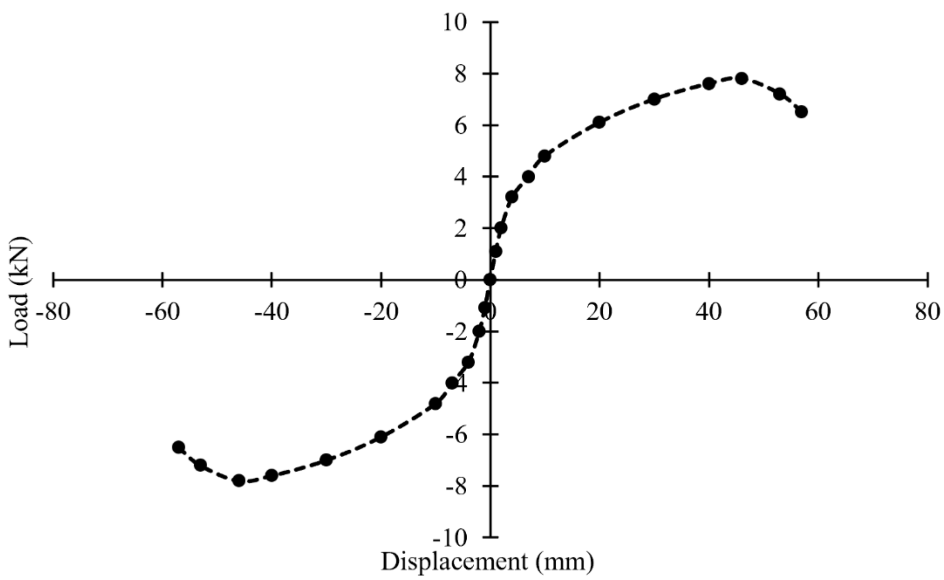

(c) Vertical joint shear

Figure 6.8: *Mechanical properties of hold-down and vertical joint (a) hold-down tension, (b) hold-down shear and (c) vertical joint shear (Masroor et al., 2024)*

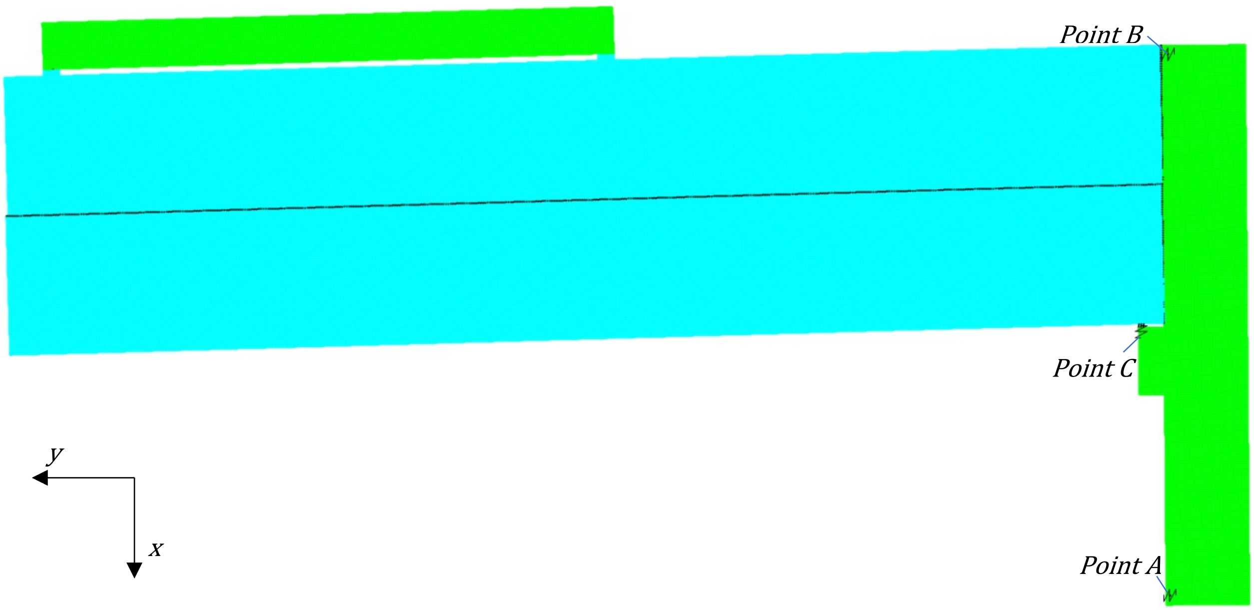

(a) Numerical model with foundation

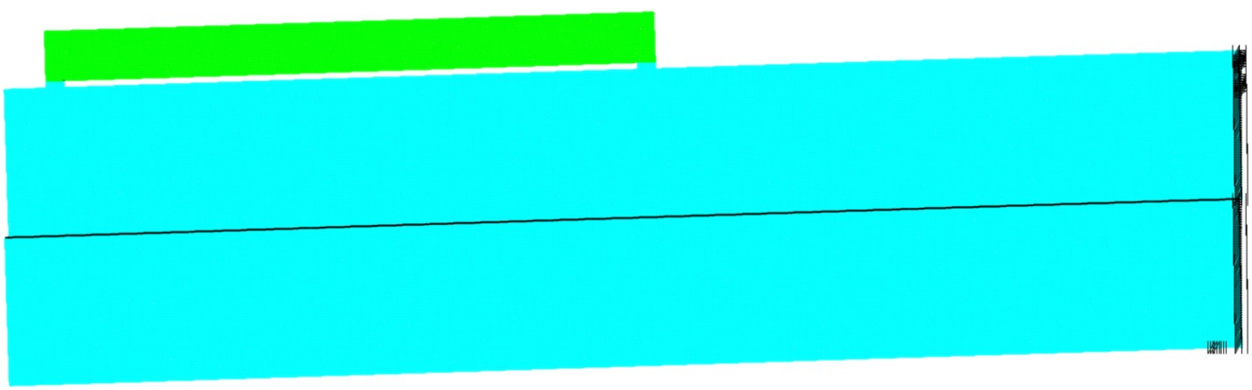

(b) Numerical model without foundation

Figure 6.9: *Numerical model for specimen S5/0.6-P2-H2V32 in both conditions (a) with and (b) without foundation*

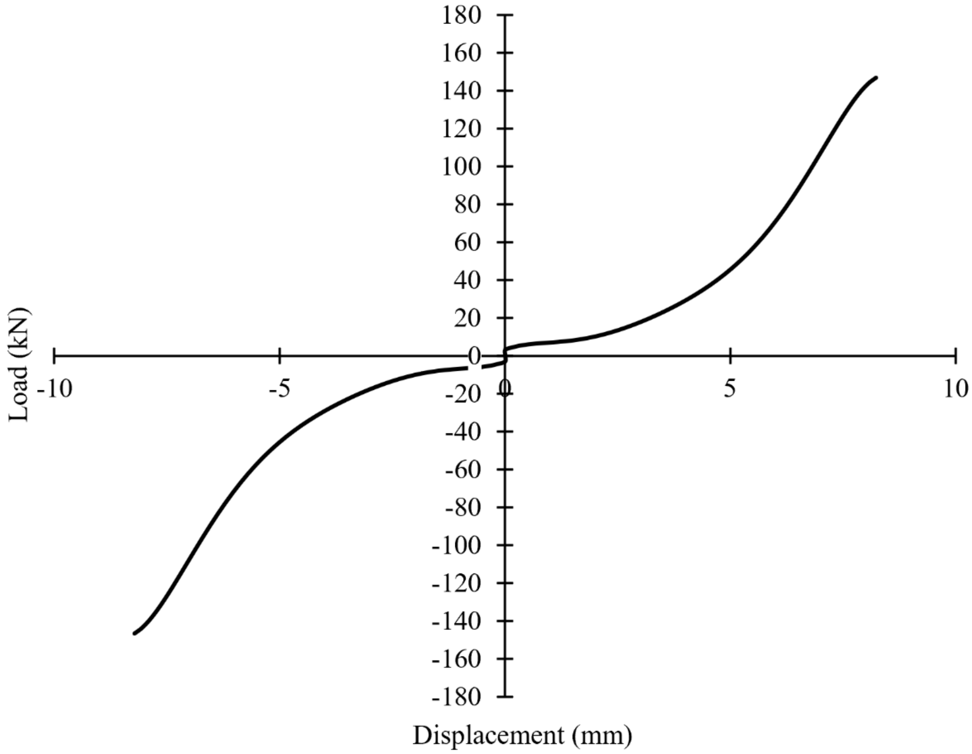

(a) At Point A and B

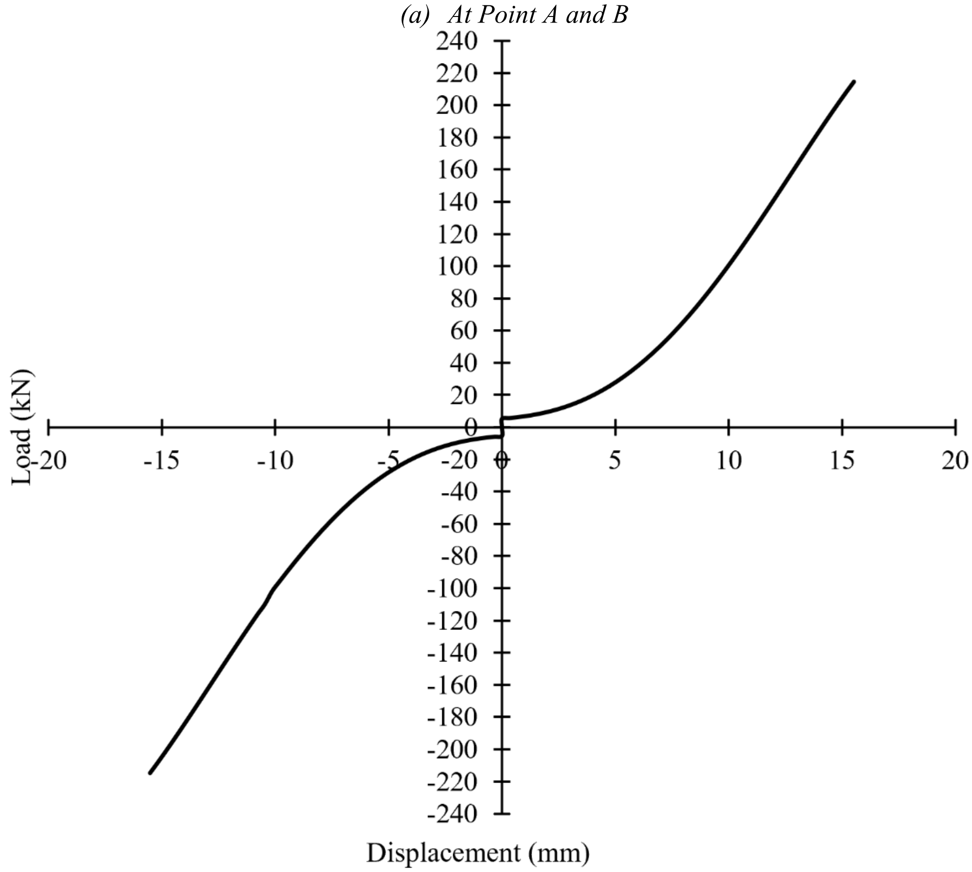

(b) At Point C

Figure 6.10*: Mechanical properties of the foundation beam movement along (a) y-axis direction and (b) x-axis direction in FE modelling*

6.4. Analytical model

As the analytical model presented in Chapter 4 is limited to predicting the lateral displacement of shearwalls within the elastic range (i.e., initial stiffness), only the elastic stiffness of the connectors was considered. Accordingly, the stiffness values of the hold-downs k_{hd} and vertical joints k_{vj} were determined based on the elastic properties obtained following ASTM E2126 (ASTM International, 2019). The total lateral deformation Δ_{total} was therefore calculated and compared at a load level of $0.4F_{max}$ for each specimen, where the elastic assumption remains valid.

Since the number of storeys in the experimental campaign was fixed at two and there was no vertical (gravity) load applied, the total deformation obtained from the analytical model described in Chapter 4 for the walls consisting of two panels can be simplified. Table 6.2 summarised the main parameters of the analytical model and provides calculation results of the total deflection, Δ_{total}. Considering the limitation of analytical model, those specimens more than two panels are not included in the table.

Table 6.2: *Basic parameters used in the analytical model and estimated total lateral deformation*

Specimens	***W0.6-P2-H1V32***	***W0.6-P2-H2V32***	***W0.6-P2-H4V32***	***W0.6-P2-H2V8a***	***W0.6-P2-H1V65***	***W1.2-P2-H2V32***
Panel height h (mm)	*4800*	*4800*	*4800*	*4800*	*4800*	*4800*
Panel width b (mm)	*600*	*600*	*600*	*600*	*600*	*1200*
Total stiffness of vertical joints k_{vj} (elastic) (kN/mm)	*12.7*	*25.3*	*50.8*	*25.4*	*12.7*	*25.4*
Total stiffness of hold-downs k_{hd} (elastic) (kN/mm)	*25.8*	*25.8*	*25.8*	*6.5*	*52.5*	*25.8*
Lateral load on each storey F ($0.4F_{max}$) (kN)	*7.1*	*12.6*	*18.0*	*7.6*	*5.4*	*26.4*
Effective bending stiffness EI_{eff} (10^{10} kN·mm^2)	*6.1*	*6.1*	*6.1*	*4.9*	*7.4*	*4.3*
Effective shear stiffness G^*A (10^4 kN)	*8.0*	*8.0*	*8.0*	*8.0*	*8.0*	*16.0*
Kinematic modes	*SW*	*CP*	*CP*	*CP*	*SW*	*SW*
Total lateral deformation Δ_{total} (mm)	*26.2*	*34.6*	*38.4*	*30.9*	*16.8*	*16.6*

6.5. Comparisons between modelling techniques and experimental results

Figure 6.11 compares the pushover curves obtained from the experimental results with those predicted by the FE models, both with and without consideration of foundation beam movement. The figure also includes the results from the analytical model based on the (initial) elastic stiffness. Overall, the numerical curves show good agreement with the experimental responses in terms of global behaviour. The FE models successfully reproduce the general trends, exhibiting comparable peak lateral resistances, and for most specimens, reasonably consistent displacements at peak load. The analytical estimation also aligns reasonably well with most of the test curves, further supporting its suitability for approximating the initial stiffness.

A notable difference was observed between the FE results and those obtained experimentally from specimen W0.6-P2-H2V8a, where substantially larger uplift was recorded by the LVDTs due to the hold-down failure. As a result, the original hold-down constitutive properties used in the FE model no longer reflected the actual behaviour. A re-evaluation of the hold-down properties was therefore carried out based on the recorded uplift response during loading (Figure 6.12a), and the corrected properties were employed into related FE simulations. More details about the re-evaluation method of the hold-down properties can be found in Appendix D. The updated model, shown in Figure 6.12b and c, exhibits a markedly improved agreement with the experimental response.

In addition to the specimen-specific issues described above, discrepancies ε between the numerical and experimental results may also stem from inherent variability in material properties and the idealised multi-linear constitutive models adopted to represent the nonlinear behaviour of mechanical connectors. Despite these limitations, the overall correlation between the FE predictions and the experimental results demonstrates that the numerical approach provides a reasonably accurate representation of the structural performance of the tested CLT shearwalls.

A quantitative summary of the comparison is provided in Table 6.3. The peak lateral resistance shows good agreement, with all errors within 10%. Larger deviations are observed for the lateral displacement at peak load and the initial stiffness, however, for the majority of specimens, the discrepancies remain within 20%.

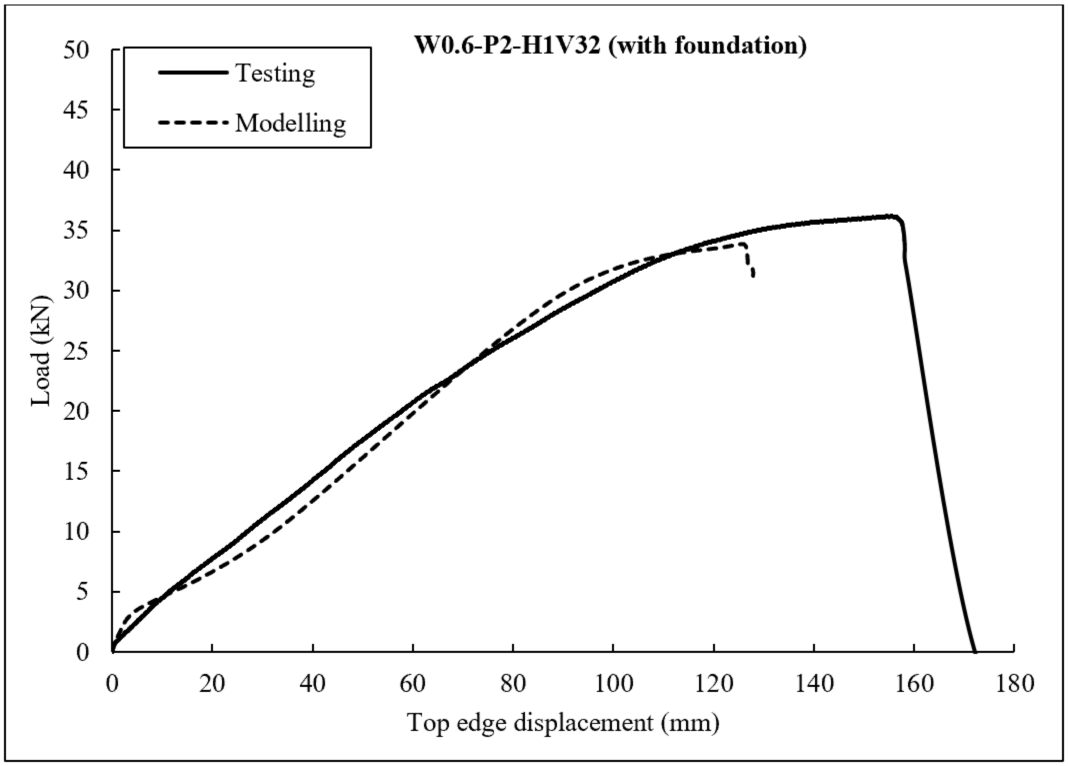
W0.6-P2-H1V32 (with foundation)
Testing
Modelling
Load (kN)
0
5
10
15
20
25
30
35
40
45
50
0
20
40
60
80
100
120
140
160
180
Top edge displacement (mm)

(a)

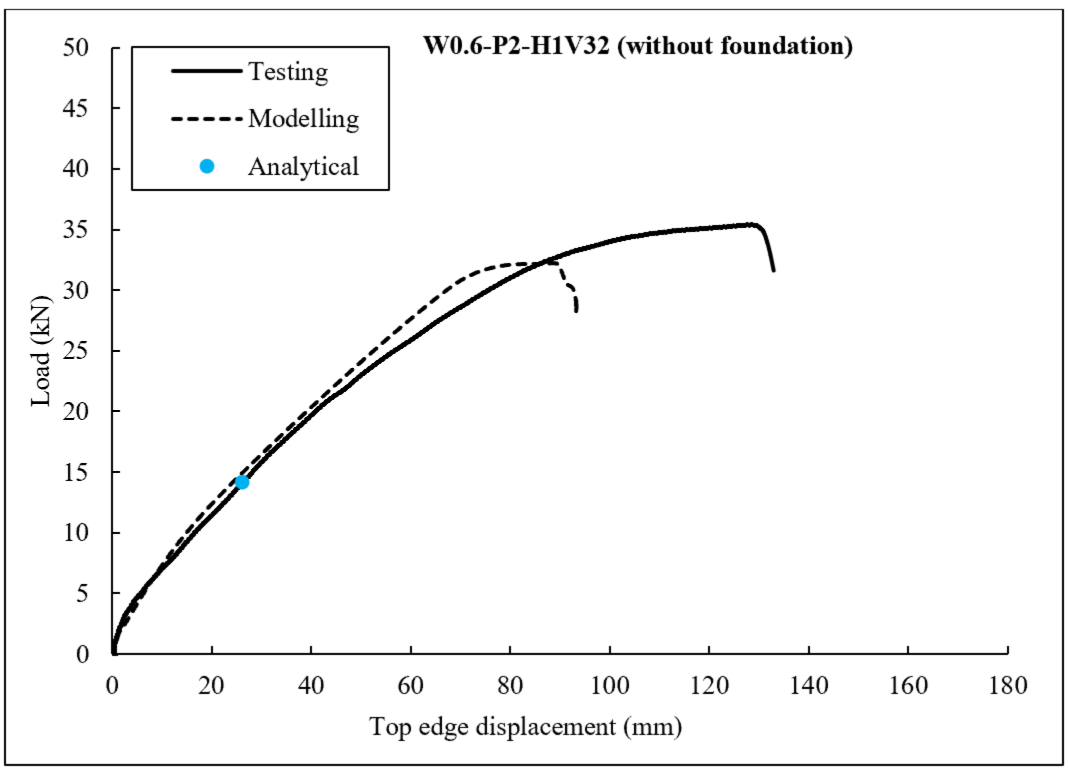
W0.6-P2-H1V32 (without foundation)
Testing
Modelling
Analytical
Load (kN)
0
5
10
15
20
25
30
35
40
45
50
0
20
40
60
80
100
120
140
160
180
Top edge displacement (mm)

(b)

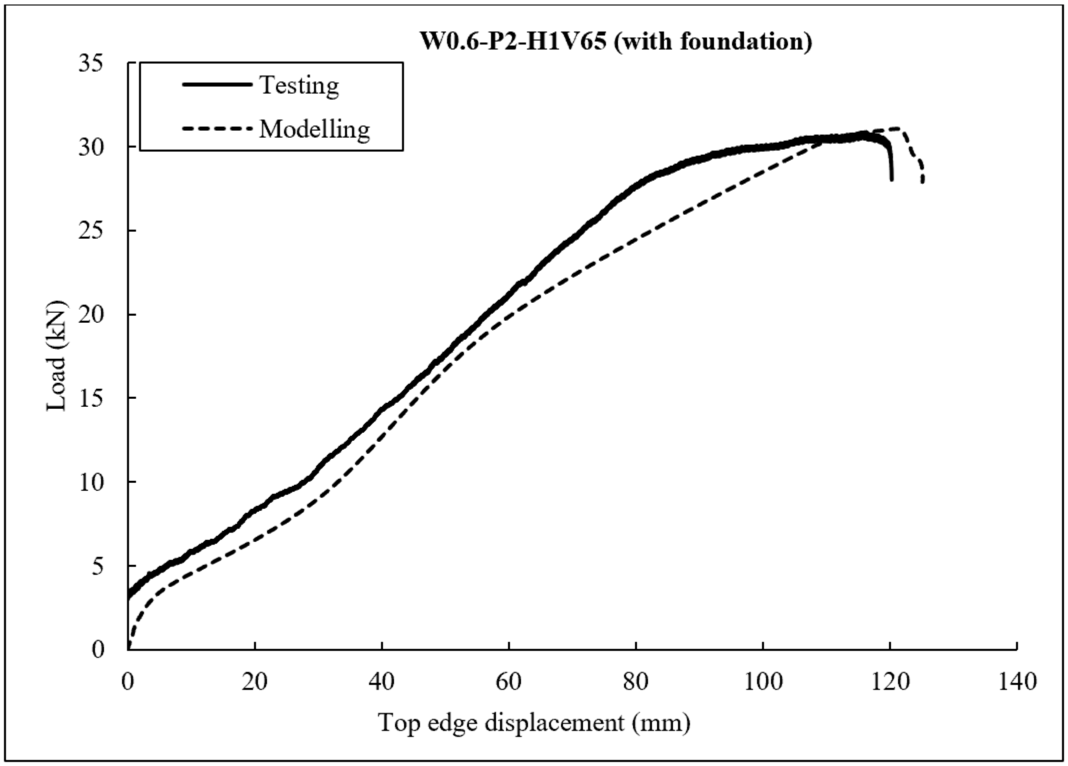
W0.6-P2-H1V65 (with foundation)
Testing
Modelling
Load (kN)
0
5
10
15
20
25
30
35
0
20
40
60
80
100
120
140
Top edge displacement (mm)

(c)

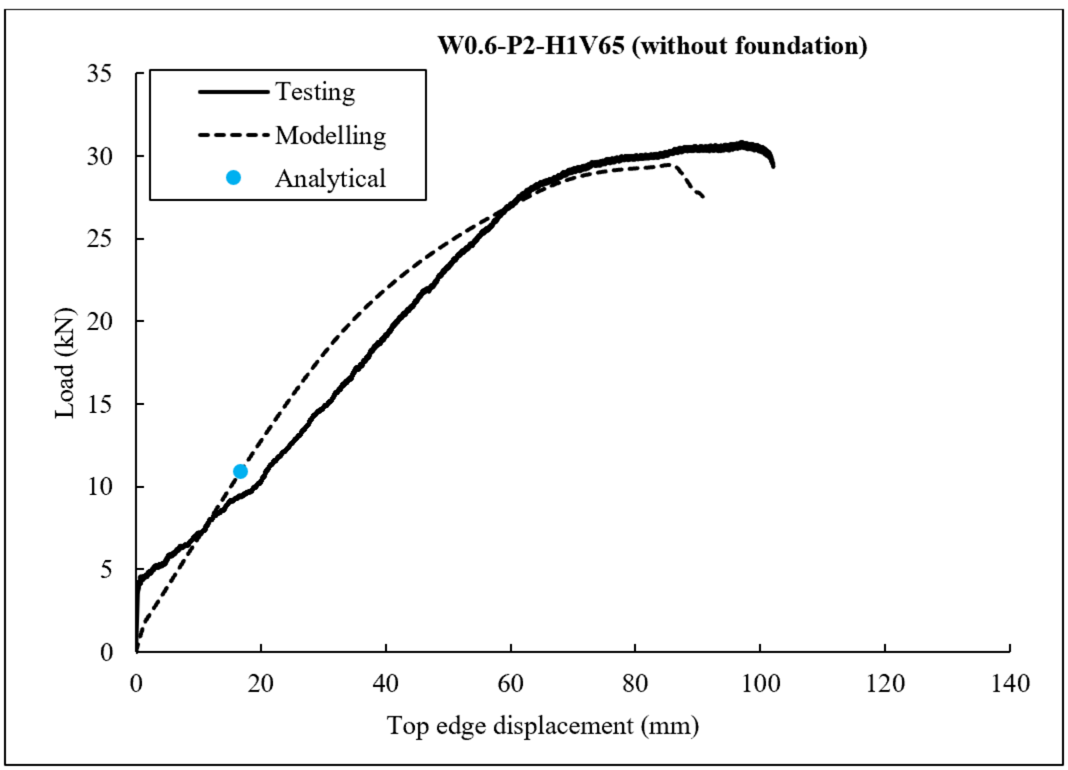
W0.6-P2-H1V65 (without foundation)
Testing
Modelling
Analytical
Load (kN)
0
5
10
15
20
25
30
35
0
20
40
60
80
100
120
140
Top edge displacement (mm)

(d)

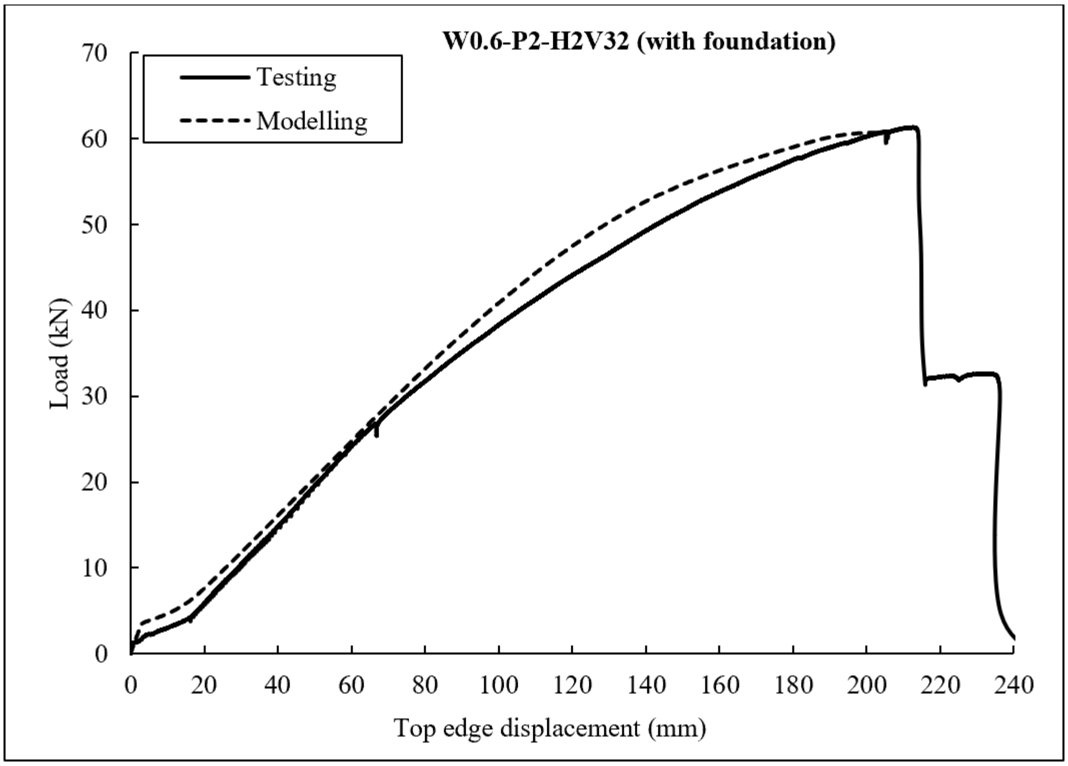
W0.6-P2-H2V32 (with foundation)
Testing
Modelling
Load (kN)
0
10
20
30
40
50
60
70
0
20
40
60
80
100
120
140
160
180
200
220
240
Top edge displacement (mm)

(e)

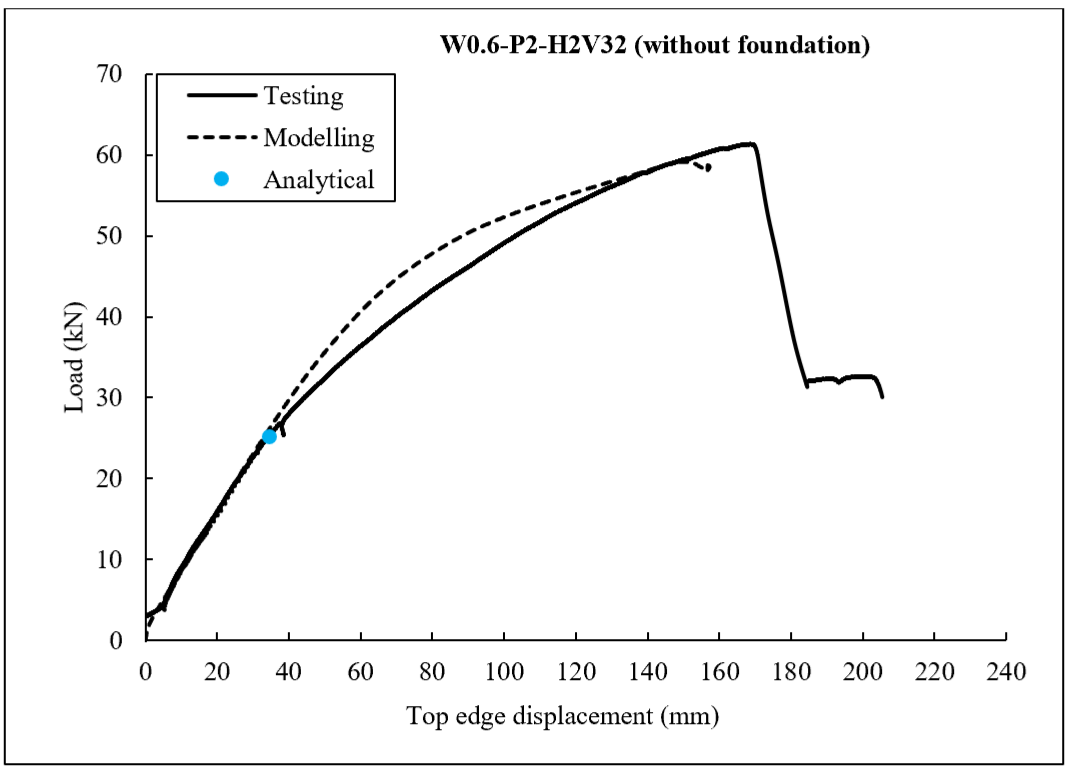
W0.6-P2-H2V32 (without foundation)
Testing
Modelling
Analytical
Load (kN)
0
10
20
30
40
50
60
70
0
20
40
60
80
100
120
140
160
180
200
220
240
Top edge displacement (mm)

(f)

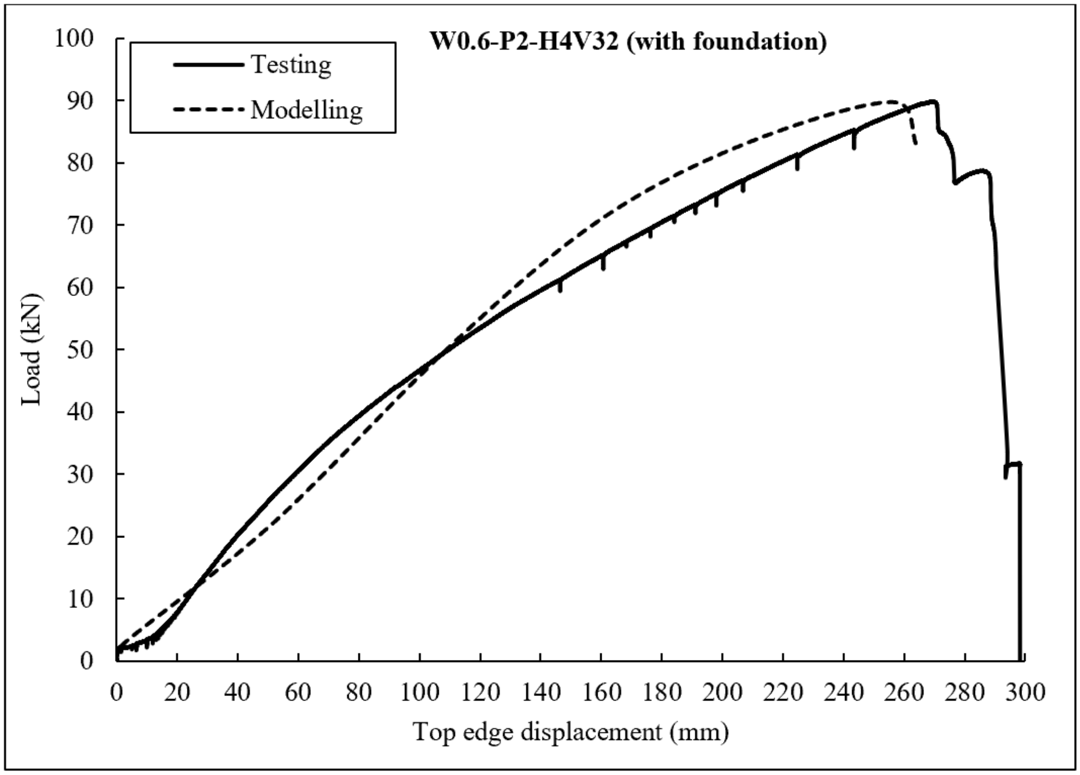

W0.6-P2-H4V32 (with foundation)
Testing
Modelling
Load (kN)
Top edge displacement (mm)
0
10
20
30
40
50
60
70
80
90
100
0
20
40
60
80
100
120
140
160
180
200
220
240
260
280
300

(g)

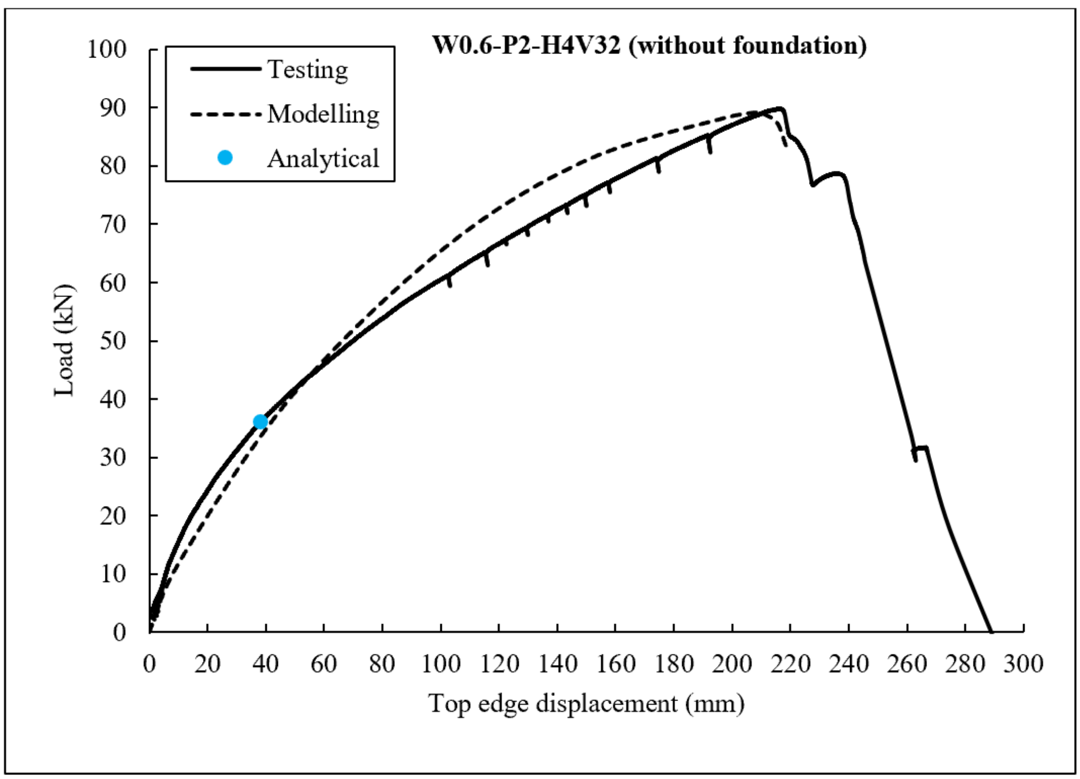

W0.6-P2-H4V32 (without foundation)
Testing
Modelling
Analytical
Load (kN)
Top edge displacement (mm)
0
10
20
30
40
50
60
70
80
90
100
0
20
40
60
80
100
120
140
160
180
200
220
240
260
280
300

(h)

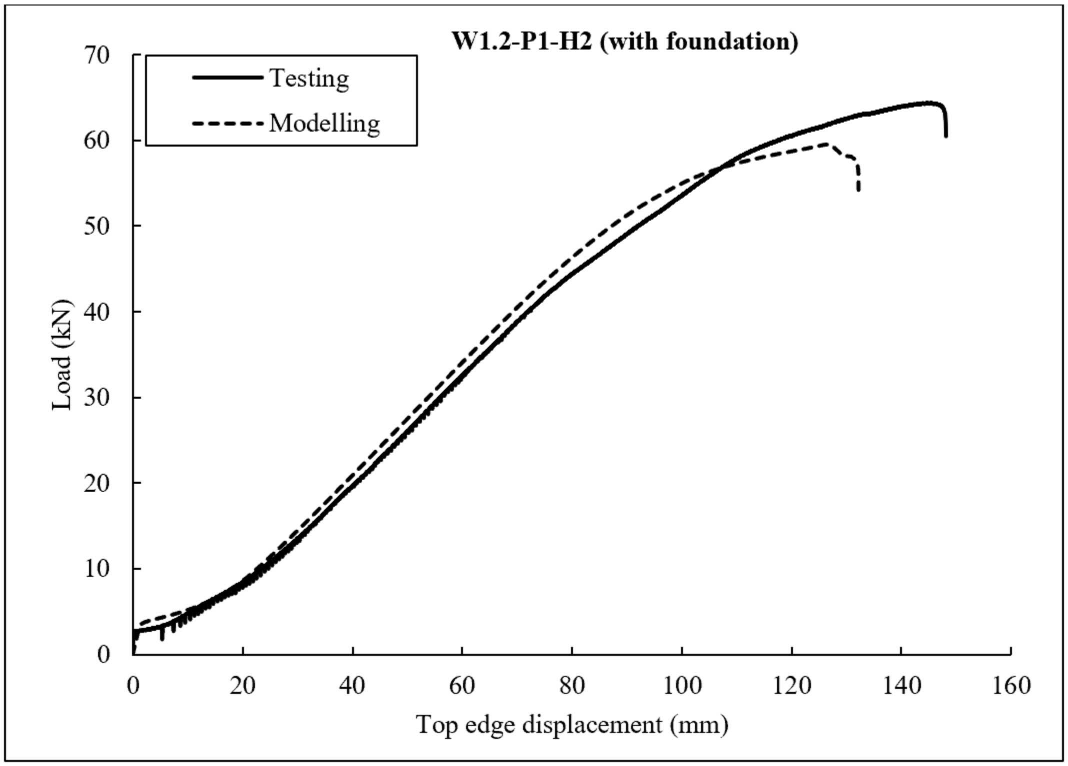
W1.2-P1-H2 (with foundation)
Testing
Modelling
Load (kN)
Top edge displacement (mm)
0
10
20
30
40
50
60
70
0
20
40
60
80
100
120
140
160

(i)

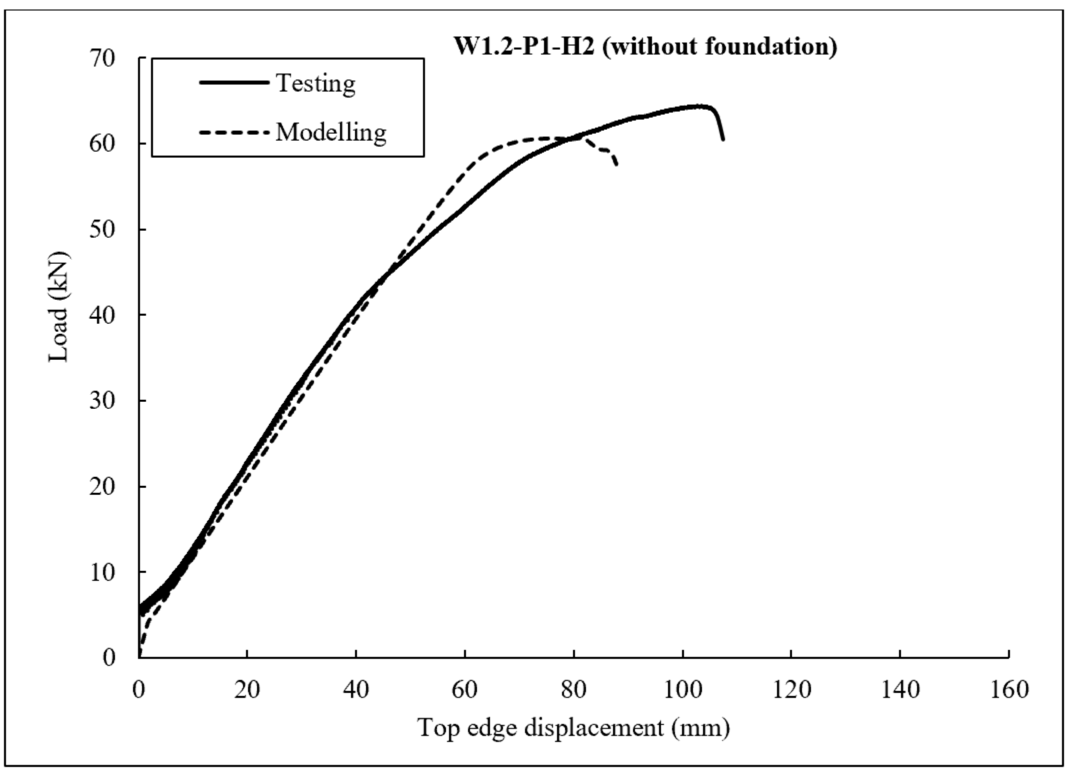
W1.2-P1-H2 (without foundation)
Testing
Modelling
Load (kN)
Top edge displacement (mm)
0
10
20
30
40
50
60
70
0
20
40
60
80
100
120
140
160

(j)

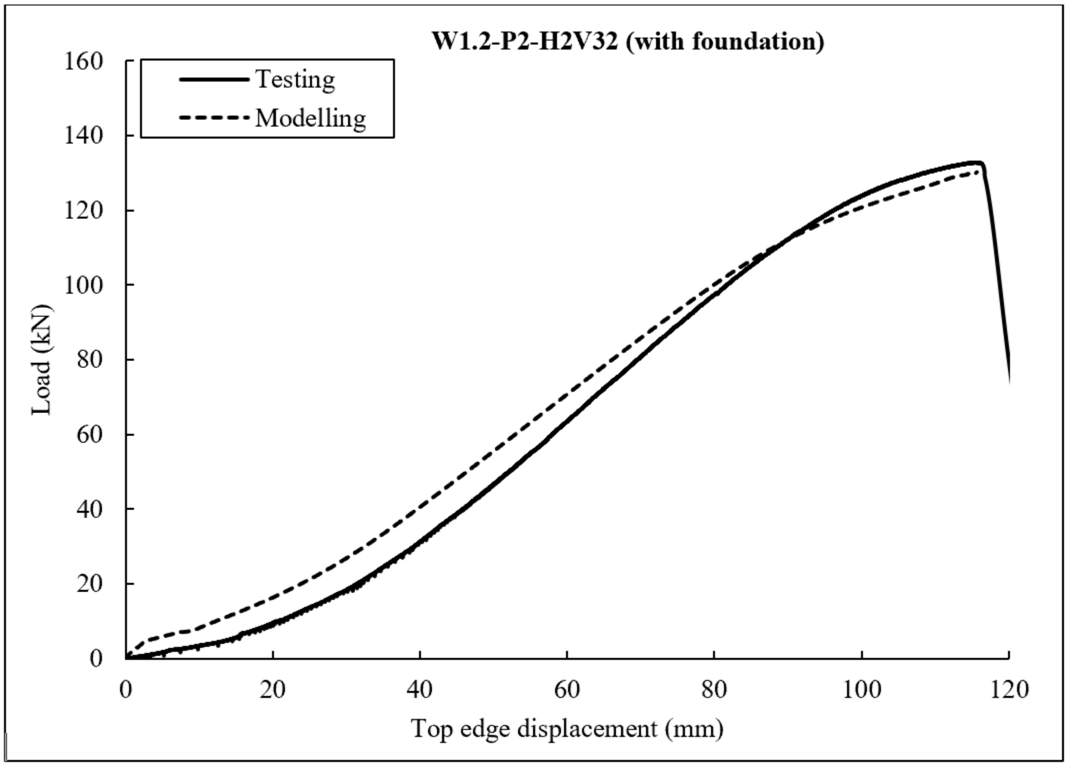
W1.2-P2-H2V32 (with foundation)
Testing
Modelling
Load (kN)
Top edge displacement (mm)
0
20
40
60
80
100
120
140
160

(k)

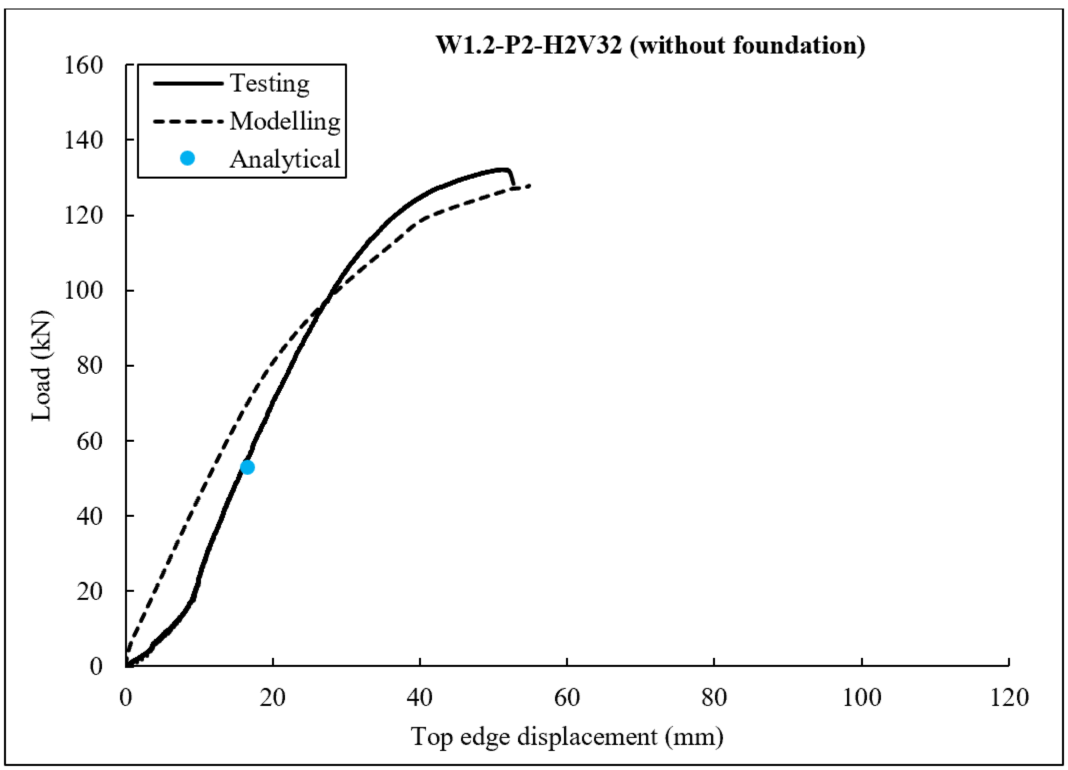
W1.2-P2-H2V32 (without foundation)
Testing
Modelling
Analytical
Load (kN)
Top edge displacement (mm)
0
20
40
60
80
100
120
140
160

(l)

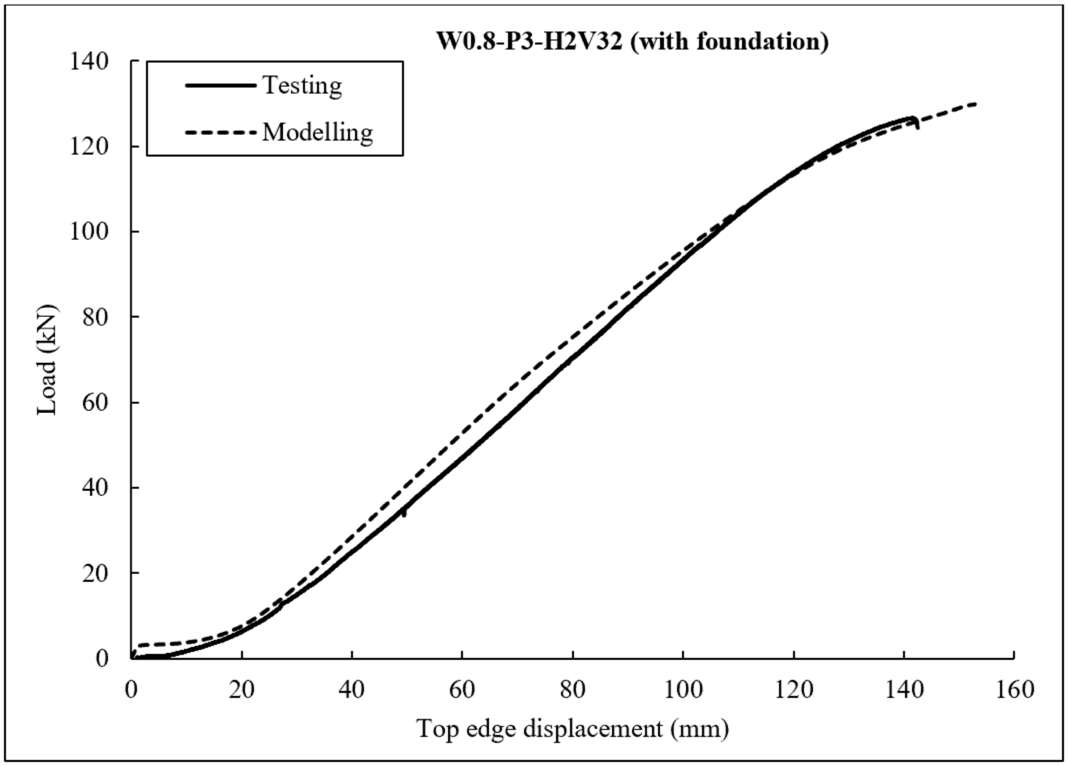
W0.8-P3-H2V32 (with foundation)
Testing
Modelling
Load (kN)
Top edge displacement (mm)
0
20
40
60
80
100
120
140
160

(m)

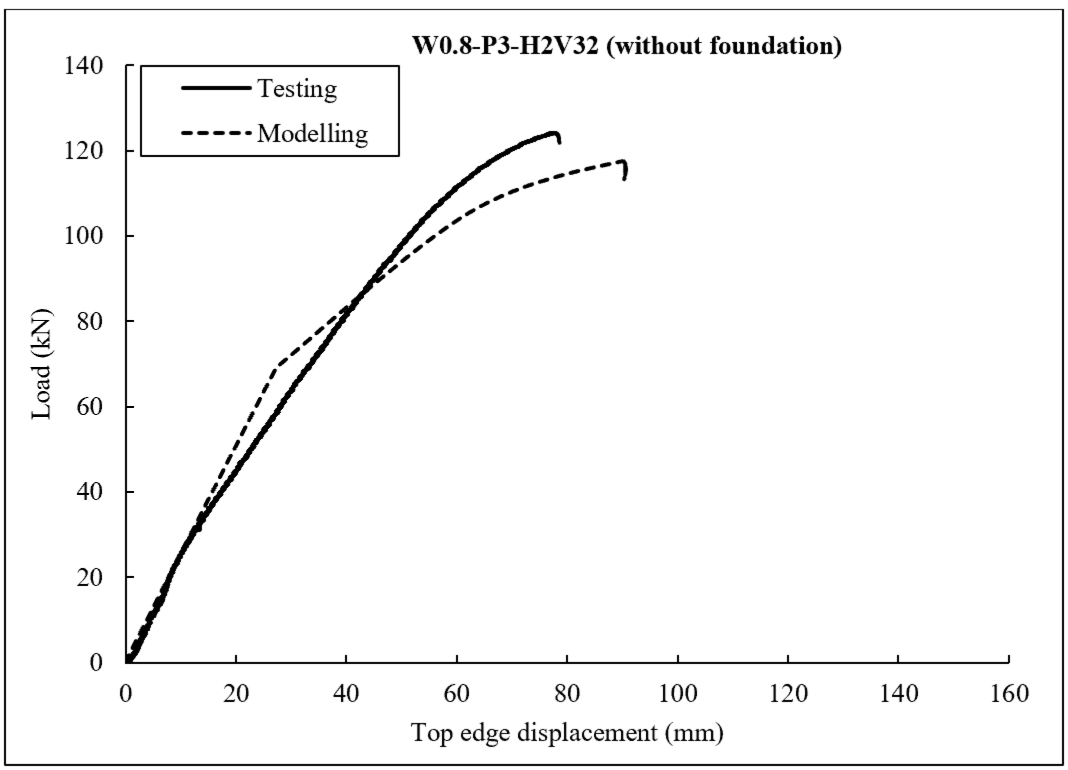
W0.8-P3-H2V32 (without foundation)
Testing
Modelling
Load (kN)
Top edge displacement (mm)
0
20
40
60
80
100
120
140
160

(n)

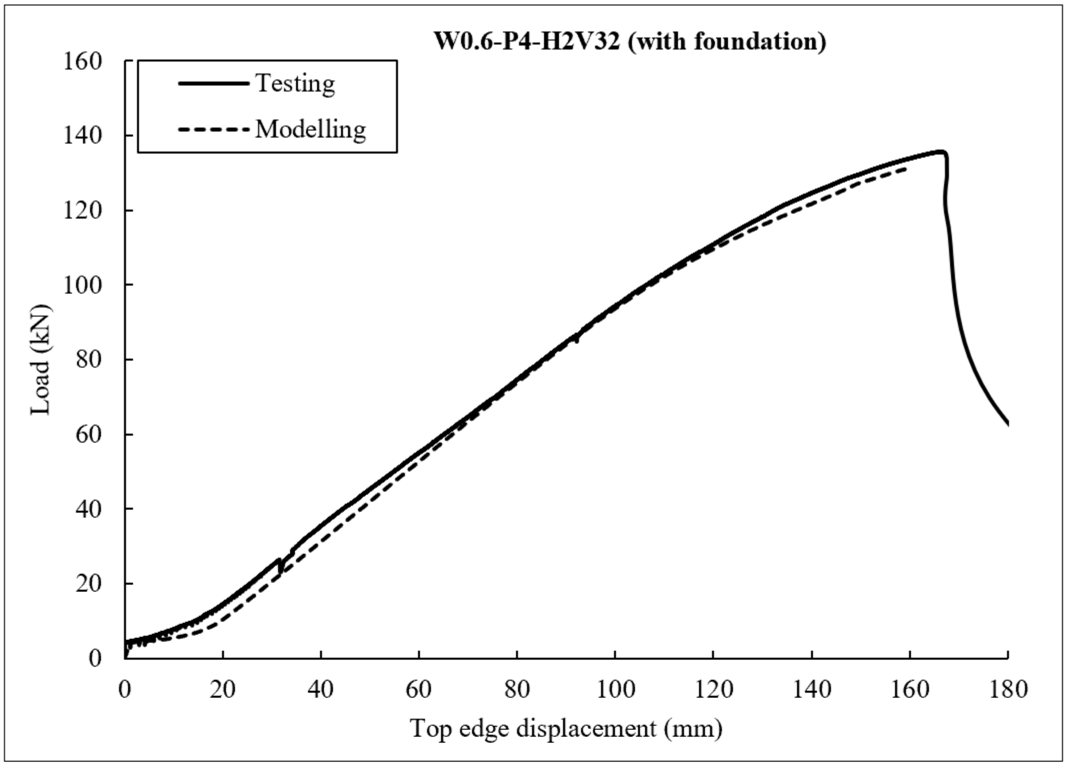
W0.6-P4-H2V32 (with foundation)
Testing
Modelling
Load (kN)
0
20
40
60
80
100
120
140
160
Top edge displacement (mm)
0
20
40
60
80
100
120
140
160
180

(o)

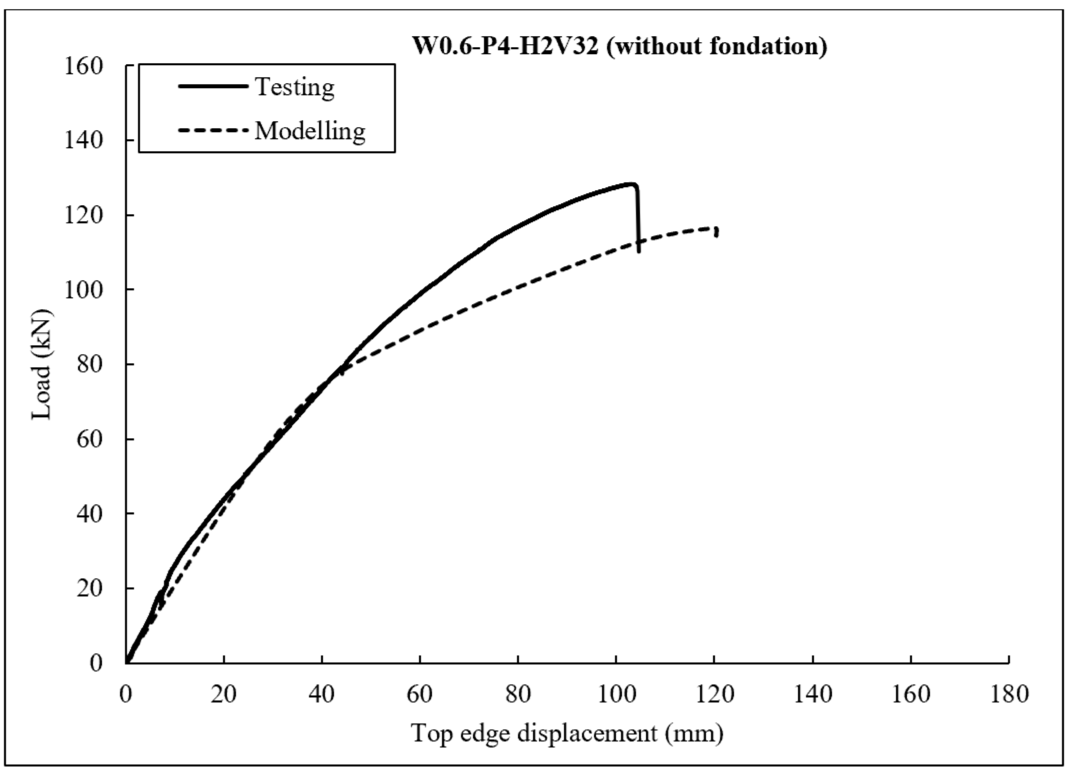
W0.6-P4-H2V32 (without fondation)
Testing
Modelling
Load (kN)
0
20
40
60
80
100
120
140
160
Top edge displacement (mm)
0
20
40
60
80
100
120
140
160
180

(p)

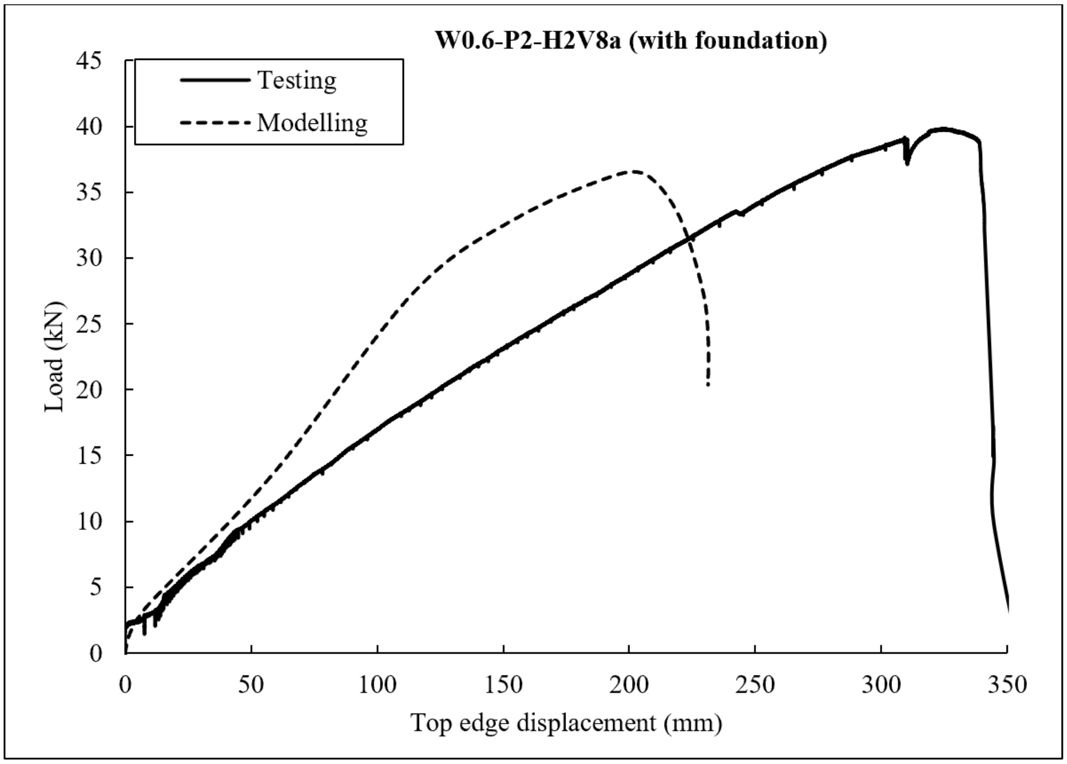

(q)

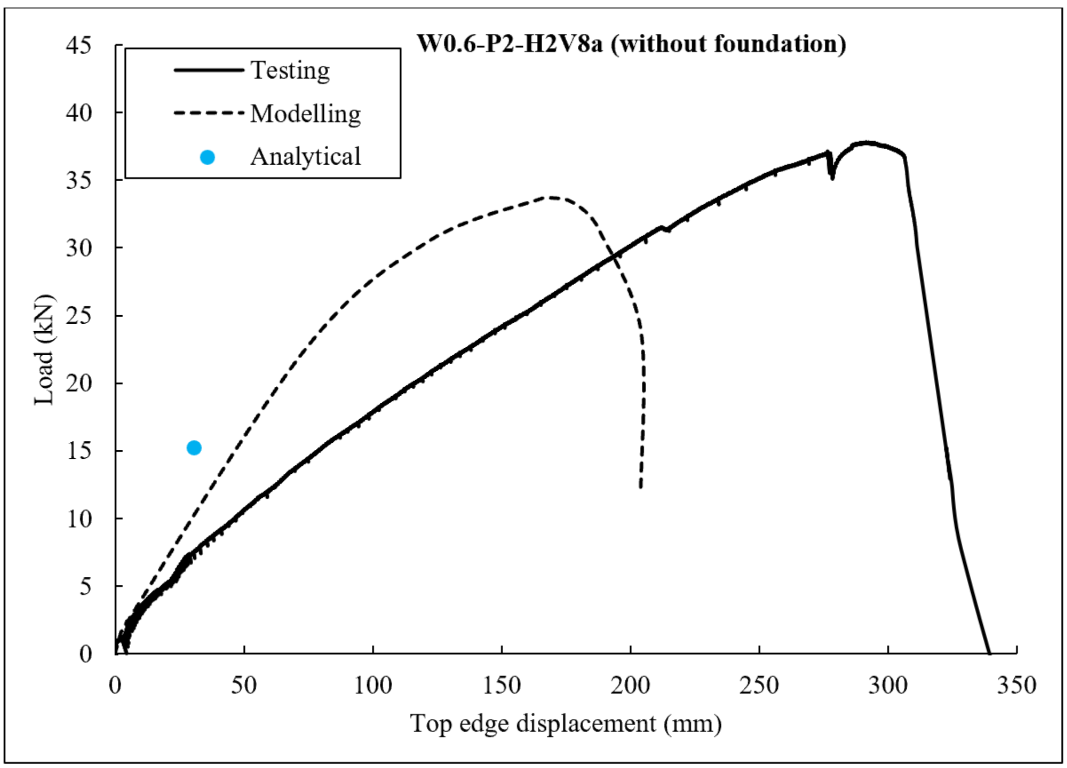

(r)

Figure 6.11: *Comparisons between experimental results, FE numerical modelling and analytical estimation for the tested specimens*

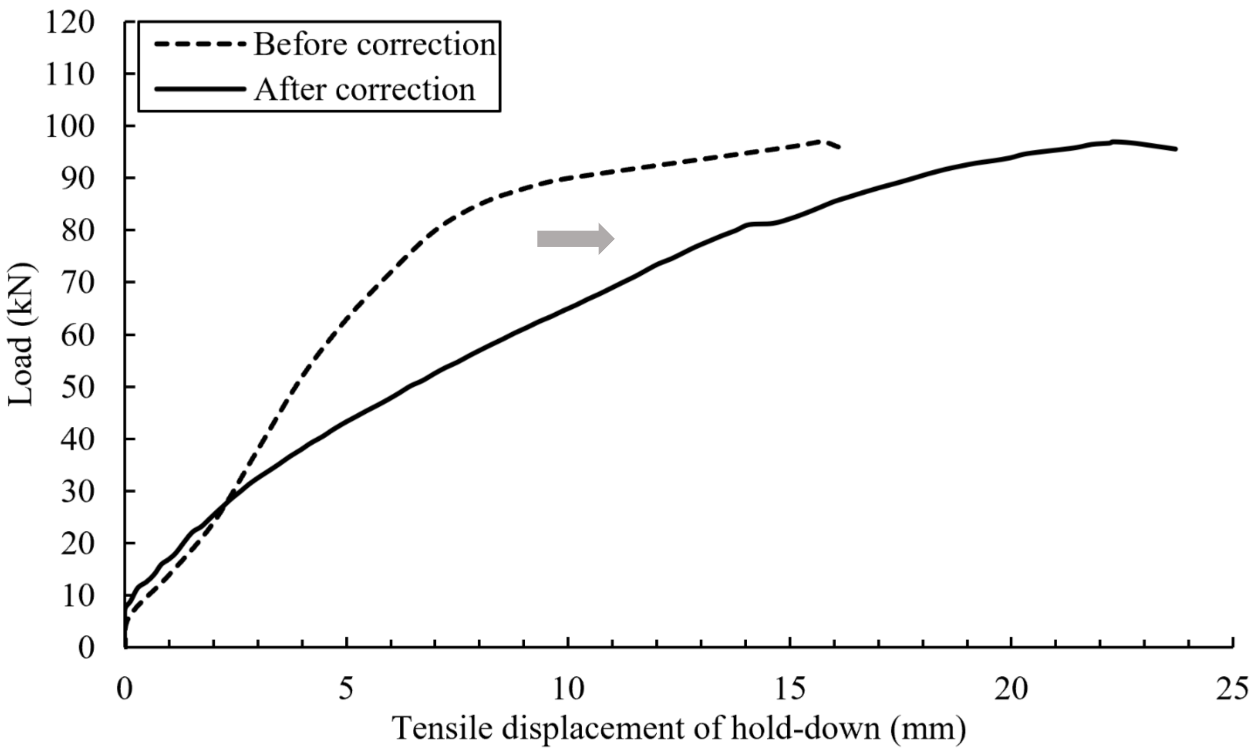
Before correction
After correction
Load (kN)
Tensile displacement of hold-down (mm)
0
10
20
30
40
50
60
70
80
90
100
110
120
0
5
10
15
20
25

(a)

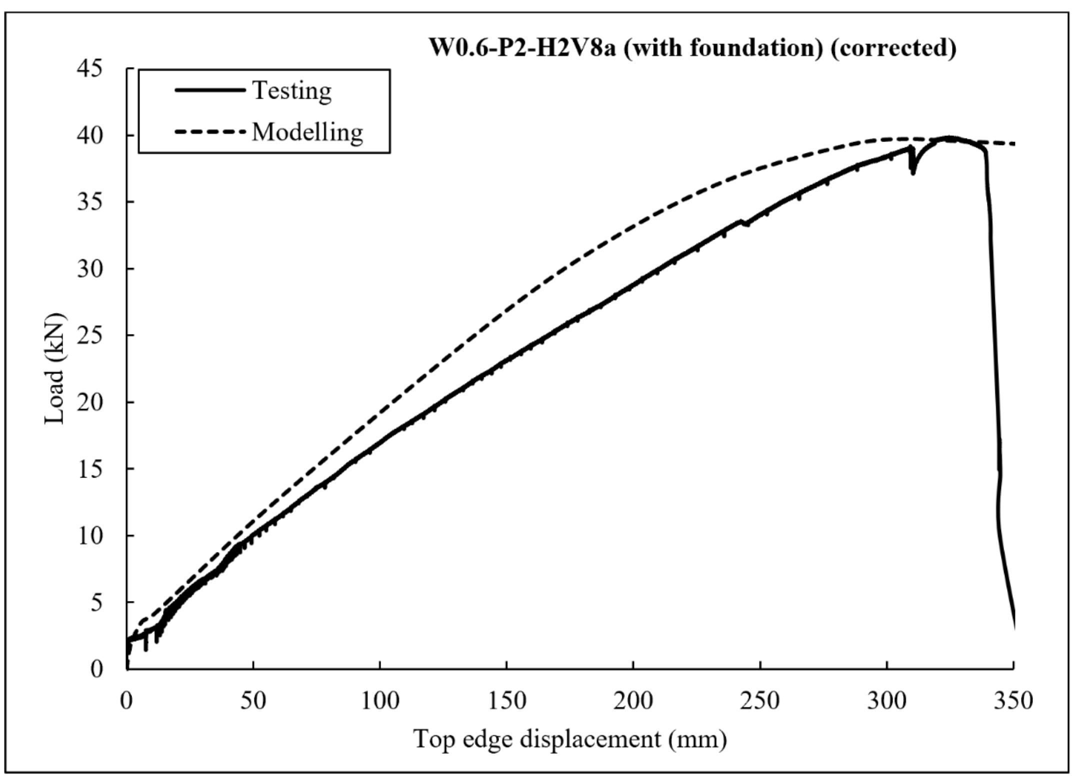
W0.6-P2-H2V8a (with foundation) (corrected)
Testing
Modelling
Load (kN)
Top edge displacement (mm)
0
5
10
15
20
25
30
35
40
45
0
50
100
150
200
250
300
350

(b)

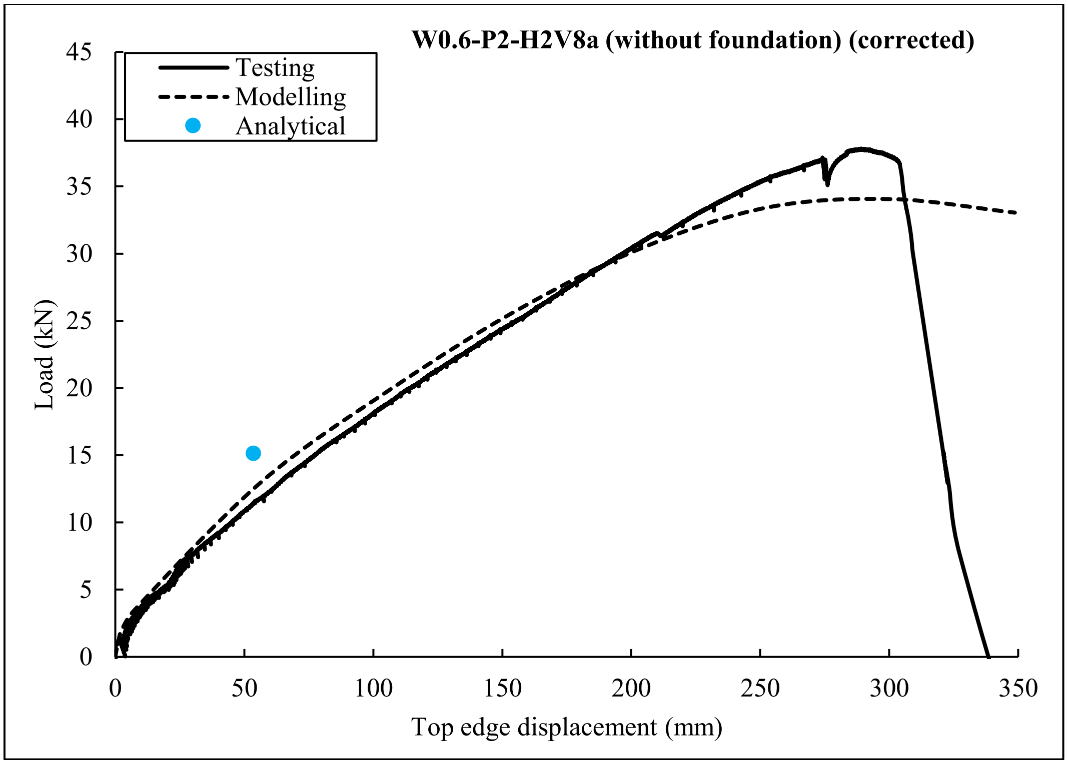

(c)

Figure 6.12: *(a) Corrected hold-down uplift property, and (b) corrected FE modelling curves with foundation and (c) without foundation for specimen W0.6-P2-H2V8a*

Table 6.3: *Comparisons of peak lateral load, corresponding displacement and lateral stiffness of specimens between FE modelling and testing results*

	Peak lateral load F_{max} (kN)		***Error ε (%)***	***Displacement at peak load Δ_{max} (mm)***		***Error ε (%)***	***Stiffness (1) $k_{l,40}$ ($\times 10^{-1}$ kN/mm)***		***Error ε (%)***
	Modelling	***Testing***		***Modelling***	***Testing***		***Modelling***	***Testing***	
W0.6-P2-H1V32	*32.2*	*35.4*	*-9.0*	*88.5*	*126.6*	*-30.0*	*5.1*	*5.6*	*-8.9*
W0.6-P2-H2V32	*59.1*	*61.3*	*-3.6*	*150.5*	*168.7*	*-10.8*	*7.4*	*7.4*	*0.0*
W0.6-P2-H4V32	*89.2*	*89.9*	*-0.7*	*209.2*	*216.3*	*-3.3*	*8.7*	*9.5*	*-8.0*
W1.2-P1-H2	*60.6*	*64.4*	*-5.8*	*81.5*	*99.6*	*-18.2*	*10.0*	*11.2*	*-18.0*
W0.6-P2-H1V65	*29.5*	*30.8*	*-4.3*	*85.2*	*95.6*	*-10.9*	*6.1*	*5.2*	*+16.9*
W1.2-P2-H2V32	*127.9*	*132.1*	*-3.2*	*54.8*	*51.1*	*+7.2*	*41.9*	*33.2*	*+26.1*
W0.8-P3-H2V32	*117.0*	*124.1*	*-5.8*	*90.5*	*77.8*	*+16.3*	*25.4*	*23.3*	*+9.0*
W0.6-P4-H2V32a	*116.5*	*128.3*	*-9.2*	*120.1*	*103.2*	*+16.4*	*19.7*	*20.5*	*-4.2*
W0.6-P2-H2V8a (Corrected k_{hd})	*34.1*	*37.8*	*-9.9*	*300.7*	*289.1*	*+3.8*	*2.3*	*1.9*	*+18.6*

Note: (1) Total lateral stiffness $K_{l,40}$ is calculated according to ASTM-E 2124 (ASTM International, 2019).

CHAPTER SEVEN

CONCLUSIONS AND FUTURE RESEARCH STUDIES

7. Conclusions and future research studies

This chapter presents the main conclusions drawn from the research described in the preceding chapters and outlines recommendations for future research.

7.1. Conclusions

This research provides a systematic investigation of the lateral deformation behaviour and kinematic mechanisms of balloon-type CLT shearwall systems, based on FE numerical, analytical, and experimental approaches. The following conclusions presents key findings related to deformation components, kinematic modes, and their implications for structural performance and design:

- In the sensitivity analysis it was found that a nonlinear relationship between the relative wall stiffness, normalised relative to the stiffness of hold-down or vertical joints, and the hold-down stiffness k_{hd}, was observed for low values of k_{hd}, while reaching an almost linear relationship for high values of k_{hd}. The results indicated that the rocking deformation contribution dominates the behaviour for low values of hold-down stiffness (i.e., flexible hold-down). The transition between SW and CP kinematic mode was strongly influenced by the aspect ratio of the panels.
- The sensitivity analysis further indicated that the influence of hold-down stiffness on the relative wall stiffness follows a trend comparable to that observed for variations in vertical joint stiffness. A significant change in slope is observed when the kinematic mode changes from CP to SW, which can be attributed to the fact that in SW, the contribution of vertical joints is less significant than it is in CP mode.

- Furthermore, the rocking deformation dominates the behaviour for low panel aspect ratios and low values of hold-down and vertical joint stiffness. The percentage of rocking deformation seems to drop significantly when the stiffness of hold-downs or vertical joints increases, particularly in the case of hold-down stiffness increase and slender panels (i.e., panels with high aspect ratios).
- The proposed analytical model was verified against 45 cases implemented in numerical models yielding an average error in the prediction of top lateral displacement of less than 5%.
- The experimental results generally confirmed the observations from the sensitivity analysis, highlighting the significant contribution of bending and shear deformation components to the overall lateral response of balloon-type CLT shearwalls.
- Although rupture of hold-down connections was identified as the dominant failure mechanism in most tested shearwalls, panel cracking governed the failure of two specimens. These observations indicate that the characteristics of CLT, such as the presence of finger joints and the width of individual lumber strips, can play a critical role in determining the overall structural resistance.
- For shearwalls with high panel aspect ratios and high relative stiffness, the uplift demand was unevenly distributed among individual panels. This uneven uplift induced additional bending in the hold-downs, increasing their susceptibility to bending-related failure.
- As lateral loading increased, degradation of connector stiffness promoted a progressive shift in kinematic behaviour from CP mode towards SW mode, accompanied by an increasing contribution of rocking deformation across all tested shearwalls.

- For a fixed total wall width, the use of slenderer CLT panels enhances lateral deformation capacity without compromising lateral strength, thereby improving the ductility of balloon-type shearwalls and offering a favourable design strategy for seismic applications.

7.2. Future research studies

Based on the findings of the present research, several directions for future study are identified and suggested as follows:

- Extension of analytical models to multi-panel configurations: although balloon-type CLT shearwalls comprising more than two panels were investigated through full-scale testing and FE modelling in this study, the corresponding analytical formulations have not yet been fully established. Future research is therefore recommended to extend the proposed analytical framework to multi-panel shearwall configurations, enabling a more comprehensive analysis about bending deformation and deformation compatibility among panels. In addition, the analytical model could be further developed to explicitly account for vertical anchorage systems that lengthen shearwall panels and transfer forces along the height of the structure, which are commonly adopted in practical applications but were not explicitly addressed in the current analytical formulation. Furthermore, the impact of uneven uplifts of panels and different load patterns also needs to be considered in future models.
- Consideration of system-level and three-dimensional structural effects: in the present study, shearwalls were analysed as isolated structural systems in order to focus on their fundamental lateral deformation and kinematic behaviour. However, in real buildings, the response of CLT shearwalls is influenced by interactions with surrounding structural

components, such as floor diaphragms and transverse walls. Future studies should therefore investigate balloon-type CLT shearwalls within a three-dimensional structural context, for example by analysing box-type configurations that account for wall-to-wall and wall-to-floor interactions, to better capture global resistance mechanisms and deformation characteristics.

- Investigation under cyclic loading conditions: the loading protocol adopted in this research was monotonic, consistent with pushover analysis objectives to evaluate lateral resistance and deformation mechanisms. Nevertheless, it is well recognised that the seismic performance of shearwall systems needs to be better evaluated by their cyclic response, including strength degradation, ductility, and energy dissipation capacity. Future experimental and numerical investigations should therefore focus on cyclic loading protocols to evaluate the hysteretic behaviour of balloon-type CLT shearwalls and to support the development of performance-based seismic design provisions.

References

AIJ (2018). *Standard for Structural Design of Timber Structures*. Architectural Institute of Japan, Tokyo.

American Wood Council (2021) *Special Design Provisions for Wind and Seismic (SDPWS-2021)*. Leesburg, VA: American Wood Council.

Amini, M.O. (2018). 'Evaluation of Seismic Performance of CLT Shear Wall Connections Using Different Fasteners'. Master's Thesis. University of Ottawa.

ANSI/APA (2021). *ANSI/APA PRG 320: Standard for Performance-Rated Cross-Laminated Timber*. Tacoma, WA: APA – The Engineered Wood Association.

ASTM International (2019). ASTM E2124-19: *Standard Test Methods for Cyclic (Reversed) Load Test for Shear Resistance of Framed Walls for Buildings*. West Conshohocken, PA: ASTM International.

Bejtka, I. and Lam, F. (2008). 'Cross laminated timber – A design approach', *Proceedings of the 10th World Conference on Timber Engineering (WCTE)*, Miyazaki, Japan.

Blass, H.J. and Fellmoser, P. (2004). 'Design of solid wood panels with cross layers', *Proceedings of the 8th World Conference on Timber Engineerin g (WCTE)*, Lahti, Finland.

Bogensperger, T., Moosbrugger, T. and Schickhofer, G. (2010). 'New design model for CLT and application with connections', *Proceedings of the 11th World Conference on Timber Engineering (WCTE)*, Riva del Garda, Italy.

Brandner, R., Flatscher, G., Ringhofer, A., Schickhofer, G. and Thiel, A. (2017). 'Cross laminated timber (CLT): overview and development’, *European Journal of Wood and Wood Products*, 74(3), pp. 331–351. https://doi.org/10.1007/s00107-015-0999-5

Casagrande, D., Piazza, M., Tomasi, R. and Polastri, A. (2018). ‘Coupled-panel behaviour of cross-laminated timber (CLT) walls: Experimental and numerical investigations’, *Construction and Building Materials*, 169, pp. 694–707.

Casagrande, D., Polastri, A. and Piazza, M. (2016). ‘Modelling cross-laminated timber structures: a refined FE model for diaphragm action’, *Engineering Structures*, 125, pp. 548–564.

Casagrande, D., Pozza, L., Ceccotti, A. and Fragiacomo, M. (2020). ‘Low-cycle fatigue strength of timber connections under seismic loading’, *Engineering Structures*, 211, 110454. https://doi.org/10.1016/j.engstruct.2020.110454

Casagrande, D., Pozza, L., Ceccotti, A. and Polastri, A., (2020). ‘Evaluation of seismic low-cycle fatigue strength of timber connections’. *Engineering Structures*, 206, p.110141.

Ceccotti, A. (2008). ‘New technologies for construction of medium-rise buildings in seismic regions: the XLAM case’, *Structural Engineering International*, 18(2), pp. 156–165.

Ceccotti, A. and Follesa, M. (2006). ‘Which seismic behaviour factor for multi-storey buildings made of cross-laminated wooden panels?’, *Proceedings of the 39th CIB-W18 Meeting*, Florence, Italy.

Ceccotti, A., Sandhaas, C., Okabe, M. and Yasumura, M. (2013). ‘SOFIE project–3D shaking table test on a seven-storey full-scale cross-laminated timber building’, *Structures and Buildings*, 166(3), pp. 161–171.

Ceccotti, A., Sandhaas, C., Yasumura, M., Minowa, C. and Okabe, M. (2010). ‘Seismic performance of X-Lam buildings: the Italian SOFIE project', *Proceedings of the World Conference on Timber Engineering*, Riva del Garda, Italy.

CEN (2004). *EN 1995-1-1 Eurocode 5: Design of Timber Structures – Part 1-1: General – Common Rules and Rules for Buildings*. Brussels: European Committee for Standardization.

CEN (2025). *prEN 1995-1-1:2025 – Eurocode 5: Design of Timber Structures – Part 1-1: General – Common Rules and Rules for Buildings (Draft for Second Generation)*. Brussels: European Committee for Standardization.

Chen, C., Popovski, M. and Tannert, T. (2018). 'Structural performance of post-tensioned CLT shear walls with energy dissipators', *Journal of Structural Engineering*, 144(10), 04018188.

Chen, Z. and Popovski, M. (2020). 'Mechanics-based analytical models for balloon-type cross-laminated timber (CLT) shearwalls', *Engineering Structures*, 208, 109916.

Costa, A.C., Dias, A.M.P.G. and Frangi, A. (2013). 'Experimental tests on a three-storey XLAM building', *Proceedings of the 11th World Conference on Timber Engineering (WCTE 2013)*, Trentino, Italy.

CSA Group (2024). *CSA O86:24 - Engineering Design in Wood*. Mississauga, ON: CSA Group.

Dickof, C., Shahnewaz, M. and Tannert, T. (2020). 'Experimental evaluation of ledger connections in balloon-type CLT walls', *Construction and Building Materials*, 254, 119206.

Dires, A. and Tannert, T. (2022). 'Performance of CLT walls with internal perforated steel plate joints under monotonic and cyclic loads', *Construction and Building Materials*, 328, 127055.

Dujic, B., Pucelj, J. and Zarnic, R. (2006). 'Experimental investigation of massive wooden wall panel systems subjected to seismic excitation', *Proceedings of the First European Conference on Earthquake Engineering and Seismology (ECEES)*.

Dunbar, A., Bregulla, J. and Buchanan, A. (2014). 'Timber core-walls for lateral load resistance of multi-storey timber buildings', *Australian Journal of Structural Engineering*, 15(2), pp. 133–140.

Fragiacomo, M., Dujic, B. and Sustersic, I. (2011). 'Elastic and ductile design of multi-storey cross-laminated timber buildings under seismic actions', *Bulletin of the New Zealand Society for Earthquake Engineering*, 44(3), pp. 195–206.

Gavric, I., Fragiacomo, M. and Ceccotti, A. (2013). 'Cyclic behaviour of typical metal connectors for cross-laminated (CLT) structures', *Materials and Structures*, 48, pp. 1841–1857.

Gavric, I., Frangi, A. and Wüest, J. (2015a). 'Experimental and numerical seismic analysis of CLT structures', *Journal of Structural Engineering*, 141(11), 04015030. https://doi.org/10.1061/(ASCE)ST.1943-541X.0001272

Gavric, I., Frangi, A. and Wüest, J. (2015b). 'Component and system testing of cross-laminated timber structures under seismic loading', *Bulletin of Earthquake Engineering*, 13(5), pp. 1403–1422.

Hashemi, A., Masroor, A. and Tesfamariam, S. (2017). 'Seismic performance of timber shear wall systems with resilient slip friction joints', *Construction and Building Materials*, 134, pp. 369–382. https://doi.org/10.1016/j.conbuildmat.2016.12.101

Hashemi, A., Masroor, A. and Tesfamariam, S. (2018). 'Design and analysis of slip friction joints in timber buildings', *Engineering Structures*, 165, pp. 36–47. https://doi.org/10.1016/j.engstruct.2018.03.033

Hashemi, A., Quenneville, P. and Fragiacomo, M. (2017). 'Resilient slip friction (RSF) joints used as wall panel connections in multi-storey timber buildings', *Construction and Building Materials*, 150, pp. 548–556.

Hashemi, A., Quenneville, P. and Fragiacomo, M. (2018). 'Seismic performance of resilient slip friction joints in timber buildings', *Earthquake Engineering & Structural Dynamics*, 47(12), pp. 2437–2455.

Hayes, C., Chui, Y.H. and Hu, L. (2023). 'Seismic behavior of balloon frame cross-laminated timber connections', *Journal of Structural Engineering*, 149(7), 04023078. https://doi.org/10.1061/(ASCE)ST.1943-541X.0003420

Hossain, A., Beji, S. and Tesfamariam, S. (2015). 'In-plane shear performance of CLT connections: A state-of-the-art review', *Construction and Building Materials*, 101, pp. 112–121. https://doi.org/10.1016/j.conbuildmat.2015.10.025

Hristovski, V., Smith, I. and Ceccotti, A. (2013). 'Full-scale shaking-table tests of XLam panel systems and numerical verification–specimen 1', *Journal of Structural Engineering*, 139(10), pp. 1753–1761.

Hummel, J., van de Kuilen, J.W.G. and Ceccotti, A. (2013). 'CLT wall elements under cyclic loading – details for anchorage and connection', *Proceedings of the 11th World Conference on Timber Engineering (WCTE 2013)*, Trentino, Italy.

International Organization for Standardization (2010). *ISO 21581:2010 Timber structures — Static and cyclic lateral load test methods for shear walls*. Geneva: ISO.

Izzi, M., Polastri, A. and Pozza, L. (2018). 'Numerical modeling of CLT wall-to-floor joints subjected to cyclic loads', *Engineering Structures*, 160, pp. 73–86. https://doi.org/10.1016/j.engstruct.2018.01.029

Izzi, M., Polastri, A. and Fragiacomo, M. (2018). 'Numerical modelling of cross-laminated timber (CLT) structures: Overview and future research needs', *Engineering Structures*, 180, pp. 405–423.

Jafari, A., Shen, Y., Pan, Y. and Tannert, T. (2022). 'Effects of ground motion duration on the seismic performance of a two-storey balloon-type CLT building', *Engineering Structures*, 253, 113702.

Karacabeyli, E. and Gagnon, S. (2019). *CLT Handbook: Cross-Laminated Timber*. 2nd edn. Pointe-Claire, QC: FPInnovations.

Khajehpour, M., Casagrande, D. and Doudak, G. (2022). 'The role of lintels and parapets on the mechanical performance of multi-storey cross laminated timber shearwalls with openings'. *Engineering structures.* [Online] 255.

Khajehpour, M. Casagrande, D., Doudak, G., Gupta, R., Ng, K.T.W., Sun, M., Lim, C., Alam, M.S., El Damatty, A., Li, J. and Brzev, S. (2023). 'Investigating the Influence of Openings on the Mechanical Performance of Cross-Laminated Timber Shearwalls', *in Proceedings of the Canadian Society of Civil Engineering Annual Conference 2022.* [Online]. Switzerland: Springer. pp. 281–292.

Krauss, D., Popovski, M. and Casagrande, D. (2024). ‘Experimental and numerical investigation of the cyclic behaviour of coupled balloon-type CLT shear walls with high-capacity base connections’, *Engineering Structures*, 297, 116641.

Li, Z., Wang, Q. and He, M. (2020). ‘Comparative study of platform-type and balloon-type CLT shear walls under cyclic loading’, *Journal of Building Structures*, 41(6), pp. 78–85.

Li, Z., Wang, Y. and He, M. (2020). ‘Experimental and analytical study on balloon-type and platform-type cross-laminated timber (CLT) shear walls’, *Construction and Building Materials*, 261, 120506.

Loo, W.Y.H., Quenneville, P. and Chouw, N. (2014a). ‘A numerical study of a slip-friction connector for timber shear walls under seismic loading’, *Engineering Structures*, 59, pp. 320–333. https://doi.org/10.1016/j.engstruct.2013.10.040

Loo, W.Y.H., Quenneville, P. and Chouw, N. (2014b). ‘Cyclic performance of high-capacity slip friction connections for timber buildings’, *Construction and Building Materials*, 72, pp. 421–428. https://doi.org/10.1016/j.conbuildmat.2014.09.004

Masroor, A., Hashemi, A. and Tesfamariam, S. (2024). ‘Experimental study on hold-down and bracket connections in CLT shear walls for capacity-based design’, *Construction and Building Materials*, 406, 132688. https://doi.org/10.1016/j.conbuildmat.2023.132688

Masroor, A., Mohammad, M., Tesfamariam, S. and Goda, K. (2020). ‘The effect of bi-axial behaviour of mechanical anchors on the lateral response of multi-panel CLT shearwalls’, *Engineering Structures*, 224, 111202.

Masroor, A., Mohammad, M., Tesfamariam, S. and Goda, K. (2021). ‘Design of multipanel CLT shearwalls with bidirectional mechanical anchors following capacity-based design principle', *Engineering Structures*, 243, 112699.

Masroor, A., Popovski, M. and Tannert, T. (2024). 'Experimental parameter study of two-story platform-type CLT shear walls', *Engineering Structures*, 297, 117195.

Mestek, P., Kreuzinger, H. and Winter, S. (2008). 'Design of cross laminated timber (CLT)', *Proceedings of the 10th World Conference on Timber Engineering (WCTE)*, Miyazaki, Japan.

Ministry of Housing and Urban-Rural Development of the People's Republic of China (MHURD) (2012). *Technical code of glued laminated timber structures (GB/T 50708-2012)*, Beijing: China Architecture & Building Press.

Ministry of Housing and Urban-Rural Development of the People's Republic of China (MHURD) (2017). *Standard for design of timber structures (GB 50005-2017),* Beijing: China Architecture & Building Press.

Nolet, V., Casagrande, D. and Doudak, G. (2019) 'Multipanel CLT shearwalls: An analytical methodology to predict the elastic–plastic behaviour', *Engineering Structures*, 179, pp. 640–654. https://doi.org/10.1016/j.engstruct.2018.11.017

Pan, Y., Jafari, A. and Tannert, T. (2023a). 'Seismic performance and collapse fragility of balloon-framed CLT school building', *Engineering Structures*, 276, 115231.

Pan, Y., Jafari, A. and Tannert, T. (2023b). 'Seismic performance evaluation of self-centering balloon-framed CLT building', *Journal of Structural Engineering*, 149(6), 04023070.

Pei, S., van de Lindt, J.W. and Popovski, M. (2012). 'Seismic design of a multi-story cross-laminated timber building based on component level testing', *Journal of Earthquake Engineering*, 16(9), pp. 1407–1423.

Pei, S., van de Lindt, J.W., Popovski, M. and Berman, J.W. (2019). 'Response of a resilient 2-story mass-timber building with post-tensioned rocking walls', *Engineering Structures*, 183, pp. 533–543.

Pei, S., van de Lindt, J.W., Popovski, M., Dolan, J.D. and Line, P. (2012). 'Performance-based design and force modification factors for CLT structures', *Proceedings of the World Conference on Timber Engineering*, Auckland, New Zealand.

Pei, S., van de Lindt, J.W., Popovski, M. and Dolan, J.D. (2013). 'Approximate R-factor for cross laminated timber walls in multistory buildings', *Journal of Architectural Engineering*, 19(4), pp. 245–255.

Pei, S., van de Lindt, J.W., Popovski, M., Dolan, J.D., Ricles, J.M. and Sause, R. (2013). 'Analytical study on seismic force modification factors for cross-laminated timber buildings', *Journal of Structural Engineering*, 139(4), pp. 653–661.

Pei, S., van de Lindt, J.W. and Popovski, M. (2018). 'Full-scale shake table test of a two-story mass-timber building with resilient rocking walls', *Journal of Structural Engineering*, 144(5), 04018032.

Polastri, A. and Casagrande, D. (2022). 'Mechanical behaviour of multi-panel cross laminated timber shear-walls with stiff connectors', *Engineering Structures*, 258, 114014.

Polastri, A., Casagrande, D., Piazza, M. and Tomasi, R. (2019). 'Numerical modelling of cross-laminated timber structures with ductile connections under seismic loading', *Engineering*

Structures, 188, pp. 454–470.

Popovski, M., Schneider, J. and Schweinsteiger, M. (2010). ‘Lateral load resistance of cross-laminated wood panels’, *Proceedings of the 11th World Conference on Timber Engineering (WCTE2010)*, Trentino, Italy.

Pozza, L., Casagrande, D. and Polastri, A. (2018). ‘Axial-shear interaction in CLT hold-down connections: Experimental results and mechanical interpretation’, *Construction and Building Materials*, 191, pp. 574–586.

Pozza, L., Casagrande, D., Tomasi, R. and Piazza, M. (2016). ‘Experimental tests and numerical modelling of connections for cross-laminated timber buildings’, *Engineering Structures*, 127, pp. 512–529.

Pozza, L. and Trutalli, D. (2017). ‘Numerical assessment of a new high-performance timber connection system for seismic areas’, *Construction and Building Materials*, 140, pp. 193–205.

Pulgar, F., Sandhaas, C., Frangi, A. and Fontana, M. (2018). ‘Damping characteristics and ductility capacity of timber wall joint configurations’, *Engineering Structures*, 172, pp. 198–208.

Pulgar, J., Pei, S., Popovski, M. and van de Lindt, J.W. (2018). ‘Seismic energy dissipation and damping in tall CLT buildings’, *Journal of Structural Engineering*, 144(5), 04018027.

Rinaldin, G. and Fragiacomo, M. (2016). ‘Modelling of connections for cross-laminated timber structures’, *Engineering Structures*, 127, pp. 277–294.

Schneider, J., Schweinsteiger, M. and O’Ceallaigh, C. (2012). ‘Damage assessment of cross laminated timber connections subjected to simulated earthquake loads’, *World Conference* *on Timber Engineering*, Auckland, New Zealand.

Shahnewaz, M., Dickof, C. and Tannert, T. (2017). 'In-plane stiffness of cross-laminated timber panels with openings', *Construction and Building Materials*, 146, pp. 452–463.

Shahnewaz, M., Dickof, C. and Tannert, T. (2021). 'Performance of ledger-supported balloon-type CLT walls under lateral loading', *Journal of Structural Engineering*, 147(12), 04021193.

Shen, Y., Popovski, M., Tannert, T. and Smith, I. (2013). 'Analysis of CLT wall systems with flexible hold-downs', *World Conference on Timber Engineering*, Auckland, New Zealand.

Standards Australia (2010). *AS 1720.1: Timber Structures – Design Methods*. Sydney: Standards Australia.

Sustersic, I., Dujic, B., Fragiacomo, M. and Ceccotti, A. (2016). 'Seismic analysis of cross-laminated multistory timber buildings using code-prescribed methods: influence of panel size, connection ductility, and schematization', *Engineering Structures*, 125, pp. 386–397.

Tamagnone, G. and Fragiacomo, M. (2018). 'An analytical method for the calculation of rocking behaviour of cross-laminated timber shear walls', *Engineering Structures*, 173, pp. 905–917.

Tomasi, R. and Smith, I. (2015). 'Capacity design for CLT structures under seismic loads', *Proceedings of the 12th World Conference on Timber Engineering (WCTE)*, Quebec City, Canada.

Trutalli, D., Agheshlui, H., Fragiacomo, M. and Pizzi, A. (2019). 'Development of a ductile X-bracket connector for CLT structures', *Construction and Building Materials*, 195, pp. 398–411.

Trutalli, D., Tomasi, R. and Piazza, M. (2019). 'Development and experimental testing of X-bracket: A novel connector for CLT walls', *Engineering Structures*, 191, pp. 252–263.

Van de Lindt, J.W., Pei, S., Popovski, M., Berman, J.W. and Dolan, J.D. (2018). 'Seismic performance factors for cross-laminated timber shear wall systems in the United States', *Journal of Structural Engineering*, 144(4), 04018025.

Van de Lindt, J.W., Pei, S., Popovski, M., Berman, J.W., Dolan, J.D. and Line, P. (2019). 'Experimental seismic behavior of a two-story CLT platform building', *Journal of Structural Engineering*, 145(10), 04019114.

Wang, Q., Li, Z., He, M. and Zhang, Q. (2023). 'Experimental testing of platform-type and balloon-type cross-laminated timber (CLT) shear walls with supplemental energy dissipators', *Engineering Structures*, 278, 115574.

Yang, R., Tannert, T. and Gattulli, V. (2022). 'Seismic performance evaluation of innovative balloon type CLT rocking shear walls', *Engineering Structures*, 254, 113837.

Yasumura, M. and Ito, T. (2014). 'Racking resistance and ductility of CLT shear walls under horizontal and vertical loads', *European Journal of Wood and Wood Products*, 72(1), pp. 127–133.

Yasumura, M., Kobayashi, K., Okabe, M., Miyake, T. and Matsumoto, K. (2016). 'Full-scale tests and numerical analysis of low-rise CLT structures under lateral loading', *Journal of Structural Engineering*, 142(4), p.04015126. https://doi.org/10.1061/(ASCE)ST.1943-541X.0001440

Zhang, X., Pan, Y. and Tannert, T. (2021). 'Experimental and numerical investigation of the cyclic behaviour of coupled balloon-type CLT shear walls with high-capacity base connections', *Engineering Structures*, 244, 112732.

Zhang, X., Popovski, M., Casagrande, D., Chen, Z. and van de Lindt, J.W. (2021). 'Seismic performance of 3-storey CLT buildings constructed with platform and balloon framing', *Proceedings of the 2021 World Conference on Timber Engineering (WCTE 2021)*, Santiago, Chile.

Zhang, Y., Popovski, M. and Pei, S. (2018). 'Development of high-capacity hold-down for tall CLT buildings', *Proceedings of the World Conference on Timber Engineering (WCTE)*, Seoul, South Korea.

Zhang, X., Popovski, M., van de Lindt, J.W., Casagrande, D. and Chen, Z. (2018). 'High-capacity hold-downs for mass timber shear walls', *Construction and Building Materials*, 195, pp. 327–336.

Appendices

Appendix A.

Construction details of the steel foundation beam and lateral sliding restraint

A.1. Steel foundation beam

The steel foundation beam is a built-up welded member composed of three main components, as illustrated in Figure A.1. The top assembly (Part 1) consists of two steel plates, while the bottom assembly (Part 2) is formed by four steel plates. These plates are connected by an I-shaped steel section placed at the centre of the beam (Part 3) with all components welded together to form an integral assembly. Full-penetration V-groove welds are provided along the four outer seams of the assembled plates, while fillet welds are applied along the four inner seams, as indicated in the drawings. This welding configuration was adopted to achieve sufficient bending and shear capacity of the foundation beam, while maintaining fabrication feasibility.

A.2. Steel sliding restraint

The steel sliding restraint assembly comprises a welded shear key (Part 1), a grooved steel plate (Part 2), and a steel rod (Part 3), as illustrated in Figure A.2. The shear key is formed by welding two rectangular steel plates with two transverse triangular stiffeners to enhance stiffness. This restraint system effectively restrains lateral sliding of the specimens while permitting in-plane rotation.

It is noted that all dimensions in the drawings are given in millimetres. Dimensions highlighted in red denote key dimensions critical to fabrication and assembly, while weld details are indicated in green.

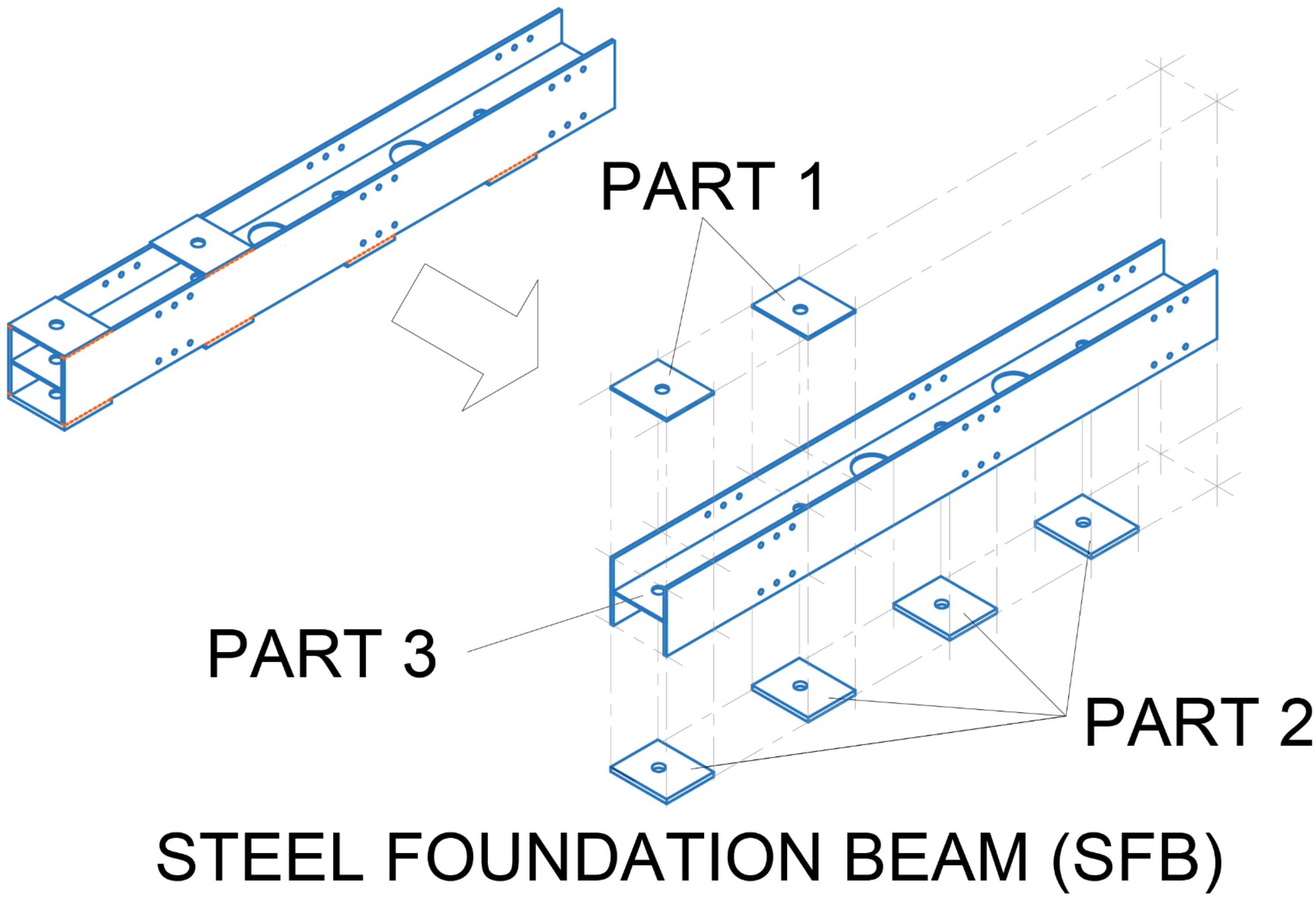

(a) Components of the steel foundation beam

PART 1

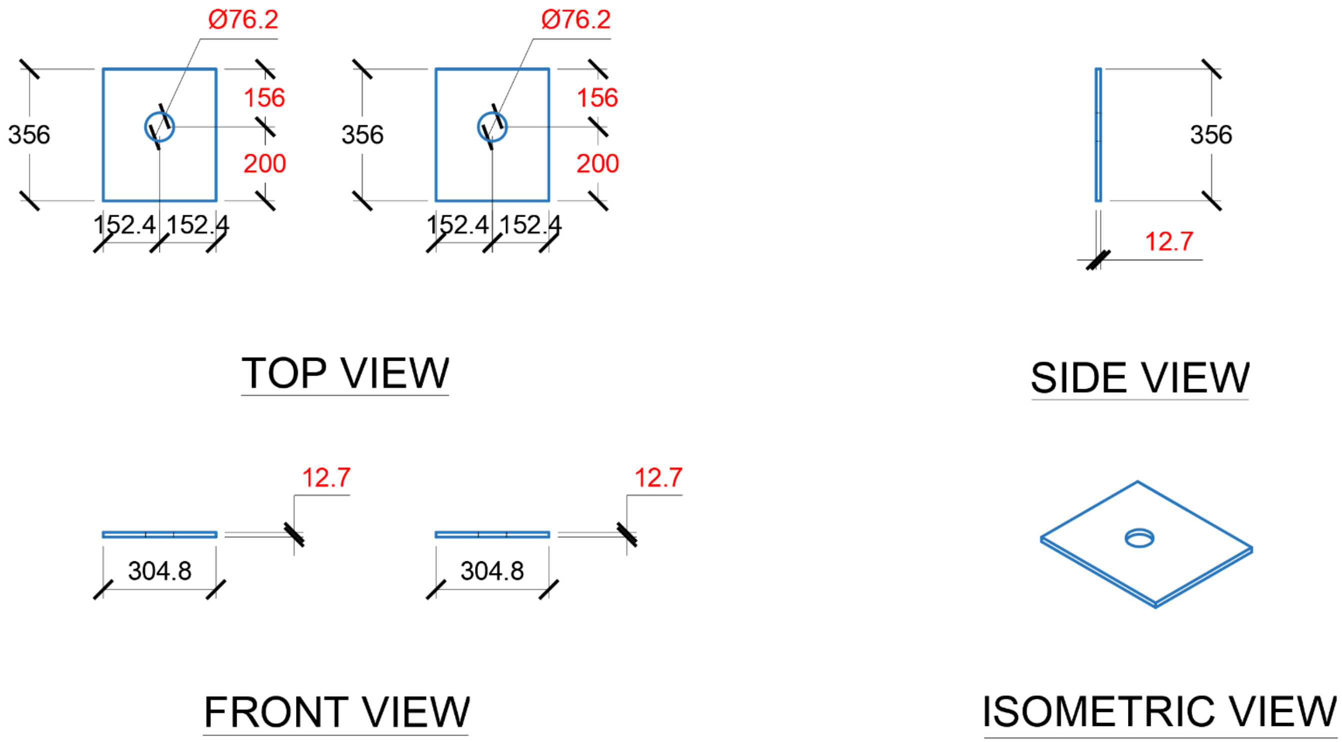

(b) Details of the steel foundation beam: Part 1

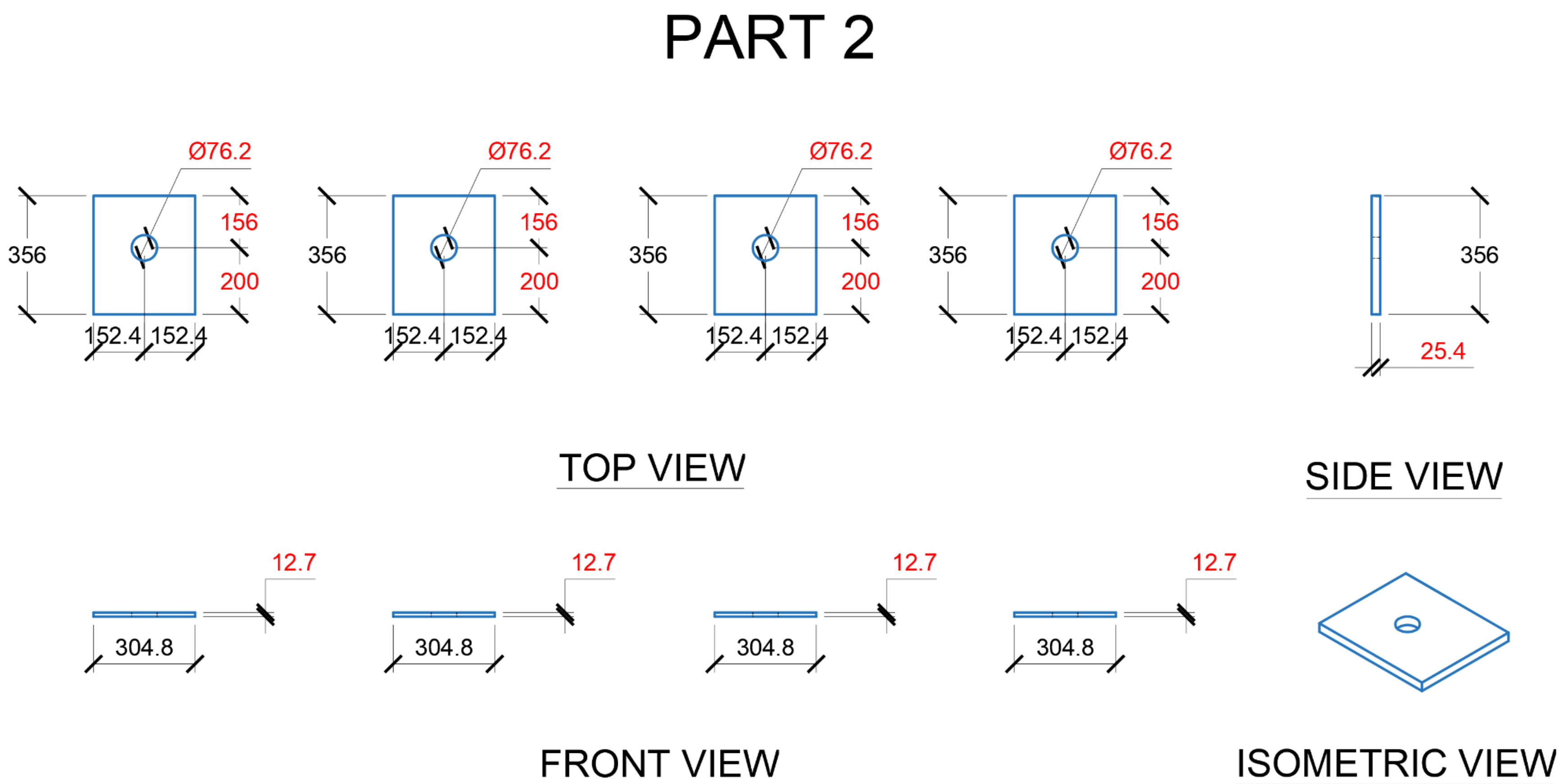

(c) Details of the steel foundation beam: Part 2

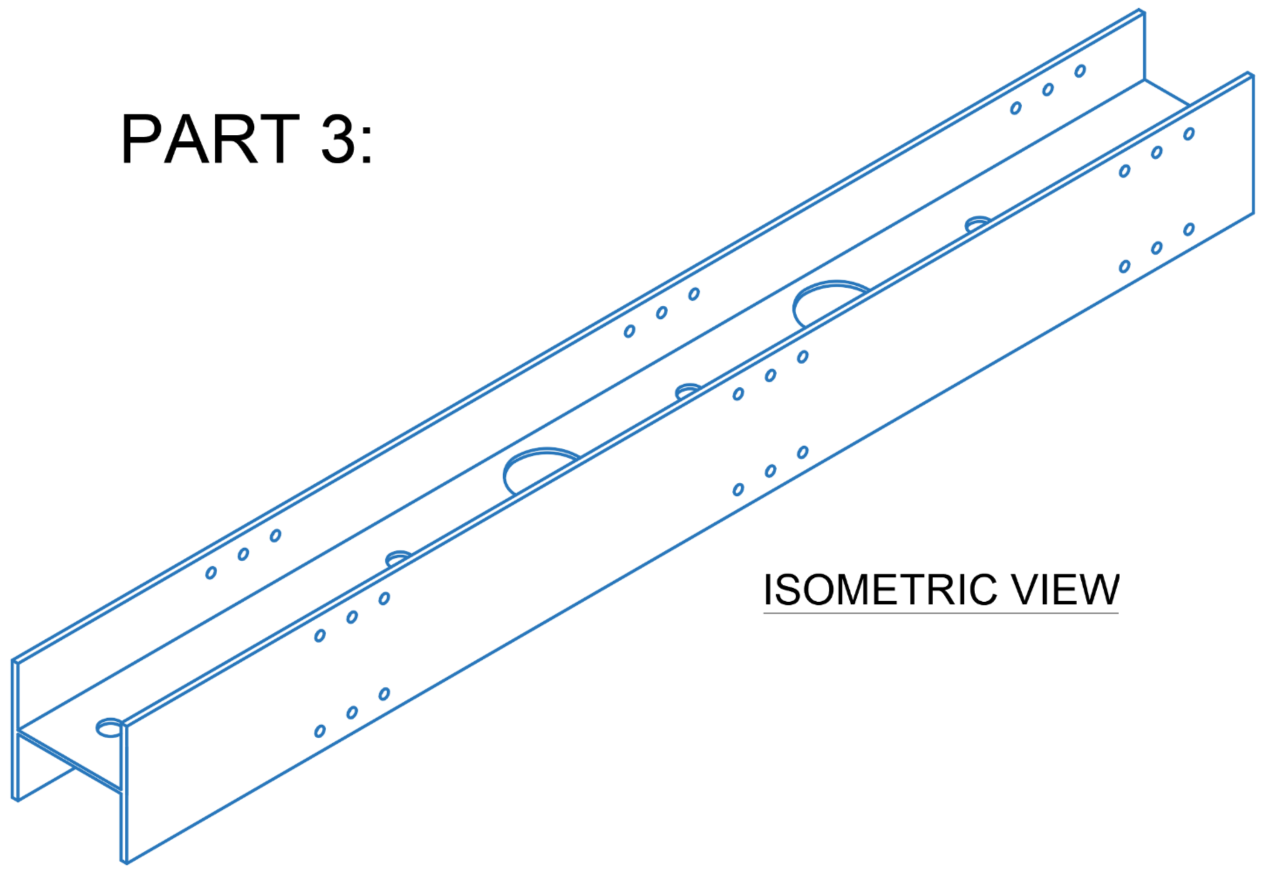

(c) Details of the steel foundation beam: Part 3

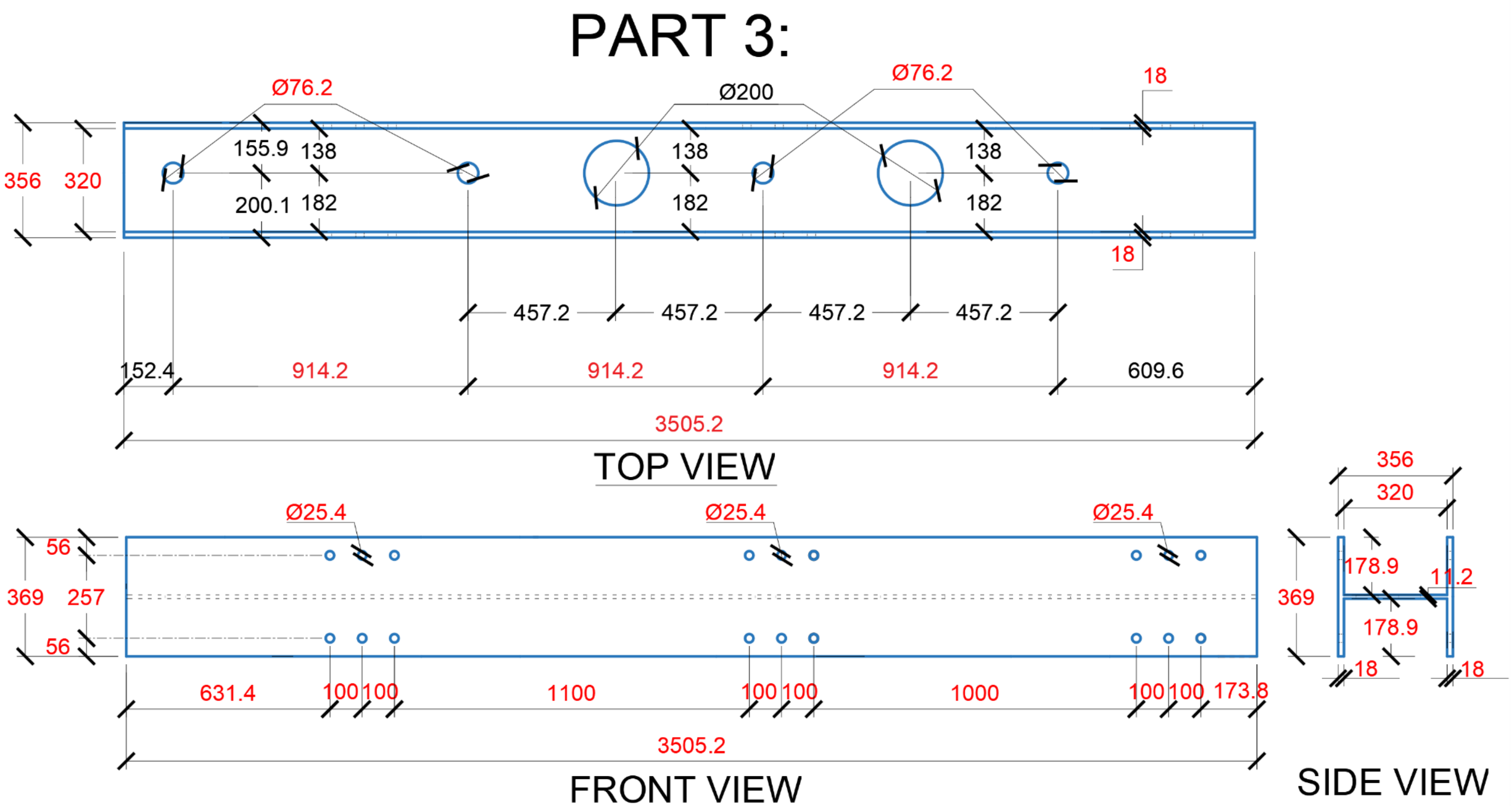

(c) Details of the steel foundation beam: Part 3 (Continued)

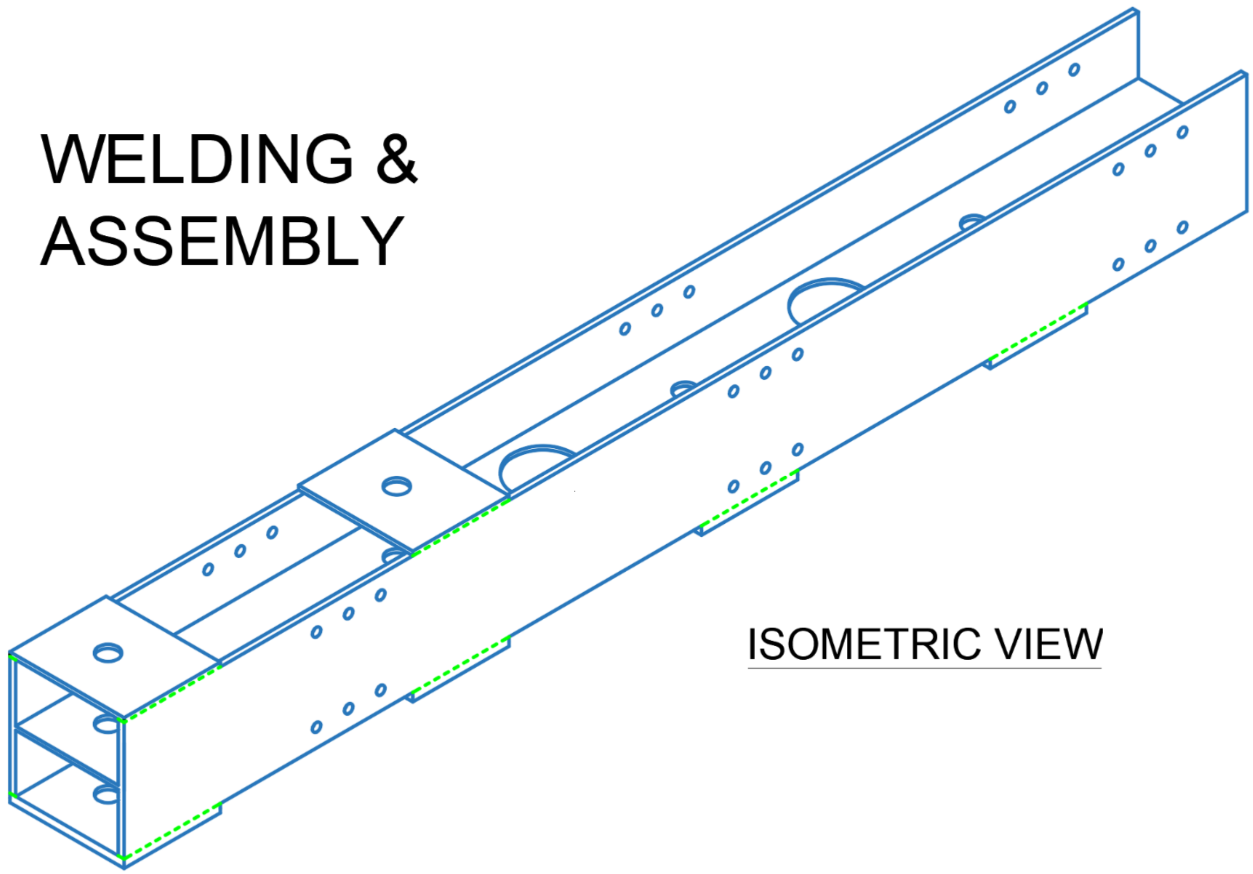

(d) Details of the steel foundation beam: Welding and assembly

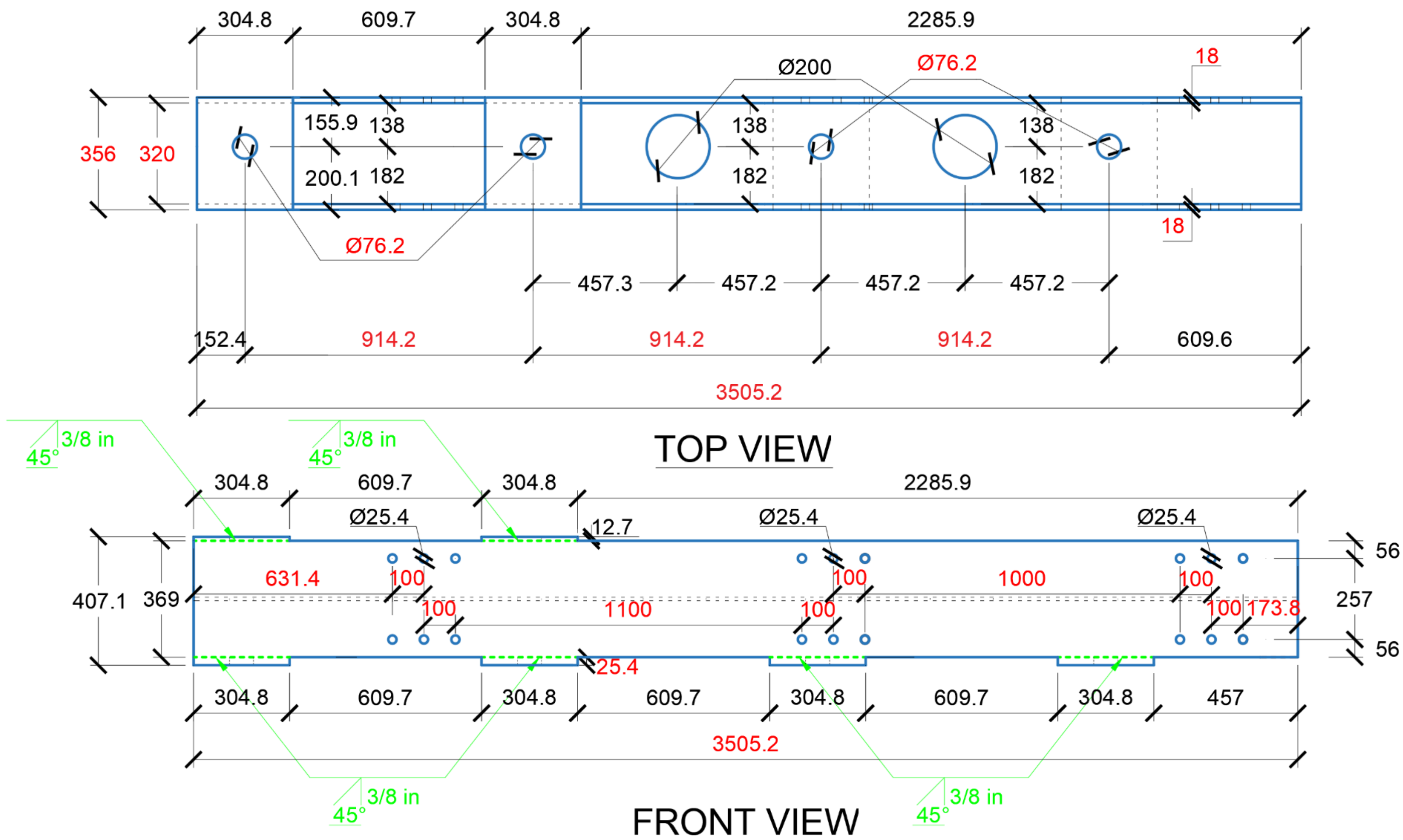

(d) Details of the steel foundation beam: Welding and assembly (Continued)

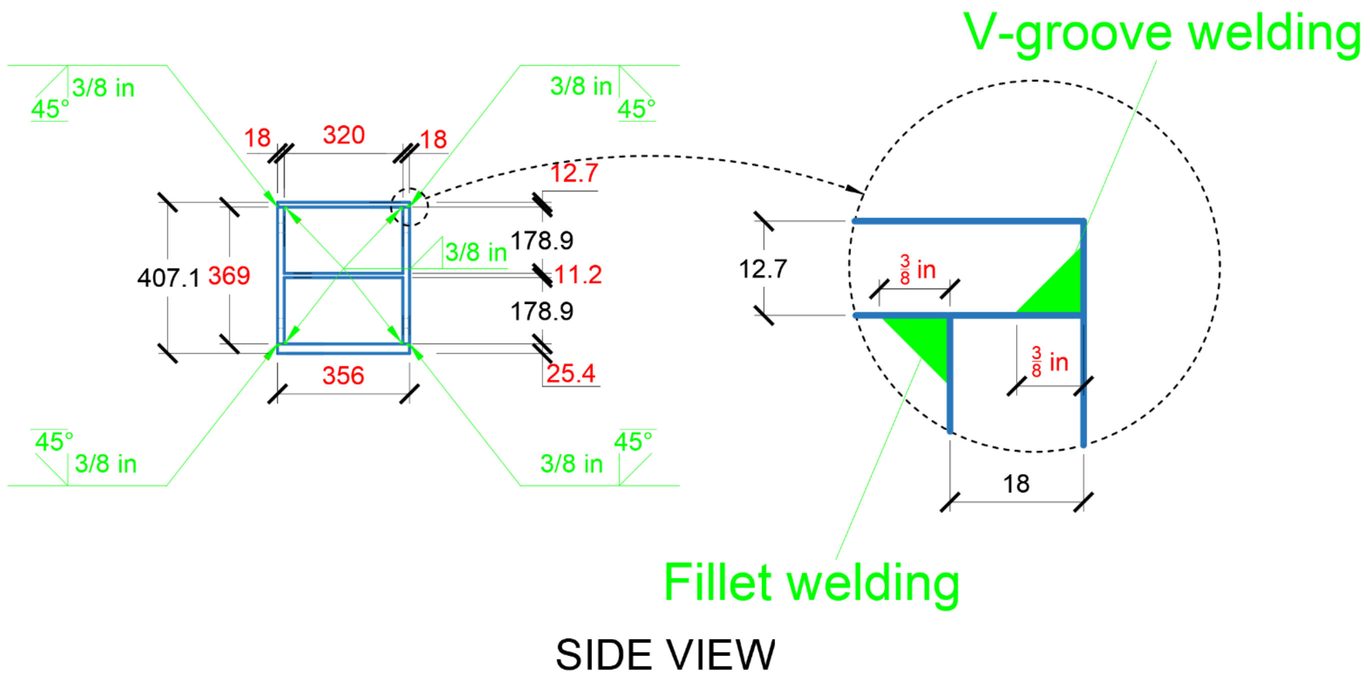

(d) Details of the steel foundation beam: Welding and assembly (Continued)

Figure A.1: *Drawings of steel foundation beam*

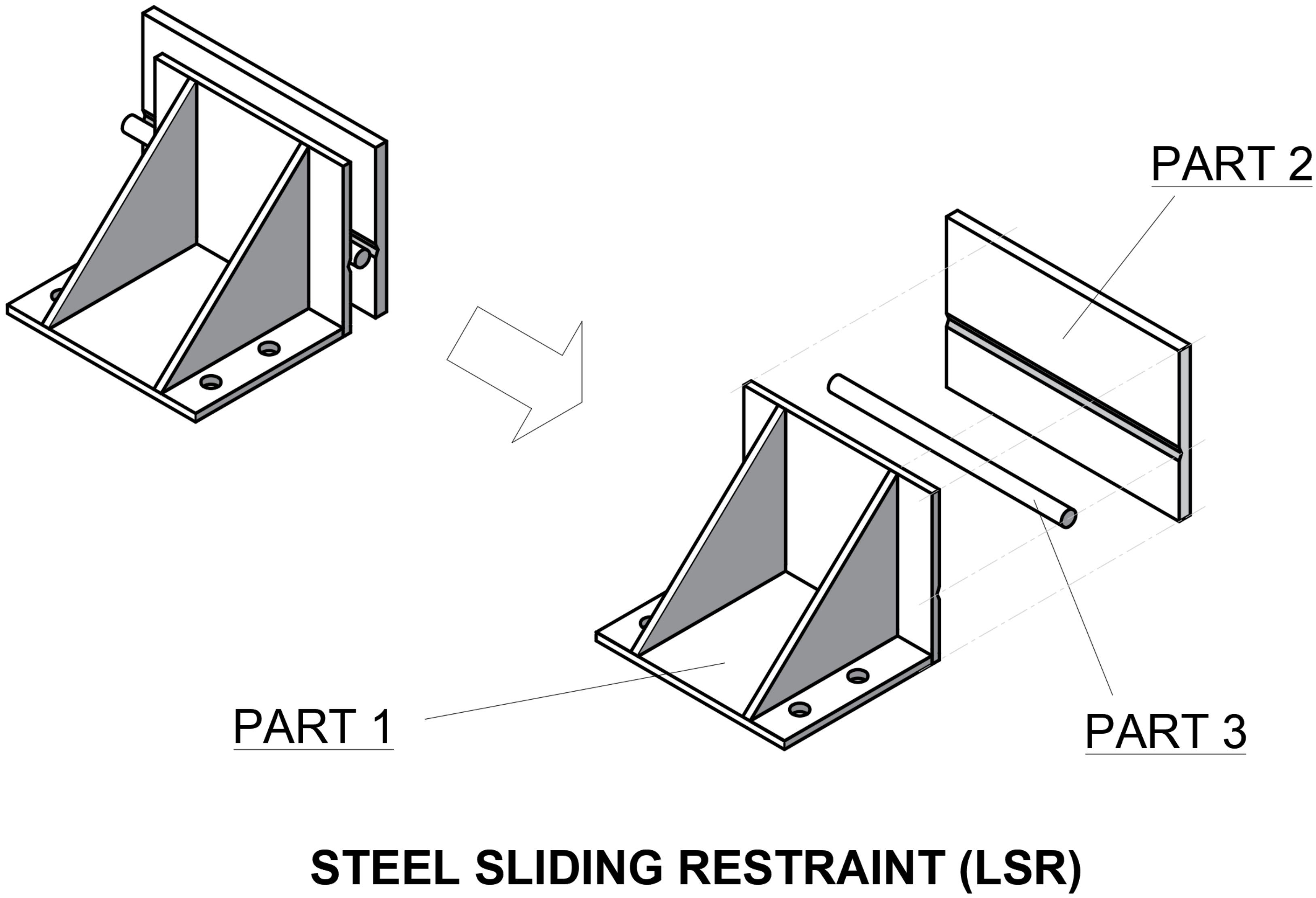

(a) Components of the steel sliding restraint

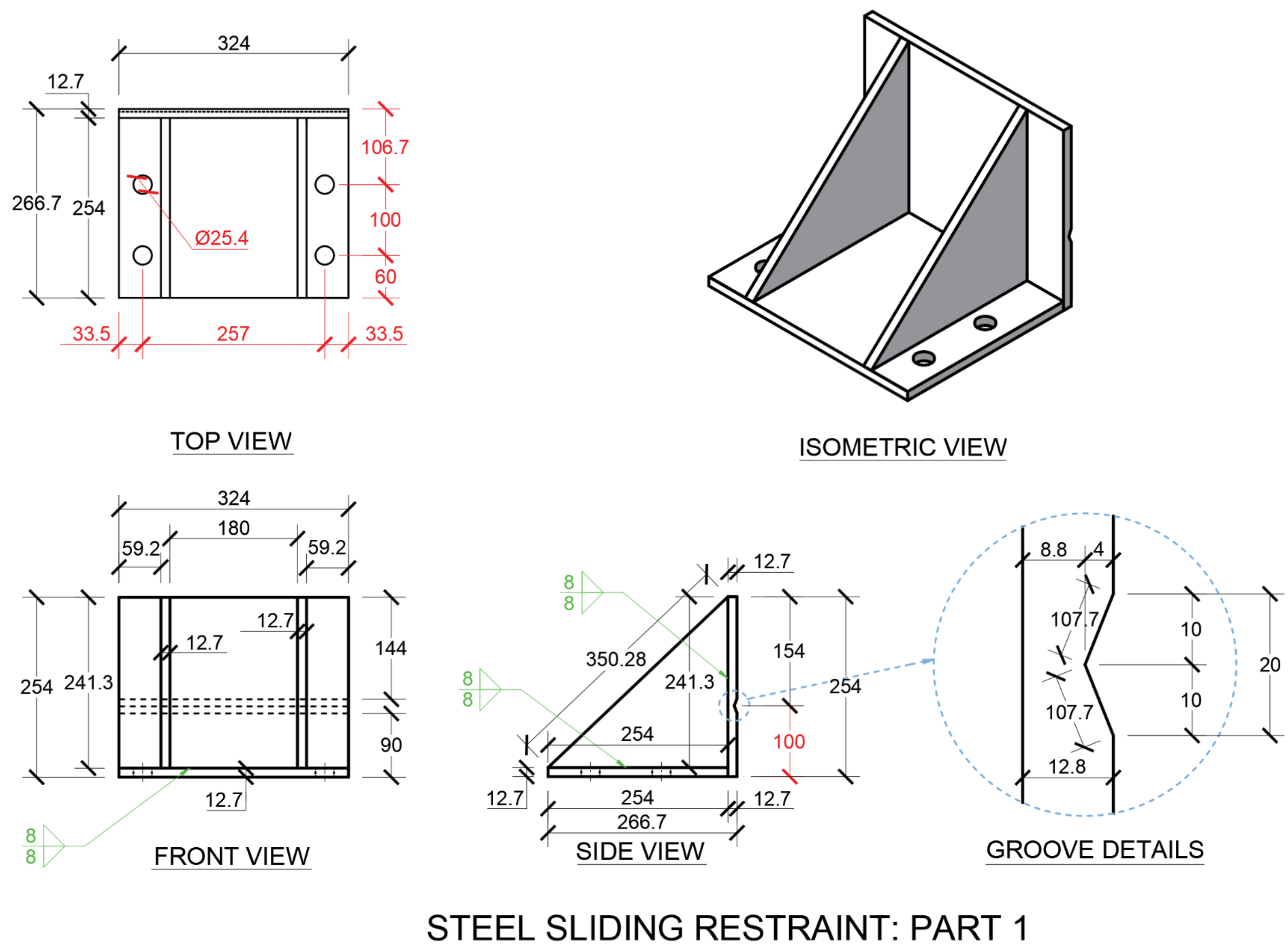

(b) Details of the steel sliding restraint: Part 1

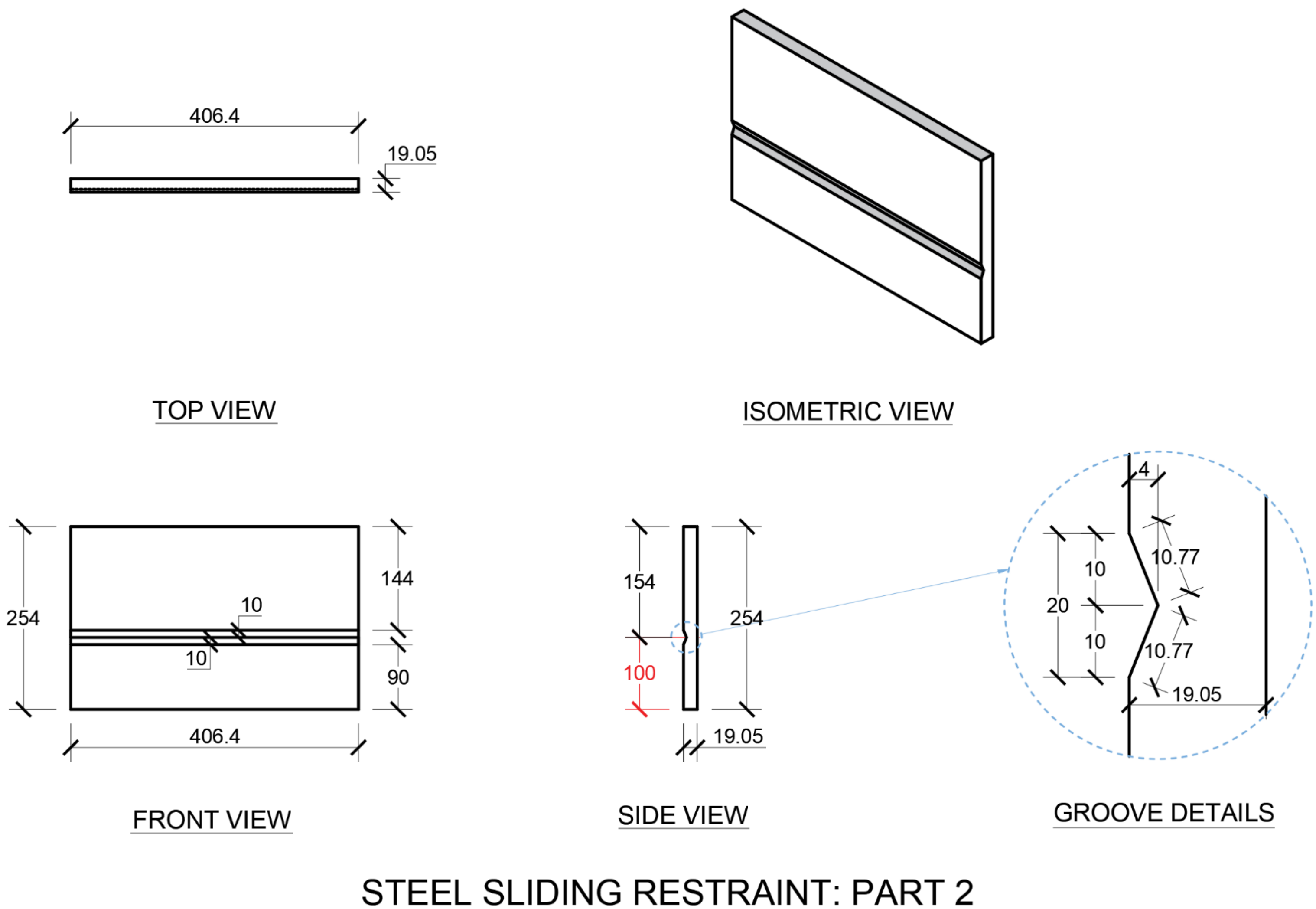

(c) Details of the steel sliding restraint: Part 2

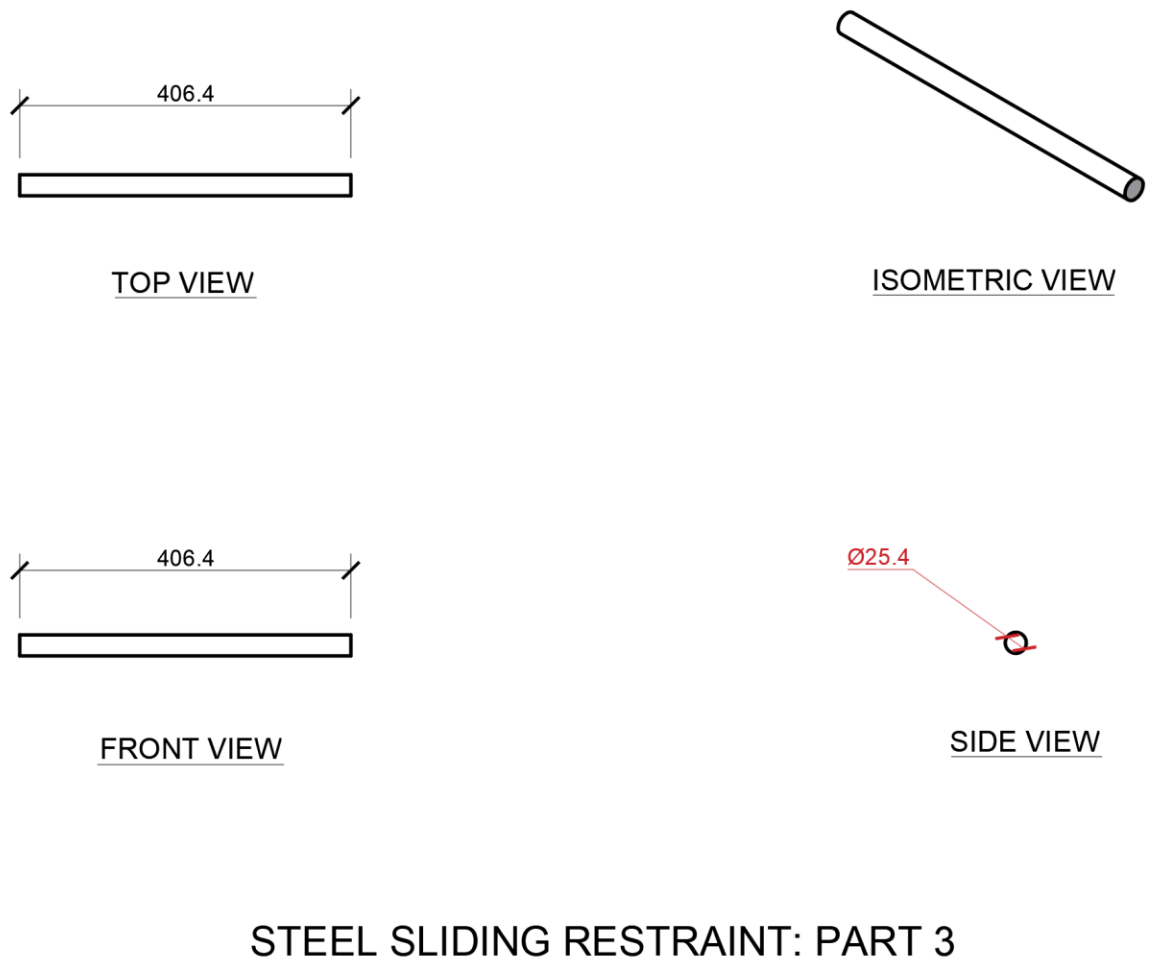

(d) Details of the steel sliding restraint: Part 3

Figure A.2: *Drawings of steel sliding restraint*

Appendix B.

Correction for deformation of the steel foundation beam

As discussed in Section 6.1, the steel foundation beam in the test setup exhibits finite stiffness, therefore, a portion of the measured global displacement includes deformation of the foundation beam itself. To obtain the lateral deformation response of the shearwall specimens, the contribution from translation and rotation of foundation beam is removed from the recorded top displacement.

B.1. Definition of corrected displacement

The corrected total lateral displacement at the top of the shearwall, $\Delta_{\text{total},C}$, is evaluated as

$$\Delta_{total,C} = \Delta_{total,G} - \Delta_{rocking,B} - \Delta_{sliding,B} \tag{B.1}$$

where

$\Delta_{total,G}$ is the gross total lateral displacement measured at the top of shearwalls (height of the second diaphragm),

$\Delta_{rocking,B}$ is the component induced by rotation of the foundation beam,

$\Delta_{sliding,B}$ is the component induced by rigid-body translation (sliding) of the foundation beam in the global x-direction. In this study, $\Delta_{sliding,B}$ is taken as the measured lateral displacement at Point C, which equals to $\Delta_{Point\ C}$.

B.2. Instrumentation and monitored points

Figure B.1 illustrates the locations of the displacement monitoring points on the foundation beam:

- Point A: located at the shearwall end to capture possible compressive vertical deformation of the foundation beam (displacement in the global y-direction);
- Point B: aligned with the centreline of the outermost hold-down to record possible uplift of the foundation beam (displacement in the global y-direction);
- Point C: aligned with the roller centre of the sliding restraint to monitor the global lateral translation of the foundation beam (displacement in the global x-direction).

These points are also used to define the equivalent spring locations employed in the FE model to represent foundation-beam flexibility (shown in Chapter 6).

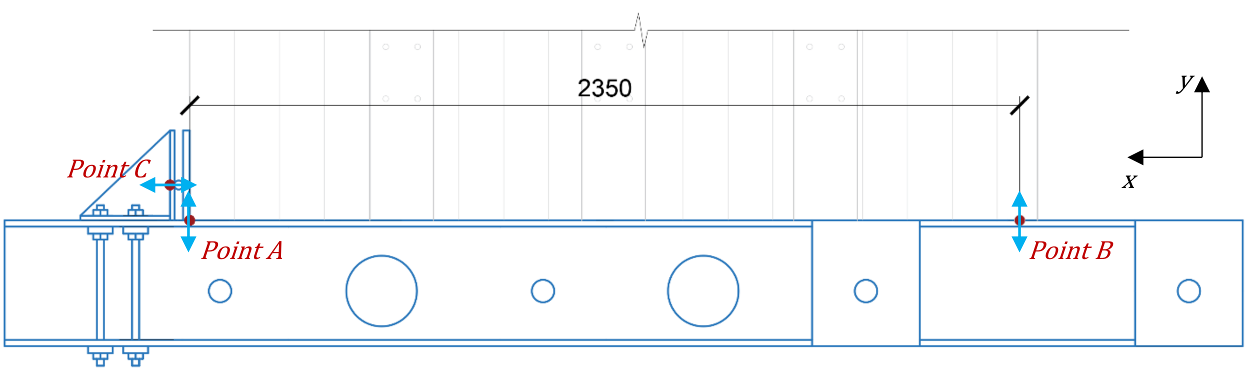

Figure B.1: *Displacement monitor points on the foundation beam*

B.3. Rocking component induced by foundation-beam rotation

Figure B.2 shows a typical development of foundation-beam rotation during loading (specimen W0.8-P3-H2V32 is shown as an example). Assuming small rotations, the rocking-induced lateral displacement at the top of the shearwall is

$$\Delta_{rocking,B} = \varphi h = \frac{\Delta_{Point\ B}}{d} \cdot h \tag{B.2}$$

where

φ is the rotation angle of the foundation beam,

h is the height of shearwalls (taken as 4,800 mm for the height of the second diaphragm),

$\Delta_{Point\ B}$ is the vertical displacement measured at Point B,

d is the distance between point B and rotation centre. Across the test series, the rotation centre remained approximately stationary and d was consistently close to 1,200 mm.

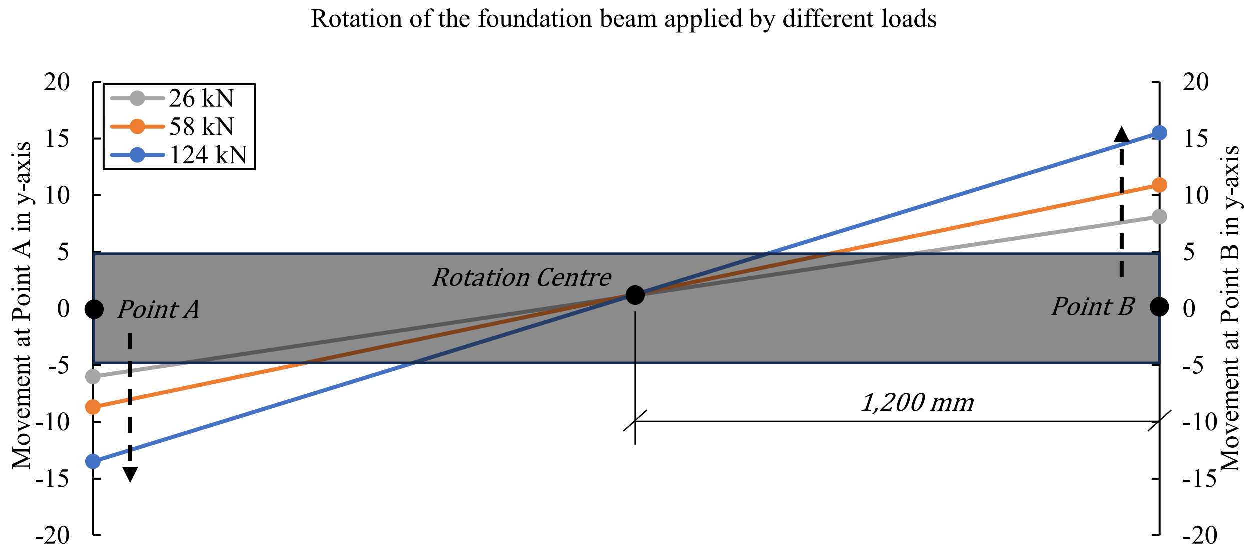

Figure B.2: *Rotation development of the foundation beam in the loading process of specimen W0.8-P3-H2V32 as an example*

B.4. Estimation of foundation-beam movement for early-stage tests

Due to the limited number of LVDTs during the early stage of testing, the foundation-beam displacements at Points A~C were not fully recorded for the specimens with a total wall width of 1.2 m (i.e., W0.6-P2). For these specimens, the foundation-beam movement was estimated using complete displacement records obtained from subsequent tests on wider specimens (i.e., W0.6-P4, W0.8-P3, and W1.2-P2). These wider specimens generally developed higher lateral resistance and more pronounced deformation of the foundation beam, providing sufficiently reliable data to characterise the foundation-beam stiffness and deformation trend for the overall experimental campaign.

Figure B.3 presents the measured relationships between load and the displacements at Points B and C for the selected wider specimens, together with representative fitted curves used for interpolation.

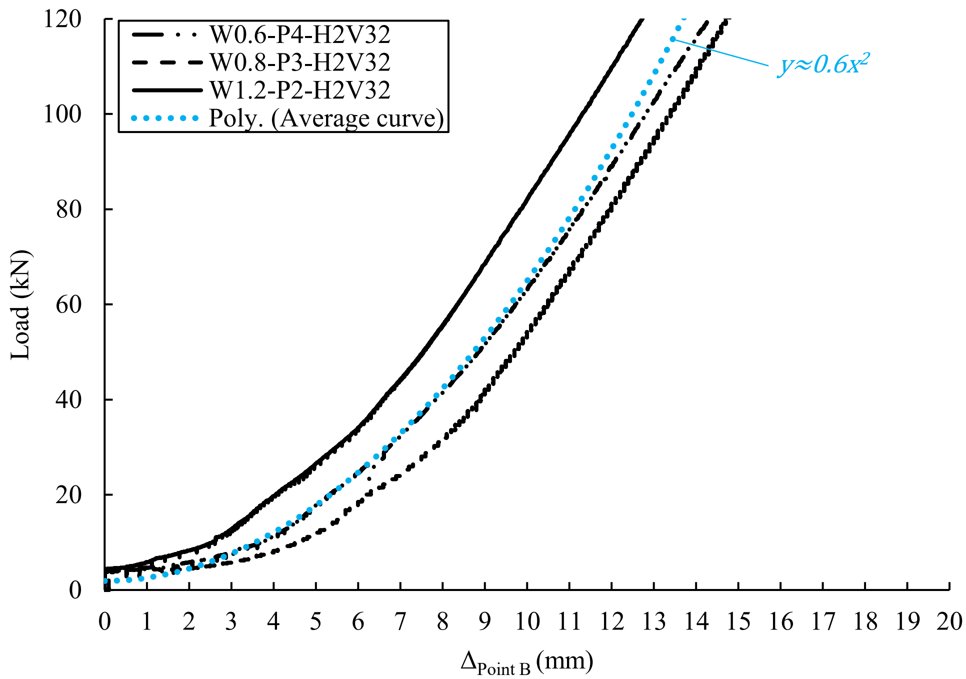

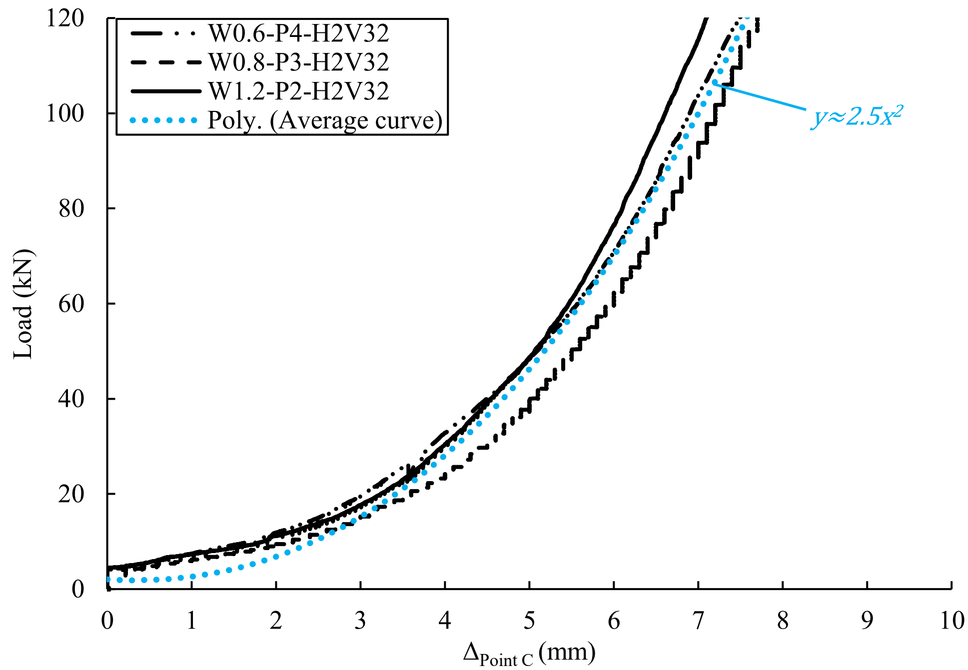

Figure B.3: *Load-displacement relationships measured at Point B (uplift displacement in the vertical direction) and Point C (lateral sliding displacement) for specimens W0.6-P4-H2V32, W0.8-P3-H2V32, and W1.2-P2-H2V32, together with the corresponding averaged polynomial fitting curves used for estimating movement of the foundation beam*

B.5. Correction procedure

The correction procedure is summarised as follows:

1. Compile the load-displacement curves at Point B and Point C from specimens with complete records (W0.6-P4, W0.8-P3, and W1.2-P2), and obtain representative fitted expressions (e.g., polynomial fitting) for $\Delta_{Point\ B}(F)$ and $\Delta_{Point\ C}(F)$.
2. For a given load F recorded in a target specimen (e.g., W0.6-P2), evaluate $\Delta_{Point\ B}$ and $\Delta_{Point\ C}$ from the fitted expressions.
3. Compute $\Delta_{rocking,B}$ using Eq. B.2, take $\Delta_{sliding,B} = \Delta_{Point\ C}$ and obtain the corrected top displacement $\Delta_{total,C}$ using Eq. B.1.

This procedure aims to remove the contribution of experimental fixture compliance from the measured deformation of the shearwall specimens, thereby enabling a more accurate comparison of lateral stiffness, deformation capacity, and load-displacement response among different configurations. Figure B.4 presents calculation results of $\Delta_{rocking,B}$ and $\Delta_{sliding,B}$ for tested specimens.

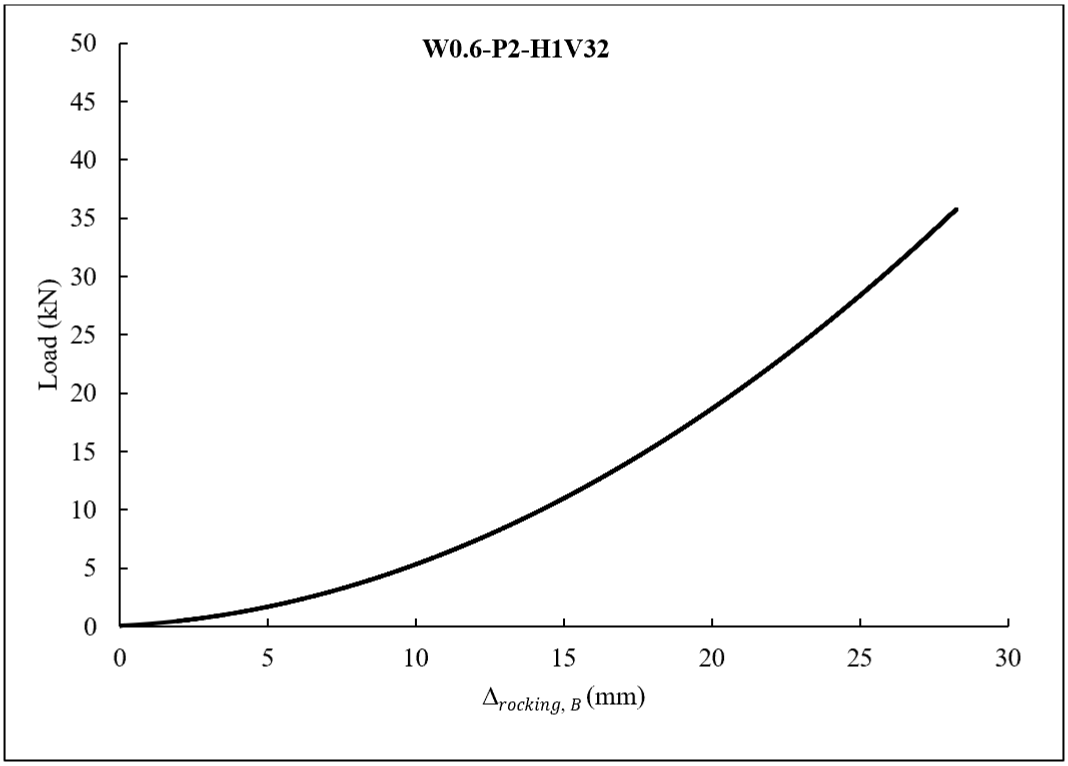
W0.6-P2-H1V32
Load (kN)
50
45
40
35
30
25
20
15
10
5
0
0
5
10
15
20
25
30
$\Delta_{rocking,\,B}$ (mm)

(a)

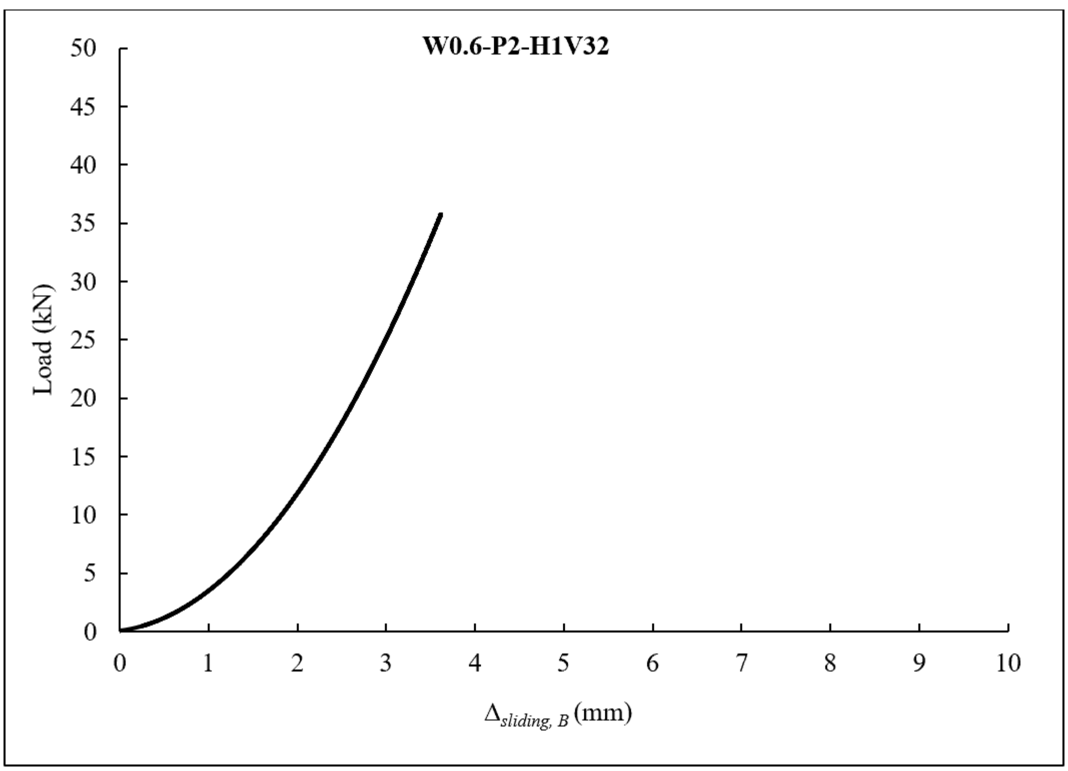
W0.6-P2-H1V32
Load (kN)
50
45
40
35
30
25
20
15
10
5
0
0
1
2
3
4
5
6
7
8
9
10
$\Delta_{sliding,\,B}$ (mm)

(b)

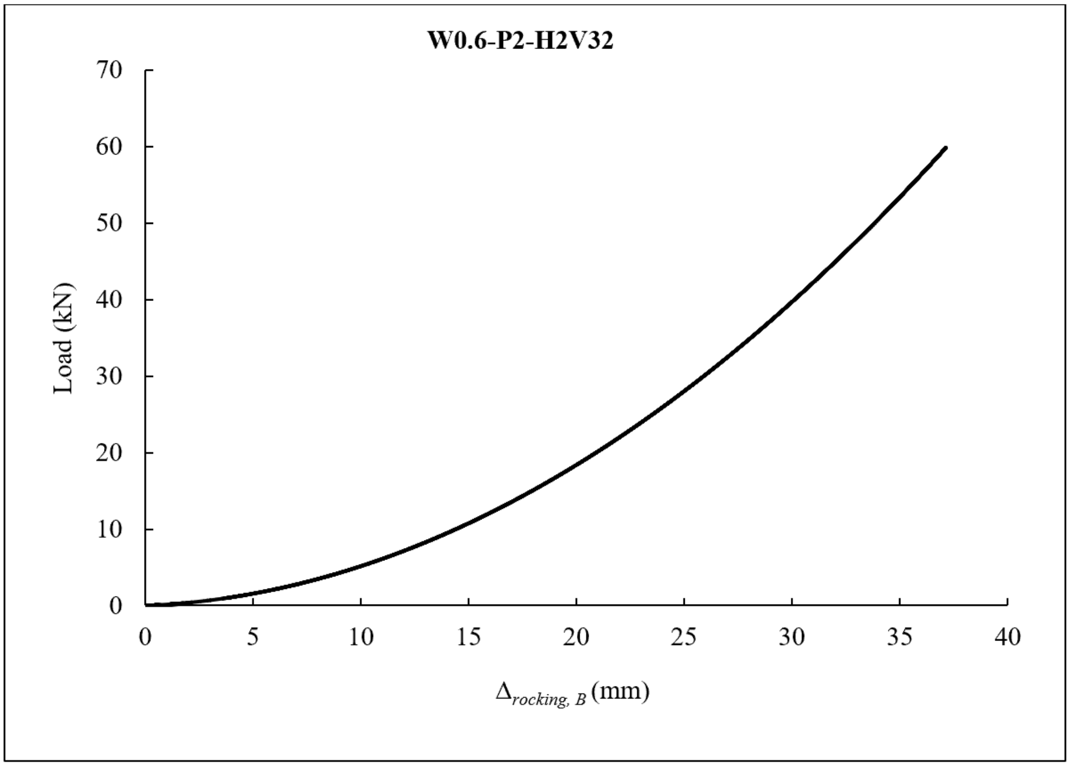
W0.6-P2-H2V32
Load (kN)
70
60
50
40
30
20
10
0
0
5
10
15
20
25
30
35
40
$\Delta_{rocking, B}$ (mm)

(c)

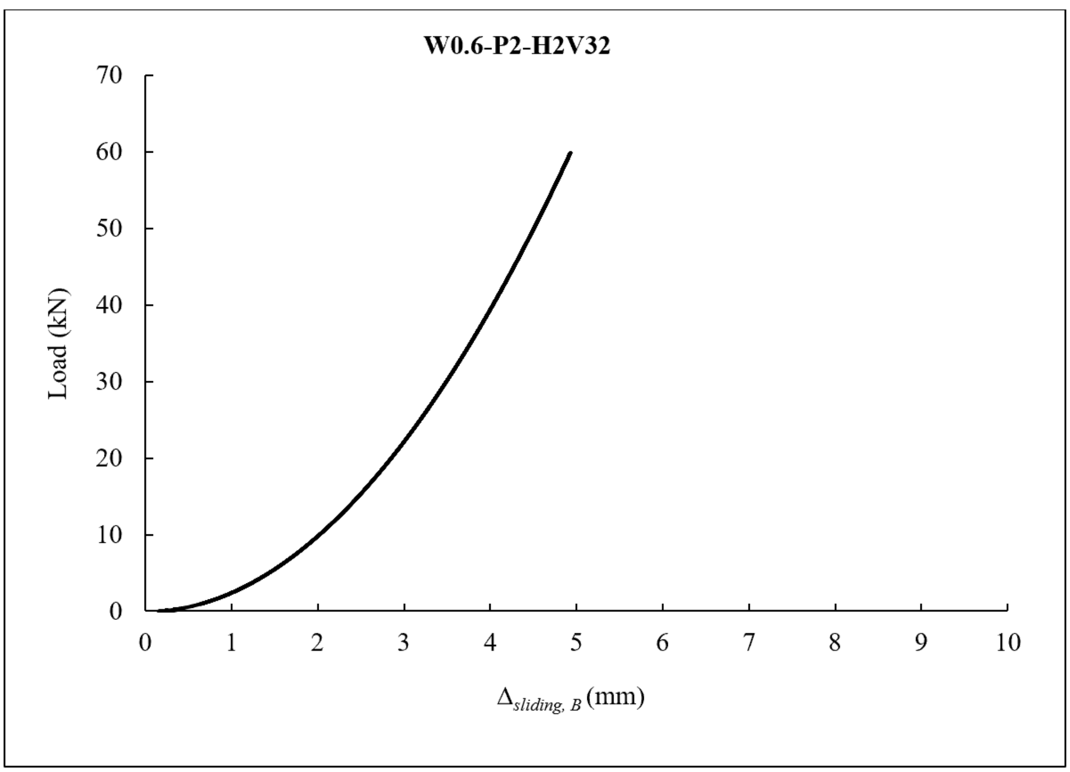
W0.6-P2-H2V32
Load (kN)
70
60
50
40
30
20
10
0
0
1
2
3
4
5
6
7
8
9
10
$\Delta_{sliding, B}$ (mm)

(d)

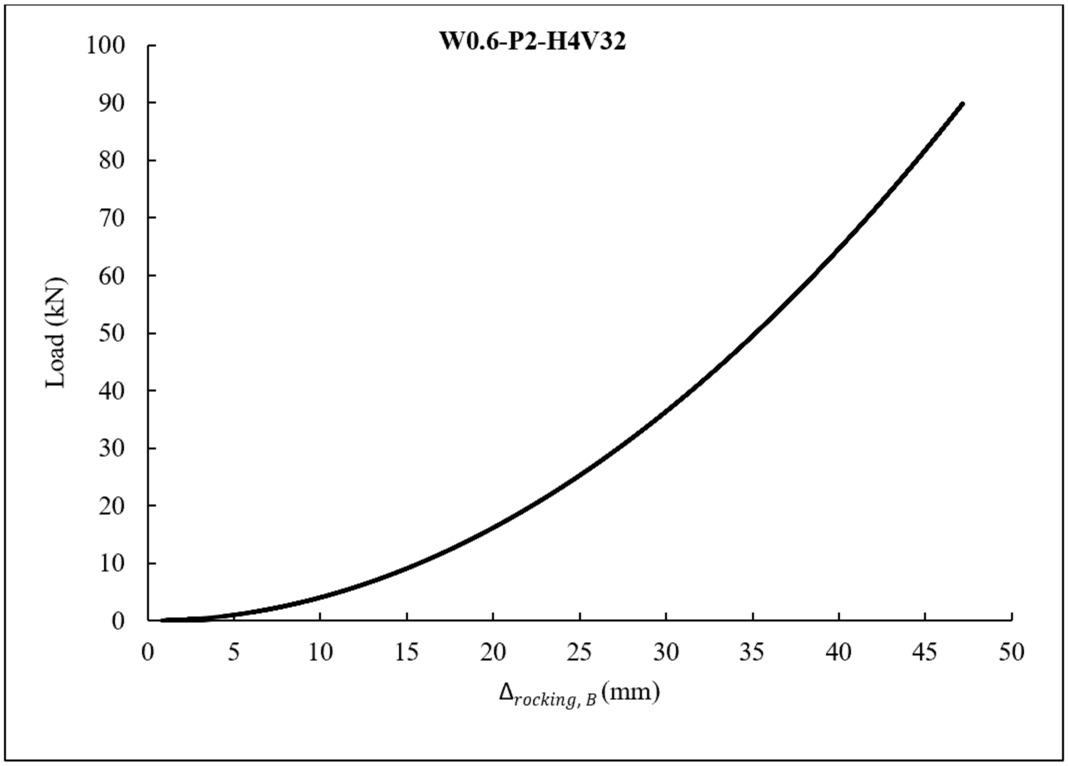
W0.6-P2-H4V32
Load (kN)
100
90
80
70
60
50
40
30
20
10
0
0
5
10
15
20
25
30
35
40
45
50
$\Delta_{rocking,\,B}$ (mm)

(e)

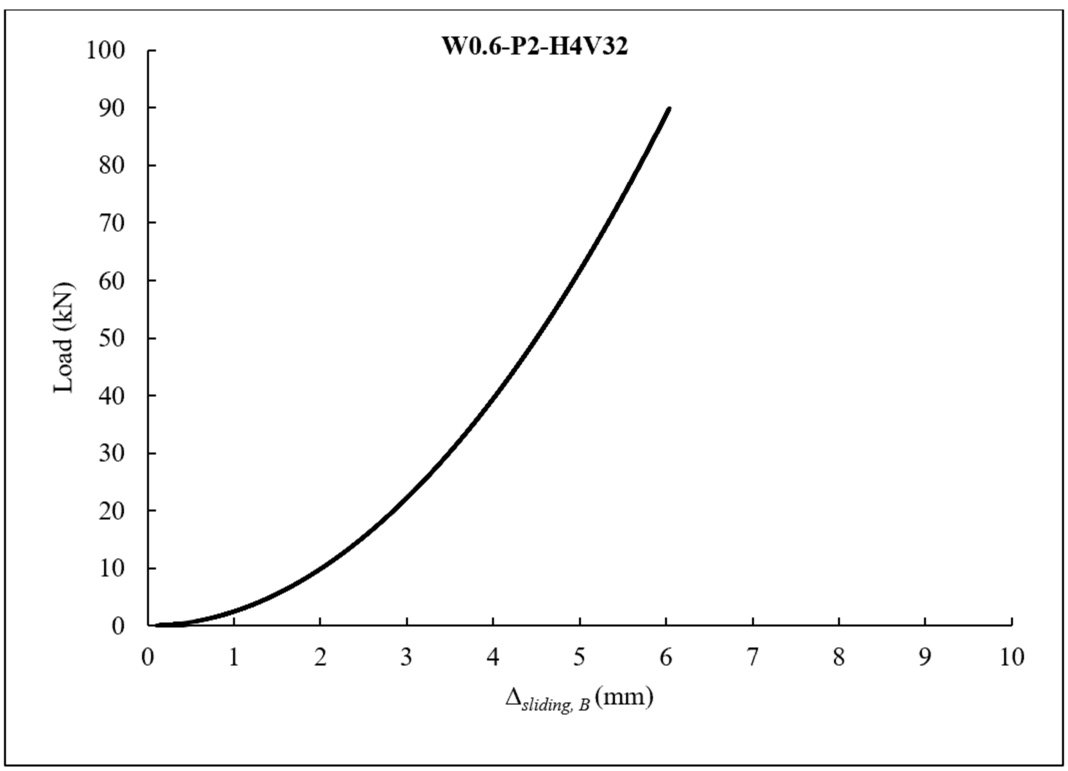
W0.6-P2-H4V32
Load (kN)
100
90
80
70
60
50
40
30
20
10
0
0
1
2
3
4
5
6
7
8
9
10
$\Delta_{sliding,\,B}$ (mm)

(f)

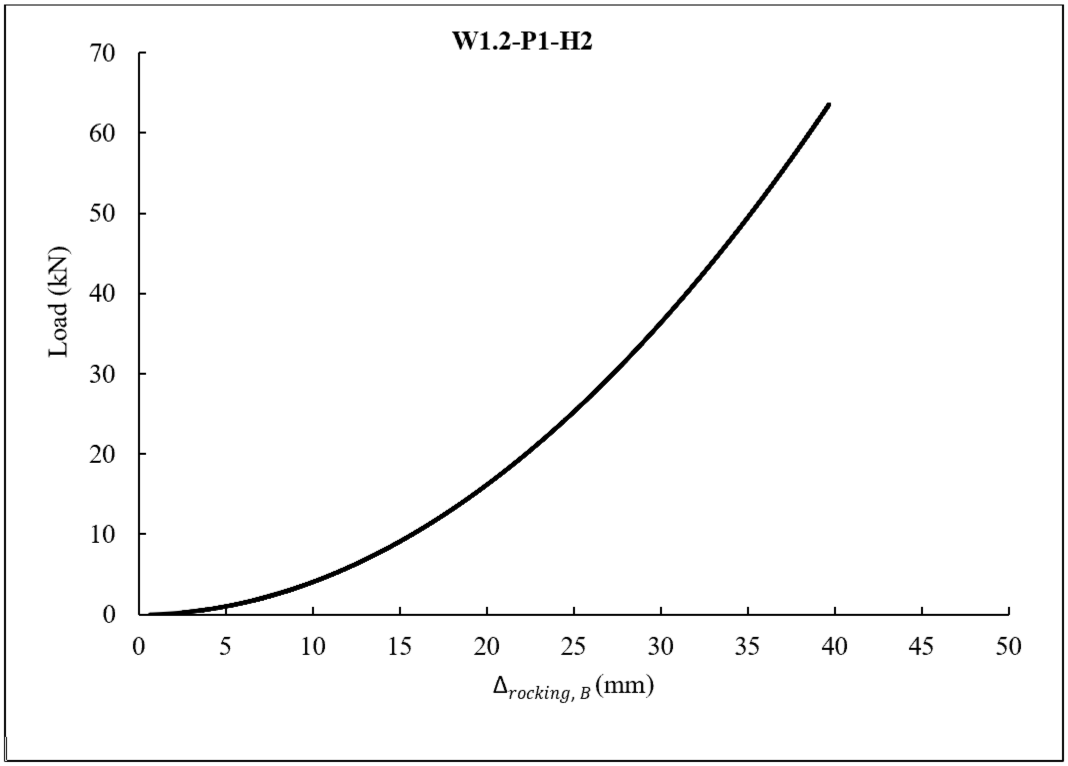
W1.2-P1-H2
Load (kN)
70
60
50
40
30
20
10
0
0
5
10
15
20
25
30
35
40
45
50
$\Delta_{rocking, B}$ (mm)

(g)

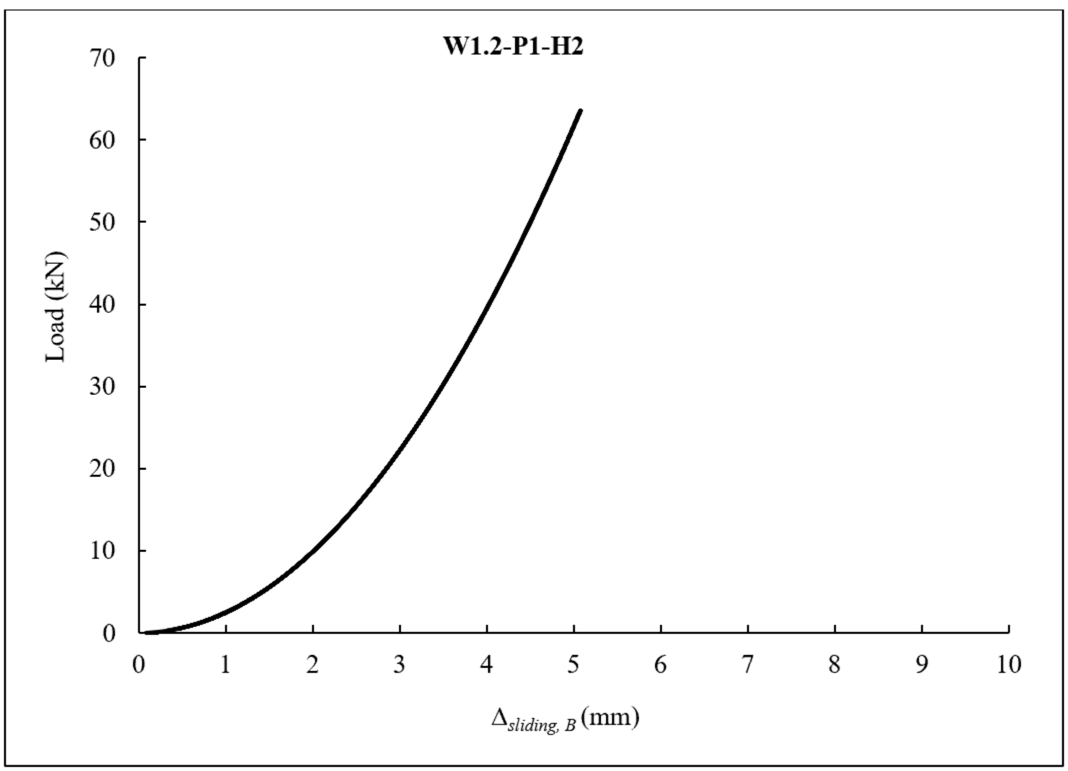
W1.2-P1-H2
Load (kN)
70
60
50
40
30
20
10
0
0
1
2
3
4
5
6
7
8
9
10
$\Delta_{sliding, B}$ (mm)

(h)

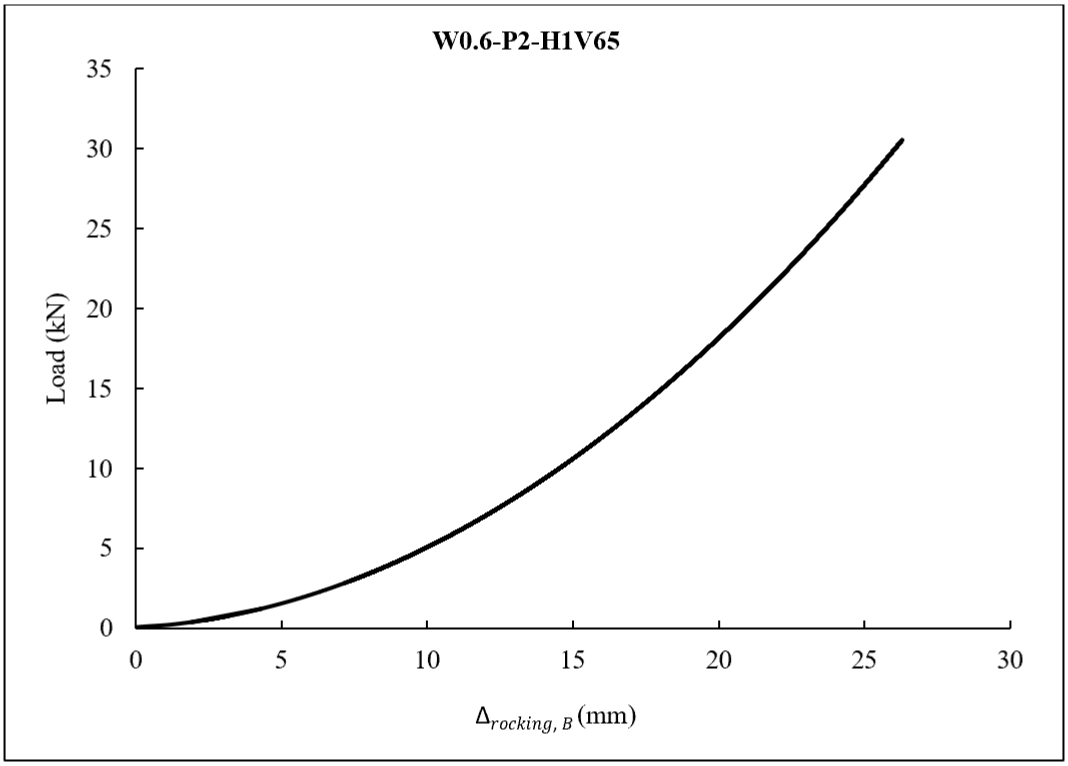

W0.6-P2-H1V65
Load (kN)
35
30
25
20
15
10
5
0
0
5
10
15
20
25
30
$\Delta_{rocking,\,B}$ (mm)

(i)

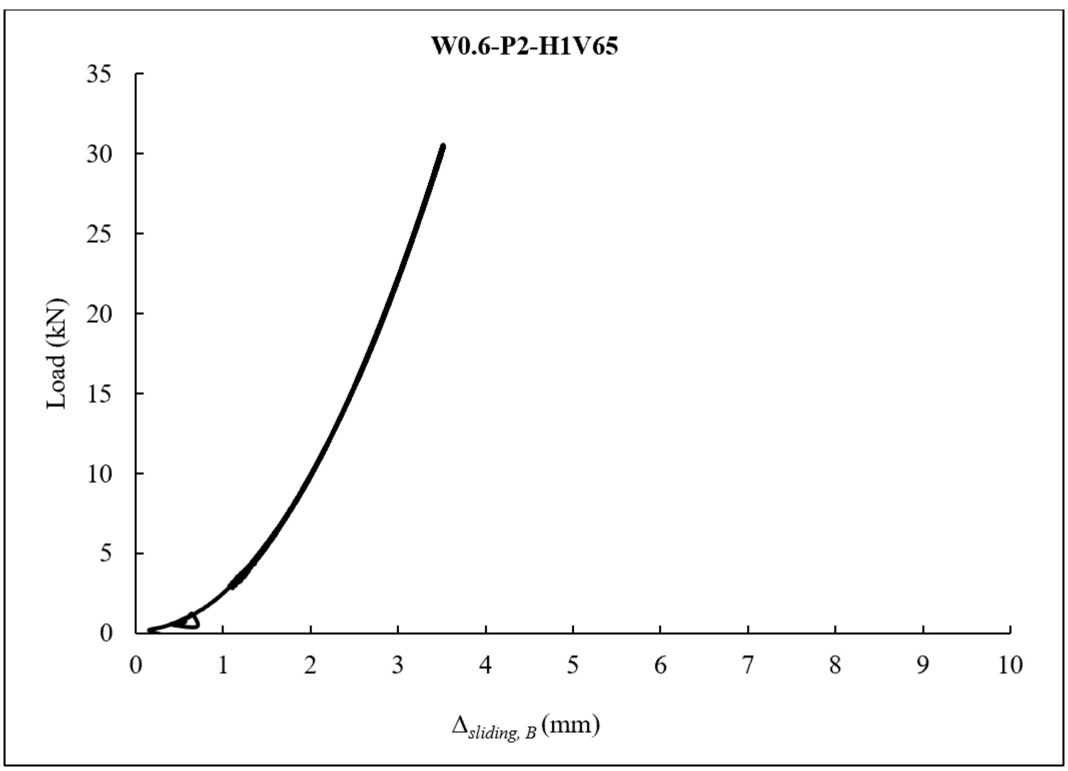

W0.6-P2-H1V65
Load (kN)
35
30
25
20
15
10
5
0
0
1
2
3
4
5
6
7
8
9
10
$\Delta_{sliding,\,B}$ (mm)

(j)

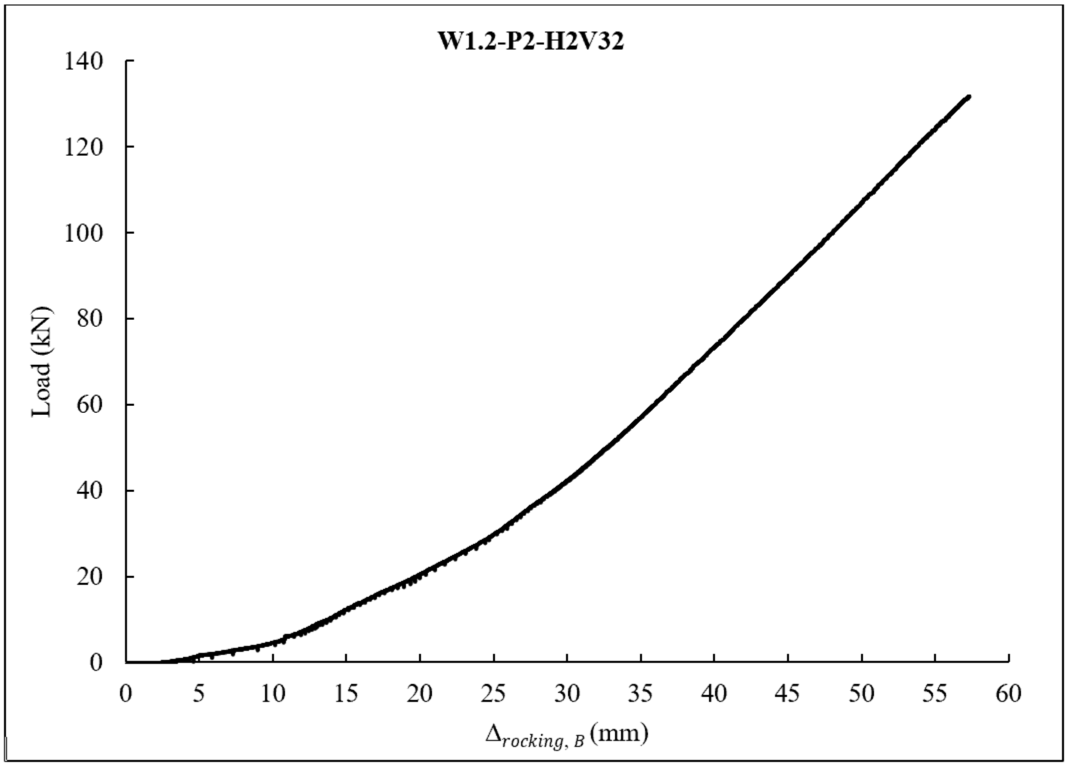
W1.2-P2-H2V32
Load (kN)
$\Delta_{rocking,\,B}$ (mm)
0
20
40
60
80
100
120
140
0
5
10
15
20
25
30
35
40
45
50
55
60

(k)

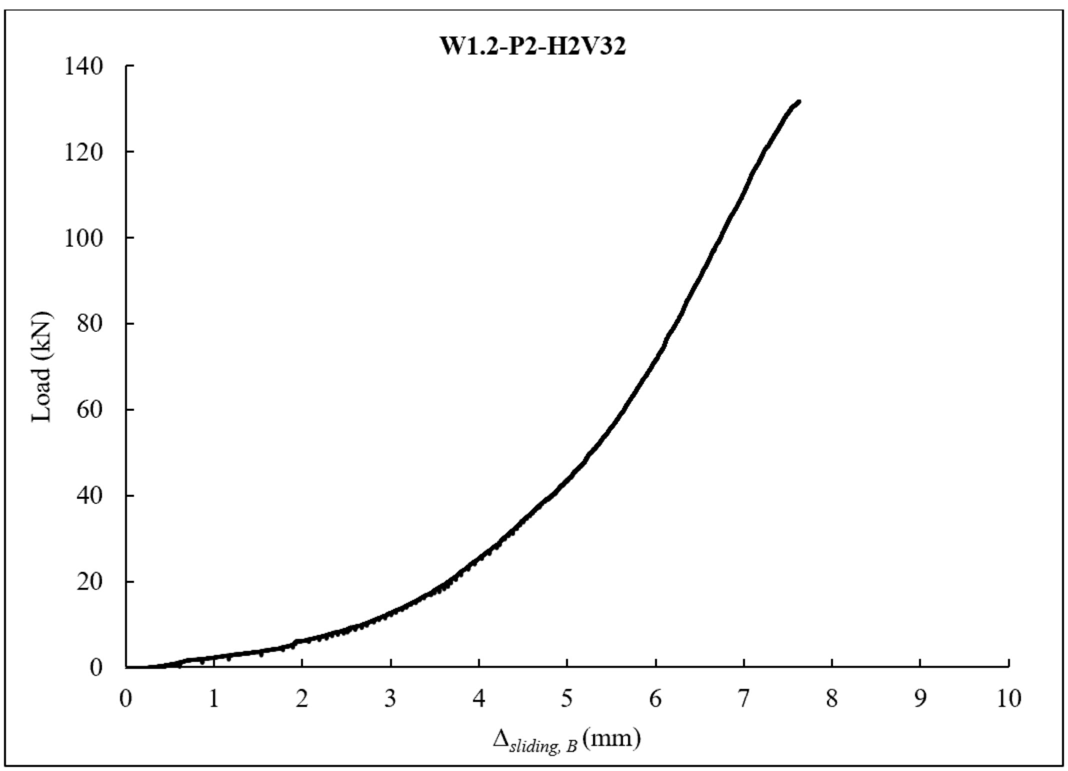
W1.2-P2-H2V32
Load (kN)
$\Delta_{sliding,\,B}$ (mm)
0
20
40
60
80
100
120
140
0
1
2
3
4
5
6
7
8
9
10

(l)

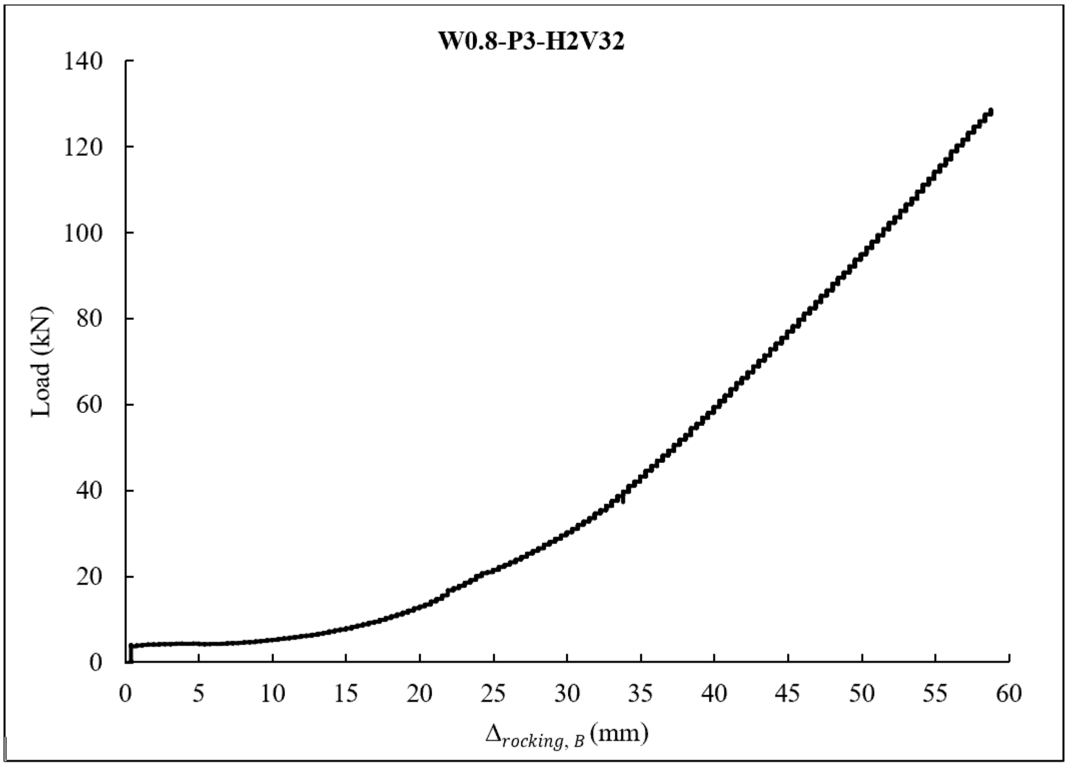
W0.8-P3-H2V32
Load (kN)
140
120
100
80
60
40
20
0
0
5
10
15
20
25
30
35
40
45
50
55
60
$\Delta_{rocking,\ B}$ (mm)

(m)

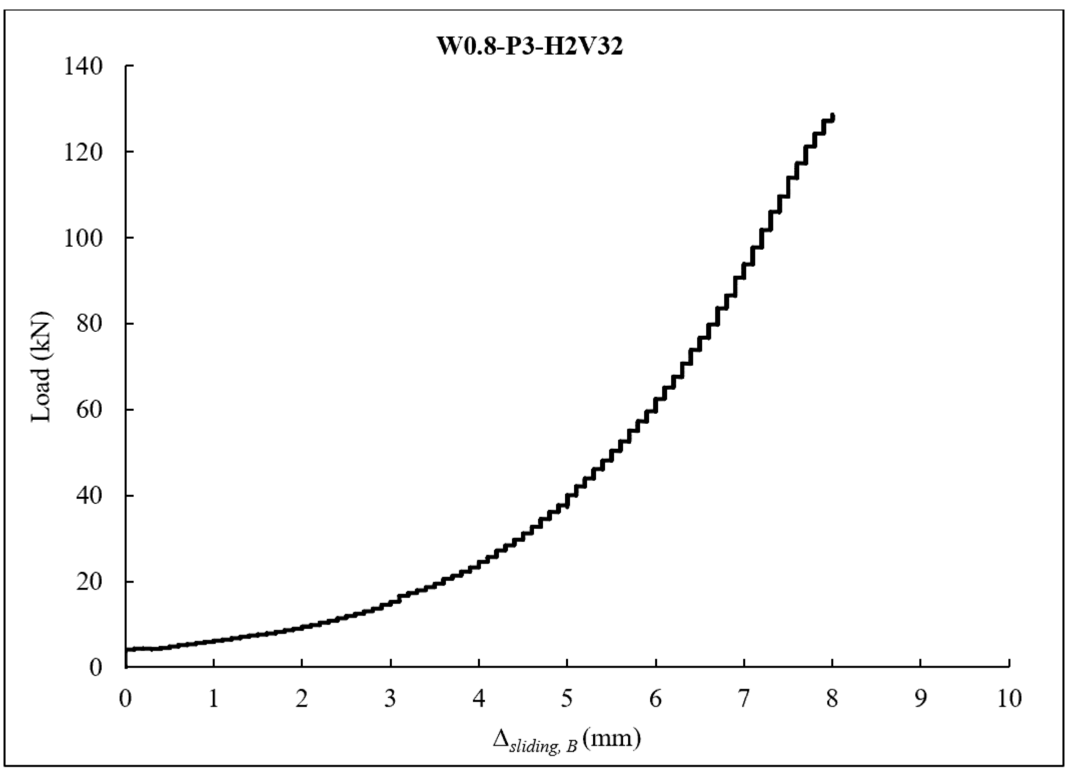
W0.8-P3-H2V32
Load (kN)
140
120
100
80
60
40
20
0
0
1
2
3
4
5
6
7
8
9
10
$\Delta_{sliding,\ B}$ (mm)

(n)

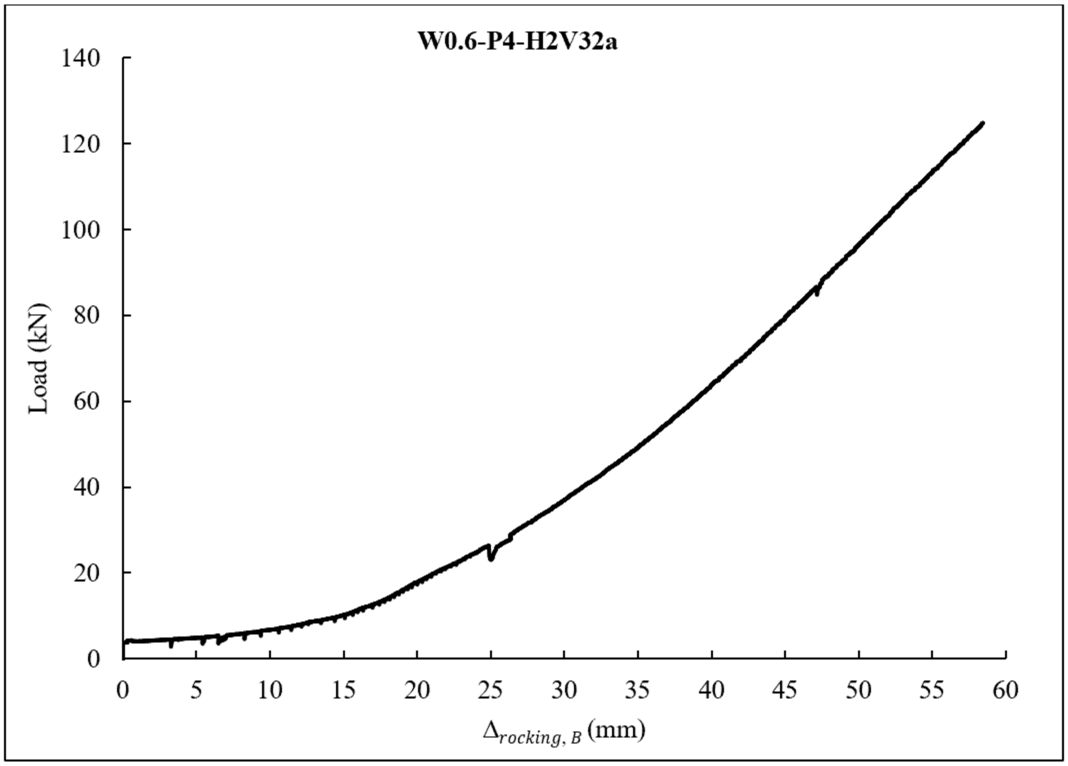
W0.6-P4-H2V32a
Load (kN)
0
20
40
60
80
100
120
140
0
5
10
15
20
25
30
35
40
45
50
55
60
$\Delta_{rocking,\,B}$ (mm)

(o)

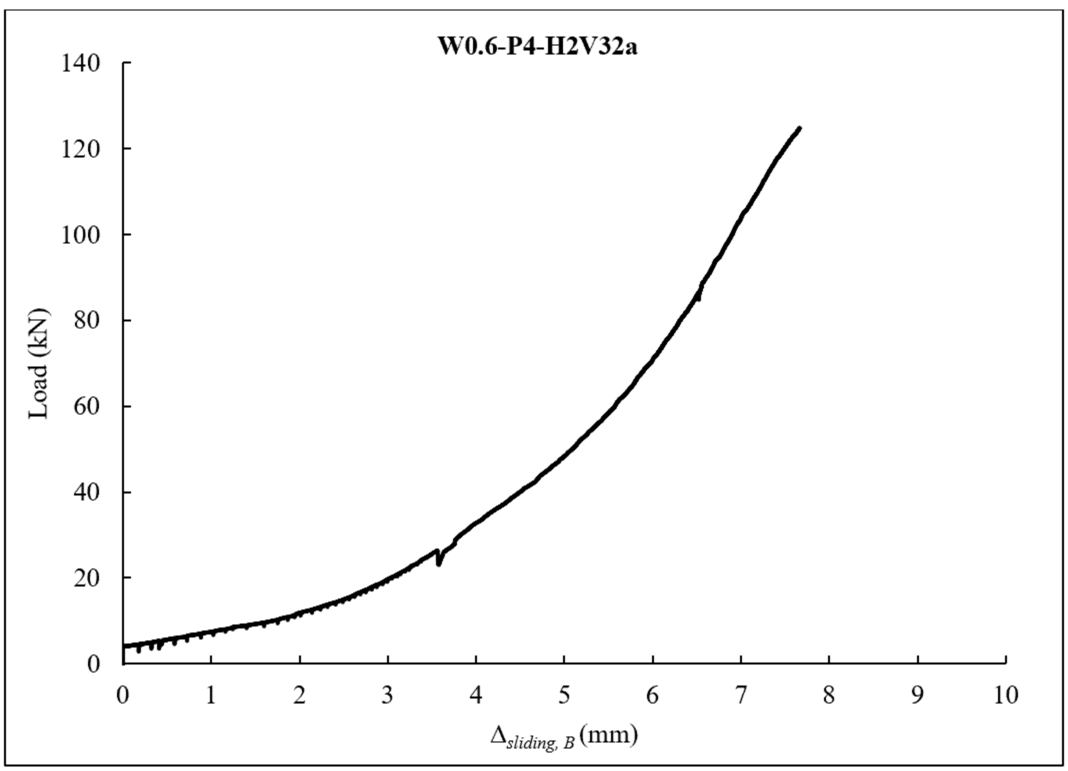
W0.6-P4-H2V32a
Load (kN)
0
20
40
60
80
100
120
140
0
1
2
3
4
5
6
7
8
9
10
$\Delta_{sliding,\,B}$ (mm)

(p)

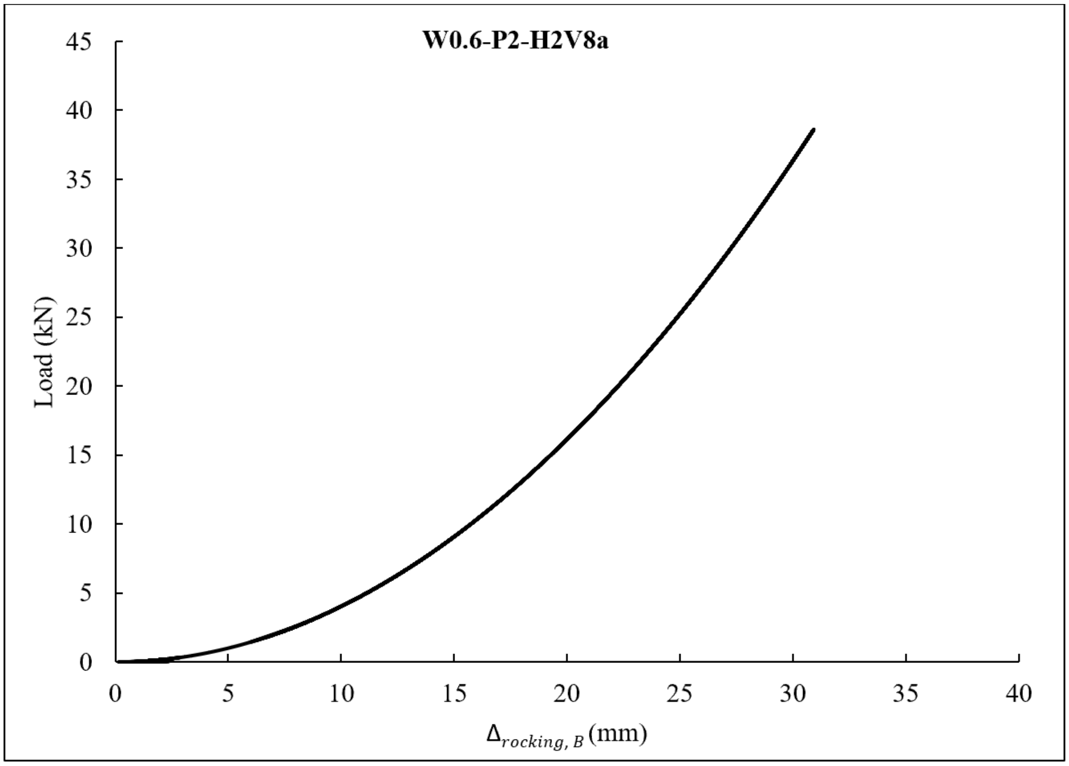

(q)

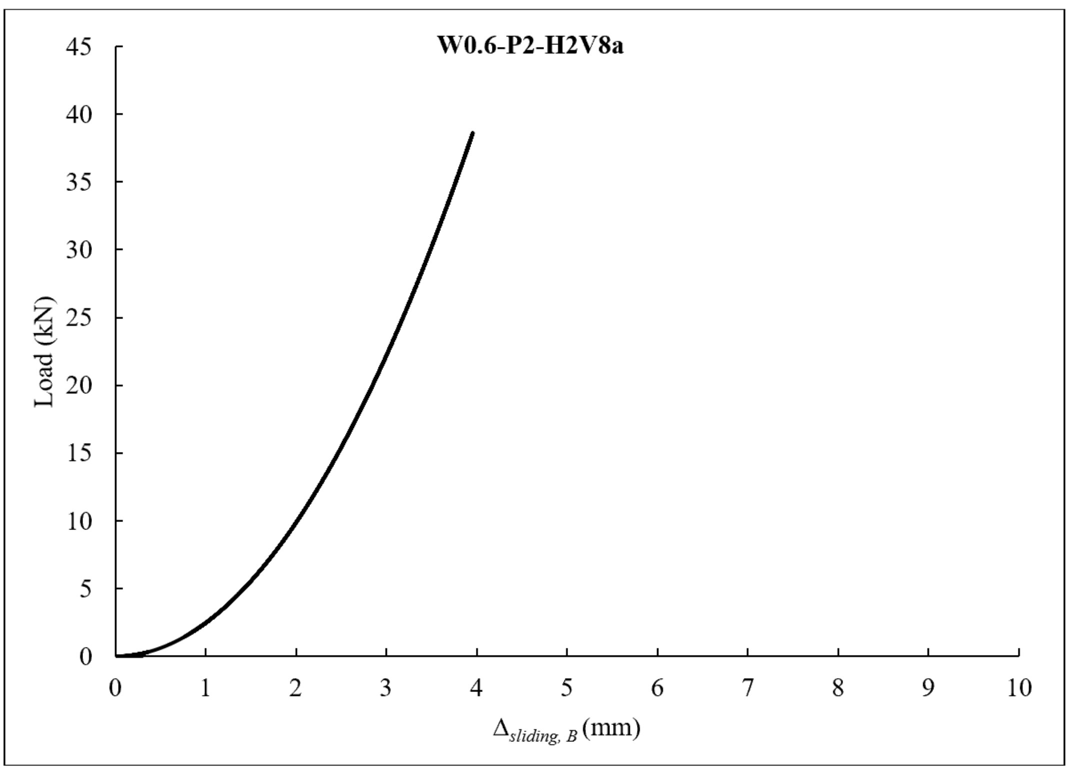

(r)

Figure B.4: *Calculated results of $\Delta_{rocking,B}$ and $\Delta_{sliding,B}$ for tested specimens*

Appendix C.

Estimation of mechanical properties of the foundation beam

In the finite-element (FE) modelling presented in Chapter 6, the deformation of the steel foundation beam was idealised by three non-linear spring elements located at the same positions as those defined in Chapter 6 and Appendix B. These springs were introduced to represent the translational and rotational compliance of the foundation beam observed during the experimental programme.

To derive the constitutive relationships of the individual springs, a simplified static force analysis of the shearwall system was conducted, as illustrated in Figure C.1. The analysis was performed based on the following assumptions:

- Frictional effects between the foundation beam and the supporting system are neglected.
- The shearwall system is treated as a quasi-static system throughout the loading process.
- All springs are idealised as single-direction springs acting independently.
- The vertical springs located at Points A and B are assumed to possess identical stiffness.

Under these assumptions, static equilibrium of the system yields the following reaction forces at the spring locations:

$$R_{Point\ A} = R_{Point\ B} = 1.53F_T \tag{C.1}$$

$$R_{Point\ C} = F_T \tag{C.2}$$

where

F_T denotes the applied lateral load (total load) by actuator,

$R_{Point\ A}$ is reaction force (y-direction) of the spring placed at Point A,

$R_{Point\ B}$ is reaction force (y-direction) of the spring placed at Point B,

$R_{Point\ C}$ is reaction force (x-direction) of the spring placed at Point C.

Since the deformation behaviour of the steel foundation beam has been quantified in Appendix B, the corresponding force-displacement relationships of the equivalent springs can be determined. Consequently, the mechanical properties of the foundation beam, including its translational and rotational stiffness components, can be established. These properties are subsequently implemented in the FE model and are summarised in Figure 6.10.

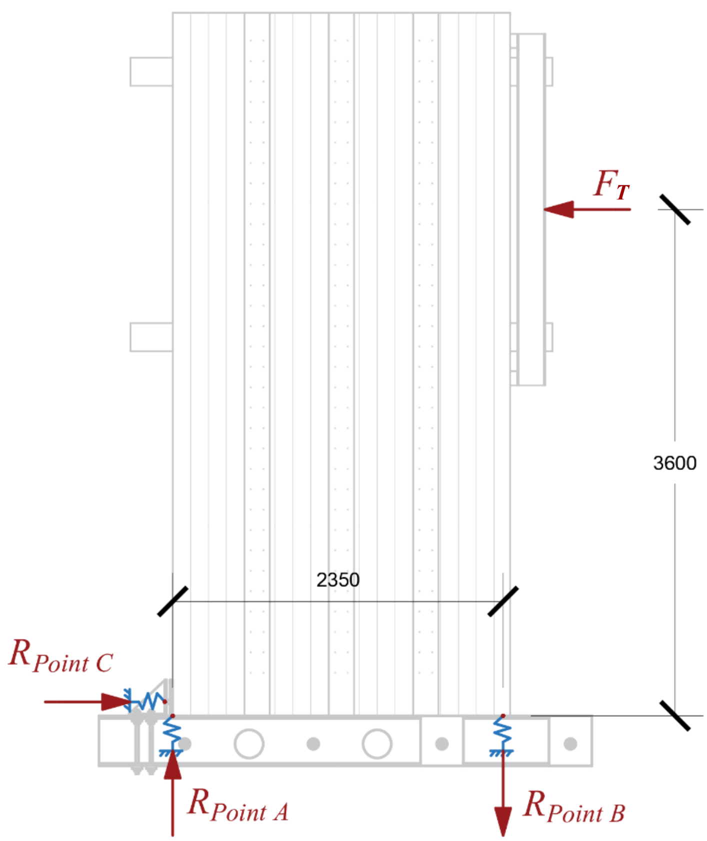

Figure C.1: *Simplified static force model of the shearwall-foundation beam system used for estimating the equivalent spring properties of the steel foundation beam.*

Appendix D.

Re-evaluation of tensile stiffness of hold-down for specimen W0.6-P2-H2V8a

A notable discrepancy was observed between the tensile displacement recorded for the hold-downs in specimen W0.6-P2-H2V8a and the corresponding experimental results reported by Masroor et al. (2024). In addition, a significant mismatch was identified between the FE-predicted total lateral displacement and the experimentally measured response for this specimen. These inconsistencies motivated a re-evaluation of the tensile stiffness assigned to the hold-downs in specimen W0.6-P2-H2V8a.

It is acknowledged that the tensile deformation of hold-downs in this specimen may have been influenced by additional deformation components, such as bending effects, which were observed during testing. Nevertheless, the ultimate tensile resistance of the hold-downs is expected to remain comparable to previously reported values by Masroor et al. (2024). Accordingly, the average maximum tensile resistance of a single hold-down based on Masroor et al.'s study, was adopted as a reference value for re-evaluating the tensile behaviour of the hold-down system.

The re-evaluation procedure was conducted as follows. First, the loading stage corresponding to the peak actuator force of 37.8 kN was identified from the experimental results. At this loading level, the hold-downs were assumed to have reached their maximum tensile resistance of 93.4 kN according to Masroor et al. (2024). A scaling ratio between the actuator load and the corresponding hold-down tensile force was then established. This ratio was subsequently applied to all other loading stages to rebuild the tensile force-displacement relationship of the hold-downs.

Through this procedure, the original tensile properties of hold-down derived by Masroor et al. were adjusted to better reflect the measured global response of specimen W0.6-P2-H2V8a. The corrected tensile stiffness of hold-down was then used in the FE modelling to improve consistency between numerical predictions and experimental observations, which is shown in Figure 6.12.